D4.1

BEACON
Bentonite Mechanical Evolution

Bentonite mechanical evolution – experimental work for the support of model development and validation

DELIVERABLE (D4.1/2)
Report

Author(s): Patrycja Baryla, Fabien Bernachy-Barbe, José A. Bosch, Gemma Campos, Beatriz Carbonell, Katherine A. Daniels, Alessio Ferrari, William Guillot, Carlos Gutiérrez-Álvarez, Jon F. Harrington, Rubén J. Iglesias, Markku Kataja, David Mašín, Jan Najser, Franz Rinderknecht, Thorsten Schäfer, Haiquan Sun, Joni Tanttu, María Victoria Villar, Klaus Wieczorek

Reporting period: 01/12/18 – 31/05/20

Date of issue of this report: **30/08/19**

Start date of project: **01/06/17**   Duration: 48 Months

DISTRIBUTION LIST

Name	Number of copies	Comments
Renata Bachorczyk-Nagy (EC) Christophe Davies (EC) Beacon partners		

Abstract

The objectives of the Beacon experimental studies are to provide input data and parameters for development and validation of models and to reduce uncertainties about conditions and phenomena influencing bentonite homogenisation. Both the homogenisation of an initially inhomogeneous bentonite system and the persistence or development of inhomogeneities in the bentonite system under various mechanical and hydraulic conditions are investigated. Eight experiment teams perform tests involving different bentonite materials and different hydraulic and mechanical boundary conditions.

The experiments performed within Beacon address the hydro-mechanical behaviour of macroscopically homogeneous bentonite materials, (the influence of initial granulometry and of hydro-mechanical paths on the final properties of bentonite, constant load and constant volume tests on the Czech Cerny vrch bentonite), the issue of swelling into a limited void (experiments performed in constant volume cells partially filled with bentonite, at different scales and with different emphases), binary mixtures or artificial inhomogeneities (experiments using bentonite block/pellet or pellet/powder mixtures, and the influence of the degree of saturation on the shearing behaviour at a bentonite – steel interface.

This report is the first Beacon WP4 deliverable on experimental work and presents the status at Beacon mid-term.

Content

1   Introduction

Bentonite plays an important role in the engineered barrier system (EBS) concept in many radioactive waste management programmes. Understanding of the fundamental processes governing bentonite barrier evolution is therefore essential. The Beacon project aims at an increased understanding and modelling capability of the bentonite mechanical evolution, especially with respect to material homogenisation. The key work packages of model development (work package WP3) and model validation (WP5) are using existing experimental data which have been compiled for this purpose in WP2.

The existing database is, however, limited, because the focus has generally been on hydration, and the mechanical part was not always captured or evaluated. Therefore, additional laboratory testing is performed in WP4.

The objectives of the Beacon experimental studies are to provide input data and parameters for development and validation of models and to reduce uncertainties about conditions and phenomena influencing bentonite homogenisation. Both the homogenisation of an initially inhomogeneous bentonite system and the persistence or development of inhomogeneities in the bentonite system under various mechanical and hydraulic conditions are investigated. Eight experiment teams perform tests involving different bentonite materials and different hydraulic and mechanical boundary conditions.

Within the first two years of Beacon, many experiments have been planned and started, and some of them have even been completed. This report presents the current state of experimental work performed in Beacon. It combines the deliverables D4.1 "Homogenisation of an initially inhomogeneous bentonite system – experimental input to model development" and validation and D4.2 "Persistence or development of inhomogeneities in the bentonite system – experimental input to model development and validation". Many f the results presented here are preliminary; the complete results will be found in final WP4 report (Deliverable D4.4) due near the end of the Beacon project.

2   Overview of Work Package 4

Evolution of a bentonite EBS will be influenced by a whole range of conditions and phenomena. The most important are

1. Initial state of the EBS: For bentonite homogenisation or, on the other hand, the evolution of heterogeneity, there will be a difference between initially single density (i.e., a bentonite block) or multi-density (pellets, blocks/gaps, blocks/pellets) systems. In this context, the scale of observation is important (a pellet system might be considered as homogeneous in the large scale, while being highly inhomogeneous on the pellet scale).
2. Hydration conditions and history: Solution composition, thermal and mechanical load and hydration history will have an impact on the evolution of buffer texture, swelling pressure and hydraulic properties.
3. Interplay between heterogeneity and swelling pressure as well as mechanical properties: Evolution of heterogeneities in the buffer will possibly affect the overall swelling pressure and mechanical properties, e.g., shear strength. Especially at interfaces, e.g., between buffer and waste package, shearing behaviour can be relevant with respect to the homogenisation process.

The experiments have been designed to investigate the relevant phenomena. Different bentonites are investigated to broaden the spectrum of observations. Different analysis techniques are applied by different partners, so that a more complete and reliable characterization of bentonite behaviour is obtained, improving the reliability of results.

The experiments performed within Beacon are presented in the chapters 3 to 6. The organisation is as follows:

1. Hydro-mechanical behaviour of macroscopically homogeneous bentonite material: Experiments of EPFL addressing the influence of initial granulometry and of hydro-mechanical paths on the final properties of MX-80 as well as constant load and constant volume tests, performed by CU and CTU, on the Czech Cerny vrch bentonite are found in Chapter 3.
2. Swelling into limited void: Chapter 4 includes experiments performed in constant volume cells partially filled with bentonite. BGS, CIEMAT, JYU and KIT perform respective tests at different scales and with different emphases.
3. Binary mixtures or artificial inhomogeneities: Experiments of CIEMAT and CEA using bentonite block/pellet or pellet/powder mixtures, respectively, are presented in Chapter 5.
4. Chapter 6 deals with EPFL's experiments on the influence of the degree of saturation on the shearing behaviour at a bentonite – steel interface

All the experiments planned and performed in WP4, together with information on the setup, material, experiment conditions, and expected outcome, have been assembled early in the project in an experiment table (Table 2-1) which is meant as a help for WP3/5 to facilitate the selection of tests and data suitable for each modeller's development and validation task. The experiment table is available to the project participants as an excel file on the project web server.

Table 2-1. WP4 experiment table

Identification			Setup		Material					Experiment conditions			Outcome		
Partner in charge	Experiment name	Main objective	Type of experiment	Sample size	Bentonite	Block/granular	Dry density	Initial degree of saturation / water content	Solution	Mechanical boundary conditions	Hydraulic boundary conditions	Temperature	Measurements	Data resolution	Remarks
KIT	SPIN (Single Pellet Investigations - preliminary title)	Density / porosity distribution evolution on pellet-scale and influence on overall buffer permeability	Swelling test, limited volume increase	≈ 10 mm	MX-80	Single pellet	Will be determined	Will be determined	Pearson water	Constant volume cell, limited volume increase of pellet	One-sided re-saturation	Ambient	Spatially resolved - swelling pressure - water content - porosity distribution overall permeability	mm	
BGS	SITS (Swelling in to voids - very preliminary title!)	Evolution in swelling pressure, porosity and denisty as different height blocks of bentonite swell into a fixed volume. Tests repeated with ambient and elevated temperatures at with two different salinities	Swelling test into fixed volume	Diameter 60mm, vessel length 120 mm. Sample length variable.	MX-80	Blocks	Will be determined axially and radially to determine variations after swelling	Will be measured but blocks will start at ≈ 100% to reduce test times	Distilled and NaCl balance to Swedish groundwater	Constant volume with multiple stress measurements	Resaturation from both ends of the vessel	Ambient and 90° C	Spatially resolved: swelling pressure; porosity, water content, density, etc, plus potentially bulk permeability	Around 10 mm for post-mortem sub sampling	
CIEMAT	MGR	Check density homogenisation upon saturation of two materials initially different (pellets/block)	Hydration at constant volume in an oedometer	Cylinder, 100x100 mm	FEBEX (MX-80?)	Combination of block/granular	1.6 g/cm³ (block), 1.3 g/cm³ (pellets)	13.5% (block), 10.1% (pellets)	Deionised water	Constant volume	Saturation through the pellets surface under controlled low flow	Ambient	Water intake, swelling pressure, postmortem (density, water content, MIP, XRD)		
CIEMAT	Window	Check density homogenisation upon saturation of two materials initially different (pellets/block)	Hydration at constant volume in a transparent cell	121x121x20 mm	FEBEX (MX-80?)	Combination of block/granular	1.6 g/cm³ (block), 1.3 g/cm³ (pellets)	13.5% (block), 10.1% (pellets)	Deionised water	Constant volume	Saturation through the pellets surface under low pressure	Ambient	Water intake, images, postmortem (density, water content, MIP, XRD)	mm	Complementary to MGR, qualitative
CIEMAT	GAP liquid	Follow density changes in a block sample saturated under limited axial swelling conditions	Hydration of a block sample with liquid water allowing limited axial swelling (initial gap)	Cylinder, 50x25 mm	FEBEX (MX-80?)	Block	1.65 g/cm³	13.5%	Deionised water	Limited axial swelling (depending on the size of the gap)	Saturation from the surface opposite to the gap	Ambient	Water intake, postmortem (density, water content, MIP)	mm	
CIEMAT	GAP vapour	Follow density changes in a block sample saturated under limited axial swelling conditions	Hydration of a block sample with vapour water allowing limited axial swelling (initial gap). Perforated cell	Cylinder, 38x28 mm	FEBEX	Block	1.7-1.5 g/cm³	14%	Water vapour	Limited axial swelling (depending on the size of the gap)	Saturation from the gap surface	20° C	Water intake, postmortem (density, water content, MIP)	mm	
JYU	Partly constricted swelling experiment - preliminary title	Dry density and water content profiles and axial swelling pressures from both ends of the chamber as a function of time during wetting.	Swelling test, limited volume increase (initial sample 10 mm high with 4 mm gap)	20 mm	Bara Kade	Block	Initially 1.5-1.7 g/cm³	≈ 17% water content	Will be dettermined	Constant volume cell, limited volume increase of block	One-sided re-saturation	Ambient	1D water content and dry density distributions and axial swelling pressure from both ends of the chamber	Sub mm	Full measurement series to be started soon
JYU	Small scale homogenization experiment - preliminary title	Wetting of block-air-block-air... kind of sample and the state of its homogenization as a function of time	Swelling test, limited volume increase	10-20 mm, to be determined	Bara Kade	Block	Will be determined	Will be determined	Will be dettermined	Constant volume cell, limited volume increase of block	Will be determined	Ambient	1D water content and dry density distributions and axial swelling pressure from both ends of the chamber	Sub mm	In planning
CU	Investigation of microstructure, hydraulic and mechanical properties of the Czech bentonite	Description of microstructural changes under different hydraulic paths and mechanical response on the saturation of compacted samples	WRC, MIP, ESEM, swelling experiments in oedometer	5 cm diameter, 1 cm height (oedometer tests)	BCV	Block (oedometer tests)	1,27; 1,6 and 1,9 g/cm³ for WRC, MIP and ESEM. Dry densities for oedometer tests will be determined	Corresponding to initial water content of bentonite powder (≈ 10%)	Distilled water	Constant load swelling + compression (oedometer tests)	One-side saturation (oedometer tests)	Ambient	Swelling under constant load, swelling pressure after re-compression		

Table 2-1. WP4 experiment table (continuation)

Partner	Topic	Objective	Test type	Dimensions	Material	Form	Density	Initial water content	Water	Cell/Apparatus	Saturation	Temperature	Measurements	Resolution/Accuracy	Notes
CTU	Hydraulic and mechanical properties of the Czech bentonite	Hydraulict properties, density distribution, total pressure	Swelling tests - constatn volume and constant load	Constant volume - 3 cm diameter, 2 cm heigh; constant load - 5 cm diameter, 1 cm initial height	BCV, B75	Block	Dual density - 1.3 & 1.7 for constant volume; 1.3 - 1.8 for constant volume; initial 1,27; 1,6 and 1,9 g/cm3 for constatn load	10%	Water	Constant volume cell (attached to permeameter); constant load swelling + compression (oedometer tests)	One side saturation	Ambient and 60°C	Constant volume cells - water intake, total pressure at one end, densiti distrubution at the end; swelling under constant load ("deformation" on each load step)		
CEA	Stress Field evolution during Bentonite Ho-mogeneization (preliminary title)	Density evolution and pressure field on simplified heterogeneities	Isochoric swelling test	Diameter 57 mm	MX-80	Several (>=4) configurations	Will be determined (average ≈ 1.5 g/cm³)	Will be determined	LSMHM synthetic site water	Constant volume cell	One-sided / two-sided re-saturation	Ambient	Axial stress, 9 local pressure sensors (3 heights, 3 radial positions), 3 RH sensors (3 heights)		Post-mortem density and water content local measurements, some MIP
CEA	Tomobento	Qualitative evaluation of the homogeneization of a pellet/powder mix using in-situ X-ray tomography	Swelling test, limited volume increase	Diameter 57 mm	MX-80	Single pellet + powder	Will be determined	Will be determined	LSMHM synthetic site water	Quasi-constant volume cell	One-sided re-saturation	Ambient	3D X-ray absorption coefficient field	30 µm	
EPFL		The influence of initial granulometry on finall as-hydrated state	Isochoric saturation followed by compaction	Height 12.5 mm, diameter 35 mm	MX-80	Granular	Various	Hygroscopic water content	Distilled water	Oedometric cell, radial displacement prevented	Two-sided saturation	Ambient	Swellig pressure, final granulation	Displacement: micron; swelling pressure: 0.6 MPa, saturation pressure: 1 kPa	
EPFL		The influence of initial granulometry on finall as-compacted state	Compaction	Height 12.5 mm, diameter 35 mm	MX-80	Granular	Various	Hygroscopic water content and $w_{init} \approx 20\%$	Distilled water	Oedometric cell, radial displacement prevented	For samples of $w_{init} = 20\%$ - saturation by vapour equilibrium technique	Ambient	Final void ratio, final granulation	Displacement: micron; swelling pressure: 0.6 MPa, saturation pressure: 1 kPa	
EPFL		The influence of the different hydro-mechanical paths on finall macroscopic properties and local homogeny of compacted samples	Free swelling; free swelling followed by compaction: isochoric saturation followed by compaction	Height 12.5 mm, diameter 35 mm	MX-80	Granular	1.4 kg/cm³	Hygroscopic water content	Distilled water	Oedometric cell, radial displacement prevented	Two-sided saturation	Ambient	Final void ratio after each type of experiment, finall pore size distribution, swellig pressure in case of isochoric saturation test	Displacement: micron; swelling pressure: 0.6 MPa, saturation pressure: 1 kPa	
EPFL		Volumetric response of bentonite sample during air injection phase	Isochoric saturation followed by the measurement of water permeability and gas injection	Height 20 mm, diameter 40 mm	MX-80	Granular	1.4 kg/cm³	Hygroscopic water content	Distilled water	Triaxial cell	Two-sided saturation	Ambient	Radial and axial swellig pressure, coefficient of permeability, volumetric responce on air injection	Displacement: micron; swelling pressure: 0.8 MPa, saturation pressure: 1 kPa	
EPFL		Influence of the degree of saturation on the shearing behaviour at the bentonite – steel interface	Isochoric saturation using vapour equilibrium technique followed by shearing test	Height 15 mm, base 30x30 mm	MX-80; FEBEX	MX-80: granular; FEBEX: blocks	To be determined	To be determined	Various	Direct shear apparatus	Two sided saturation with vapour equilibrium technique	Ambient; (60° C)	Swellig pressure; interface friction angle; interface adhesion	Displacement: micron; swelling pressure: to be determined, saturation pressure: to be determined	

3 Hydro-mechanical behaviour of macroscopically homogeneous bentonite material

3.1 Influence of initial granulometry on final state – isochoric hydration followed by compaction (EPFL)

Segregation during bentonite emplacement is one of the issues that could be encountered in nuclear waste repositories that consider granular bentonite as a sealing material. This would lead to an initial heterogeneity in bentonite grain size distribution (GSD) within a given section in the repository. In order to determine the influence of the initial GSD on the final (as-saturated) state of granular MX80 bentonite, a series of laboratory tests were conducted at EPFL. Three granulations were tested and compared. The hydration process, as well as saturated states as a function of the initial states were studied.

3.1.1 Tested material

The tested material is granular MX-80 bentonite. Some basic and index properties are reported in Table 3-1 (after Seiphoori et al. 2014). Dry density of the grains is approximately equal to 2.1 Mg/m^3.

Table 3-1. Basic properties of the MX80 bentonite used in the tests

Smectite content	Specific surface	Specific gravity	Liquid limit	Plastic limit
85%	523 m^2/g	2.74	420%	65%

Samples characterised by three types of GSD, corresponding to Fuller-type, unifractional and bifractional, as shown in Figure 3-1, were tested.
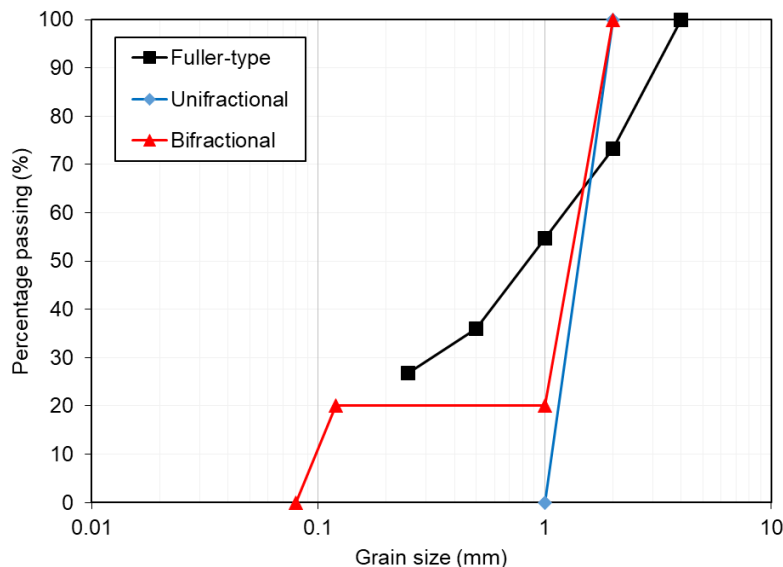
Figure 3-1. Grain size distribution (GSD) curves of the samples tested

The Fuller-type GSD is characterised by a curvature coefficient Cc=1.3 and uniformity coefficient CU = 13.38, and corresponds to the recommended site granulation to be used in

the Swiss concept of high level radioactive waste disposal (Plötze and Weber, 2007). In the as-poured state, the dry density of the samples characterized by this granulometry is around 1.50 Mg/m^3. The unifractional GSD consists 100% of the fraction 1-2 mm, characterised by a curvature coefficient Cc=0.77 and uniformity coefficient CU =1.43, leading to a dry density in the as-poured state of around 1.30Mg/m3. The bi-fractional granulation is composed by 80% of the fraction 1-2 mm and 20% of the fraction 0.08-0.125 mm, a curvature coefficient Cc=7.87 and a uniformity coefficient CU =14, resulting in a dry density around 1.45 Mg/m^3 at as-poured state.

3.1.2   Experimental setup

Tests were performed using a high-pressure oedometric cell. A complete description of the apparatus is provided in Ferrari et al. (2016). The cell is made of stainless steel and holds an oedometric ring with height of 12.5 mm and diameter of 35.0 mm. This ring is inserted into a high-rigidity cylindrical cell (Figure 3-2a). The top and the bottom of the sample are in contact with metallic porous plates, which are connected to the drainage lines (Figure 3-2b).

The cell is placed in a high-stiffness frame equipped with a hydraulic jack, which allows to control the axial total stress up to 100 MPa (resolution of 0.06 MPa) (Figure 3-3). The vertical displacement is measured by LVDTs (resolution of 1 μm) fixed on the upper part of the oedometric cell.

Water is supplied with a Pressure/Volume (PV) controller (resolution of pressure control of 1kPa), from the bottom and top bases of the oedometric cell (Figure 3-2b).
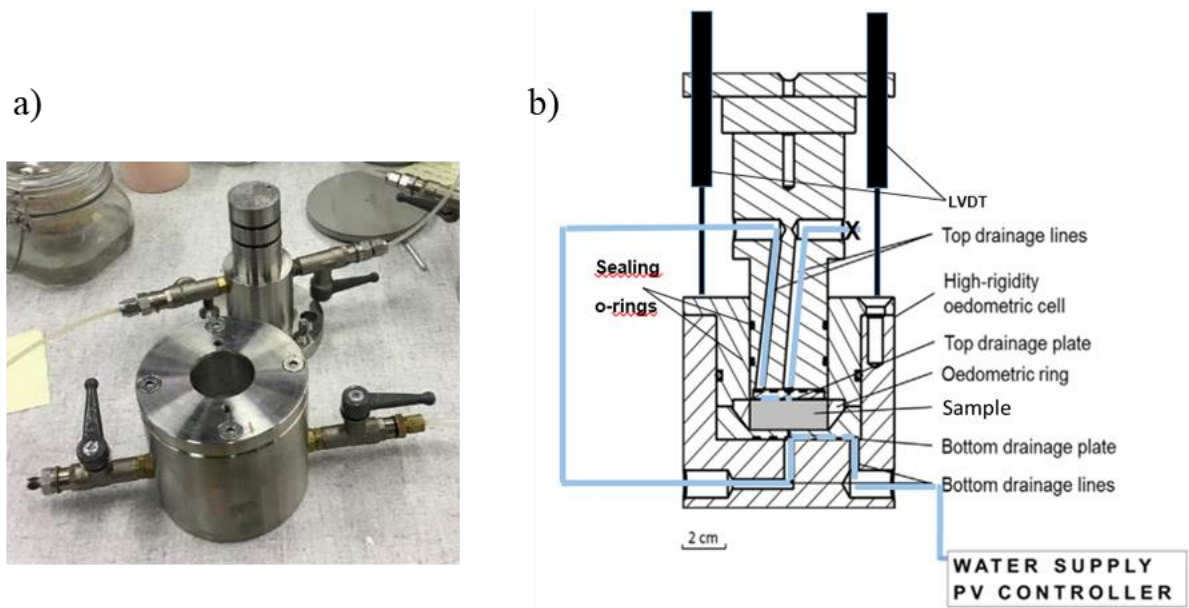
Figure 3-2. (a) High-rigidity oedometric cell. (b) Schematic layout of the cell showing the drainage system
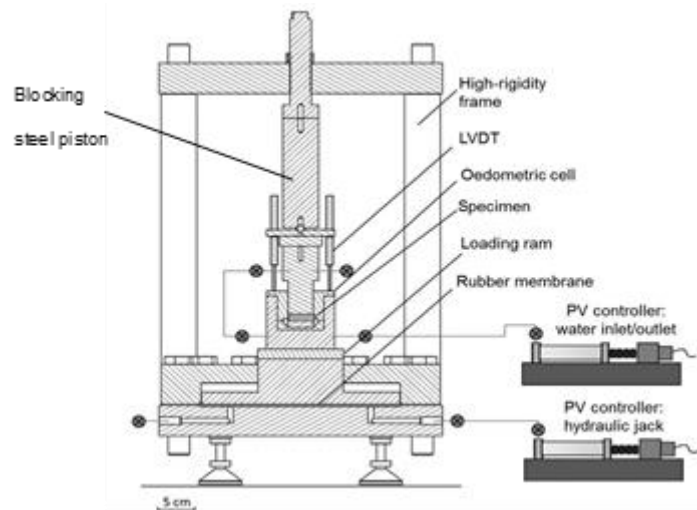
Figure 3-3. Schematic layout of the test for saturating the sample with liquid water in isochoric conditions

3.1.3 Testing procedure

The granular MX80 bentonite at hygroscopic conditions was poured into the oedometric cell. As in the Swiss concept of repository, this corresponded to the initial state.

Inside the oedometer, samples were hydrated up to equilibration with distilled water in liquid phase following two different paths as shown in Figure 3-4; point A corresponds to the initial state of the samples (as poured state). Water pressure applied in both cases was constant at 20 kPa.
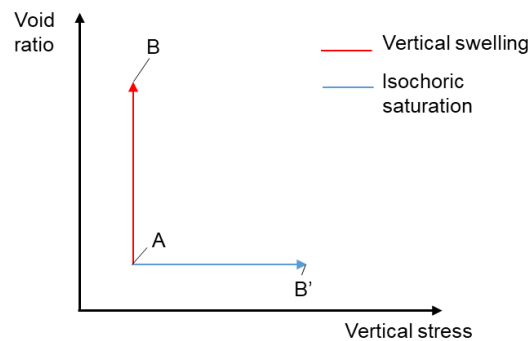
Figure 3-4. Hydro-mechanical paths followed to study the influence of initial granulation

The first wetting scenario (wetting path A-B) included saturation in oedometric conditions (radial displacement prevented) with a low constant vertical load of 20.78 kPa, allowing free vertical (axial) swelling conditions. To minimize friction effects, the surfaces in contact with the samples, as well as all sealing rings of the oedometric cell, were lubricated with grease.

The second wetting scenario (path A-B') involved isochoric hydration. To prevent volume changes during hydration, vertical displacement was constantly monitored and controlled. The maximum vertical displacement was 0.6%, corresponding to a maximum variation of dry density of 0.01 Mg/m^3.

Initial state of the samples tested are summarized in Table 3-2 (isochoric saturation) and Table 3-3 (free swelling saturation). Total suction at hygroscopic conditions was measured using a

12

chilled-mirror WP4c psychrometer. Of particular interest is the dependency of the initial dry density on granulation. Samples of the Fuller-type (series P) were further used to study the stress path dependency response (see Section 3.1.2).

Table 3-2. Nomenclature, grain size distribution and initial state of the samples subjected to isochoric hydration

	Grain size distribution	Degree of saturation (-)	Water content (-)	Total suction (MPa)	Dry density (Mg/m^3)	Void ratio (-)
P2-1	Fuller-type	0.20	0.06	104.20	1.49	0.85
P2-2		0.20	0.06	106.36	1.49	0.84
GU-1	Unifractional	0.14	0.06	92.98	1.31	1.10
GU-2		0.16	0.07	101.28	1.30	1.12
GB-1	Bifractional	0.21	0.07	97.41	1.44	0.91
GB-2		0.22	0.07	91.07	1.45	0.90

Table 3-3. Nomenclature, grain size distribution and initial state of the samples subjected to hydration allowing vertical swelling

	Grain size distribution	Degree of saturation (-)	Water content (-)	Total suction (MPa)	Dry density (Mg/m^3)	Void ratio (-)
P1-1	Fuller-type	0.20	0.06	99.49	1.48	0.86
P1-2		0.19	0.06	98.73	1.47	0.87
P1-3		0.23	0.07	90.45	1.50	0.83
GU-3	Unifractional	0.15	0.07	101.28	1.27	1.16
GU-4		0.16	0.07	94.04	1.27	1.16
GB-3	Bifractional	0.18	0.07	91.07	1.44	0.91
GB-4		0.25	0.08	90.86	1.45	0.89

3.1.4 Results

In the following sections the results obtained are summarised. The sign convention used is negative for expansion strains and tensile stress; and positive for contractive strains and compression stress.

Isochoric saturation

The applied vertical strains and development of swelling pressure for two samples with Fuller-type GSD, upon hydration under isochoric conditions is represented in Figure 3-5. Before hydration, a total axial stress of 0.19 MPa was applied in order to ensure contact of the sample with the set up.

13
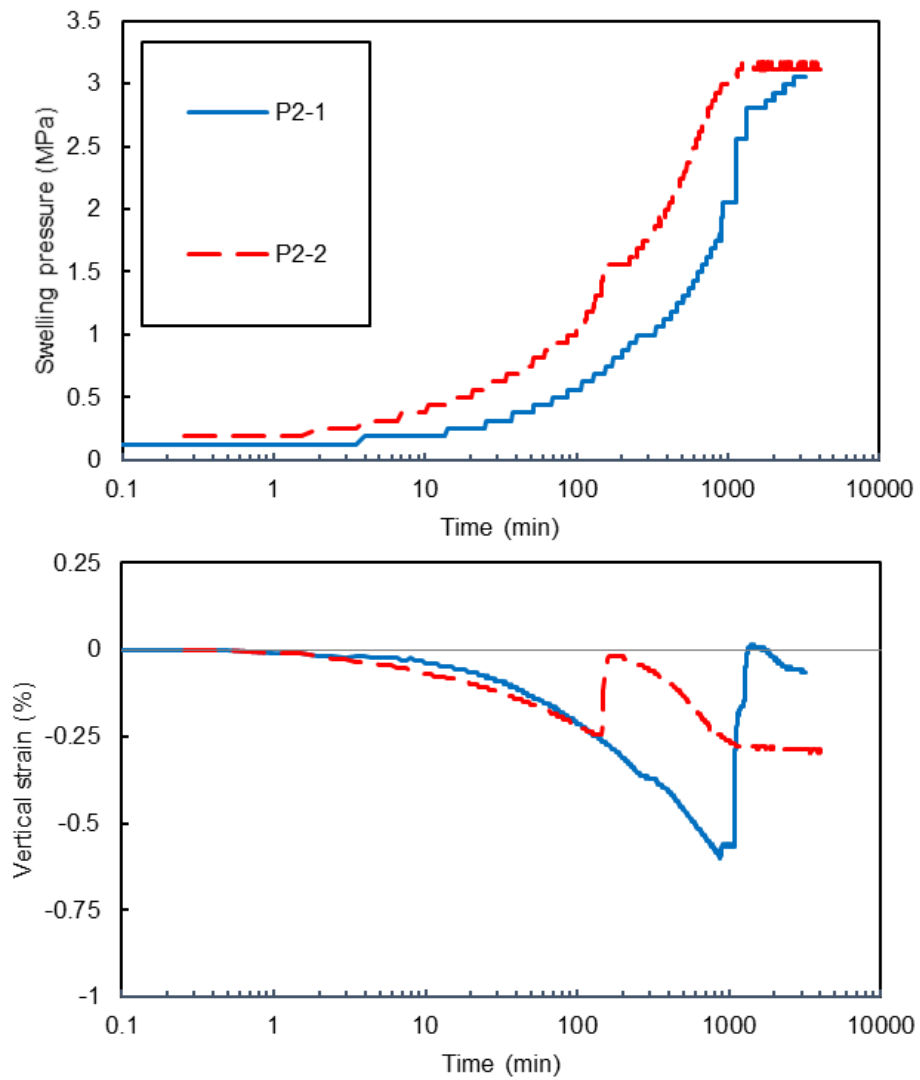
Figure 3-5. Evolution of swelling pressure and vertical strain applied in time during isochoric saturation of samples characterized by a Fuller-type grain size distribution

The vertical strains and swelling pressure in time of the samples with unifractional GSD, upon hydration under isochoric conditions is represented in Figure 3-6.
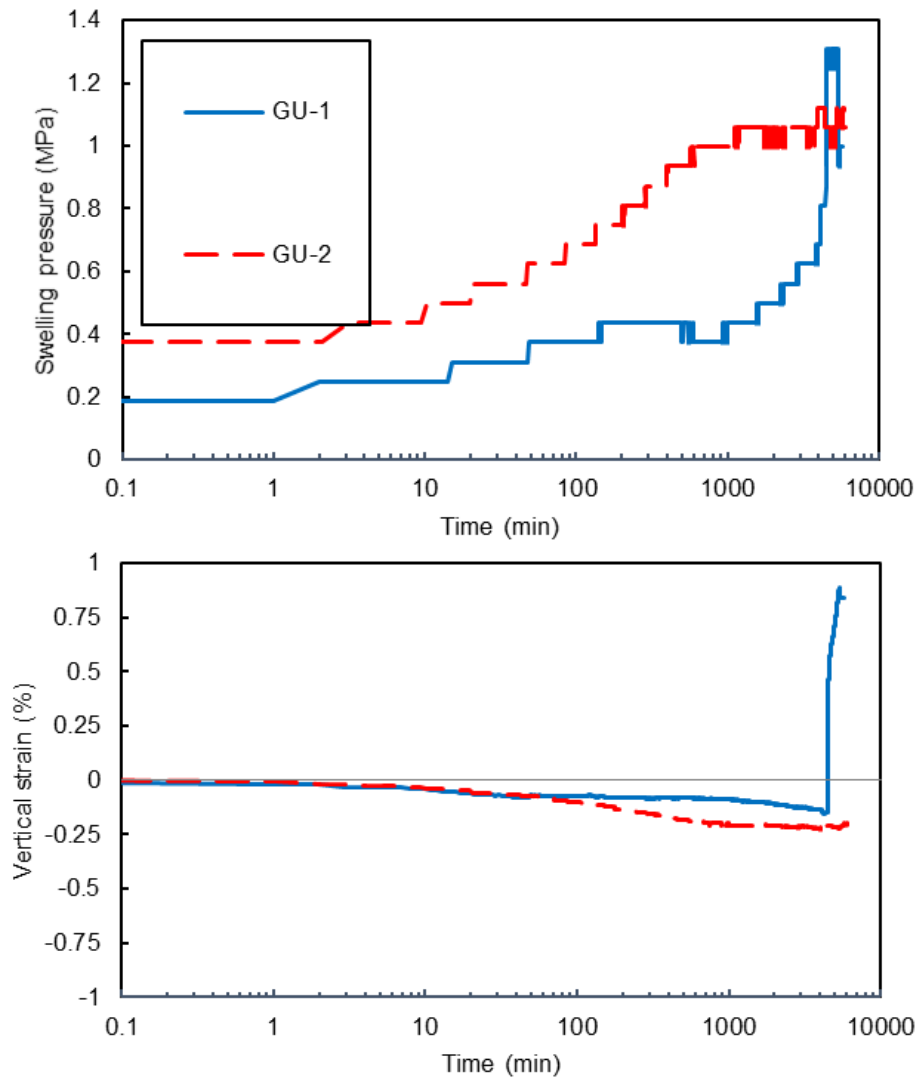
Figure 3-6. Evolution of swelling pressure and vertical strain applied in time during isochoric saturation of samples characterized by a unifractional GSD

The applied vertical strains and corresponding development of swelling pressure upon hydration for two samples with bifractional GSD, is represented in Figure 3-7.

The swelling pressure developed in a slightly different way for each sample. An important factor influencing the course of wetting process was the manual increase of the swelling pressure. The time of the intervention and the value of pressure increment affected the stabilization time of the saturation process as well as the axial swelling. Nevertheless, final values of swelling pressure at equilibrium were fairly similar for samples having the same granulation.
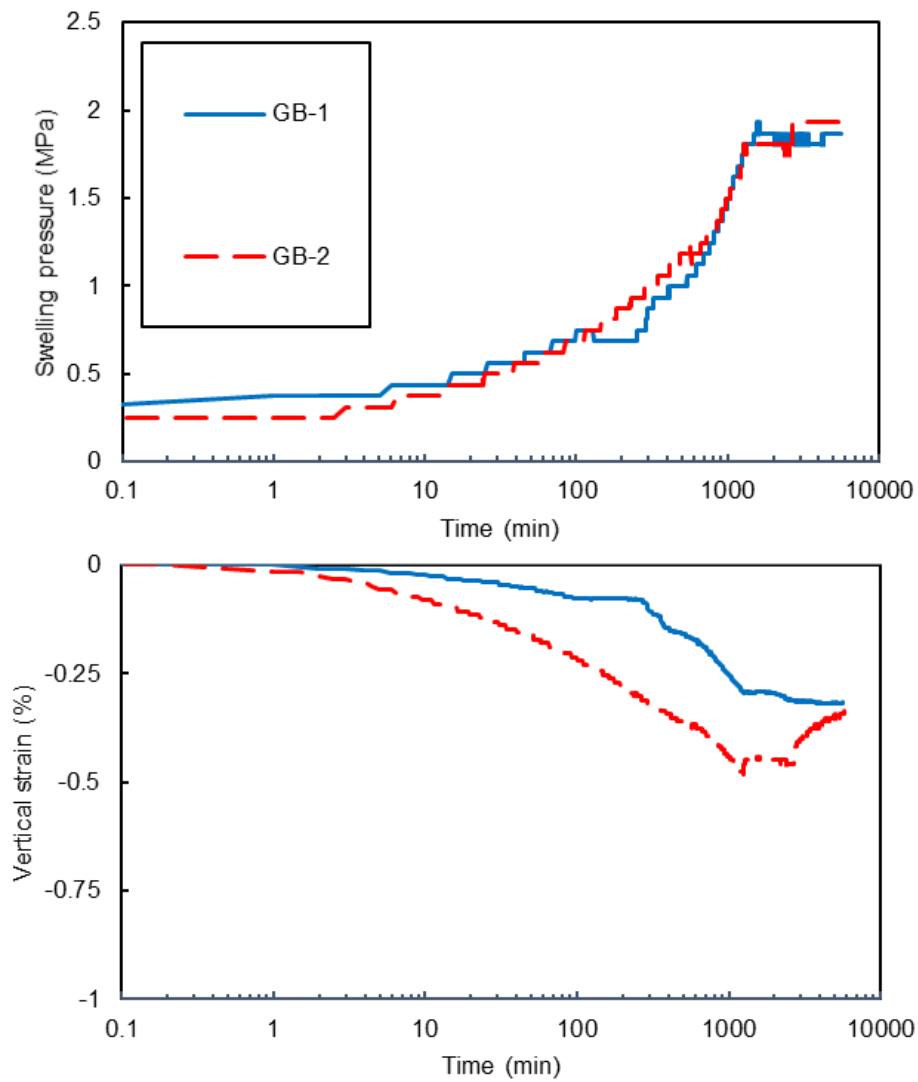
Figure 3-7. Evolution of swelling pressure and vertical strain applied in time during isochoric saturation of samples characterized by a bifractional grain size distribution

A dependency between final value of swelling pressure and granulation can be observed. Unifractional samples reached the lowest values of swelling pressure. This can be explained by the different dry densities achieved upon pouring the granular material with different granulations. Overall, the obtained values of swelling pressure as a function of dry density are in agreement with the tendency reported in the literature for MX80 bentonite (Figure 3-8).
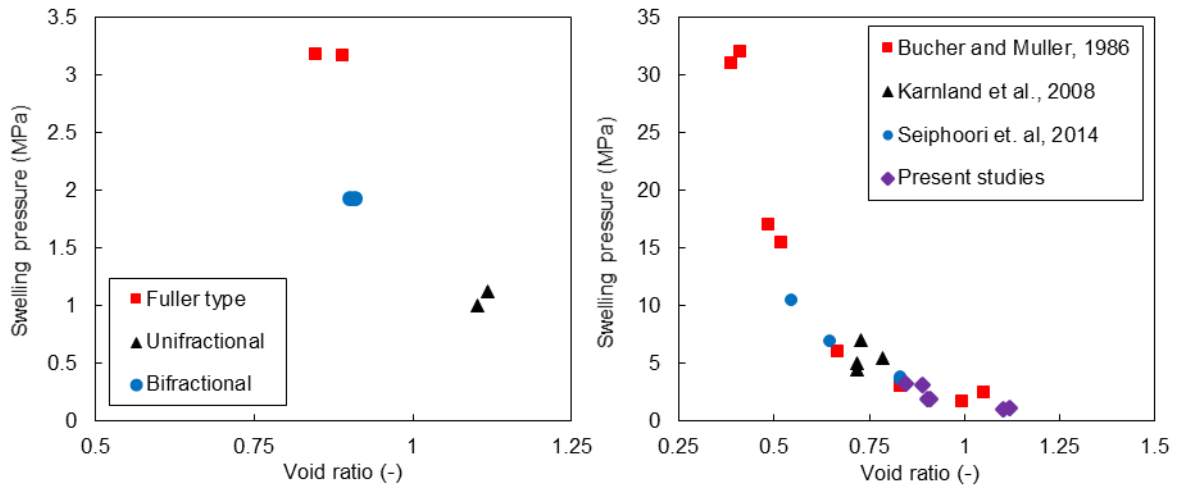
Figure 3-8. Left: Relationship between void ratio and swelling pressure of tested samples. Right: comparison with the values reported in the literature (data from Bucher and Müller-Vonmoos, 1989; Karnland et al., 2008; Seiphoori, 2014)

Vertical swelling tests

In Figure 3-9 the evolution of axial displacement of the samples with Fuller-type GSD hydrated under vertical-free swelling conditions is presented. Initially all samples swelled with the same rate, up to vertical strains around 50%. After around 300 minutes of hydration, the swelling process developed slightly different for each sample. Nevertheless, the final value of vertical strain stabilized at 80% for all samples.
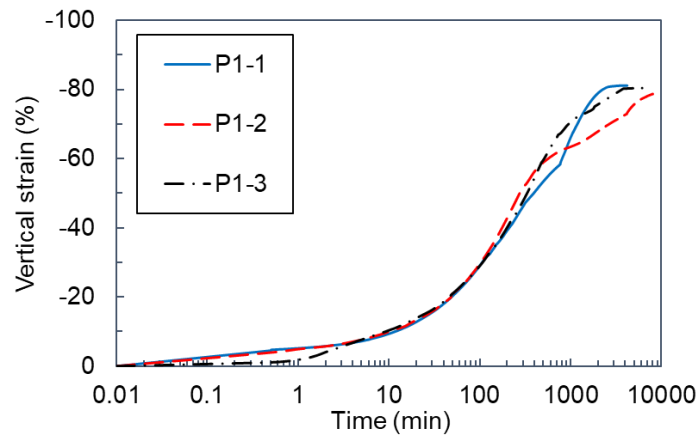
Figure 3-9. Evolution of vertical (axial) strain in time during free swelling saturation of samples characterized by a Fuller – type GSD

The hydration of two samples with unifractional GSD developed in a very similar trend (Figure 3-10). The process stabilized after around 1700 minutes.
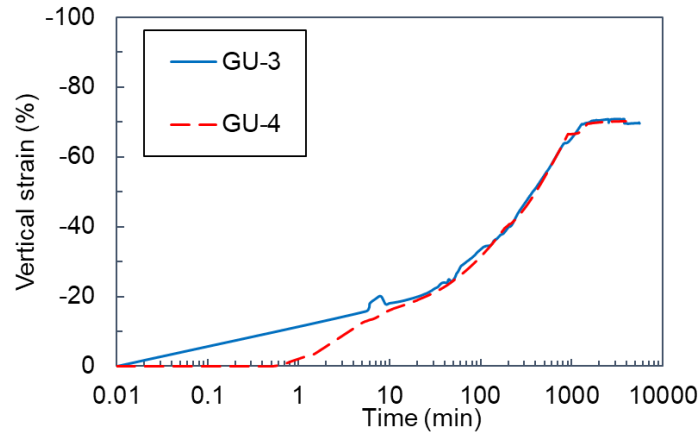
Figure 3-10. Evolution of vertical (axial) strain in time during free swelling hydration of samples characterized by a unifractional GSD

The development of swelling strains upon hydration for two samples with a bifractional GSD is presented in Figure 3-11. Initially both specimens swelled with similar increment rate. Afterwards, swelling trends differed significantly. Although the saturation process of both samples reached the stabilization after a similar time, the final values of vertical strains differed by 10%.
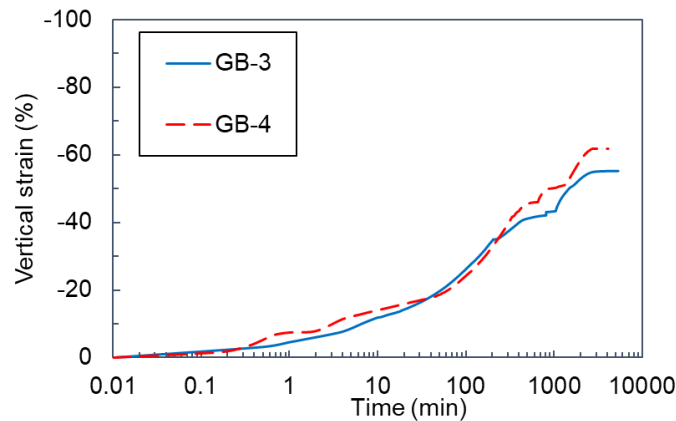
Figure 3-11. Evolution of vertical (axial) strain in time during free swelling saturation of samples characterized by a bifractional GSD

As with swelling pressure tests, the swelling process developed slightly different manner for each bentonite sample. In Figure 3-12 the final vertical strains are presented as a function of initial dry density for all tested samples.
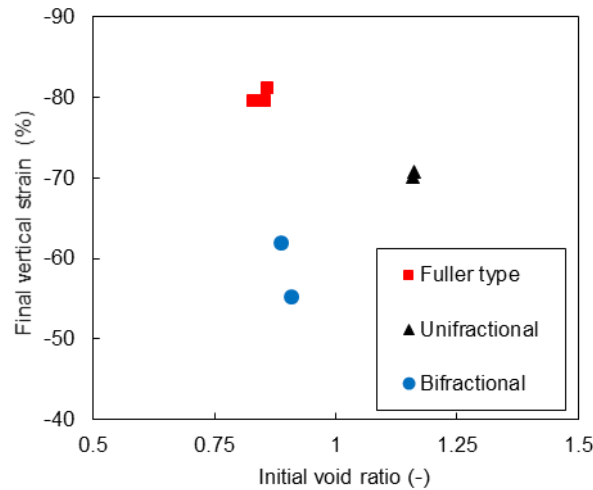
Figure 3-12. Final axial strain upon free swelling as a function of void ratio for different gain size distributions

Data in Figure 3-12 suggests that there is not a direct relationship between initial void ratio and swelling potential when different granulations are compared. The initial dry density of the samples characterised by a unifractional granulation (1.27 Mg/m^3) was lower than for a bifractional granulation (1.45 Mg/m^3); however, final values of vertical strains of the former granulation are 10-15% higher. This result indicates that not only dry density, but also initial granulation, should be considered when analysing swelling phenomenon. As shown in Figure 3-11, the swelling process for the samples with a bifractional granulation presented a transition zone, with some perturbations, which most likely affected the final value of swelling strains. It is also remarkable the higher dispersion of vertical strains of the samples with a bifractional granulation with respect to the other two granulations.

3.2   Influence of different hydro-mechanical paths on final macro-scopic properties and local homogeneity of compacted samples (EPFL)

Mechanical behaviour of active clays is highly stress-path dependent. For instance, the swelling pressure measured after wetting under isochoric conditions from the as-compacted state is usually different from that obtained after free swelling and compression to the initial densitiy. It is commonly accepted that microstructural evolution is the main cause of such observations (Gens & Alonso 1992). In this section, a set of experiments at the laboratory scale with the objective of assessing the influence of different hydro-mechanical paths on the final state of bentonite is presented. These tests have been complemented with microstructural observations at different stages by means of Mercury Intrusion Porosimetry (MIP) and scaning electron microscopy (SEM) techniques.

3.2.1   Experimental setup

The high pressure oedometric set-up described in section 1.2 was used to perform the tests. Vertical stress was applied by means of a hydraulic jack, in which the pressure is maintained by a pressure/volume controller. The application of high confining stress is not instantaneous and depends on the performance of pressure/volume controller, compressibility of the apparatus and compressibility of the tested material itself (Ferrari et al., 2016). Measured deformations were corrected accounting for these factors.

3.2.2   Tested material

The tested material is granular MX-80 bentonite, as presented in Section 3.1.1. All tests have been performed on samples with an initial grain size distribution corresponding to the Fuller-type distribution (see Figure 3-1).

3.2.3   Test procedure

The samples reported in Section 3.1.1 with a Fuller-type granulation saturated at constant volume and free axial swelling were further subjected to compression stages. A schematic view of the testing paths followed is shown in the "void ratio – vertical stress" plane in Figure 3-13, including the points at which microstructural testing with MIP and SEM were performed.
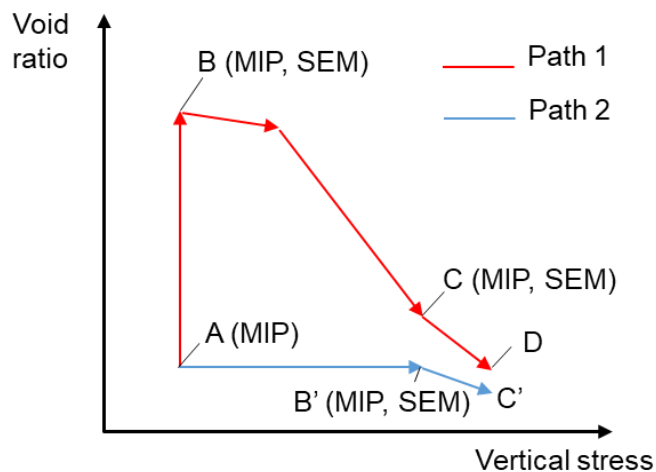
Figure 3-13. Schematic view of the testing program in terms of void ratio and vertical stress. Initial point is in both cases denoted by A and corresponds to the as–poured, hygroscopic state. The points at which MIP tests and SEM observations ere performed are also shown

The initial state of the samples corresponded to the as–poured and hygroscopic condition, with void ratios around 0.85, water content in the range of 0.06-0.07 and a total suction between 150 MPa and 170 MPa; the specific initial conditions of the tested samples are given in Table 3-2 and Table 3-3 (series "P").

Deaired, deionized water at a constant pore water pressure of 20 kPa was applied in all the stages of the experiments (saturation and loading).

Path 1 (A–B–C–D) consisted in the following two stages:

- A–B: Hydration under a constant vertical stress of 21 kPa. The stage finished once swelling strains stabilized with time.
- B–C–D: Increase of vertical stress in steps up to 20 MPa.

Path 2 (A–B'–C') consisted in following two stages:

- A–B': Hydration in constant-volume conditions. Vertical stress was increased according to the observed displacements in order to maintain as much as possible isochoric conditions. This stage finished once swelling pressure stabilized with time.
- B'–C': Increase of vertical stress in steps up to 20 MPa.

Three samples were prepared for each of the two paths; this allowed to perform MIP analyses at intermediate states of the hydro-mechanical loadings. The applied sequence for each sample is summarised in Table 3-4.

Table 3-4. Nomenclature for the samples involved in the experimental program

	Sample	Sequence (see Fig. 6)	MIP and SEM
Path 1	P1-1	A-B	At point B
	P1-2	A-B-C	At point C
	P1-3	A-B-C-D	No
Path 2	P2-1	A-B'-C'	No
	P2-2	A-B'	No
	P2-3	A-B'	At point B'

3.2.4   Results

Free swelling saturation followed by oedometric compression

The results of the two paths in terms of void ratio and total vertical stress are shown in Figure 3-14 for the samples P1-3 and P2-1. The evolutions of void ratio (Path 1, stage A-B) and vertical stress (Path 2, stage A-B') during the previous stages are also shown in the figure. Void ratios are computed accounting for the displacement recorded for each load increment, corrected to take into account the deformation of the set-up. Vertical effective stress can be computed considering that a constant back-pressure of 20 kPa was maintained during all the experiments.

MIP is available at point C (vertical stress of 3.24 MPa) from sample P1-2.
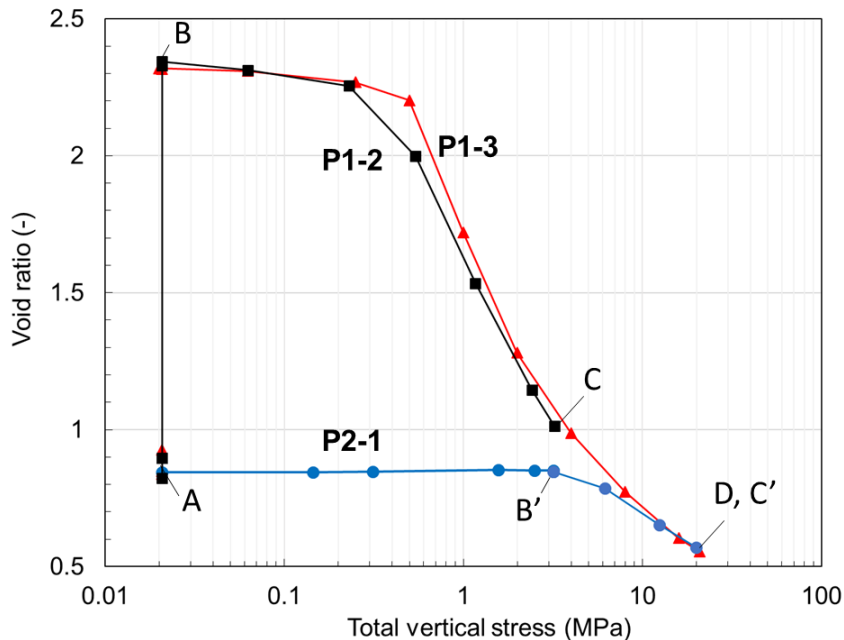
Figure 3-14. Results of the oedometric compression tests after saturation under constant axial stress (P1-2 and P1-3) and constant volume conditions (P2-1).

A clear effect of the stress path followed is observed comparing the final state of samples P1-2 and P2-1. Despite having the same degree of saturation and being subjected to the same

21

final value of vertical stress, a difference in void ratio of 0.13 (15% of initial void ratio) between the two samples was obtained.

Nevertheless, upon further compression this difference seems to decrease, as it can be seen comparing the compression curves of samples P2-1 and P1-3. Both samples followed the same asymptotic line once vertical stress exceeded 12 MPa. At the final state, at a vertical pressure of 20 MPa, both samples reached the same void ratio.

3.2.5   Microstructural analysis

The microstructure of the MX-80 granular bentonite was analysed by three techniques: Micro Intrusion Porosimetry (MIP), Scanning Electron Microscopy (SEM) and Micro Computed Tomography MCT. MIP was used to analyse the microstructure of all tested samples. The SEM observations were conducted for samples with Fuller-type GSD subjected to different hydro-mechanical conditions. Results of MIP and SEM are presented in the following.

Mercury Intrusion Porosimetry

Samples preparation

MIP technique requires full removal of the pore liquid. To minimize shrinkage effects upon drying, freeze drying technique was applied. Saturated samples were sub-cored by means of a cutting rode and dry. Sub-cored specimens were subsequently frozen in liquid nitrogen (boiling point of -196°C) and dried by sublimation inside a vacuum chamber (at 0.06 mbar and -52°C) for 24 hours. In Figure 3-15, the saturated sub-cored specimens and samples during freeze drying are presented.

Figure 3-15. Sub-cored samples before (left) and during (right) freeze drying

Testing procedure

Freeze-dried specimens were placed inside the dilatometer which was directly inserted into the MIP apparatus. Tests were carried out using a Thermo Electron Corporation MIP apparatus.

Two levels of porosity are usually distinguished from MIP tests in double-structured clayey materials. These are commonly classified between intra-aggregate (micropores) and inter-aggregates (micropores). Several criteria have been proposed in the literature to separate between the two levels. In the present study the distinction between the inter-aggregate and intra-aggregate porosity is done based on the observation of intrusion/extrusion cycles, following the method proposed by (Delage and Lefebvre, 1984). The main idea of the method is that the first intrusion of mercury fills all the accessible and interconnected pore space, giving the distribution of total porosity. After complete release of the intrusion pressure,

due to the 'ink-bottle' effect caused by clay aggregates, only some portion of the mercury is released out of the non-constricted pores. A second intrusion will follow approximately the same extrusion path, thus defining the free porosity (Romero et al., 1999). The difference between the porosity recovered by the mercury intrusion and extrusion describes the entrapped porosity, related to the inter-aggregate porosity. The free porosity is consequently associated with the intra-aggregate porosity.

Influence of hydro-mechanical path on the microstructure of saturated MX80 bentonite

In Figure 3-16, the Pore Size Distribution (PSD) of the as-poured state (Seiphoori, 2014) obtained from MIP can be compared with the PSD of the sample P2-3 saturated in isochoric conditions. Both samples were prepared according to the Fuller-type granulometry.

In the as-pored state the PSD has a bimodal character with peaks around 0.01 μm (intra-grain) and 14 μm (inter-grain porosity). The PSD of the sample saturated in isochoric conditions has several modes. Upon saturation, assemblages with intra-aggregate pores with a diameter around 0.03 μm were identified. Some larger aggregates were created with a dominant inter–aggregate pore size around 0.3 μm. A third peak, around 30 μm, suggests that some of the initial pores were preserved upon saturation. The pores larger than 80 μm are probably artefacts of sample preparation (freeze drying technique application) and were not totally resolved by MIP analysis.
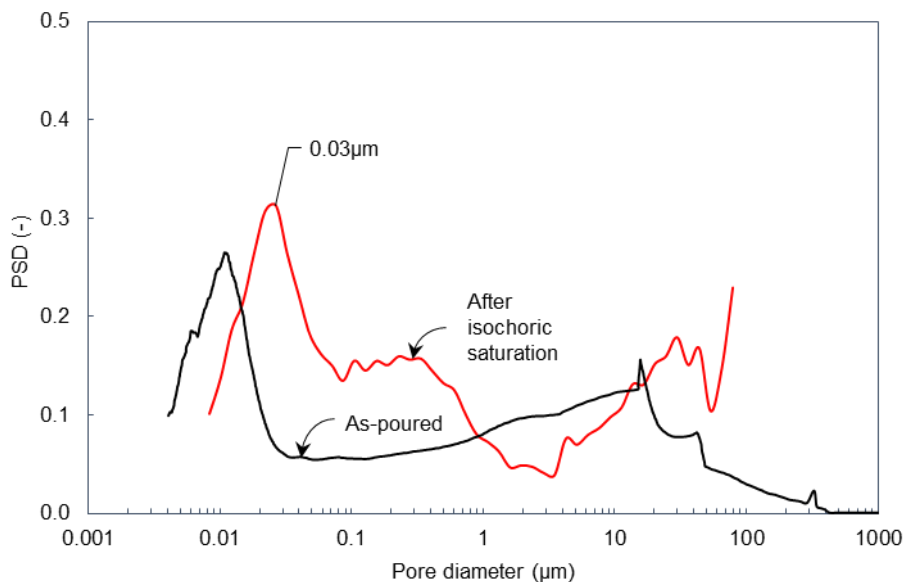
Figure 3-16. Pore size distribution function of P2-3 sample saturated in isochoric conditions, comparison with as-poured state (Seiphoori, 2014)

In Figure 3-17, the influence of the hydro-mechanical path on the intra-aggregate porosity can be observed. All PSDs depicted correspond to samples with the same initial Fuller-type granulation. Sample P1-1 was saturated in free swelling conditions, sample P2-3 in isochoric conditions and sample P1-2 was saturated in free swelling conditions and further compressed to the swelling pressure measured from sample P2-3.

The PSD of the sample saturated in free swelling conditions had three visible modes with peak values of around 0.02 μm, 1 μm and 50 μm. The first peak is related to the intra-aggregate porosity, whereas the second and third to the inter-aggregate porosity. The entrance pore size delimiting inter-aggregate and intra-aggregate porosities (determined by analysing intrusion/extrusion cycles) is around 0.2 μm. After free swelling, the inter-aggregate porosity prevailed, with the intra-aggregate porosity being 8% of the total resolved porosity.

Interestingly, the PSD of sample P1-2, saturated in free swelling conditions and compressed, suggests a transition from the PSD of sample P1-1 to that of sample P2-3. The pore size delimiting inter-aggregate and intra-aggregate porosities is around 0.05 µm. The peak value within the inter-aggregate porosity decreased to 0.4 µm while the peak value of the intra-aggregate remained at the same level of around 0.2 µm. The intra-aggregate porosity made up to 18% of the total resolved porosity. As a result of freeze drying, fissures with a size larger than 80 µm developed.

Since volume change was prevented during hydration of sample P2-3, the creation of aggregates seemed to be hindered. The inter- aggregate pores are much smaller (with the dominant value of pore size of 0.3 µm), and less pronounced than in case of samples saturated in free swelling conditions. For this sample, the intra-aggregate porosity amounted 21% of the total resolved porosity.
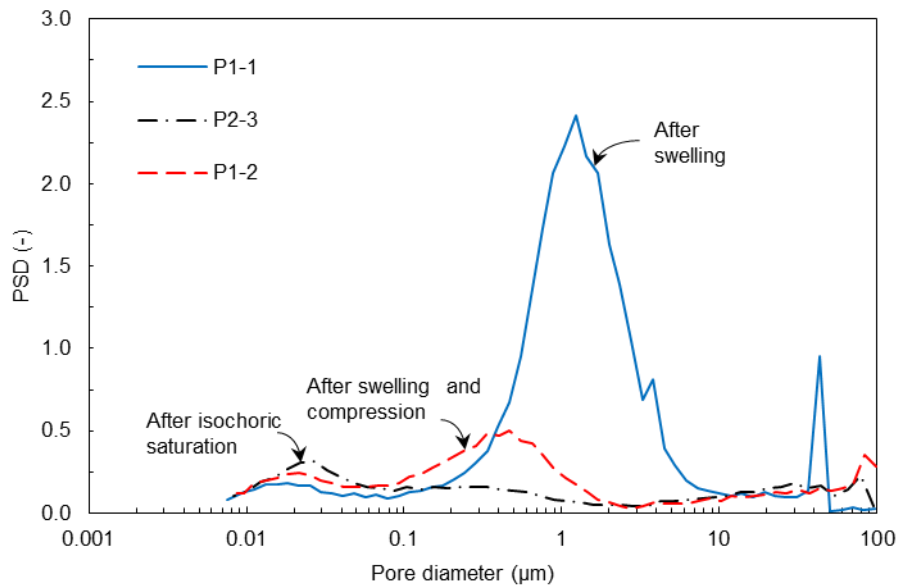
Figure 3-17. Pore size distribution of the samples with Fuller-type GSD subjected to different hydro-mechanical paths. The legend indicates the sample tested (see Table 3-4)

Influence of initial grain size distribution on the microstructure of the saturated samples

The results of MIP tests for the three samples with different grain size distributions saturated in free swelling conditions are presented in Figure 3-18. The PSD functions of all tested samples have the same three main modes. Regardless initial grain size distribution, a peak around 0.02µm, corresponding to the intra-aggregate porosity is revealed. The second peak, related to the inter-aggregate porosity, varies slightly depending on the initial grain size distribution. The value of pore size delimiting intra and inter -aggregate porosities determined analysing intrusion/extrusion cycles is around 0.2 µm for all samples. The inter-aggregate porosity prevailed in case of free swelling saturation, independently of the initial granulometry.
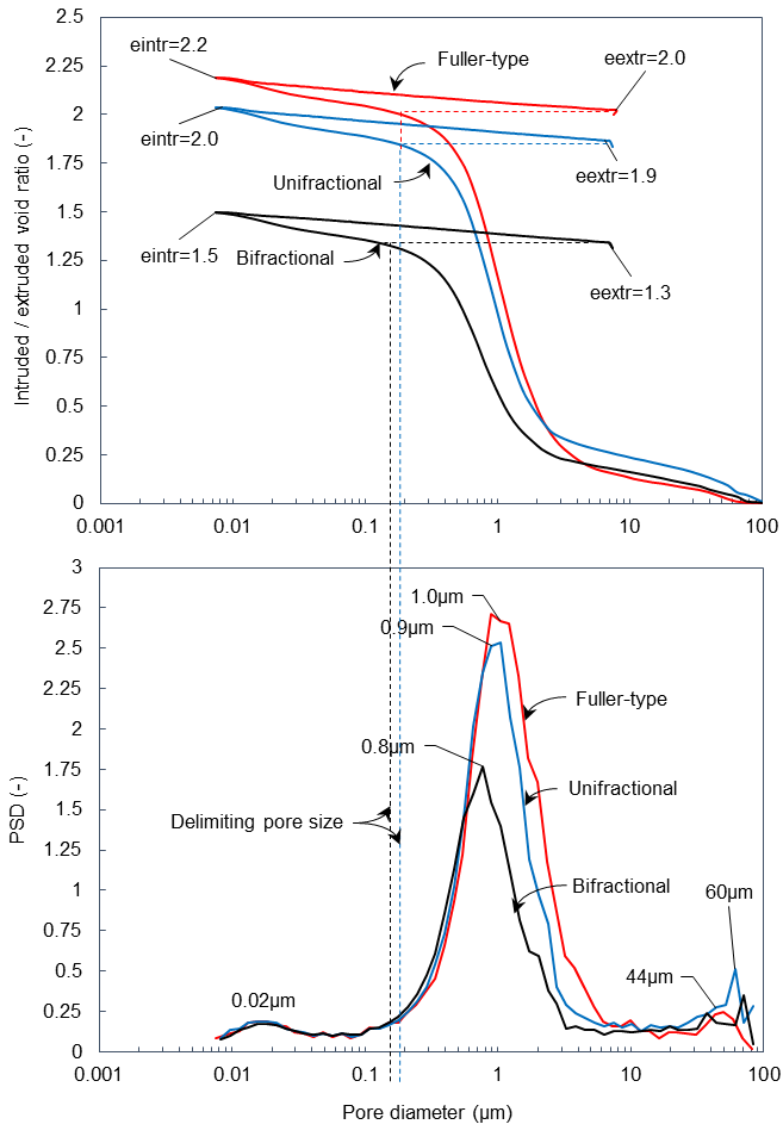
Figure 3-18. Cumulative intruded and extruded void ratio (up) and pore size distribution (down) of the samples saturated in free swelling conditions with different initial granulations

In Figure 3-19 the results of MIP tests for three samples with different grain size distributions saturated in isochoric conditions are presented. Since changes in volume were prevented upon wetting, initial porosity was preserved. The PSD functions of the samples characterized by unifractional and bifractional granulations have a bimodal distribution with peaks around 0.02 μm (related to intra aggregate porosity) and around 60 μm. The second mode of the PSD might be correlated with the pores that were not filled with low density material during saturation or, to some extent, with fissures created upon freeze drying.
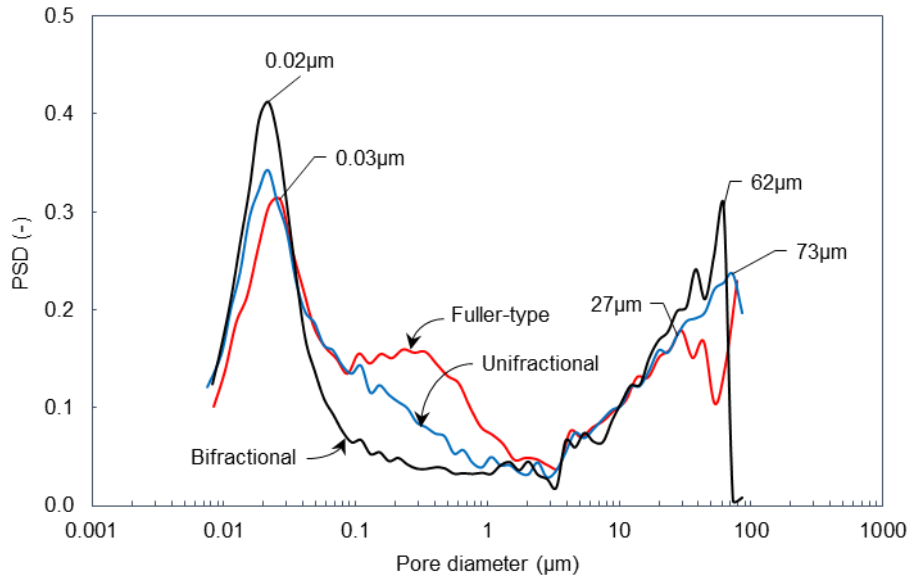
Figure 3-19. Pore size density function of the samples saturated in isochoric conditions differing in initial granulations (indicated with arrows)

Scanning Electron Microscopy

Samples preparation

Scanning Electron Microscopy Technique was applied to analyse the microstructure of the samples characterised by the Fuller type granulation after being subjected to three different hydro-mechanical paths (see Table 5). Two types of specimens: parallel and perpendicular to the axis of oedometric cell (wetting direction) were prepared (Figure 3-20). As for MIP tests, the SEM requires full removal of the pore liquid; the extraction of the pore fluid from the samples was done by freeze-drying.
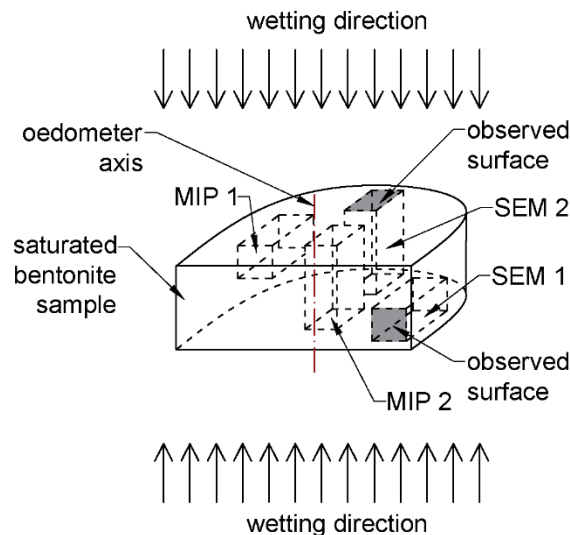
Figure 3-20. Scheme of sub-coring the sample before freeze drying

26

Testing procedure

The basic operating principle of the SEM involves the creation of a finely focused beam of energetic electrons by means of emission from an electron source (Goldstein, 2017). The electrons interact with atoms in the material and produce various signals that can be detected. This signal contains information about the material's surface topography and compositions. The electron beam is usually scanned in a raster scan pattern, and the position of the beam is combined with the detected signal in order to generate an image.

All tests were performed in a high-performance scanning electron microscope FEI Quanta 200f. Observations were carried out in high vacuum mode (HV) using the Secondary electron (SE) detector (spot 3.0) at an accelerating voltage between 20 and 30 kV. The applied working distance (WD) was up to 10-20 mm. SEM magnifications were in the range 15-50000X.

Results: Influence of hydro-mechanical paths

In Figure 3-21 the SEM microphotographs of samples subjected to different hydro-mechanical paths are summarized. For samples saturated in free swelling conditions (P1-1) and saturated in free swelling conditions and compressed (P1-2), the surfaces perpendicular and parallel to the oedometer axis were analysed. In case of the sample saturated in isochoric conditions (P2-3) only the surface perpendicular to the oedometer axis was observed.

In Figure 3-21a, b, the SEM pictures for the sample saturated in free swelling conditions (P1-1) are presented. In the surface perpendicular to oedometer axis, clay layers can be observed. No outlines of the initial granular structure are distinguished. Clay layers are oriented in both directions: parallel and perpendicular to oedometer axis. The distance between observed aggregates is in the range of 0.5 - 2.5 μm. In the surface parallel to the oedometer axis, larger aggregates can be observed to be distanced from each other in the range of 2 - 4.5 μm and oriented perpendicular to the wetting direction (oedometer axis).

In Figure 3-21c and d, the SEM pictures of the sample saturated in free swelling conditions (P1-2) and compacted are presented. In the surface perpendicular to the oedometer axis, the area is homogeneously filled with the clay. The outlines of aggregates are visible, but no pore space between the aggregates is noticed. The aggregates are layered mainly perpendicular to oedometer axis direction, which is visible from the surface parallel to the oedometer axis (Figure 3-21d). The distance measured between aggregate layers is in the range of 0.5 – 1 μm.

In Figure 3-21e the SEM picture of the sample saturated in isochoric conditions is presented. Clay layers are visibly oriented perpendicular to oedometer axis (wetting direction). Possible outlines of initial grains and some connections can be noticed.
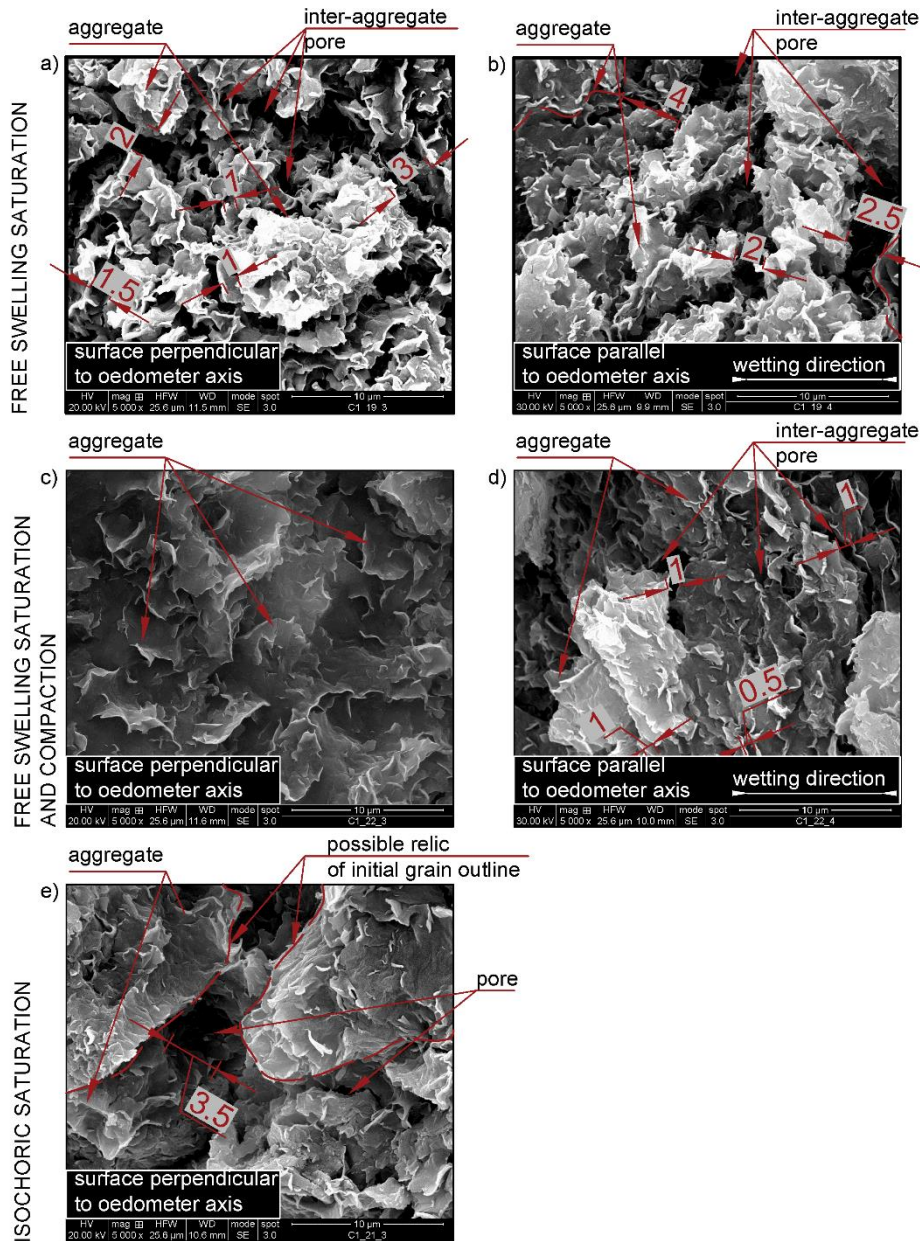
Figure 3-21. SEM photomicrographs of the bentonite subjected to different hydro-mechanical conditions. All dimensions are in micrometres

Discussion on the microstructural analysis

The results of MIP analysis combined with additional SEM observations allows to complement the interpretation of MX80 bentonite behaviour in various hydro-mechanical states.

For all tested granulations, the dominant size of micro porosity is in similar range regardless applied wetting scenario or stress level. The applied hydro-mechanical paths as well as the initial granulation influenced mostly the inter-aggregate (macro) porosity.

The microstructure of the material saturated in free swelling conditions seems to be notice-ably modified in comparison with the material in initial hygroscopic state. Upon wetting, clay aggregates tend to orient perpendicular to the oedometer axis and the overall structure homogenises with respect to the initial granular structure. Since the development of clay agglomerates in the direction perpendicular to oedometer axis was restricted, clay

aggregates grew in the direction parallel to the axis of oedometric cell. After free swelling saturation, no outlines of initial grains were visible.

For the case of isochoric saturation, full development of clay aggregates was not possible. The grains swelled in limited range. The initial structure characterised by the compacted grains was rather preserved after full saturation and outlines of the as – poured state can be distinguished.

3.3 Hydraulic and mechanical properties of Czech bentonite – constant load tests (CU) and constant volume tests (CTU)

3.3.1 Constant load tests

Outline of the tests

Laboratory tests were carried out on Czech bentonite (BCV) from Cerny vrch deposit (north western region of the Czech Republic). Compacted samples were prepared from bentonite powder of its original water content (10-11%). Three different initial dry densities of 1.27, 1.60 and 1.90 g/cm³ were investigated. The one-dimensional swelling behaviour, water retention properties and microstructure characteristics were studied. The one-dimensional swelling behaviour under constant load was performed using the conventional oedometer cell. The low and medium dry density samples were measured under five different constant loads in the range from 0.98 to 500 kPa and 0.75 to 4 MPa respectively. The water retention properties were investigated on samples, which were first equilibrated either at highest (286.7 MPa) or lowest (0.001 MPa) suction and then suction change was analysed at wetting and drying path.

Mercury intrusion porosimetry was used to analyze the pore size distribution curves at different initial dry densities and suction levels. The environmental scanning electron microscopy (ESEM) was applied to analyze the deformation of bentonite aggregate at different hydration paths including the wetting-drying-wetting (WDW) and drying-wetting-drying (DWD) paths starting from the initial state of bentonite. The overview of the experimental procedures and states of samples in the experiments is shown in Table 3-5.

Table 3.5. Test programme

Initial dry density (g/cm³)	Initial w_c (%)	Sample state	Suction paths (MPa)
1.27; 1.60; 1.90	10 - 11	Initial state	ESEM: 38→286.7→3.29→38 ESEM: 38→3.29→286.7→38 Oedometer: 0 MPa, with vertical loads 0.98, 100, 250, 400, 500 kPa for 1.27g/cm³, 0.75, 1, 2.5, 3, 4 MPa for 1.60g/cm³
		Equilibrated at suction of 0.001MPa (H₂O)	WRC: 0.001→286.7
		Equilibrated at suction of 286.7 MPa (LiCl)	WRC: 286.7→0.001 MIP: 286.7, 113.5, 38, 21.82, 3.29

Constant load swelling

The conventional oedometer apparatus shown in Figure 3-22 was used for measuring the swelling deformation of the bentonite BCV. The compacted bentonite was tested in the

29

standard fixed stainless-steel ring, 50 mm inside diameter and 20 mm height. Silicone grease was applied to the inner wall of the stainless-steel ring to reduce friction between the specimen and the wall. The filter papers were placed between the specimen and porous stones. Considering the porous stone placement and the swelling deformation, the samples were prepared with the initial height of 8-10 mm. Once the compacted bentonite was introduced in the stainless-steel ring, the prescribed vertical stress was applied. Then the specimen was flooded by distilled water. The vertical deformation and time required to reach constant deformation were recorded. The ASTM D2435/D2435M standard recommends the correction for oedometer apparatus compressibility. The deflection of the apparatus was measured for all loads applied during the tests by substituting the soil specimen by a smooth hard steel disk.
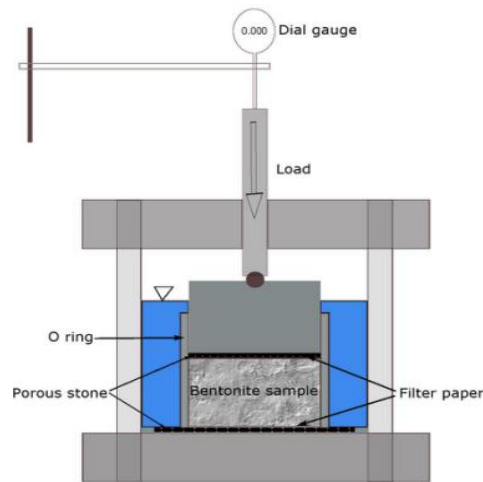
Figure 3-22. Measurement of constant load swelling

Figure 3-23 shows the evolution of the constant load swelling with time for initial dry densities of 1.27 g/cm³ and 1.6 g/cm³ for all the applied constant loads. Swelling strain equals to the ratio of swelling deformation and initial height. It increased rapidly in the initial stage after flooding. For the lowest vertical load of 0.98 kPa, which corresponds to the weight of top plate (free swelling), the equilibration of the final swelling strain took longer time (over 100 hours), while for higher loads, the time of equilibration was shorter (e.g., 50-60 hours). After the final state was reached, the final swelling strain was recorded and the final void ratio was calculated from the final water content, specific gravity and final dry density.

Figure 3-24 shows the final void ratio versus applied vertical load for dry density of 1.27 g/cm³ and 1.60 g/cm³. It shows that final void ratio decreases with increasing vertical load linearly in semi-logarithmic scale. The presented curves are independent of the initial dry density. It indicates that initial compaction has no effect on final void ratio.
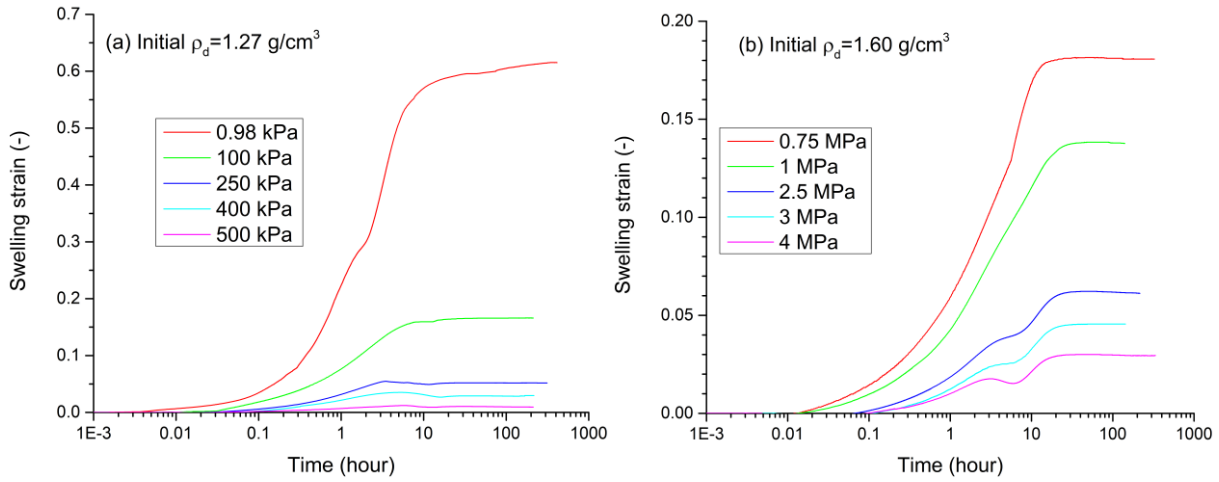
Figure 3-23. Development of swelling strain with time for dry density (a) 1.27 g/cm³ and (b) 1.6 g/cm³
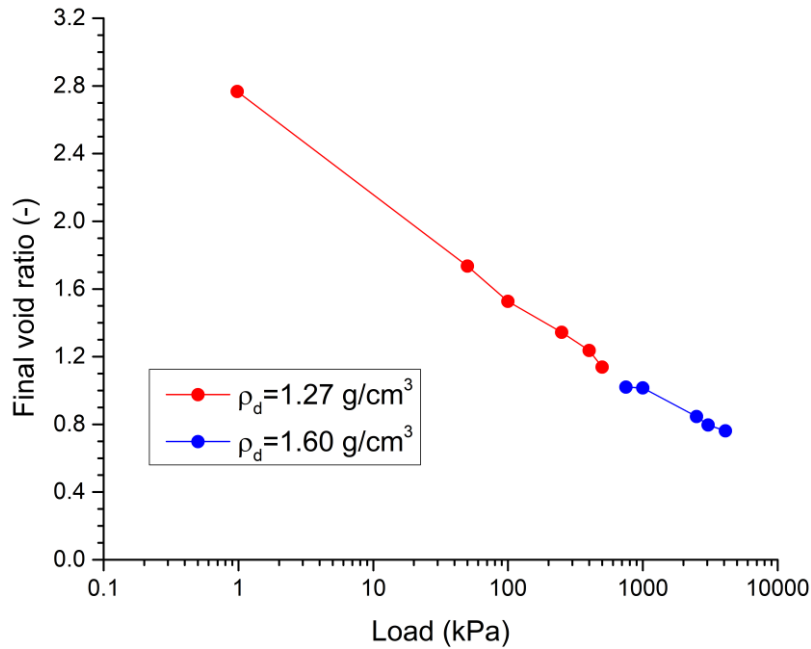
Figure 3-24. Final void ratio versus vertical load for both initial dry densities of 1.27 and 1.60 g/cm³

Water retention properties

The vapor equilibrium technique (Delage et al., 1998) was used to control suction in sealed desiccators. The relative humidity in the sealed desiccators was imposed by different saturated chemical solutions. The total suction can be calculated from Kelvin's equation by knowing the relative humidity. The desiccators with saturated solutions were placed in a room with controlled temperature to ensure constant suction. Eight different salt solutions were used generating total suction in a range from 3.29 to 286.7 MPa as shown in Table 3-6. The desiccator with distilled water (assumed suction of 0.001 MPa) was used to prepare the samples for drying path.

Table 3-6. Characterisation of salt solutions used for vapor equilibrium method measurements (at temperature of 20 °C)

Salt solutions	Relative humidity (%)	Suction (MPa)
Lithium Chloride Monohydrate (LiCl·H$_2$O)	12.0	286.7
Potassium Acetate (CH$_3$COOK)	23.1	198.14
Magnesium Chloride Hexahydrate (MgCl$_2$·6H$_2$O)	33.1	149.51
Potassium Carbonate (K$_2$CO$_3$)	43.2	113.50
Sodium Bromide (NaBr)	59.1	71.12
Sodium Chloride (NaCl)	75.5	38.00
Potassium Chloride (KCl)	85.1	21.82
Potassium Sulphate (K$_2$SO$_4$)	97.6	3.29

The compacted bentonites with three different initial dry densities were first broken into several small pieces with weight ranging from 1.5 to 8 grams. Half of the samples was placed into the highest suction desiccator (LiCl solution) to equilibrate and another half was placed into the lowest suction desiccator (distilled water). After equilibration, the samples were distributed to other desiccators to determine wetting and drying path. The weight of the samples was regularly measured until stable value was reached. The example of samples compacted to 1.27 g/cm^3 and tested at wetting path is presented in Figure 3-25. The time of equilibration took over 2 months for the samples exposed to biggest change of suction (lowest suction in Figure 3-25).
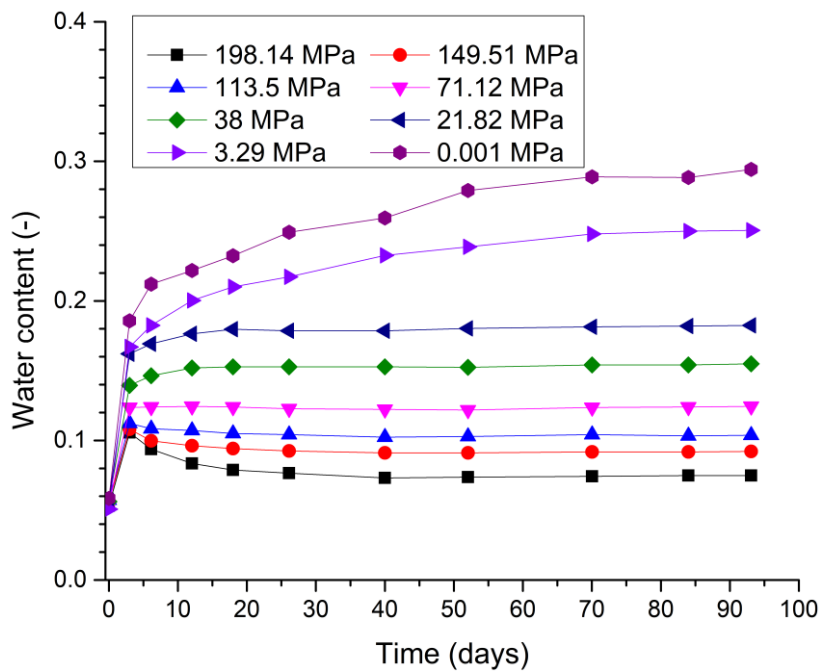
Figure 3-25. Example of water content evolution with time for different suctions obtained by vapor equilibrium method (initial dry density of 1.27 g/cm³)

Once the equilibrium was reached, one part of the samples was taken from each desiccator and used for the determination of water content. Another part (4 to 6 pieces) was immediately weighted and then covered by wax to determine their volume. The volume was measured using the wax immersion method following the ASTM C914-95 (ASTM, 2004)

procedure. The final void ratio value was determined as the average value from those obtained on all pieces from the same desiccator. The degree of saturation was calculated from the obtained values of water content and void ratio.

Figure 3-26 shows the water retention curves of three different initial dry densities and both wetting and drying paths. The water content has almost linear relationship with suction in semi-logarithmic scale and creates only narrow hysteretic loop between wetting and drying paths. It can be concluded that the initial dry density had little influence on the water content. With the assumption that most water is concentrated in the micropores at high suctions, these results suggest that micropores are only little influenced by the compaction pressures, as if their volume was to be affected, their water retention capacity (which is known to be porosity dependent) would also change.

Contrarily, quite a remarkable effect of the initial dry density was found on the degree of saturation through its effect on void ratio (Figure 3-26). The results consistently show an increase in the global degree of saturation with increasing dry density.
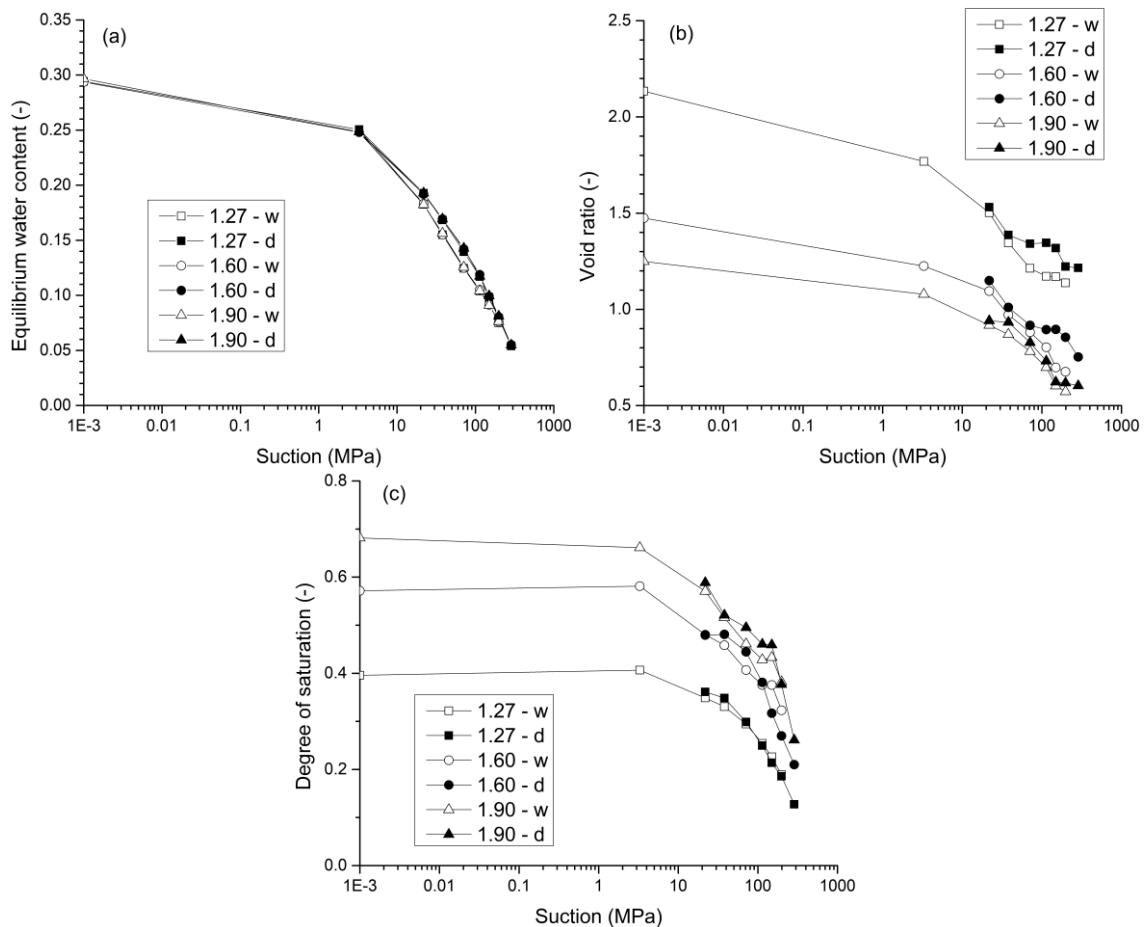
Figure 3-26. Water content (a), void ratio (b) and degree of saturation (c) with respect to suction along wetting and drying path at dry densities of 1.27, 1.60 and 1.90 g/cm³

Mercury intrusion porosimetry

Mercury intrusion porosimetry is based on the capillary law governing non-wetting liquid penetration into small pores. The pore entrance diameter can be calculated from the applied mercury pressure by assuming that the cylindrical pores exist in soil according to the Washurn equation (Juang and Holtz, 1986)

$$D = -\left(4\sigma_{Hg}\cos\theta_{nw}\right)/P$$

where D is the entrance pore diameter; σ_{Hg} is the surface tension of mercury; θ_{nw} is the contact angle between the mercury and the soil surface; and P is the intrusion pressure. In this study, the values θ_{nw} =130° and σ_{Hg} = 0·484 N/m at 25°C were considered in the pore diameter calculation.

The tests were performed at the Department of Inorganic Technology at the University of Chemistry and Technology Prague (Apparatus Autopore IV, Micromeritics). The measurement was carried out in two regimes, one was a low-pressure regime from 0.01 to 0.2 MPa (corresponding to the pore radius between 100 and 3 μm); the other one is the high-pressure regime from 0.2 to 400 MPa (corresponding to the pore radius between 3 μm and 1.5 nm). MIP tests were conducted on freeze-dried samples to retain the original microstructure. In freeze-drying methods, the samples were first immersed in liquid nitrogen and then the frozen samples were placed under a deep vacuum. Finally, the samples went through sublimation in the vacuumed chamber of a freeze dryer (Delage et al., 1996).

In the tests, samples of three different initial dry densities of the as-compacted bentonite were first equilibrated at the suction of 286.7MPa (LiCl) and then distributed to desiccators to reach suctions of 113.5, 38, 21.82 and 3.29 MPa (wetting path). The samples equilibrated at these suction levels were used for MIP tests.

Figure 3-27 shows the MIP results of three dry densities samples (1.27, 1.60 and 1.90 g/cm³) at each suction level. The comparison of different dry densities demonstrates that compaction has big influence on the predominant pore radius represented by the highest peak. An increase of dry density leads to the reduction of the peak and shifting the predominant pore size towards smaller pores. This trend is independent on the value of applied suction.

Figure 3-28 shows the same results, replotted to identify the effect of suction on pore size distribution. It shows that the peaks representing predominant pore radius are slightly affected by applied suction. With increase of suction, peak is shifted towards smaller pore radius. This effect is more obvious for high initial dry density samples (Figure 7c). Compared to the effect of initial dry density, suction has significantly smaller influence on predominant pore size.

According to the criteria to discriminate the macro and micro pore presented in Romero et al., (2011), the transition pore radius boundary between macropores and micropores is around 0.05-0.07 μm. The pore size distribution curves show that the compacted bentonites have double structure pore system, which consists of macropores (represented by pore radius around 1-2 μm) and micropores (represented by peak at approximately 5-6 nm). Pore size distribution curves show that suction and especially compaction have significant influence on the macropores. The influence on the micropores was found to be insignificant.
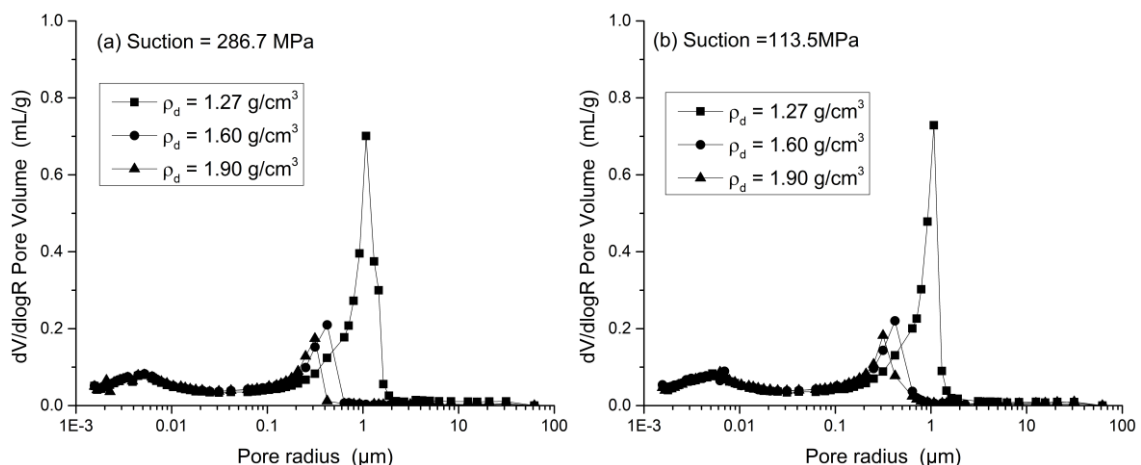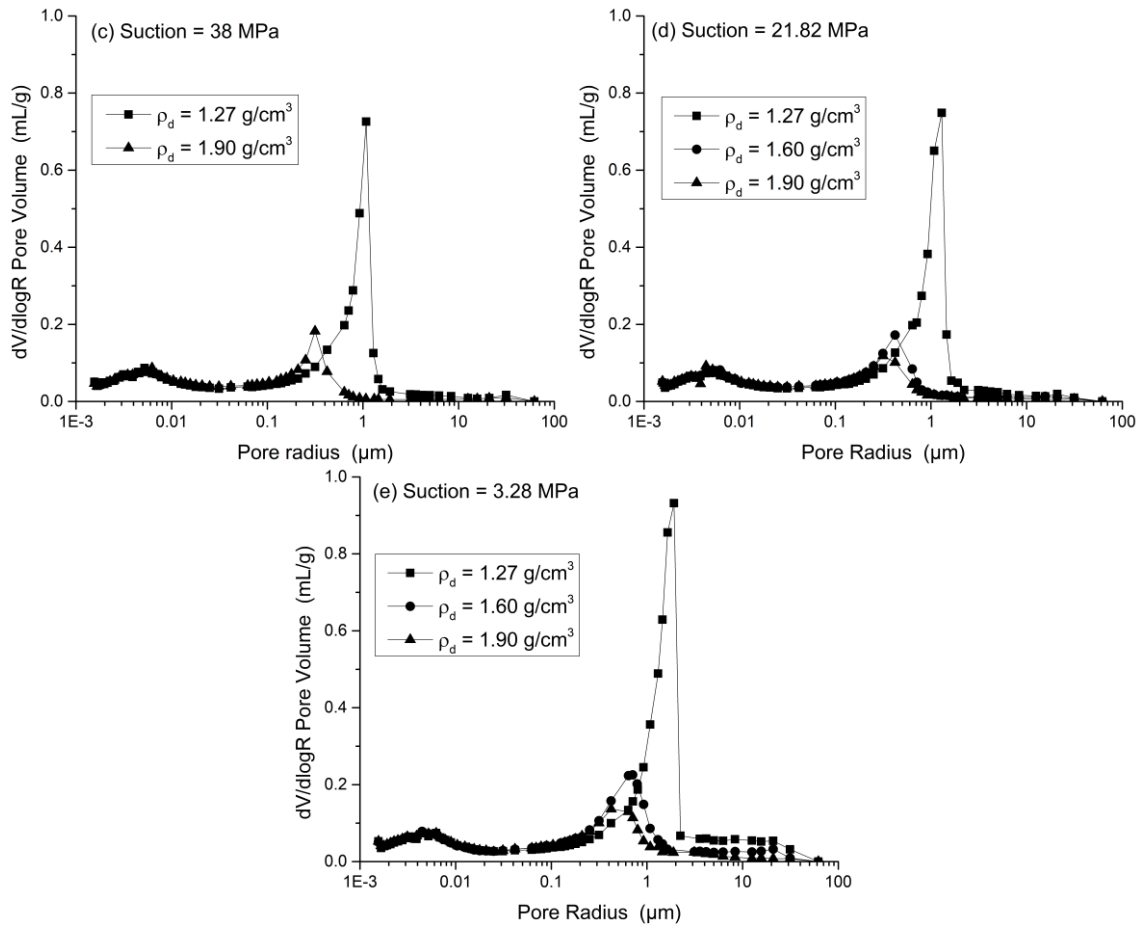
Figure 3-27. Pore size distribution curves of samples with different dry densities at constant suction
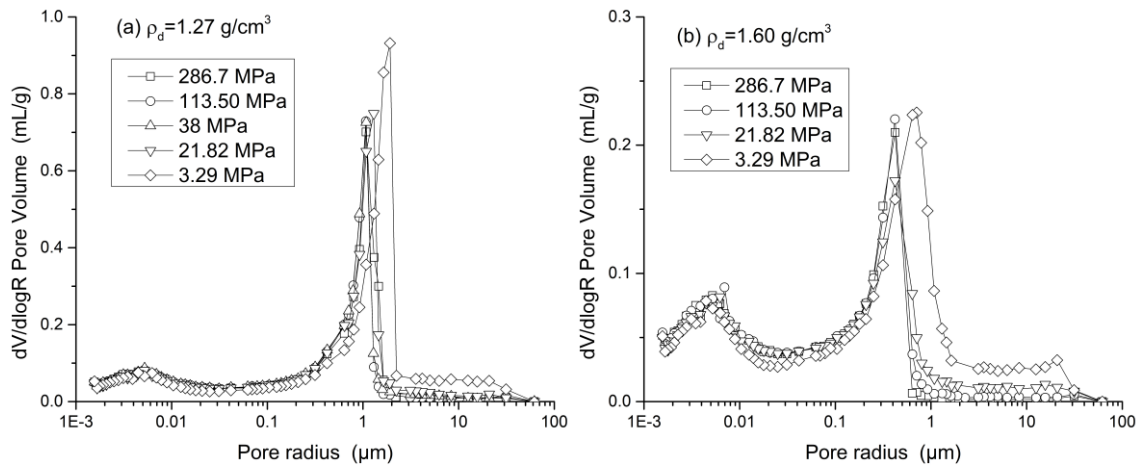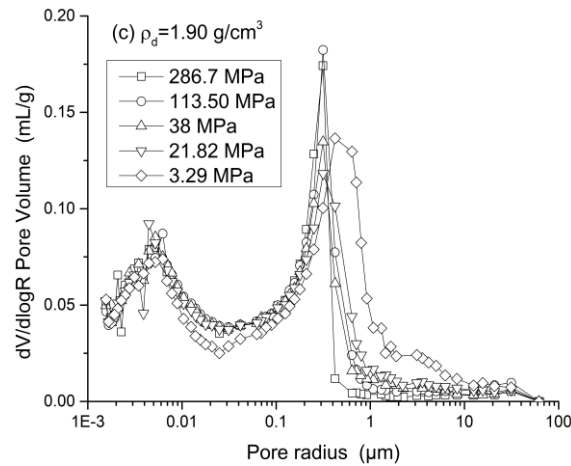
Figure 3-28. Pore size density distribution curves of three different initial dry densities with different suction

Environmental scanning electron microscopy

The environmental scanning electron microscopy (ESEM) was used to directly analyse the bentonite samples. The ESEM tests were performed using a Quanta 650 FEG scanning electron microscope at the Institute of Scientific Instruments of the Czech Academy of Sciences, Brno. The compacted samples with initial dry density of 1.27, 1.60 and 1.90 g/cm³ were used for the ESEM observations. No cutting tool was used to prepare the sample surface; instead, following the procedures of Lin & Cerato (2014), the specimen was fractured in order to expose a fresh, undisturbed section of the sample. Figure 8 shows the microphotos of compacted bentonite with initial dry density of 1.27 g/cm³ at various magnifications. Figure 3-29a shows the general view of the studied sample. With the magnification increased, more detailed observation including distinct aggregates and the macropores between them can be performed (Figure 3-29c, d, e). Figure 3-29g and h show the micropores within the aggregates. Double structure pore system, which was identified on MIP distribution curves can be confirmed by direct observation.
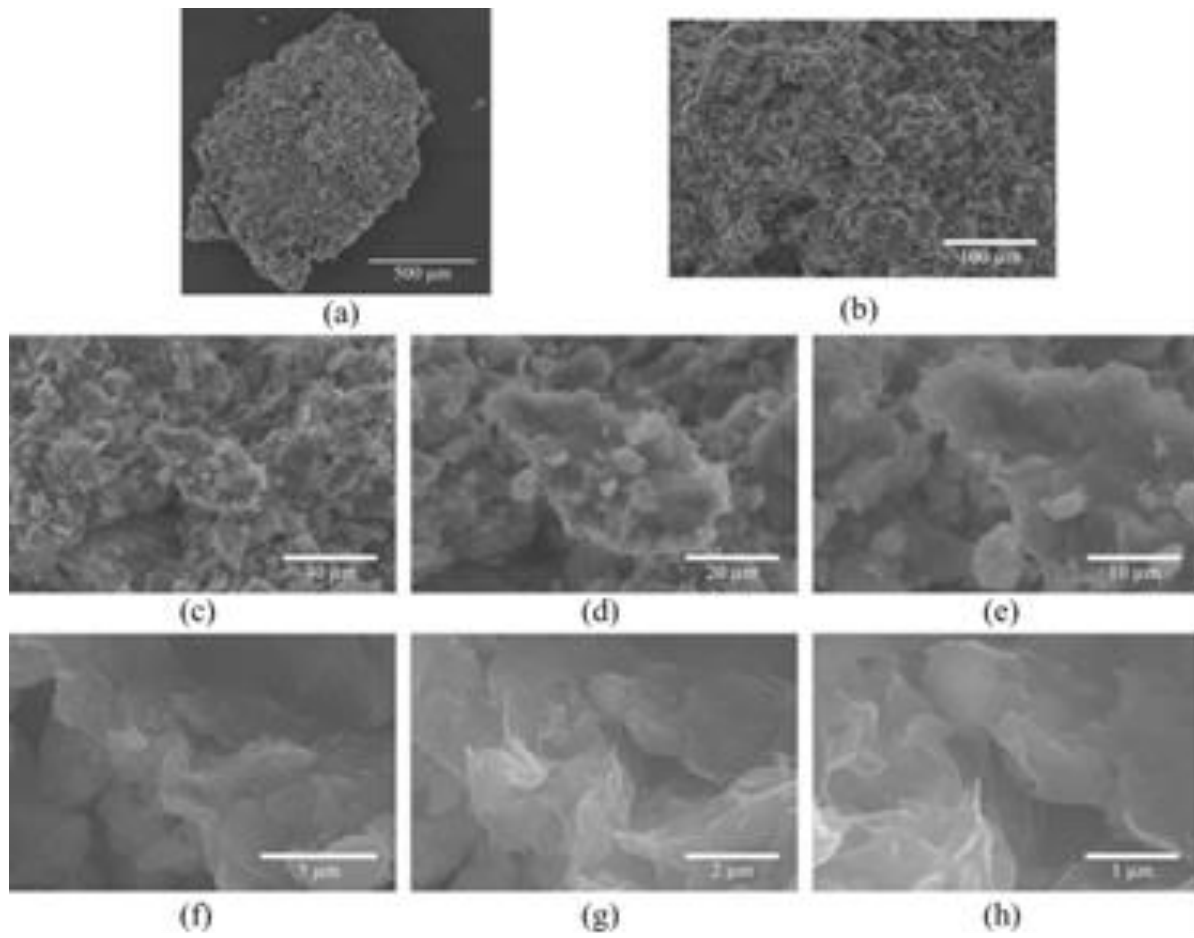
Figure 3-29. Micro-photos of compacted bentonite (1.27 g/cm³) with different magnification: (a) general view; (b) 1000x; (c) 2500x; (d) 5000x; (e)1000x; (f) 25000x; (g) 50000x; (h) 100000x

A series of ESEM observations was performed on the bentonite samples exposed to different relative humidity. The tests were carried out at constant temperature of 3°C; the water vapor pressure was imposed directly in the ESEM chamber, which made it possible to observe directly the microstructure response to suction changes. From the water retention curves obtained on similar bentonite B75 (Sun et al., 2018) and the initial water content of the samples, the water vapor pressure of 559.8 Pa (corresponding to relative humidity of 73.9% and suction of 38 MPa) was determined as the optimal initial state for the experiment. Two hydraulic paths were applied: drying-wetting-drying path (DWD) with suction path 38→287→3→38 MPa, and wetting-drying-wetting path (WDW) with suctions 38→3→287→38 MPa. A detailed plan of the imposed suction levels and test conditions is shown in Table 3-7. The interval between vapor pressure changes was 15 min. A similar interval was used also by other researchers (Montes-H, 2005; Lin & Cerato, 2014).

Table 3-7. Water vapour pressure, relative humidity, total suction adopted in ESEM measurements

Temperature = 3°C					
Drying-wetting-drying path (DWD)			Wetting-drying-wetting path (WDW)		
Relative humidity (%)	Water vapor pressure (Pa)	Total suction (MPa)	Relative humidity (%)	Water vapor pressure (Pa)	Total suction (MPa)
73.9	559.8	38.00	73.9	559.8	38.00
56.7	429.8	71.13	84.0	636.9	21.81
40.4	306.5	113.50	87.0	659.5	17.46
30.3	230.0	149.52	91.0	689.8	11.82
20.6	156.0	198.18	94.0	712.5	7.76
10.2	77.0	286.67	97.4	738.3	3.30
20.6	156.0	198.18	91.0	689.8	11.82
30.3	230.0	149.52	87.0	659.5	17.46
40.4	306.5	113.50	84.0	636.9	21.81
56.7	429.8	71.13	73.9	559.8	38.00
73.9	559.8	38.00	56.7	429.8	71.13
84.0	636.9	21.81	40.4	306.5	113.50
87.0	659.5	17.46	30.3	230.0	149.52
91.0	689.8	11.82	20.6	156.0	198.18
97.4	738.4	3.29	10.2	77.0	286.67
91.0	689.8	11.82	20.6	156.0	198.18
87.0	659.5	17.46	30.3	230.0	149.52
84.0	636.7	21.86	40.4	306.5	113.50
73.9	559.8	38.00	56.7	429.8	71.13
			73.9	559.8	38.00

Figure 3-30 shows the example of low dry density samples exposed to wetting-drying-wetting path (WDW). During the first wetting path (Figure 3-30a→f, (38→3.29 MPa)), the volume of aggregates slightly increased. Macropores remained dry, except of the lowest suction. At 3.29 MPa, water entered the macropores, which can be seen from Figure 3-30f.

In order to quantitatively analyse the aggregates volume change upon WDW and DWD paths, the digital image analysis (Sun et al., 2018) was used to calculate volume strain of the selected aggregates. Figures 3-31 and 3-32 show the selected aggregates and their volume strain on both WDW and DWD paths respectively for low initial dry density. The volume strain shows a hysteretic behaviour between wetting/drying or drying/wetting path. The volume increased sharply near the lowest suction (3.29 MPa). This effect is caused by water, which entered the macropores and caused the aggregate boundaries to be less clearly defined in the photographs. In the higher suction range (>30 MPa), the volume strain shows a linear change with the suction and hysteretic loop appears to be quite narrow. At DWD paths, this linear slope is different for the four aggregates, but the difference is quite minor. At WDW paths, suction vs. volumetric strain relationship gives almost parallel lines for all studied

aggregates (Figure 3-31). The aggregate volumetric response appears to be reversible with suction at higher values. The same results were obtained also for medium and high initial dry density samples.
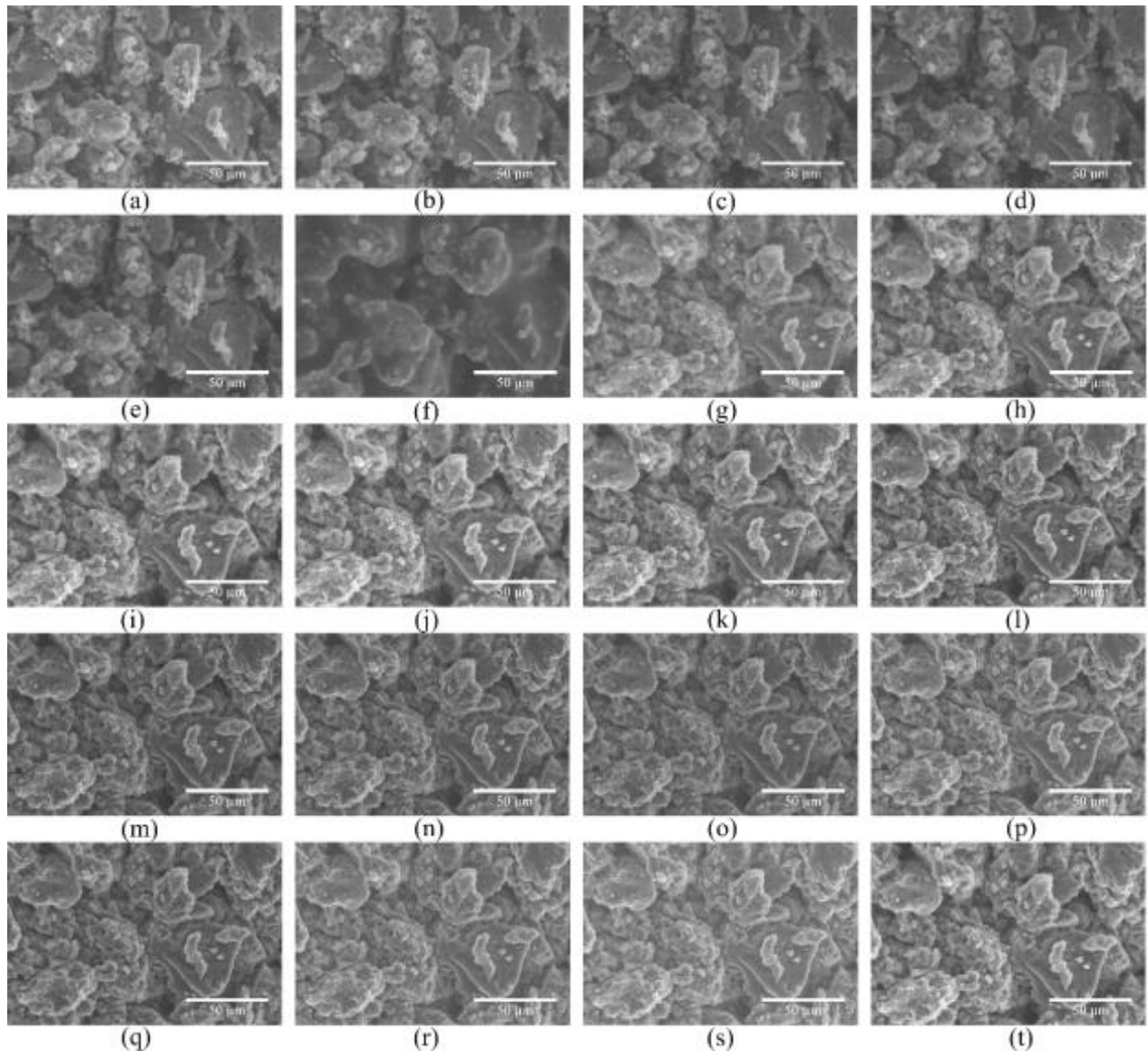
Figure 3-30. ESEM microphotos of compacted bentonite with a dry density of 1.27 g/cm³ under the wetting–drying-wetting path (WDW): (a) 38 MPa; (b) 21.81 MPa; (c) 17.65 MPa; (d) 11.82 MPa; (e) 7.76 MPa; (f) 3.29 MPa; (g) 11.82 MPa; (h) 17.46 MPa; (i) 21.86 MPa; (j) 38 MPa; (k) 71.13 MPa; (l) 113.5 MPa; (m) 149.52 MPa; (n) 198.18 MPa; (o) 286.67 MPa; (p) 198.18 MPa; (q) 149.52 MPa; (r) 113.5 MPa; (s) 71.13 MPa; (t)) 38 MPa.
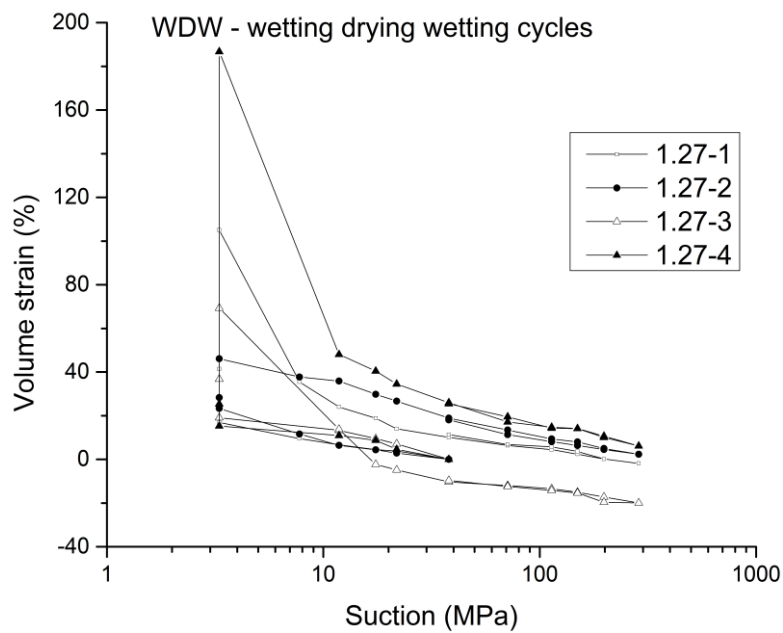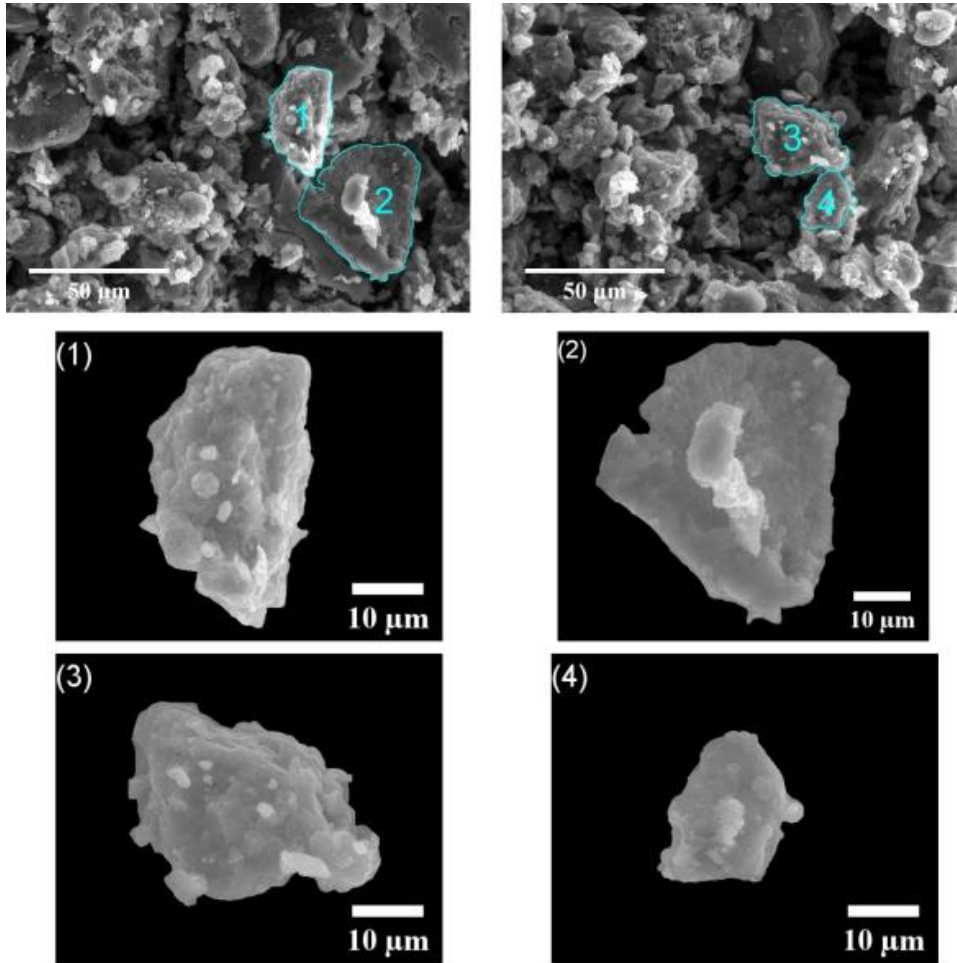
Figure 3-31. Aggregates of the initial dry density 1.27 g/cm³ samples selected for calculation of volume strain at wetting-drying-wetting path (WDW)
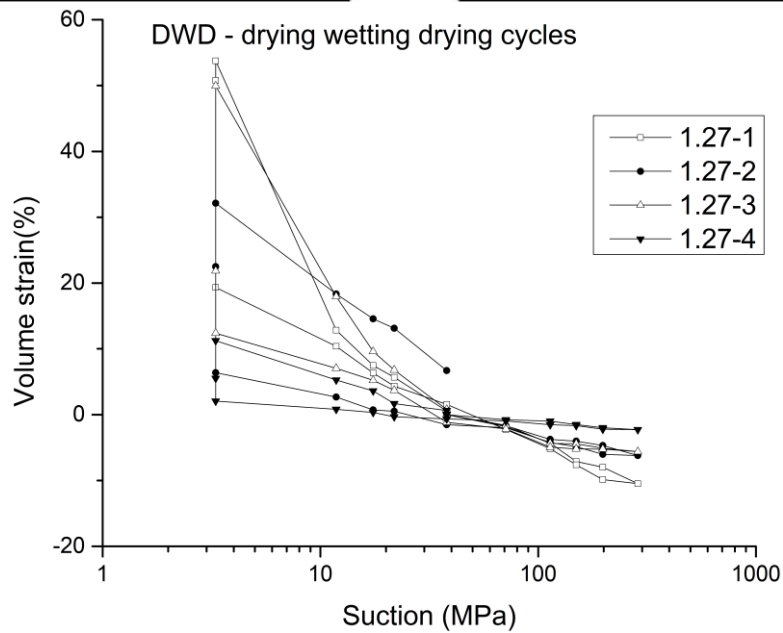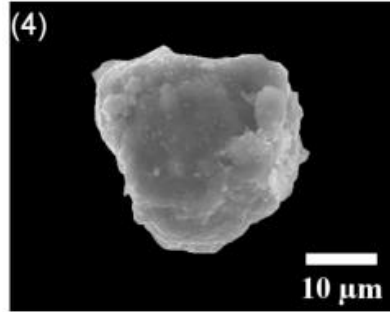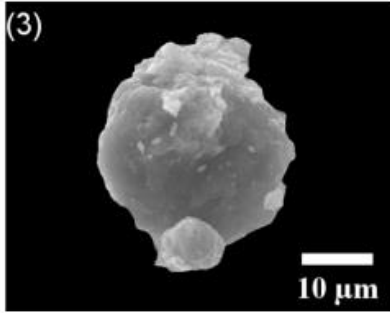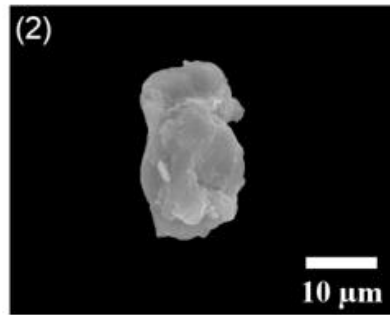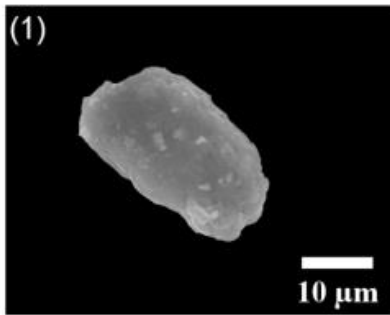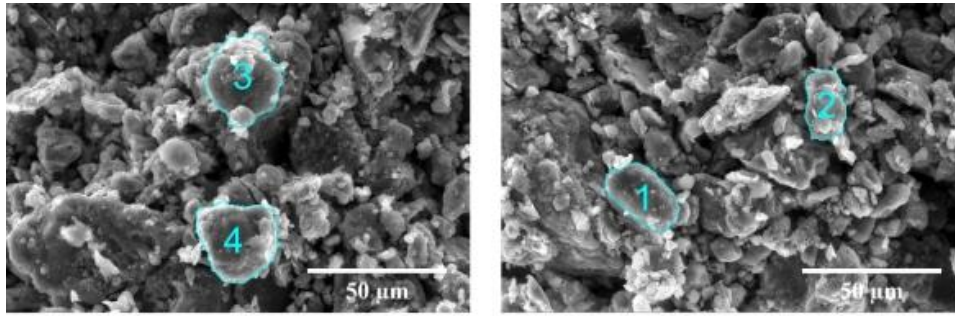
Figure 3-32. Aggregates of the initial dry density 1.27 g/cm3 samples selected for calculation of volume strain at drying-wetting-drying path (DWD)

3.3.2 Constant volume tests

Total pressure evolution, hydraulic conductivity (water flow), saturation evolution and final density (density changes) & water content distribution were investigated in constant volume cell apparatus. The aim was to obtain calibration data for mathematical model development.

The apparatus consists of cylinder with compressed argon, pressure regulator, gas water exchanger, flow meter and test cell (Figure 3-33). In the test cell the sample is on circumference confined into solid steel ring and at the top bottom by permeable plates from sintered steel. Bottom plate is fixed by steel support and top plate is supported by free floating piston. Other side of piston is fixed via force transducer (total pressure measurement) in fixed steel plate. Water is injected thought the bottom permeable plate and collected via piston.
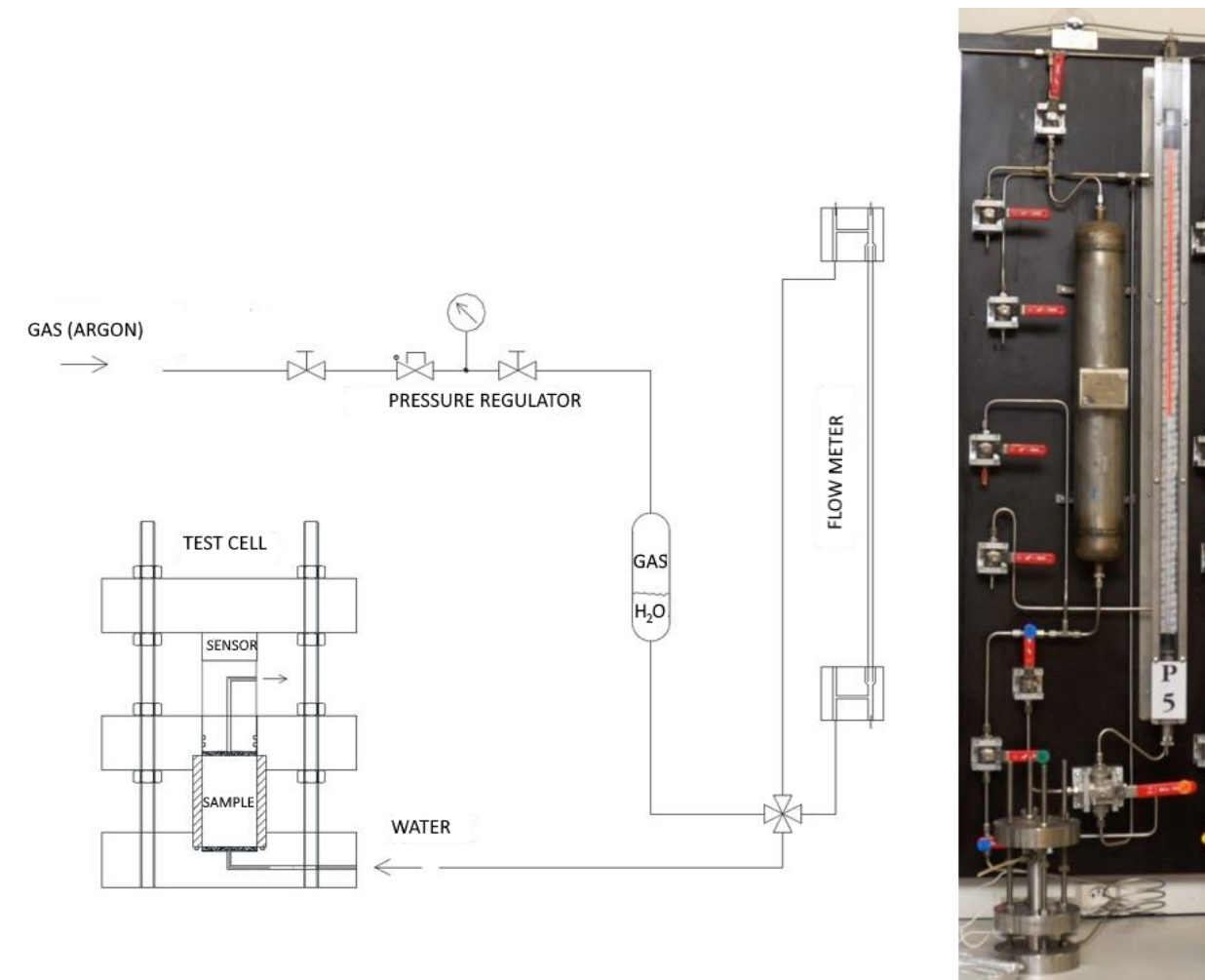
Figure 3-33. Constant volume test apparatus

The tests were performed on B75 a BCV material (Hausmannová et al., 2018). Both materials are Czech bentonites produced by Keramost a.s. with similar composition and properties. The switch from B75 (used initially) to BCV ("new" material) was made due to BCV selection new research reference material for Czech programme.

Three types of samples were investigated – homogenous samples from compacted powder bentonite, dual density samples (stack of two half height samples on top of each other with

different density) and pellets. If not mentioned otherwise the total sample height was 20 mm and diameter 30 mm with exception for pellets where diameter 120 mm was used for some of the test to accommodate for larger grains.

The exact height and weight of the samples were determined via measurement and weighing following the completion of the sample preparation stage. The initial water content was determined before the preparation of the samples via the gravimetric method using the same material.

The test procedure was as follows:

1. Samples were compacted into permeameter ring
2. Test apparatus was assembled and zero measurement recorded
3. Water was injected into sample and test begun. If water was freely flowing through the sample (typical for pellets) saturation was temporarily turned off
4. Samples were continuously (or in pulses for leaking samples) saturated by water pressure ~1 MPa. Evolution of total pressure, flow and temperature was recorded
5. Once total pressure and hydraulic conductivity were stabilised the saturation was turned off
6. Once total pressure was stabilised (no saturation pressure →swelling pressure can be determined) the test was terminated and disassembled.
7. Water content and dry density of sample was determined. Selected samples were sliced perpendicular to vertical axis when pushed out from ring. Slices were used to determine water content and rough estimated of density (exact volume of the slice could not be controlled/measured therefore the estimate is quite imprecise)

Following tests in constant volume cells were carried out:
- Homogenous samples
  - Material B75
    - Standard test - top only measurement of total pressure – 4 tests
    - Influence of temperature (20/60/20 °C) – 3 tests

  - Material BCV
    - Standard test - top only measurement of total pressure – 3 tests
    - Standard test - top and bottom measurement of total pressure – 3 tests
    - Saturation development – 5 tests
- Dual density samples
  - Material B75
    - Standard test & slicing - top only measurement of total pressure – 2 tests
  - Material BCV
    - Standard test & slicing - top only measurement of total pressure – 2 tests
- Pellets
  - Material BCV_PM2018 – 3 tests

Homogenous samples

Both materials (B75 and BCV) were tested in homogenous form. Four tests were performed on compacted B75 powder. The samples were compacted directly into test rings with no additional processing. Dry density of samples was 1300 – 1762 kg/m³. Evolution of total pressure and estimated hydraulic conductivity is shown in Figure 3-34.
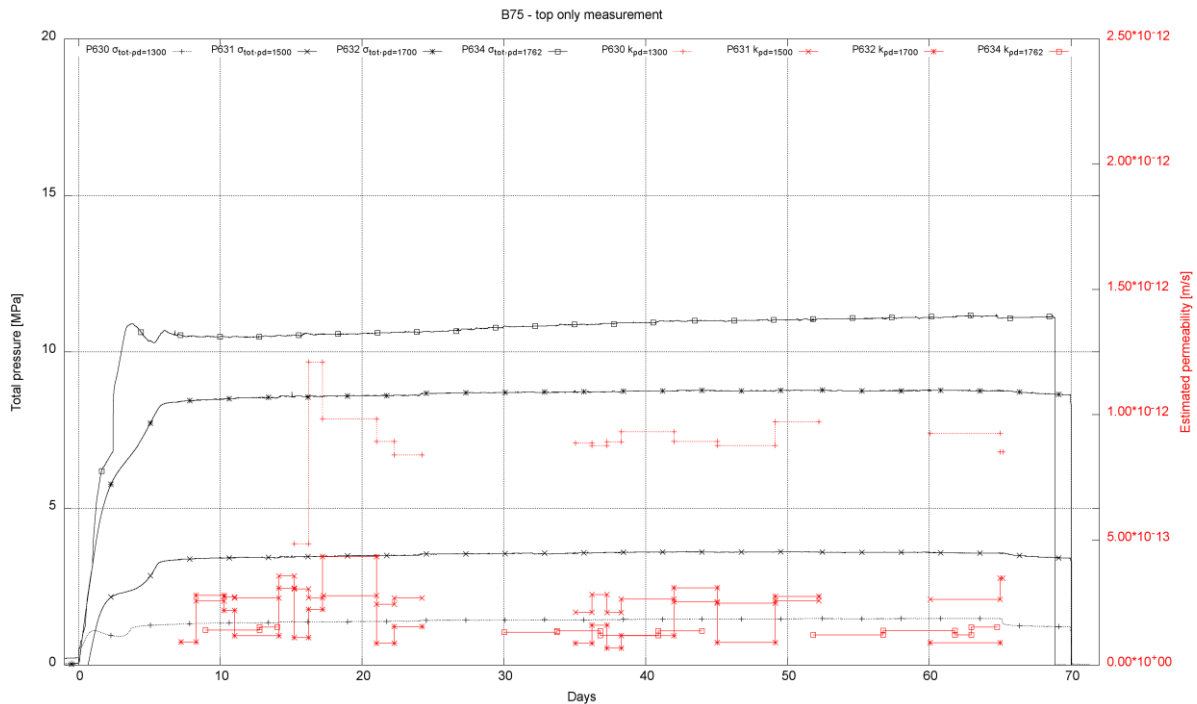
Figure 3-34. B75 homogenous samples (top only measurement)

Three additional samples of B75 (dry density 1300-1800 kg/m³) were used to investigate the influence of temperature on total pressure and hydraulic conductivity evolution. Test begun at laboratory temperature (approx. 20 °C) with forced saturation phase followed by saturation shut off. After 6 months test cells were placed into 60 °C until hydraulic conductivity stabilised. At last the samples were moved back to laboratory temperature. The results (Figure 3-35) show that change of temperature has effect on hydraulic conductivity but after sufficient time the hydraulic conductivity stabilises at the same level as before temperature change.

BCV material was investigated more thoroughly. The standard top only measurement of total pressure was for selected samples altered into top & bottom measurement by adding bottom piston and transducer. Results of standard method for samples of dry density 1250, 1500 and 1900 kg/m3 are shown in Figure 3-36.

Following the discussion at the internal WP4 workshop top and bottom measurement of total pressure was performed for three samples of dry density 1525, 1580 and 1750 kg/m³. Results (Figure 3-37) show that there is indeed difference in total pressure evolution on both sides of sample and it should be considered while developing the model.

By request from modelling team a temporal evolution of saturation was investigated. Series of samples with dry density of 1600 kg/m³ was saturated and in predetermined intervals dismantling has been performed. During dismantling the sample was sliced into pieces approximately 2 mm thin and water content of each slice was determined by gravimetric method. Figure 3-38 shows saturation development over time.
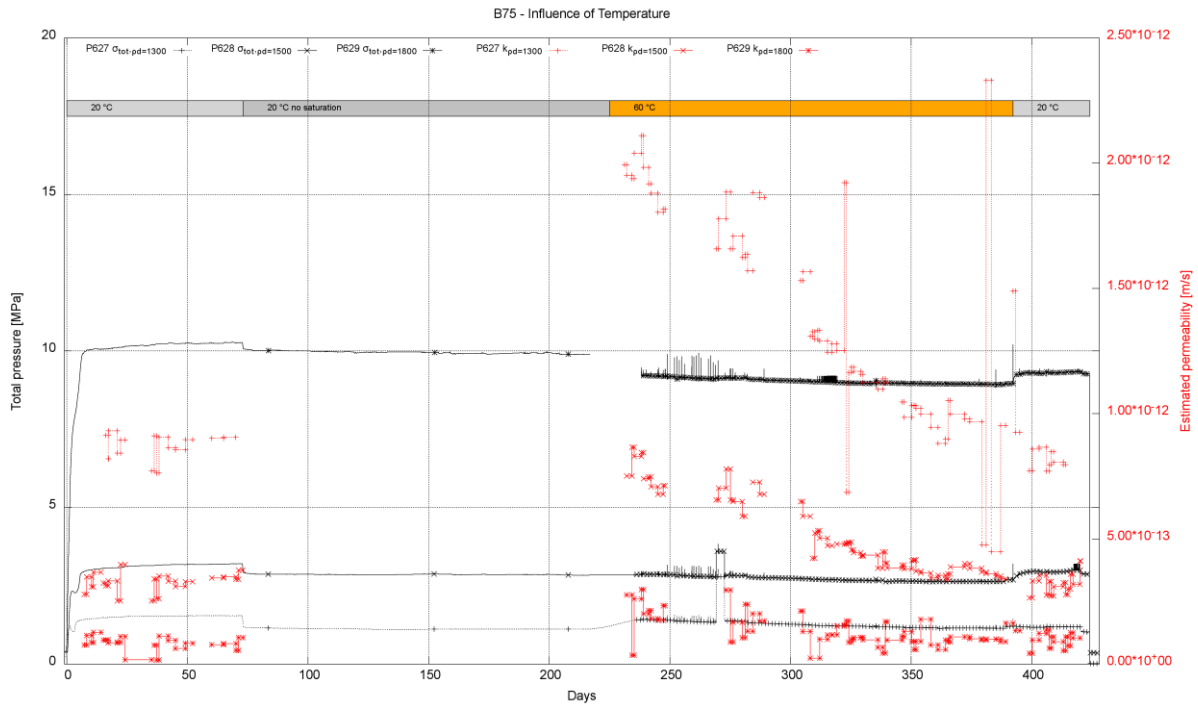
Figure 3-35. B75 Influence of temperature
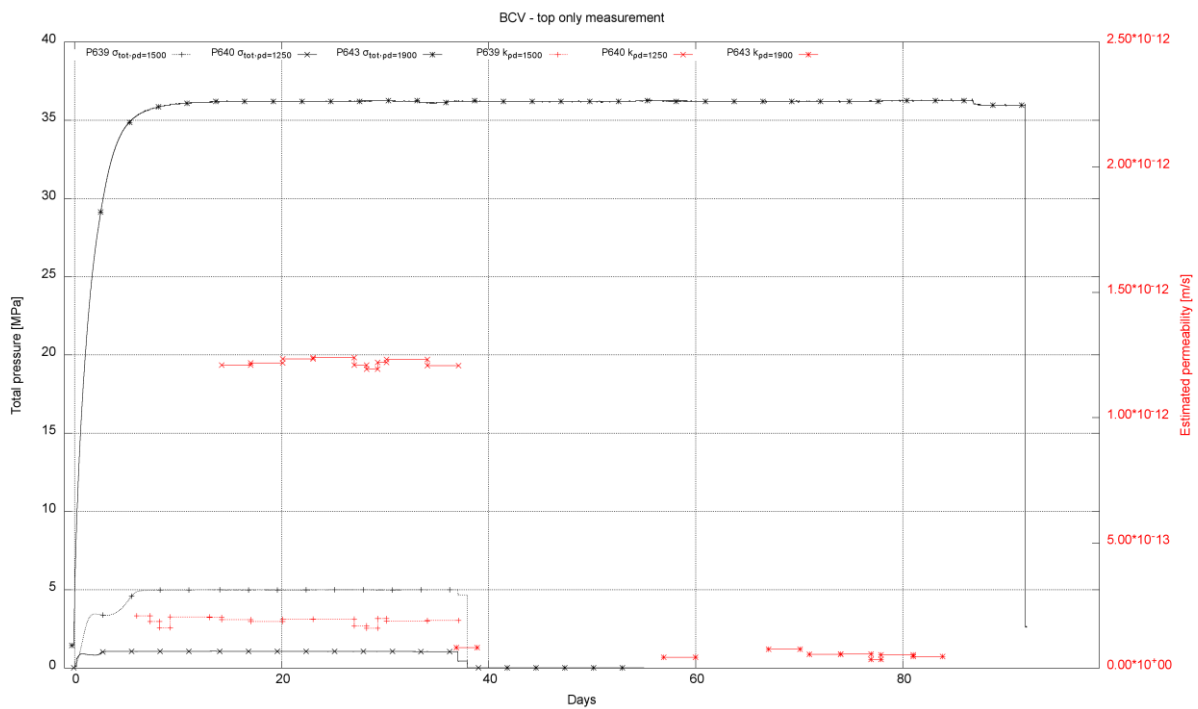
Figure 3-36. BCV homogenous samples (top only measurement)
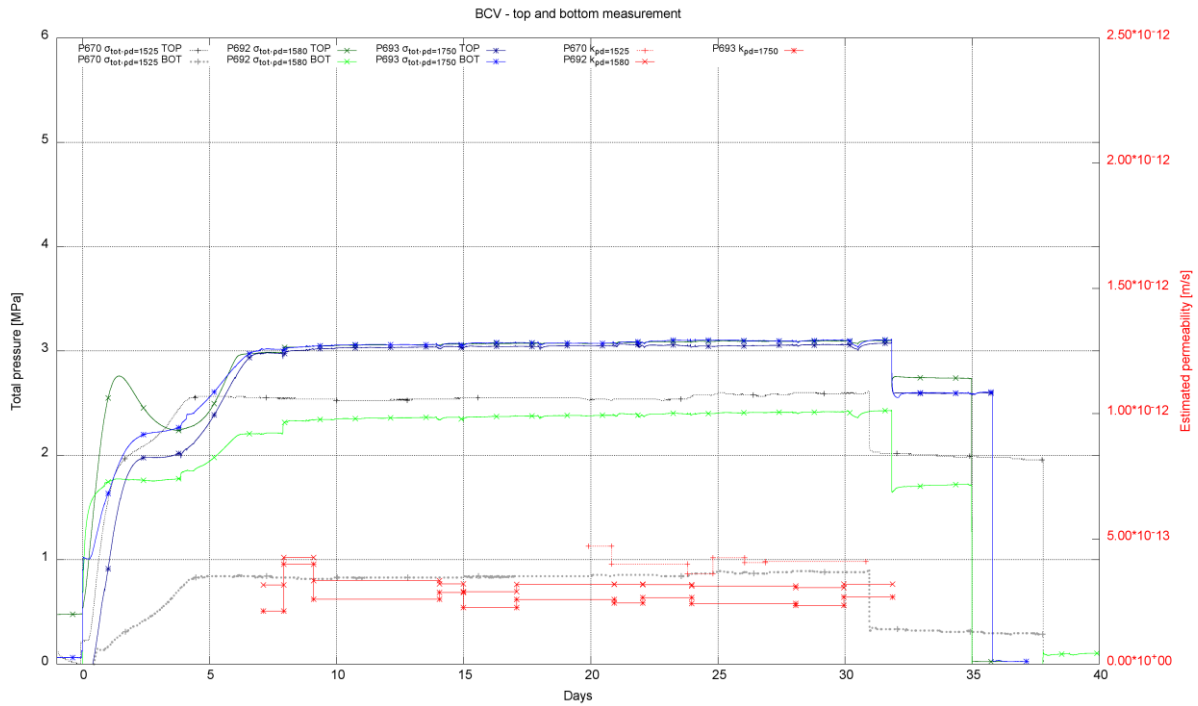
Figure 3-37. BCV homogenous samples (top & bottom measurement)
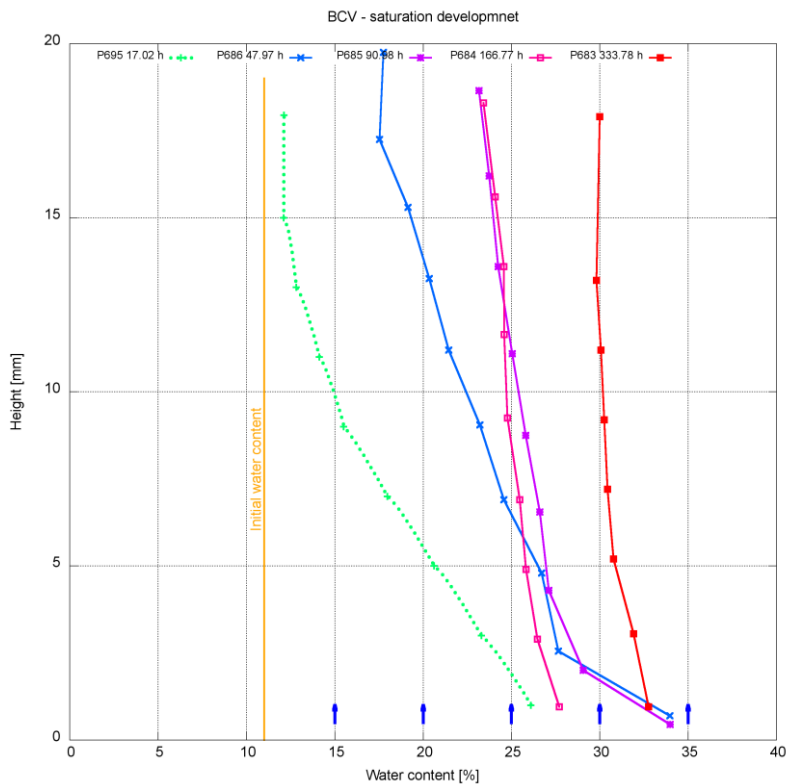
Figure 3-38. BCV Saturation development

Dual density samples

Density distribution changes have been investigated for BCV a B75 using dual density samples. In these test lower and upper part (half) of the sample had different initial dry density. The overall dimensions were same as for homogeneous samples. After the test was finished the sample was always sliced and water content distribution determined. At the same time dry density has been determined however due to irregular size of the slice its value is only indicative (more precise value of density can be calculated from water content/density at full saturation curve).

For each material two samples were tested. One sample with higher densty in the upper part and the other in lower part. This allowed to observe the influence of flow direction in the cell. Results for B75 are shown in Figure 3-39 and for BCV in Figure 3-40. The results show that significant difference for each density configuration. When the low density part is at the top there are singificant changes in density distribution. This is probably caused by highly compacted part compressing the lower density part – the high density parts gets access to the water first and starts swelling thus compacting still dry lower density part (moreover the water pressure gradient helps the compression). On the contrary when lower density part is at the bottom it swells first and resists compression from upper part which starts to swell later (moreover the water pressure gradient helps the prevent compression of lower density layer).
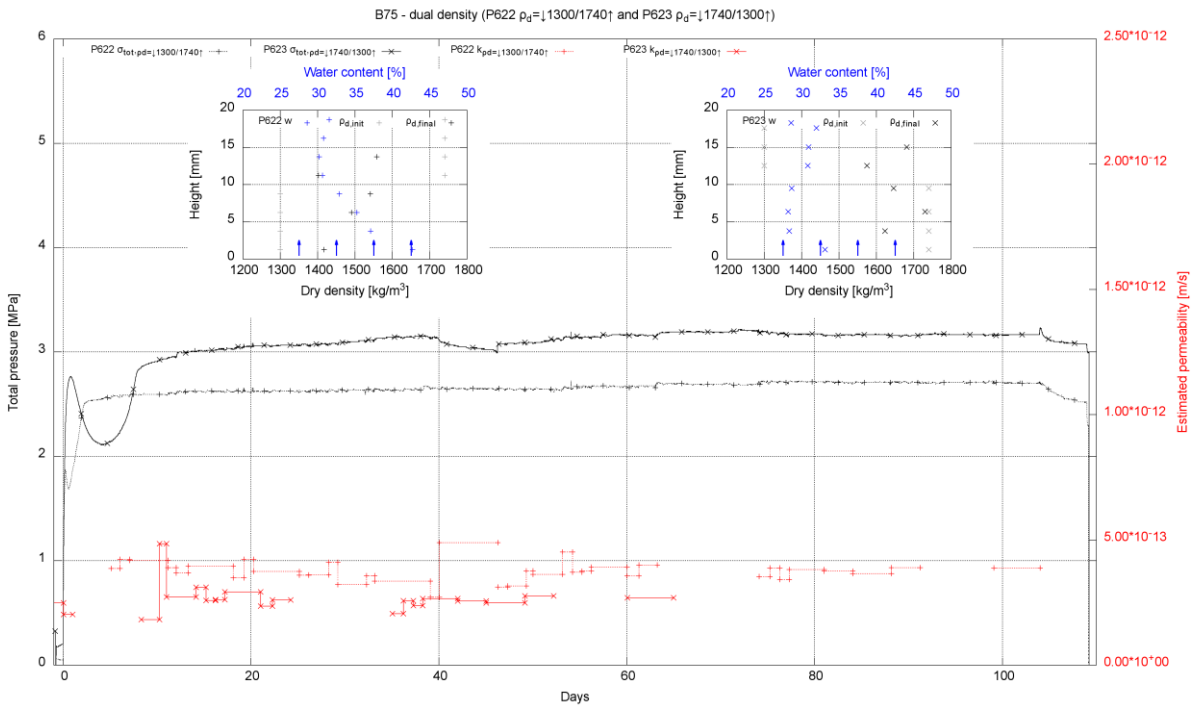
Figure 3-39. B75 dual density samples

47
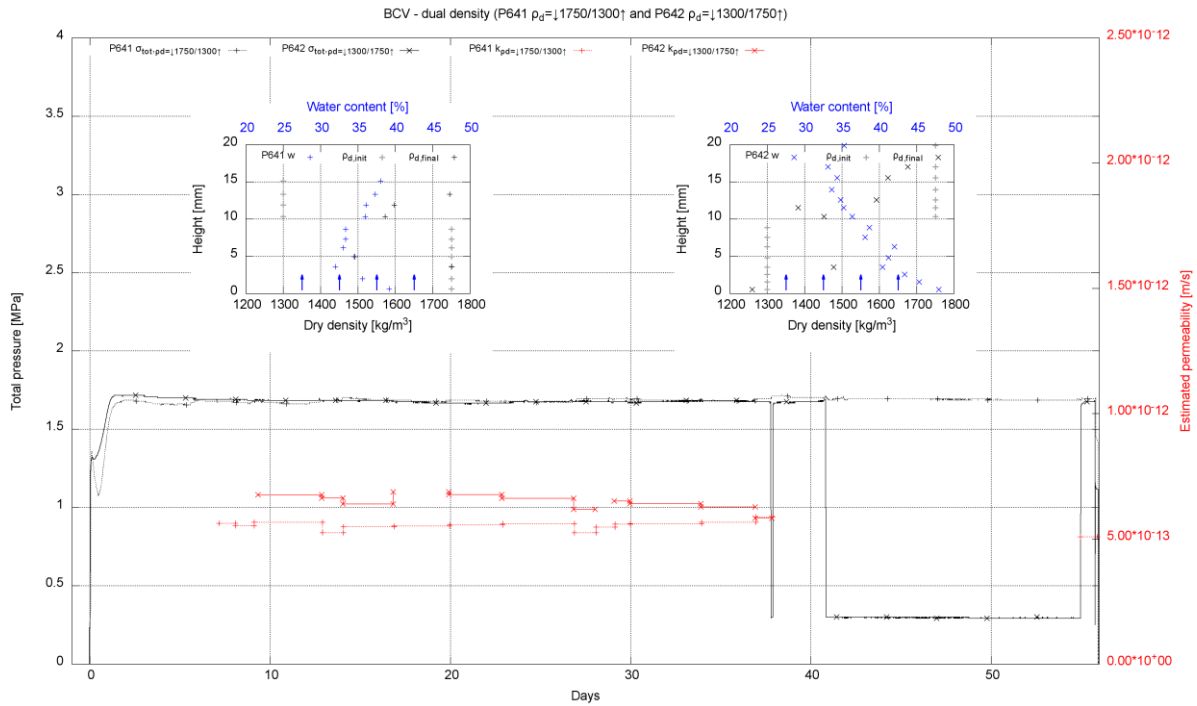
Figure 3-40. BCV dual density samples

Pellets

BCV pellets (Figure 3-41) were investigated in standard 30 mm diameter cells and in larger e.g. 120 mm diameter cells. For smaller cells fraction bellow 6 mm was used, for 120 mm cells no sieving was necessary.

Figure 3-41. BCV pellets

Test procedure for the pellets had to be modified for some samples. At the beginning of the test the saturation cannot be continuous due to voids between pellets. These voids create continuous pathway for water flow causing high water flow through the sample. Therefore, initially the water is introduced to the sample and then shut off (several times if necessary). This can be observed on fluctuation of total pressure. Once the major voids are closed full water gradient is applied and hydraulic conductivity is measured on periodic basis.
Results for top only measurement (small and big cells) is shown in Figure 3-42. Based on results of discussion at WP workshop top and bottom measurement of total pressure was carried out for one sample. Results are shown in Figure 3-43.

48
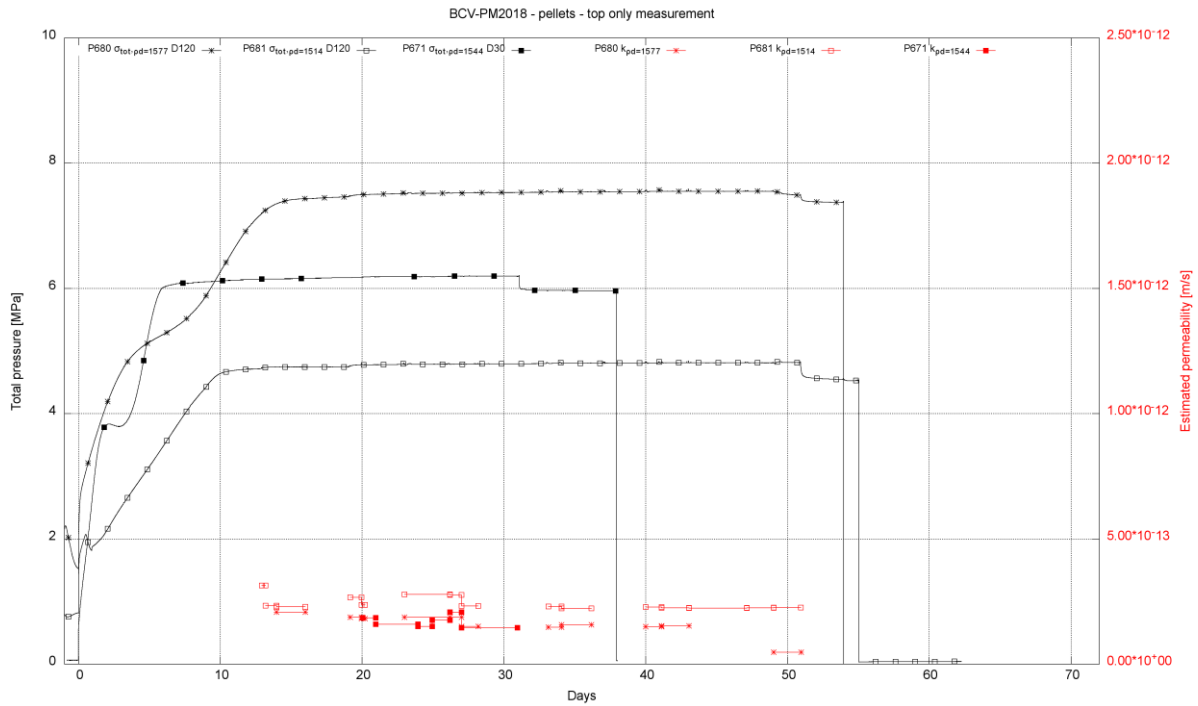
Figure 3-42. BCV pellets (top only measurement)
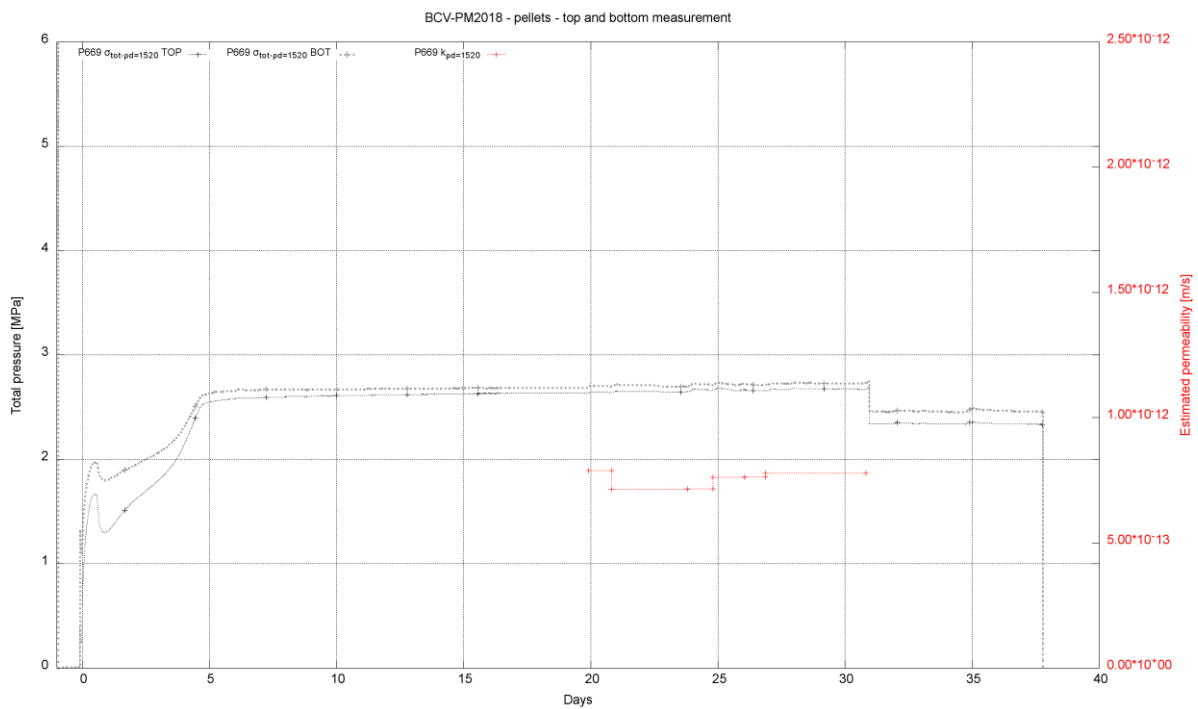
Figure 3-43. BCV pellets (top & bottom measurement)

4 Swelling into limited void

4.1 Swelling into a void as function of sample/void ratio, orientation and temperature (BGS)

Understanding the behaviour of bentonite and its long-term performance is critical for establishing a safety case for its use in the geological disposal of radioactive waste. As the bentonite expands into engineering voids within the repository setting, the non-uniform development of porewater pressure and its coupling to total stress within the bentonite, across interfaces and around its circumference, may result in persistent material heterogeneities. As hydration progresses, differential stress (difference between maximum and minimum stress) reduces (Harrington and Tamayo-Mas, 2016; Harrington et al., 2017), whilst variations in density, permeability and mechanical properties remain. The continued endurance of these property variations, along with the final degree of homogenisation, is poorly understood.

These material heterogeneities could have a deleterious effect on the long-term behaviour of the barrier, and greater certainty in the description of the long-term behaviour of the bentonite, combined with a full understanding of the development and persistence of heterogeneities (e.g. locked in stresses, density variations, persistent interfaces etc.) stored within the clay is needed. In addition, the accurate description of key parameters (swelling pressure, permeability, strength, friction coefficients etc.) will all be affected by temporal constraints encountered by the development and distribution of porewater pressure within the buffer. Indeed, such slow time dependent phenomena associated with wetting, as well as the possibility of these processes being strongly localised, may account for a significant component of the heterogeneity observed in many small- and full-scale experiments.
To address this issue, the British Geological Survey, in collaboration with Svensk Kärnbränslehantering AB (SKB) and as part of the BEACON project, has undertaken a suite of laboratory tests to examine the swelling capacity of bentonite as a function of sample size, orientation and temperature. In this report, the results of six homogenisation tests that have been successfully performed on pre-compacted samples of bentonite, are presented, whilst a further 2 tests are still underway (Table 4-1).

Table 4-1: Sample and void dimensions, porewater pressure, permeant choice and test temperature. The diameter of the sample was nominally 60 mm in each experiment

Test no.	Sample orientation	Length of sample (mm)	Void length (mm)	Water pressure (kPa)	Permeant	Temperature	Test system
1	Vertical	65	55	4500	Distilled water	Ambient (20 °C)	Apparatus 1 (Invar)
2	Vertical	65	55	4500	Distilled water	Elevated (90 °C)	Apparatus 2 (stainless steel)
3	Horizontal	65	55	4500	Distilled water	Ambient (20 °C)	Apparatus 3 (stainless steel)
4	Vertical	75	45	4500	Distilled water	Elevated (90 °C)	Apparatus 2 (stainless steel)
5	Vertical	85	35	4500	Distilled water	Ambient (20 °C)	Apparatus 1 (Invar)
6	Horizontal	65	55	4500	Distilled water	Ambient (20 °C)	Apparatus 3 (stainless steel)
7	Vertical	75	45	4500	Distilled water	Ambient (20 °C)	Apparatus 1 (Invar)
8	Vertical	85	35	4500	Distilled water	Elevated (90 °C)	Apparatus 2 (stainless steel)

4.1.1 Experimental Apparatus and Methodology

A constant volume cell was used to volumetrically constrain the samples in each test, mimicking the boundary conditions of the KBS3 disposal concept (Harrington and Tamayo-Mas 2016, Harrington et al. 2017). This configuration reproduced the borehole and unyielding surface of the host-rock wall, which are key features of the repository near-field for the purposes of this homogenisation study. Three different apparatuses were used so that tests could be run simultaneously, however each set-up shared the same basic volumetric constraint with an internal diameter of 60 mm and an internal length of 120 mm. Although they had different sensor configurations, each vessel was instrumented with a series of load cells to directly measure the development of total stress at multipole locations around the sample. The radial pressure was also measured at different locations around the sample. Apparatus 1 was fitted with 8 radial and 4 axial pressure cells to measure total stress (Figure 4-1). Apparatuses 2 and 3 had fewer load cells (3 radial and 2 axial) for measuring total stress, but were also instrumented with 12 radial pore pressure filters (Figure 4-2). In Apparatus 2, the pore pressure filters were grouped into 3 arrays along the major axis of the sample, each with 4 filters around the circumference of the clay. In Apparatus 3, the development of porewater pressure was individually recorded in all 12 radial filters.
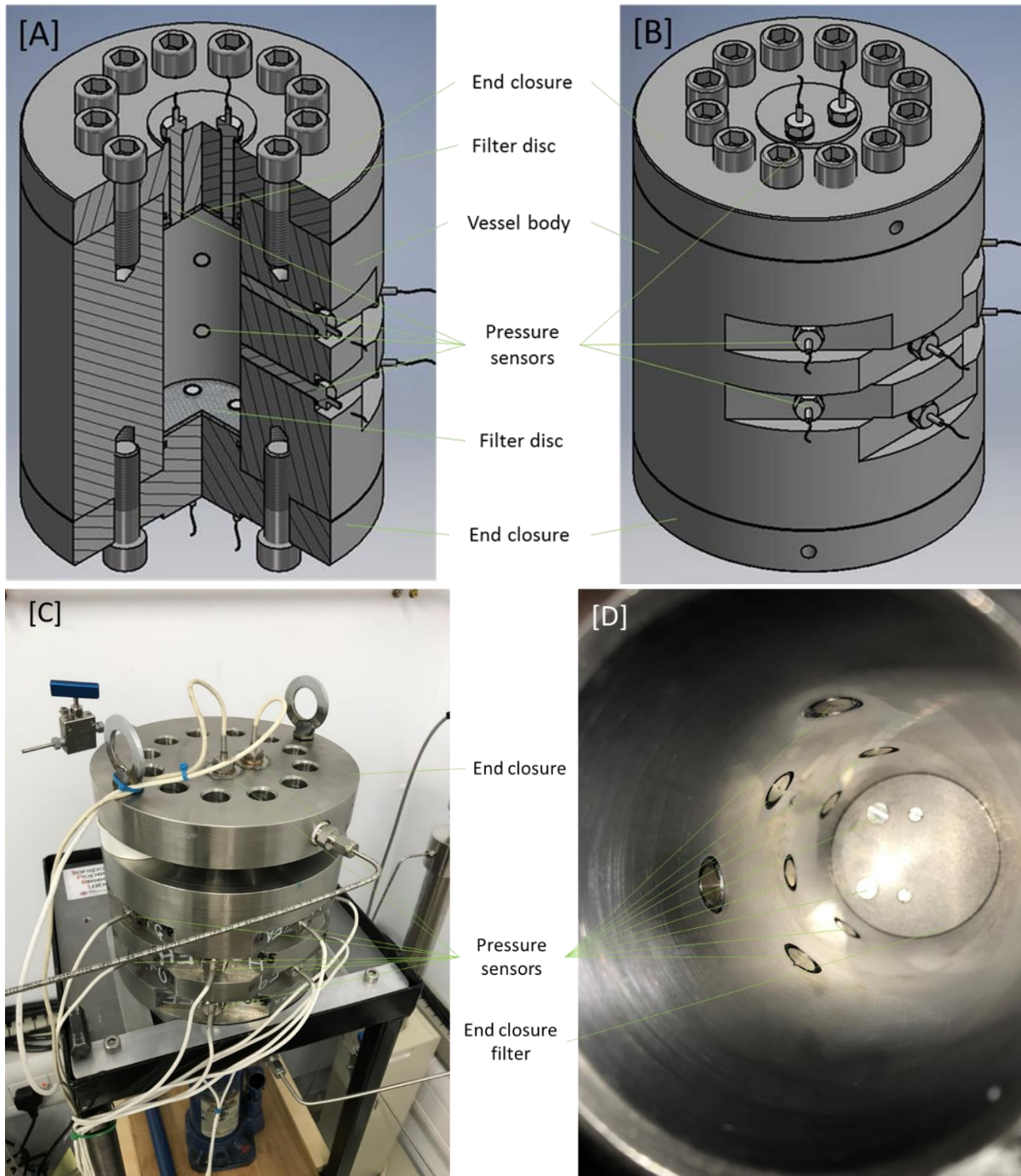
Figure 4-1: [A] and [B] cut-away diagrams of Apparatus 1 showing the positioning of the pressure sensors and axial filter discs;[C] photo of vessel, end closures and pressure sensors; [D] internal view showing the eight radial and two axial pressure sensors. The axial sensors are embedded in the end closure filter (from Harrington and Daniels, 2018)
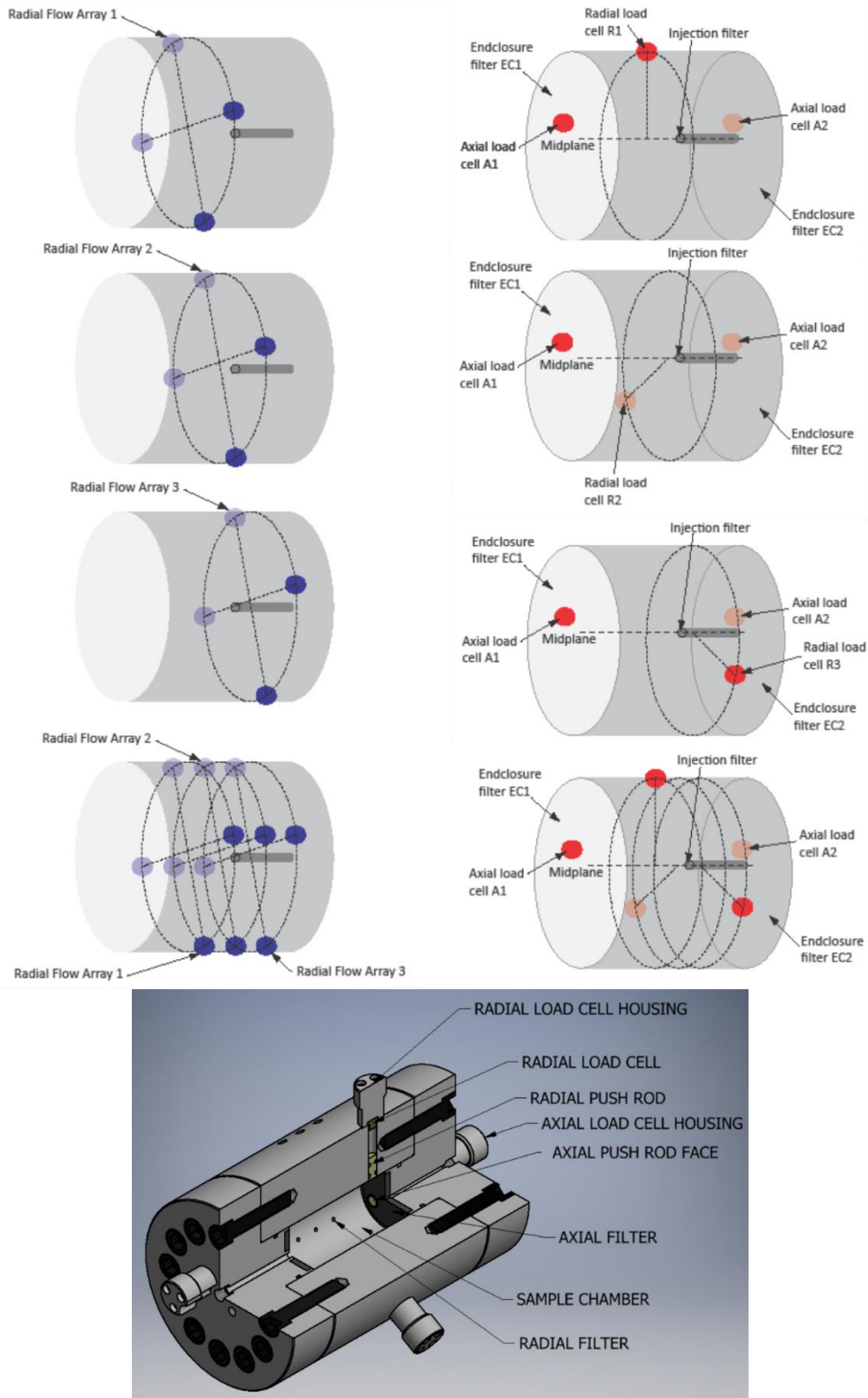
Figure 4-2: [A] Schematic representation of Apparatus 2 and 3 showing filter and total stress sensor locations. Each radial flow array comprises four filters (blue dots) set at 90° to each other. Five total stress sensors (red dots) are located around the periphery of the sample, two axial and three radial;[B] Cut-away diagram of the Apparatus 2 and 3 showing the positioning of the load cell housings and locations of the porewater pressure filters (From Harrington and Daniels, 2018)

Before the apparatuses were calibrated and the samples installed, the tubework was carefully flushed of residual gas with the test fluid (distilled water) through each the ports in

sequence. The pore pressure measurement ports were fitted with porous plugs to prevent clay material from migrating up the instrumentation holes. After calibration, the sample was immediately installed to prevent drying and the remaining void space within the apparatus was filled with distilled water.

High precision Teledyne ISCO D-Series 260D syringe pumps were used to apply a porewater pressure to each end of the sample, and then to control or monitor the flow rates into or out of the sample. All of the tests were performed with distilled water as the external pressurising fluid. Once the porewater pressure had been applied, no external hydraulic gradient was thereafter applied to the clay. The flow rates, total stress and pore pressure were all logged at an interval of 2 minutes using the FieldPointTM and cRIO logging hardware and the LabVIEWTM data acquisition software (National Instruments Corporation, Austin, TX, USA), providing a detailed time series dataset.

4.1.2 Experimental Results

The basic geotechnical properties of the samples are shown in the Table below (Table 4-2). Each sample was manufactured to a diameter of 60 mm; the starting length was varied. Following insertion of each sample into the apparatus, the pore pressure was carefully increased in a series of steps to the target value of 4.5 MPa; this value was set with SKB as a suitable reference value comparable to the current Swedish repository concept.

Table 4-2: Basic geotechnical properties of the test material. The samples are assumed to be at 100% saturation, which is a reasonable assumption based on pre-test calibration work. The dry density is a measured value obtained from a test sample made in advance of the testing program, specifically to obtain the geotechnical properties of the starting material. The test samples FPR-BE-1 to FPR-BE-8 were then manufactured using an identical method

Test no.	Sample	Material	Length (mm)	Diameter (mm)	Bulk density (g/cm³)	Dry density (g/cm³)
1	FPR-BE-1	Mx-80	65.0	59.7	2.057	1.702
2	FPR-BE-2	Mx-80	64.9	59.8	2.053	1.702
3	FPR-BE-3	Mx-80	65.2	59.7	2.047	1.702
4	FPR-BE-4	Mx-80	74.9	59.7	2.052	1.702
5	FPR-BE-5	Mx-80	85.2	59.7	2.055	1.702
6	FPR-BE-6	Ca-Clay	65.0	59.8	2.021	unknown
7	FPR-BE-7	Mx-80	74.7	59.5	2.054	1.702
8	FPR-BE-8	Mx-80	84.9	59.7	2.062	1.702

Tests FPR-BE-1, 5 and 7 (Vertical samples, ambient temperature)

Figure 4-3 shows an x-y plot of the development of pressure within the apparatus as the FPR-BE-1 clay began to swell. It is clear from the data that the development of pressure is spatially complex and a time consuming process, with significant variance still existing as the test was terminated (at day 100) (Figure 4-4). Given that the pressure change observed during the latter stages of testing is very small, extrapolation of the results suggests that homogenisation of the bentonite would not occur for many years (if at all). However, it is clear that bentonite, under zero hydraulic gradient, is able to swell and ultimately fill the start void, creating a small but measurable swelling pressure (seen in axial sensors A and B).

The first 10 days of the FPR-BE-1 test, showing the complex swelling response, is seen in Figure 4-5. After the external porewater pressure is applied, the highest force registered in the clay is at sensor R6, 17mm below the top of the sample. Significant anisotropy in the swelling

response is observed, with R5 (located in the same plane as R6, Figure 4-1) exhibiting a substantially lower pressure (a difference of >2MPa for the first 3 days of testing). Whilst this may simply reflect the availability of water during this early phase of testing, it highlights the capacity of the bentonite to sustain significant differential stress governed by its internal shear strength. The momentary drop in pressure of R5 around day 0.2 may relate to frictional issues between the vessel wall and clay (akin to stick-slip). However, the timing and magnitude of the drop is not directly observed in the other sensors, and could be explained by localised yielding of the clay. The subsequent increase in response of the R5 sensor (increasing the difference in pressure between it and the other sensors), peaking around day 1.4, suggests simple friction and movement of the sample are not the only causes of the inflections observed in the data. Indeed, the smooth evolution of the pressure traces is contrary to classic stick slip friction behaviour which is signified by abrupt changes in response. As hydration continued, swelling was focussed in radial arrays R7 and R8, which, after an initial period of anisotropy, began to converge following a similar pressure response from around day 4.5 (Figure 4-5). Sensors R7 and R8 continued to yield the highest values of pressure for the remainder of the test. Close inspection of the data (Figures 4-3 to 4-5) shows no signs of stick-slip behaviour during this phase of hydration.
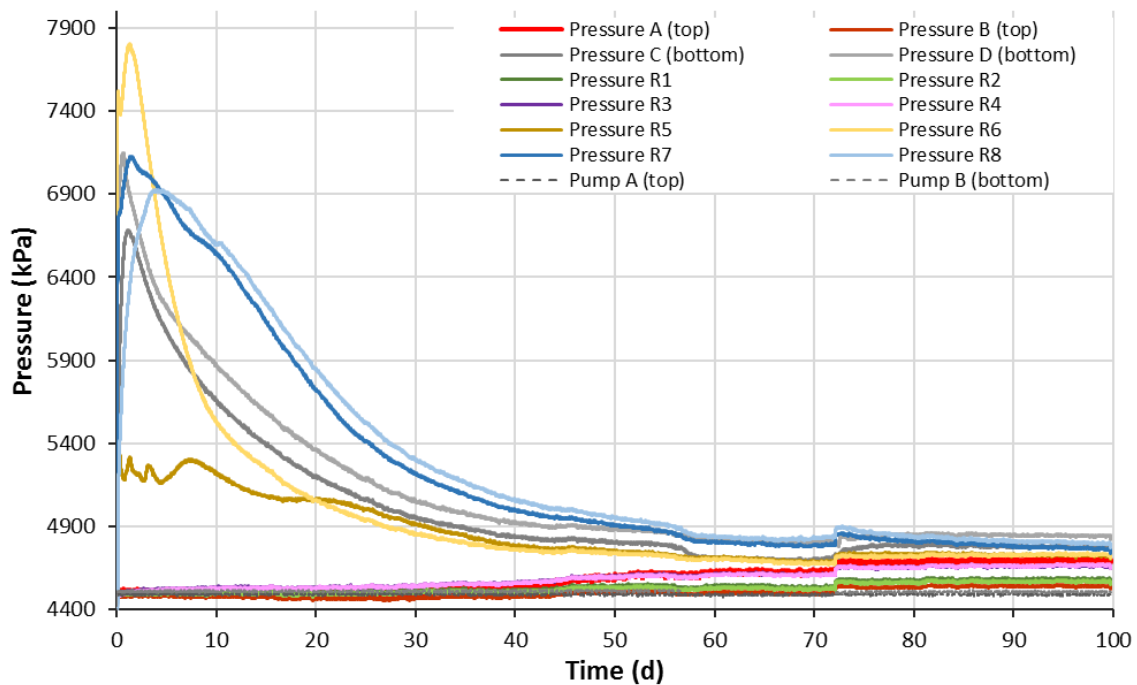
Figure 4-3: x-y plot showing the development of pressure during test FPR-BE-1. The small drop in value from day 56.6 to 72.1 was caused when the ISCO pump controlling porewater pressure in the base of the sample inadvertently turned off (From Harrington and Daniels, 2018)
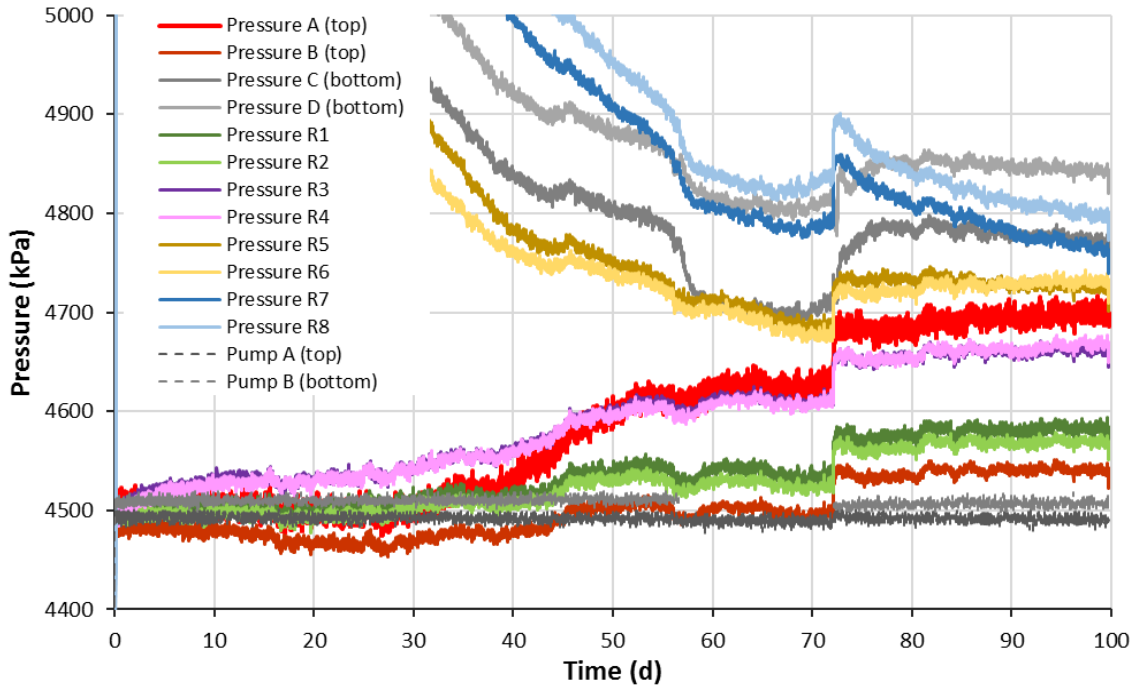
Figure 4-4: Exaggerated vertical scale showing the slow rates of pressure development before test FPR-BE-1 was terminated at day 100. Projection of the results suggest that homogenisation of the bentonite would not occur for many years (if at all) (From Harrington and Daniels, 2018)
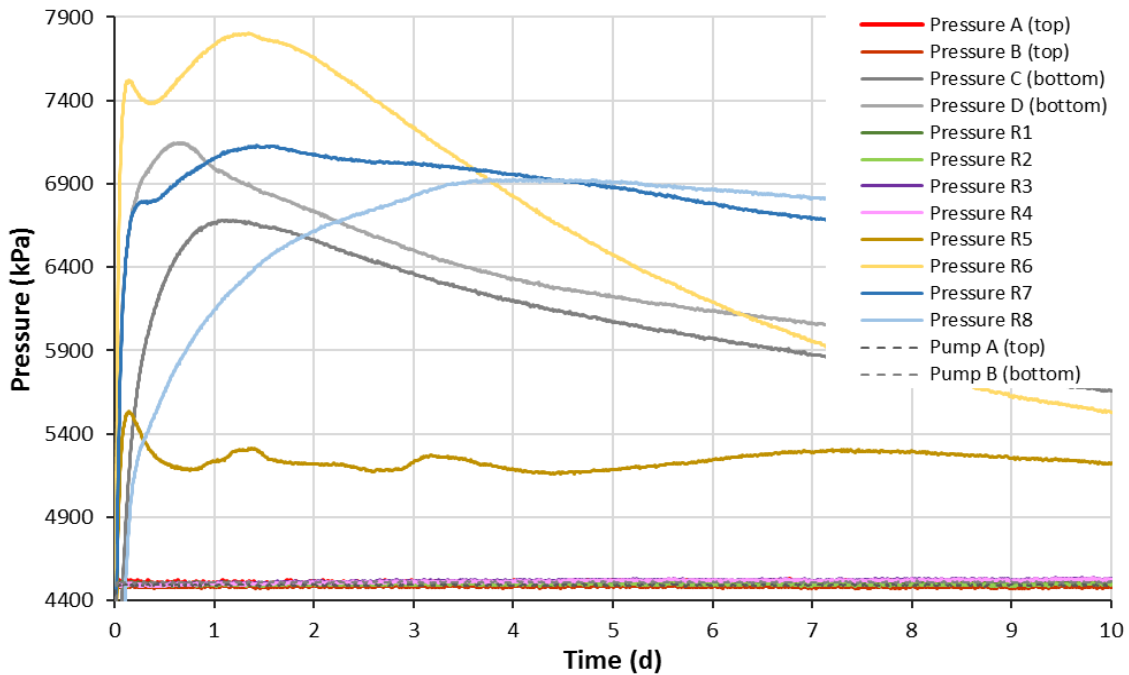
Figure 4-5: Development of pressure in test FPR-BE-1 during the first 10 days of testing. Inflections in the pressure traces may relate to friction or plastic yielding of the sample (From Harrington and Daniels, 2018)

Figure 4-6 (FPR-BE-5) and Figure 4-7 (FPR-BE-7) show that the same significant anisotropy in the swelling response is observed in the vertically oriented ambient temperature tests with longer starting sample lengths. All three vertically oriented ambient temperature tests (FPR-BE-1, FPR-

BE-5 and FPR-BE-7) show significant variance in the recorded swelling pressures at the end of the tests.
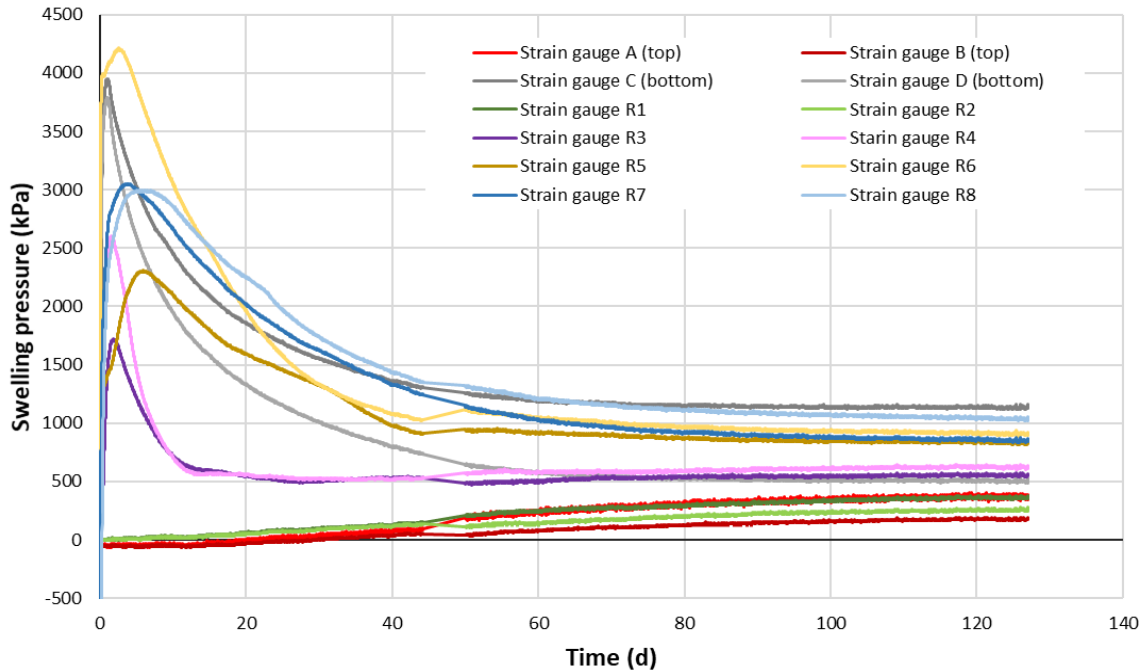
Figure 4-6: x-y plot showing the development of pressure during test FPR-BE-5
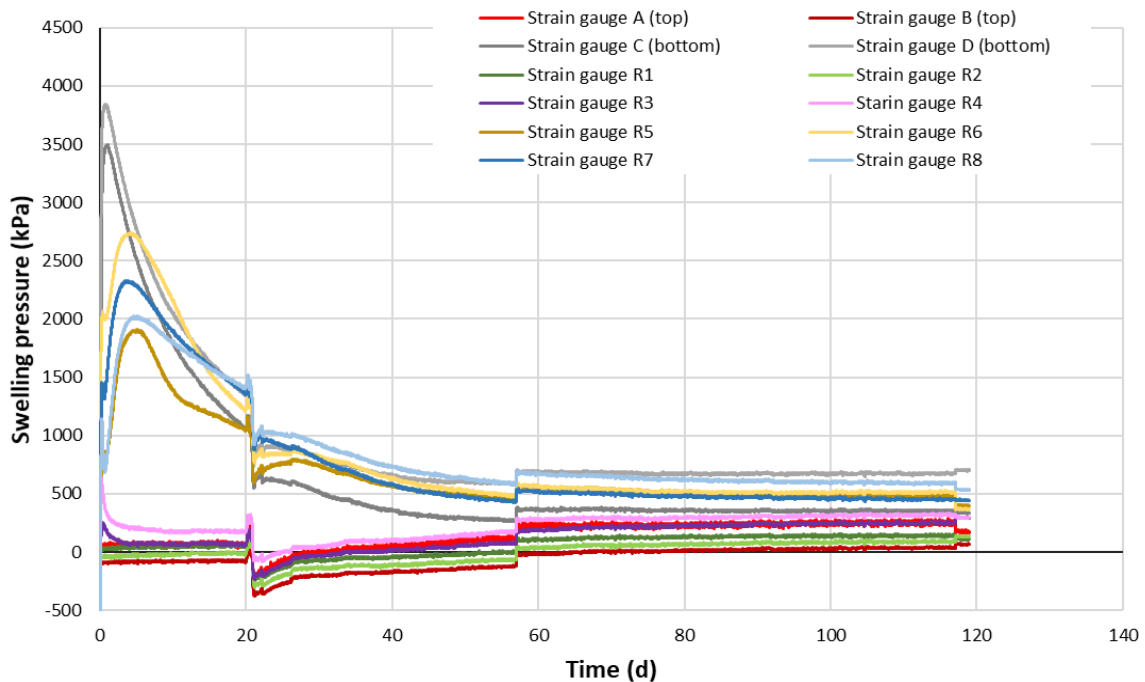
Figure 4-7: x-y plot showing the development of pressure during test FPR-BE-7. The deviation in the data collected between days 20 and 55 was due to a failure in the air conditioning system that moderates the temperature of the temperature-controlled testing room

A well-defined flow transient was observed in the flowrates into and out of the vessel from beneath and above the FPR-BE-1 sample; the inflow and outflow were roughly symmetrical, suggesting minimal net volume change within the vessel. This was not surprising, given the void above the sample was completely filled with water immediately after installation of the

57

clay. However, the data in Figure 4-8 provides a useful measure with which to apportion swelling strains crudely within the sample. Examination of the data suggests around 36 ml of water entered the sample through the base of the vessel. This quantity is relatively small, compared to the start void volume of 155.5 ml, suggesting that swelling, driven by water inflow through the base of the clay, accounted for less than 23% of the volume change required to close the void. The bulk of sample expansion clearly occurred through unconstrained swelling through the upper face of the clay. This accounted for around 77% of the swelling strains required to close the void. Post-test measurements of moisture content and dry density confirm these observations.
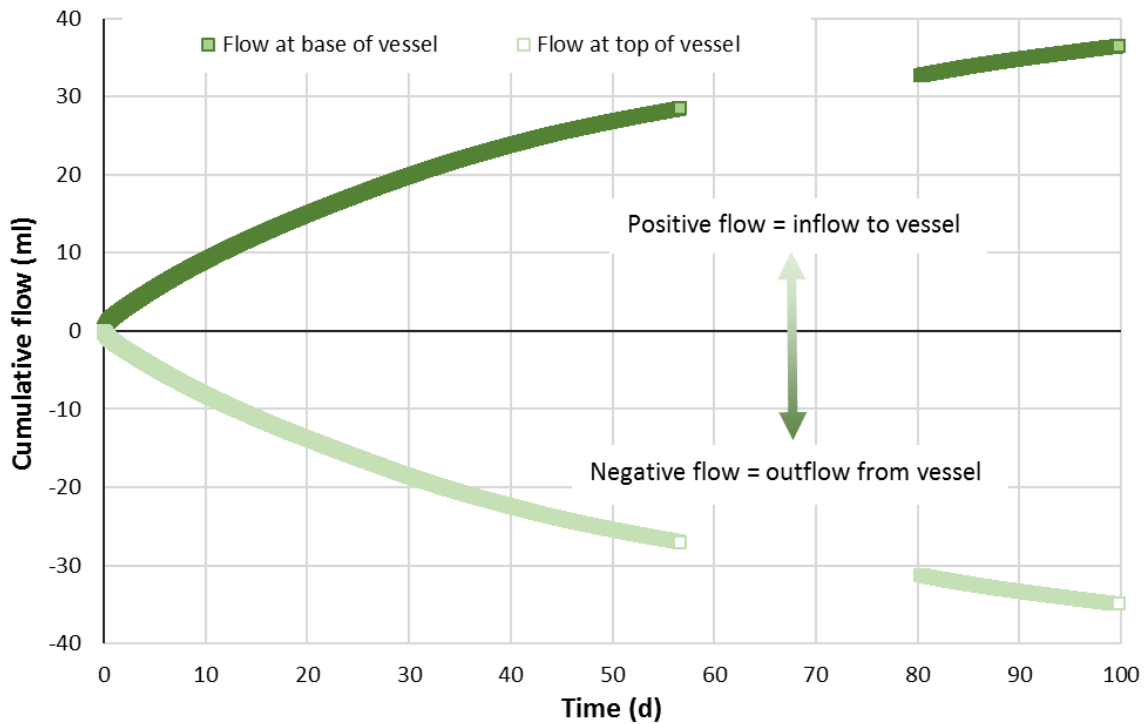
Figure 4-8: Cumulative flow into and out of the vessel from below and above the core, test FPR-BE-1 (From Harrington and Daniels, 2018)

Tests FPR-BE-2, 4 and 8 (Vertical samples, elevated temperature)

In tests FPR-BE-2, -4 and -8, the apparatus was heated prior to the flushing of the ports and installation of the sample. Following the same method as for test FPR-BE-1, the sample was pressurised incrementally through two large axial filters (EC1 and EC2, Figure 4-2) up to the 4.5 MPa target pressure. The pressure recorded by the axial and radial load cells in tests FPR-BE-2, -4 and -8 evolved in the same manner as in the ambient tests, although the maximum values observed were lower and returned to a steady value much more quickly (Figure 4-9). As with the ambient temperature tests, significant variance in the recorded values between the axial and radial load cells was seen by the end of each of the elevated temperature tests. The data from these tests have shown that at an elevated temperature of 90 °C, bentonite can swell into an engineered cavity, occupying the void and creating a swelling pressure on each end of the confining vessel. This occurred much more quickly than in the ambient temperature tests. Unlike the ambient temperature tests, there were no large inflections in the stress traces from FPR-BE-2 (Figure 4-9) suggesting that there were little, if any, frictional stick-slip issues experienced between the wall and the clay in this test; the stress traces in FPR-BE-2 evolved in a smooth manner.
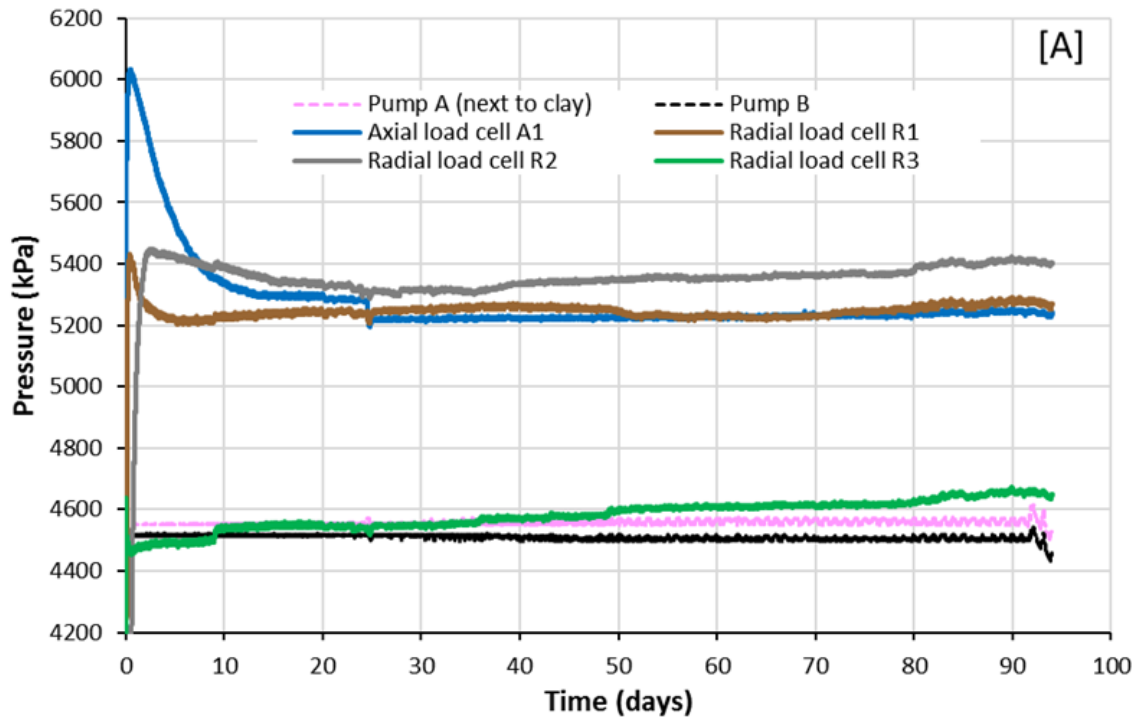
Figure 4-9: an x-y plot of the evolution of pressure within the apparatus over the duration of the test (From Harrington and Daniels, 2018)

The porepressure data for all of the elevated temperature tests (FPR-BE-2, -4 and -8) (Figure 4-10) show that the expansion and swelling of the clay occurs in a gradual and consistent manner. Not surprisingly at the start of testing the pore pressure recorded by the radial transducer, Radial Trans 3, located in the void, registers the pressurised test fluid straight away; this is not true for the 85 mm starting sample (FPR-BE-8) because the starting sample covers the radial transducer filter from the beginning of the test, however, it is the first transducer to register a response. Radial Trans 1 and 2, the filters connected to which are obstructed by the starting sample in all tests, initially see no pressure change. As the test fluid moves into the clay and the clay expands up into the test fluid, these two sensors begin registering a pressure. Radial Trans 2 is the first to respond in tests FPR-BE-2 and FPR-BE-4, with a sharp change in pressure recorded. Radial Trans 1, closest to the bottom of the vessel registers the pressure increase last (Figure 4-10). Once the pressures recorded by these sensors have reached the pressure imposed by the pumps at each end of the vessel, the recorded value remains constant. For the shortest sample starting length of 65 mm (FPR-BE-2), the time taken for each of the radial transducers to register a change in pressure is the shortest. The opposite is true for the longest starting sample of 85 mm (FPR-BE-8). The times taken for the radial transducers to register the change in pressure for the 75 mm starting sample length test (FPR-BE-4) are intermediate between tests FPR-BE-2 and FPR-BE-8.
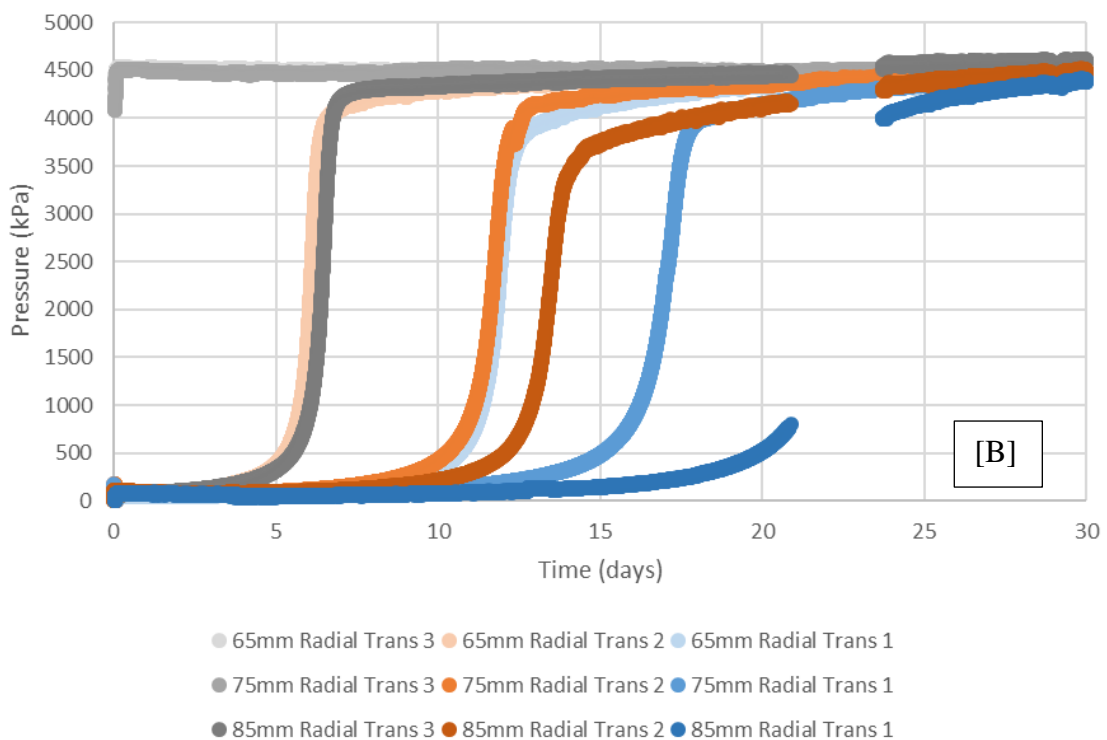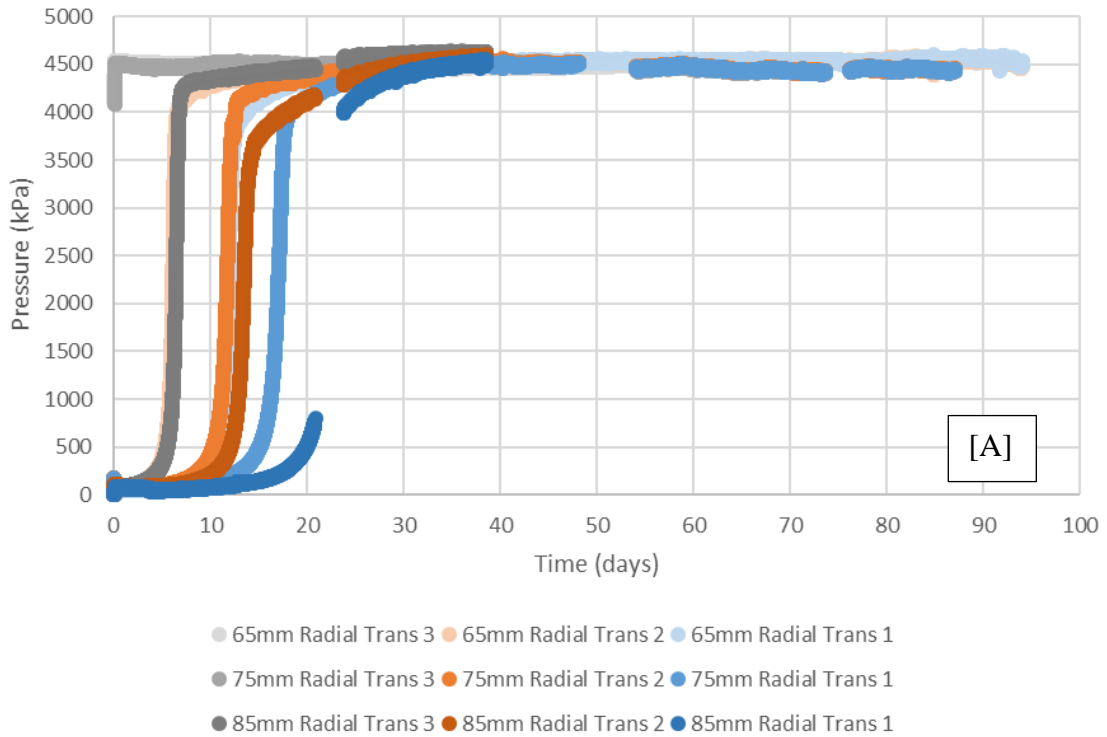
Figure 4-10: [A] x-y plot of the evolution of pore pressure over the FPR-BE-2 (65mm starting sample), -4 (75mm starting sample) and -8 (85mm starting sample) tests durations; [B] the development of the pore pressure over the first 30 days of the tests

Tests FPR-BE-3 and 6 (Horizontal samples, ambient temperature)

To examine the possible effect of gravity segregation on the swelling behaviour of bentonite, two tests were initiated in which the samples were horizontally mounted within the apparatus. Except for this geometric change, all other aspects of the FPR-BE-3 test were the same as in the ambient temperature tests FPR-BE-1, -5 and -7. In FPR-BE-6, the Mx-80 clay material was substituted for a calcium-rich Bulgarian bentonite. As before, the void next to the sample was completely filled with water by carefully tilting the apparatus during the assembly procedure. Once the final end-closure was in place the large axial filters (EC1 and EC2, Figure 4-2) were independently pressurised to 4.5 MPa.

Figure 4-11 shows the development of swelling pressure within the FPR-BE-3 test as hydration of the clay occurs. As before, axial swelling pressure next to the clay (denoted A1 in this test geometry) rapidly increased as hydration started. Similarly, to test FPR-BE-1, the radial load cell R1, location at the mid-plane of the vessel (close to the top of the sample) quickly increased and day 4.2 emerged as the highest response within the system. As before, this was accompanied by an increase in the R2 radial sensor, located close to the end of the sample nearest the initial void. However, unlike test FPR-BE-1, before the end of day 1 the value of radial swelling pressure recorded by the R2 sensor had peaked and already begun to decay. While the data is somewhat noisy, a trend for decreasing swelling pressure was measured on the A1, R1 and R2 sensors, and continued until around day 30. At this point, the swelling pressure began to increase once again before dropping to a low at ~53 days. This was accompanied by the development of radial swelling pressure at R3 and A2 (located within and above the void respectively) to match the response seen on sensors A1, R1 and R2 for the same time period. By the end of the test at day 76, a significant differential stress of nearly 1 MPa remained within the vessel. This was substantially higher than that observed in either of the FPR-BE-1 or -2 tests, but this may in part, reflect the precision of the measurement system in this apparatus.

Figure 4-12 shows the development of swelling pressure within the FPR-BE-6 test. In the first 20 days of testing, the swelling response of the Ca-rich clay is significantly larger than the Mx-80 equivalent (FPR-BE-3). However, by day 20, the swelling pressure recorded by Radial load cell 1, which recorded the largest swelling response, had dropped to the same magnitude as the swelling pressure seen in FPR-BE-3 (approximately 1.5MPa). As with the previous tests, at the point of termination at day 100, significant variance in the swelling pressures recorded still existed in the FPR-BE-6 test.

The flow rates into and out of the FPR-BE-3 and FPR-BE-6 tests exhibited the same general behaviour as seen in test FPR-BE-1. Examination of the FPR-BE-3 data suggests around 26 ml of water entered/left the sample through the vessel filters. This quantity is around 27% less than that observed in test FPR-BE-1, in part reflecting the shorter duration of the test. Using the value from FPR-BE-3, swelling through water inflow at the base of the clay, accounted for around 17% of the volume change required to close the void. As before, the bulk of sample expansion clearly occurred through unconstrained swelling through the upper face of the clay. This accounted for around 83% of the swelling strains required to close the void. Post-test measurements of moisture content and dry density again confirm these observations.
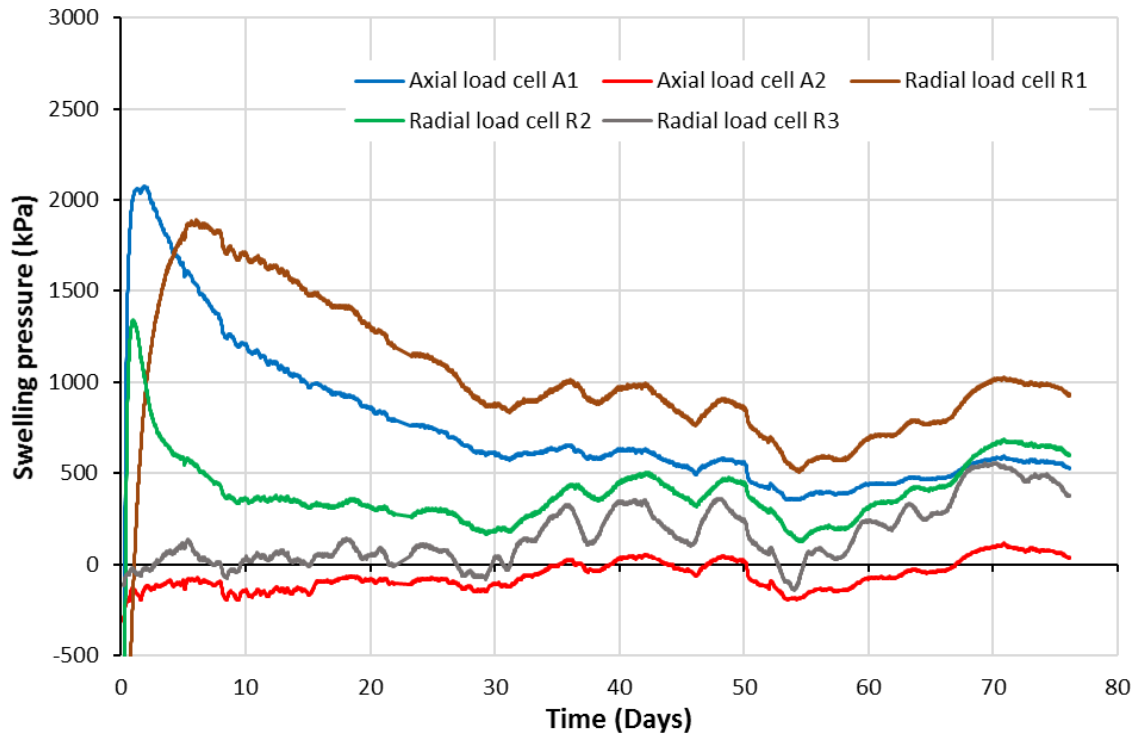
Figure 4-11: Plot showing the evolution of swelling pressure during test FPR-BE-3 (From Harrington and Daniels, 2018)
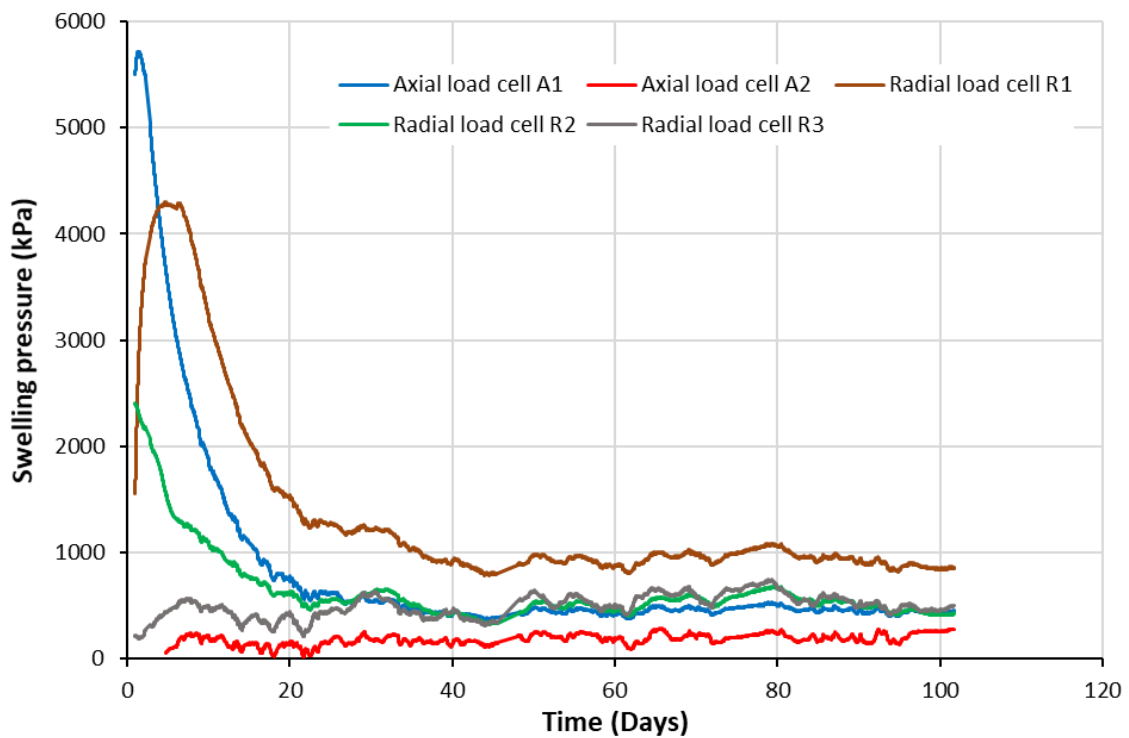
Figure 4-12: Plot showing the evolution of swelling pressure during test FPR-BE-6

Post-test analysis of the samples

Following the completion of each test, each specimen was sub-sampled in order to provide spatial data on the geotechnical properties of the clay. This information provided insight into the swelling response of the clay and the degree of homogenisation that had occurred during each test history. However, given the low strength/density of the samples, it was not feasible to directly obtain volumetrically accurate sub-samples. Instead, each sample was carefully extruded using a hydraulic ram and regular slices of core were taken, which could then be used to accurately determine the moisture content (a parameter which is not dependent on sample volume). A cross-plot of the data, versus distance from the end of the vessel against which the clay samples from FPR-BE-1, -2 and -3 was placed, is presented in Figure 4-13. All three samples show major swelling occurred during testing, with the samples exhibiting qualitatively similar responses. While significant swelling is evident within the first 45-55 mm of each sample, signified by the three-fold increase in moisture content, the values are unexpectedly uniform through these sections of each sample. Why this would be the case is unclear. Inspection of the data shows that large gradients in moisture content are observed only in the volume occupied by the initial void. This is to be expected as progressive swelling of the clay occurs.
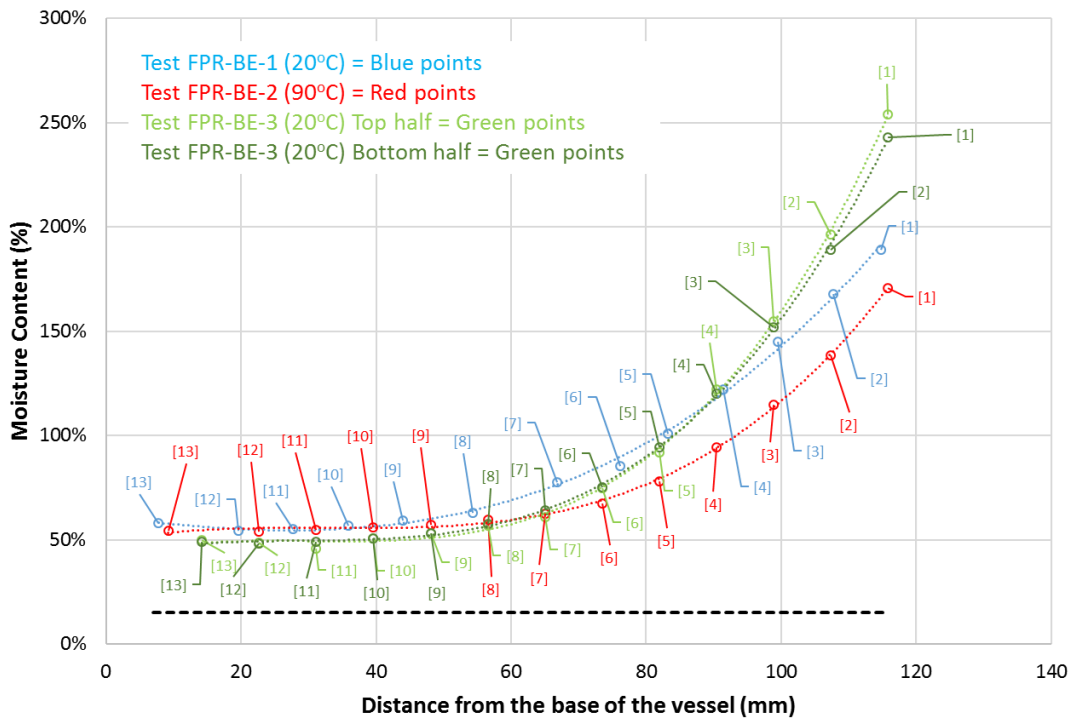
Figure 4-13: Cross-plot of moisture content against distance from the base of the vessel for the first 3 tests (FPR-BE-1 to -3). In the horizontal test FPR-BE-3, this distance equates to the end of the vessel against which the clay was placed prior to testing (From Harrington and Daniels, 2018)

Test FPR-BE-2 (performed at a temperature of 90° C) shows little, if any, additional evidence of homogenisation compared to that of the ambient temperature test FPR-BE-1. While the data from FPR-BE-2 shows less variance in value from 55 to 120 mm, the moisture content values from 0-55 mm are very similar to those of the ambient test. Intuitively, if swelling into the void had occurred at a faster rate (as inferred by the rapid asymptote of the pressure traces in Figure 4-9), moisture content values in the first 55 mm of the elevated temperature test (FPR-BE-2) core should be higher than those of the ambient temperature test (FPR-BE-1). Indeed, it is hard to understand how the clay can exhibit higher densities in one section of the vessel without there being an accompanying decrease in density in the other. These differences in

value between tests FPR-BE-1 and -2 are far larger than any error in the determination of the moisture content, and therefore remain unexplained.

In addition, data from the horizontal test FPR-BE-3 (green dots) indicate that compared to FPR-BE-1 or -2, lower moisture contents were observed in the first 0-50 mm and higher moisture contents noted from 50-120 mm. These differences are significant and are unlikely to be fully accounted for by the difference in test durations given the slow rates of stress evolution noted during the latter phase of each test (Figure 4-3, Figure 4-9 and Figure 4-11). The cause for this behaviour also remains unclear. To examine possible gravity effects on the swelling behaviour of the bentonite, the core from the horizontal test FPR-BE-3, was slabbed at its mid-plane to provide two estimates of moisture content, one in the upper half of the clay and the other in the lower half of the clay. While values are consistent through much of the sample, as moisture contents increase above approximately 150% the data diverges providing clear evidence of gravity segregation occurring in these high moisture content sections of the clay. That said, the longevity of these differences cannot be derived from the current data and further work would be required to answer this question.

Figure 4-14 shows the moisture content data from all six complete tests (FPR-BE-1 to -6). The tests with the longer starting sample lengths (FPR-BE-4 and FPR-BE-5) show a correlation with smaller moisture content increases in the volume initially occupied by the void. In addition, samples with a longer starting length also show slightly lower moisture contents throughout the final sample length. The Ca-rich clay sample (FPR-BE-6) shows very large moisture content values at the top of the void, coincident with the layer of "gel" that was observed at the top of the sample when the test was dismantled, Figure 4-22B.
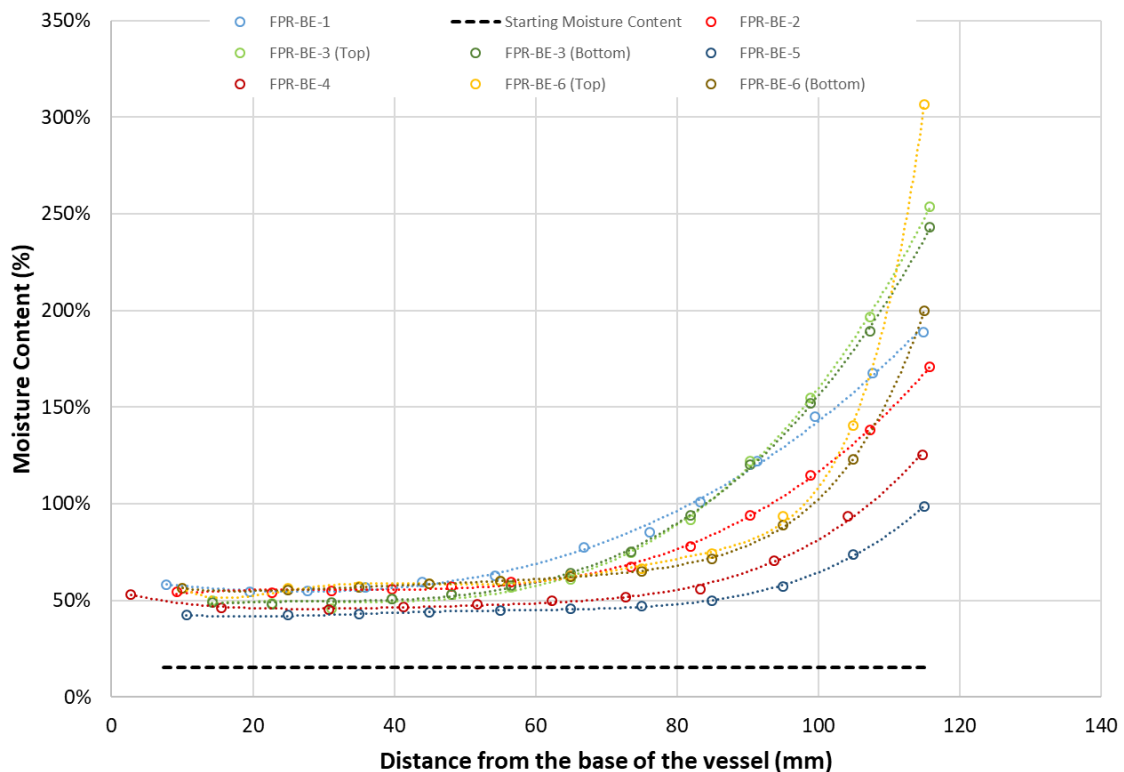
Figure 4-14: Cross-plot of moisture content against distance from the base of the vessel for the six completed tests (FPR-BE-1 to -6)

4.1.3   Discussion

A compilation of the flow rate data from the first three tests is presented in Figure 4-15. Flow into and out of the vessel during test horizontal test FPR-BE-3 is systematically smaller than the

equivalent vertically orientated sample (FPR-BE-1). However, while the cause for this difference remains unclear, the variance in flux is also evident in the moisture content data. Here, data from test FPR-BE-3 exhibits lower moisture contents in the section of the vessel occupied by the original sample, compared to those of the other ambient temperature test FPR-BE-1. Intuitively, clay with a lower moisture content should exhibit a larger swelling pressure (for a saturated sample) which may account for the higher residual stresses noted at the end of test FPR-BE-3. While this slight difference in moisture content may also explain why flows into the sample and out of the vessel were smaller in FPR-BE-3 than FPR-BE-1, the cause for this response remains unclear. In contrast, moisture contents derived from clay material that swelled into the void space are substantially higher in the horizontal test (FPR-BE-3) than those in vertical test (FPR-BE-1). While there is clear evidence of gravity segregation, the cause for the increase in moisture content in the horizontal FPR-BE-3 test is unclear; the moisture content differences are sufficiently large to exclude experimental error.

At an elevated temperature of 90 °C (test FPR-BE-2), Figure 4-15 clearly shows flux into the sample occurred at a much faster rate than in ambient temperature tests. Flows also asymptoted towards the x ordinate much sooner, taking around 40% of the time required in the ambient temperature tests. This implies that heating to 90 °C reduced the test duration by around 60%. This significant change in behaviour can be explained by the reduction in viscosity of the test permeant (in this case distilled water) which declines from 1 x10^{-3} Pa.s at 20 °C to 3.16 x10^{-4} Pa.s at 90 °C for a pressure of 4.5 MPa. This equates to a 68% reduction in viscosity, which, possibly by coincidence, is very close to the accelerated hydration time (i.e. 60% faster than ambient times) as illustrated in Figure 4-15.
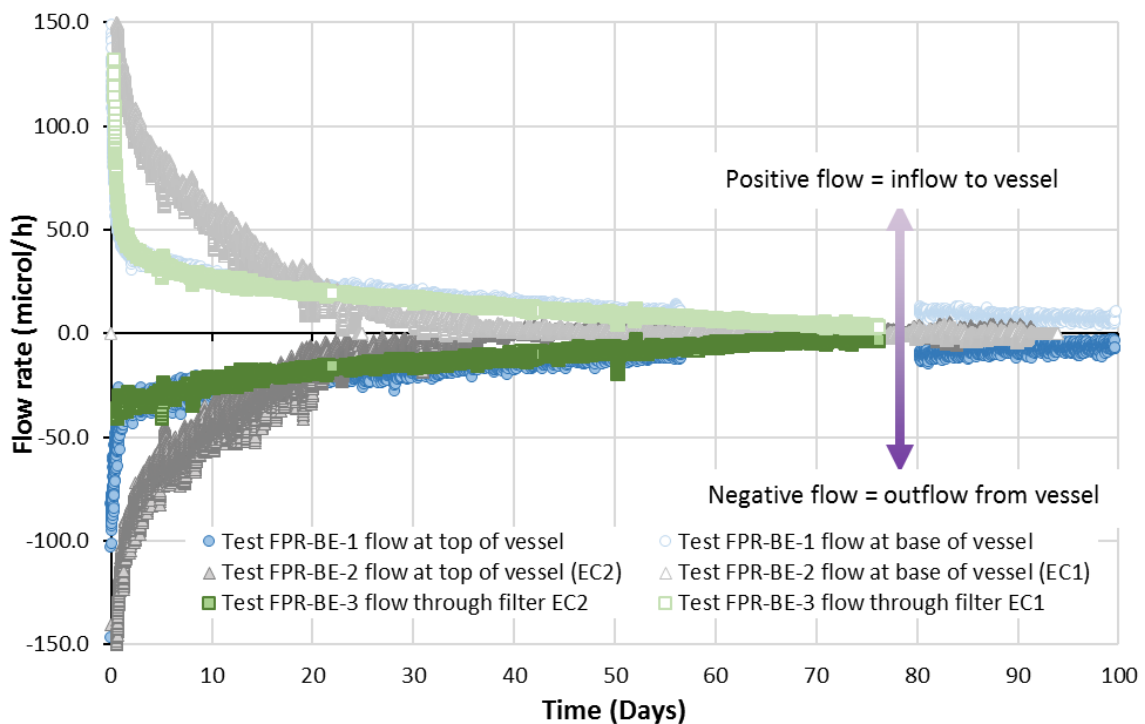
Figure 4-15: Compilation of flow data from test FPR-BE-1, -2 and -3 with samples orientated vertically, vertically and horizontally respectively

A compilation of the swelling pressure data is presented in Figure 4-16. While pressure data generated by Apparatuses 2 and 3 are noisier than for Apparatus 1, similar trends in behaviour are observed between the two ambient tests FPR-BE-1 and -3. Axial pressure values next to the core and above the engineering void are also comparable. Radial stress values from the horizontal test (FPR-BE-3) are significantly higher than those of the vertical test (FPR-

BE-1), though the cause for this result is not clear. However, the development of swelling pressure in the elevated temperature test (FPR-BE-2) is clearly different to that obtained under ambient temperature conditions. While peak values of axial and radial pressure are suppressed during thermal loading, asymptotic values are considerably higher than those observed under ambient conditions. Why this occurs is not understood at the present time. While stress development under thermal loading is significantly faster than in the equivalent ambient test, the stress data appears to show a sizeable and persistent differential stress. Looking at the data there is significant uncertainty as to how long this would last. In addition, swelling occurring on the unsupported face of the sample (into the void) would not be subject to the same frictional constraints around the periphery of the sample as those potentially imposed by the test vessel adjacent to the original sample. For that reason the role of friction (at least axially) remains uncertain.
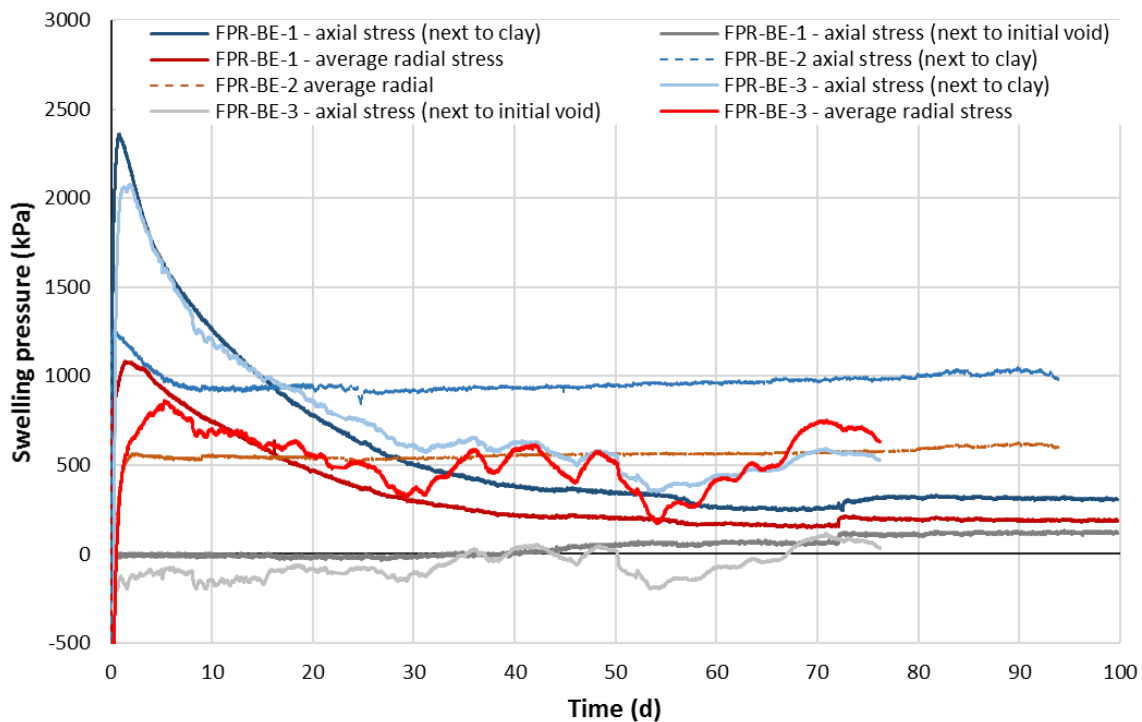
Figure 4-16: Evolution of swelling pressure above, below and radially in samples FPR-BE-1, -2 and -3

Figures 4-17 to 4-22 show the slices of the core taken incrementally along the axis of the sample in order to define the moisture content data. The numbers next to each image relate to the position of the slice along the axis of the core. The degree of shrinkage and cracking is primarily related to the moisture content, with increased cracking associated with higher moisture content values. In Figure 4-17 the faint outline of the arrow marking the orientation of the sample and the word 'top' can be seen, both having been elongated as the sample swelled. This suggests swelling was relatively uniform during this test. From image 7 onwards, the amount of cracking substantially declines, which is mirrored by only minor changes in moisture content. This pattern of behaviour is also seen in the dried post-test slices from the other tests (Figures 4-18 to 4-22). The increase in cracking noted in image 13 of each sample reflects the small increase in moisture content (compared to neighbouring material) observed at that end of the sample. While actual moisture contents of each sample have substantially increased (by a factor >3), the data presented in Figure 4-14 shows very little variation in values along the first 40 mm of each core. This suggests a continuous and roughly equal mode of swelling. The fact that moisture content does not increase substantially at the base of the sample, also indicates sidewall friction plays an important role in the redistribution of water within the clay. This reflects the volumetric boundary constraint imposed by the

apparatus and is borne out in the data where radial stress (around the base of each sample) is consistently higher than the neighbouring value of axial stress.

Figure 4-17: Slices 1-13 of the post-test FPR-BE-1 sample. The inset photograph (A) shows the complete post-test sample after extrusion from the vessel and before the sample was sliced. The slices were weighed and dried to determine the moisture content along the sample length
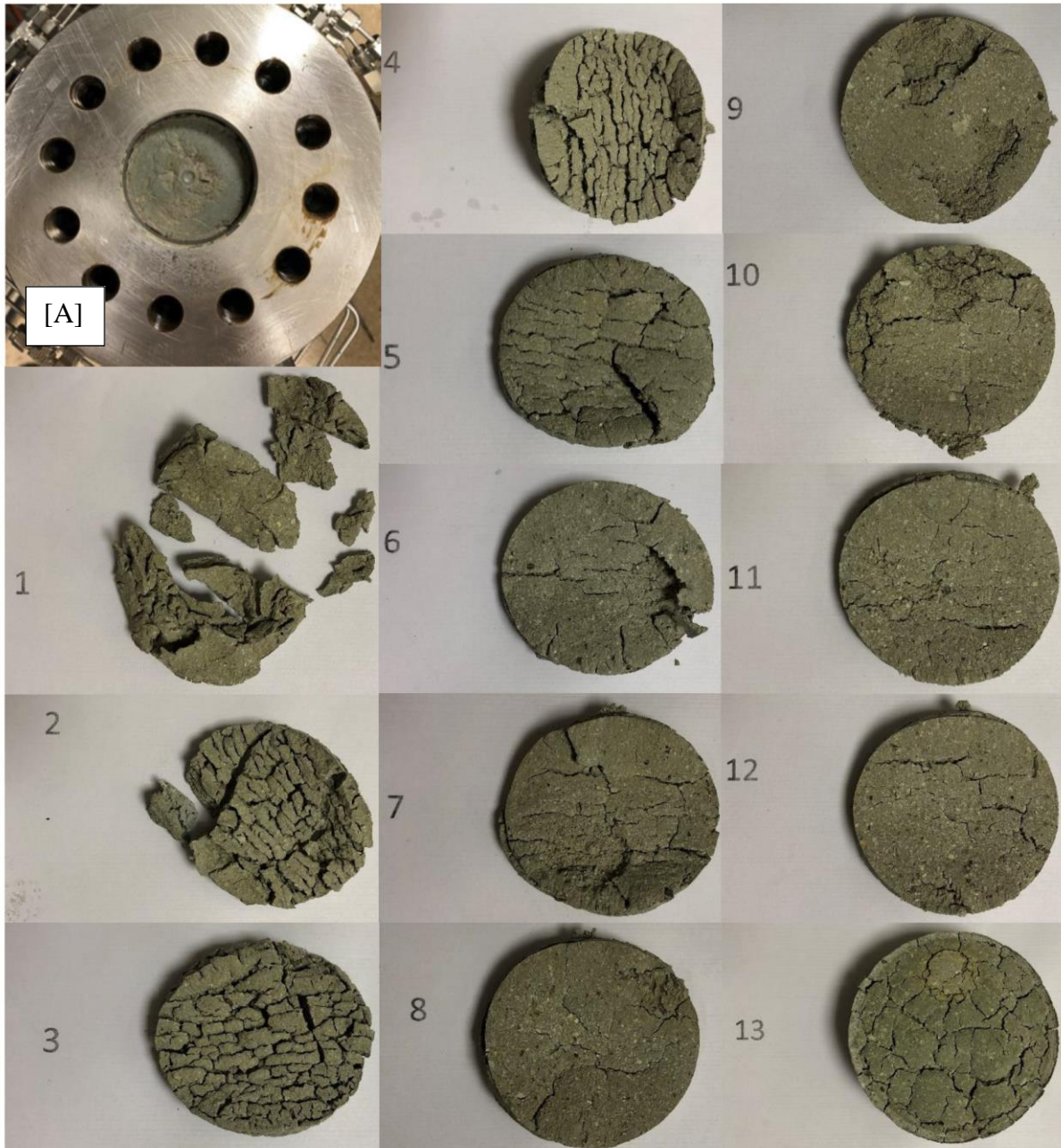
Figure 4-18: Slices 1-13 of the post-test FPR-BE-2 sample. The inset photograph (A) shows the top of the sample in the vessel as the end closure of the apparatus was removed. The slices were weighed and dried to determine the moisture content along the sample length
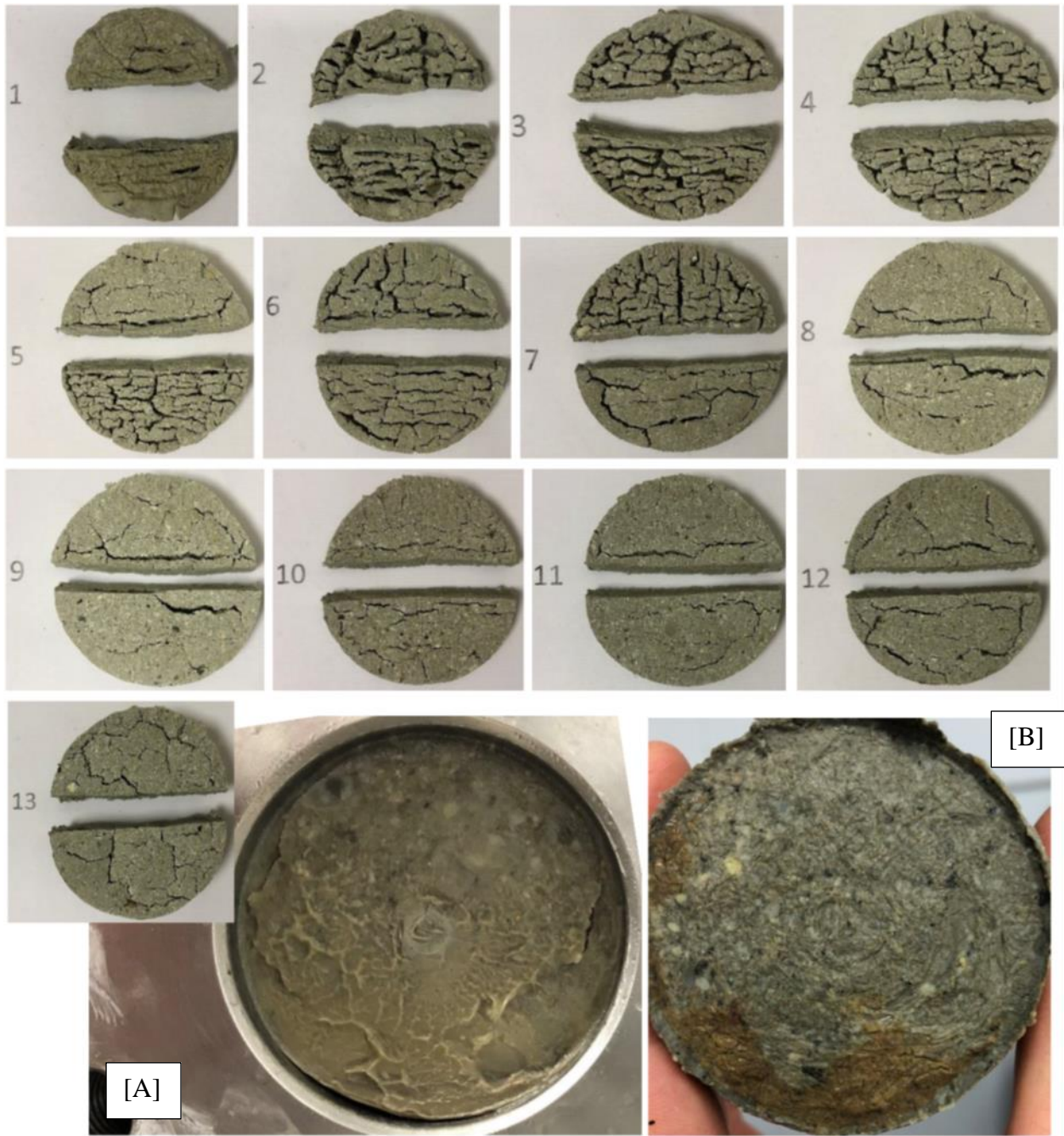
Figure 4-19: Slices 1-13 of the post-test FPR-BE-3 sample. Each slice has been cut in half and weighed before drying to determine the moisture content both along the sample length and vertically at each axial position. The inset photographs show (A) the Pump B end of the sample within the apparatus as the apparatus' end closure was removed; and (B) the Pump A end of the sample after removal from the vessel
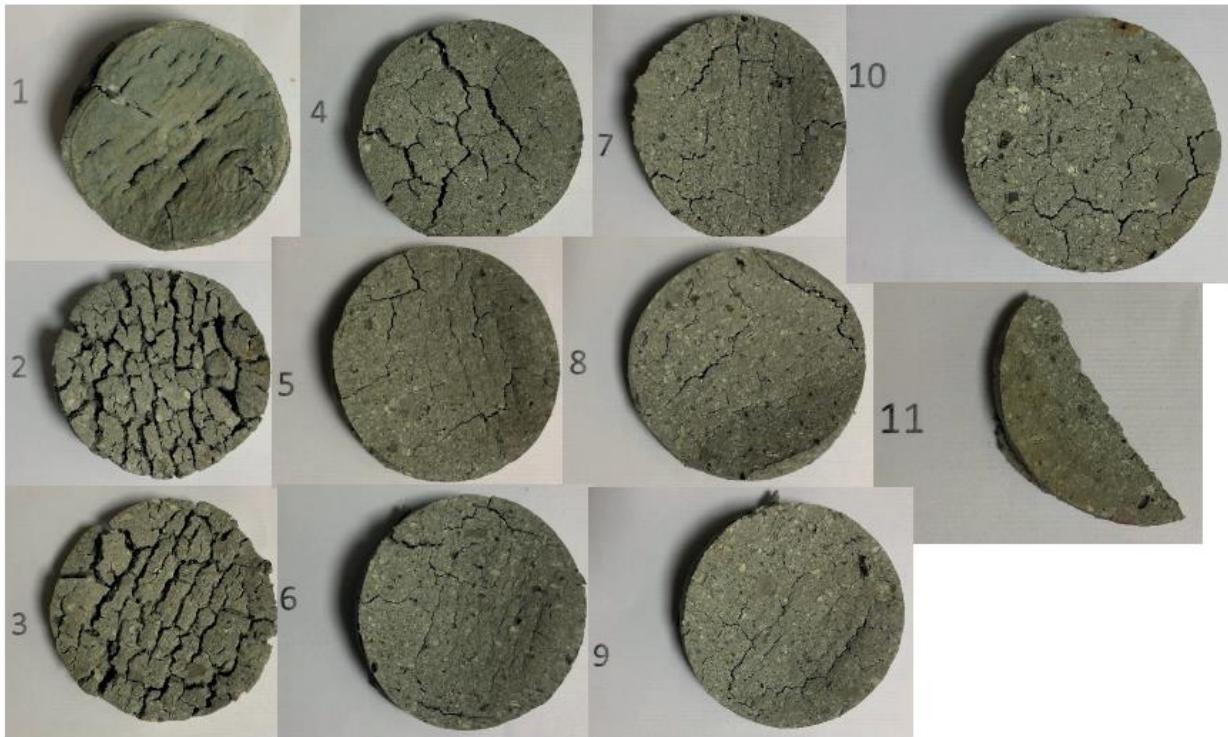
Figure 4-20: Slices 1-11 of the post-test FPR-BE-4 sample
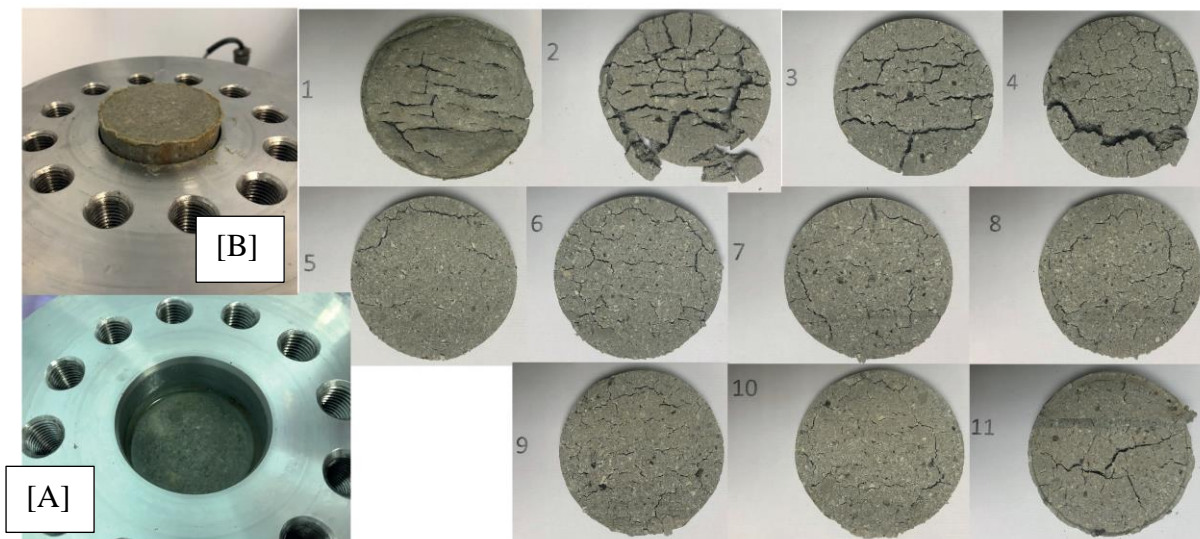
Figure 4-21: Slices 1-11 of the post-test FPR-BE-5 sample. The inset photographs show [A] the surface of the clay at the Pump B end of the sample as the end closure was removed after the test was terminated, and [B] the sample being extruded from the vessel before the first slice is removed
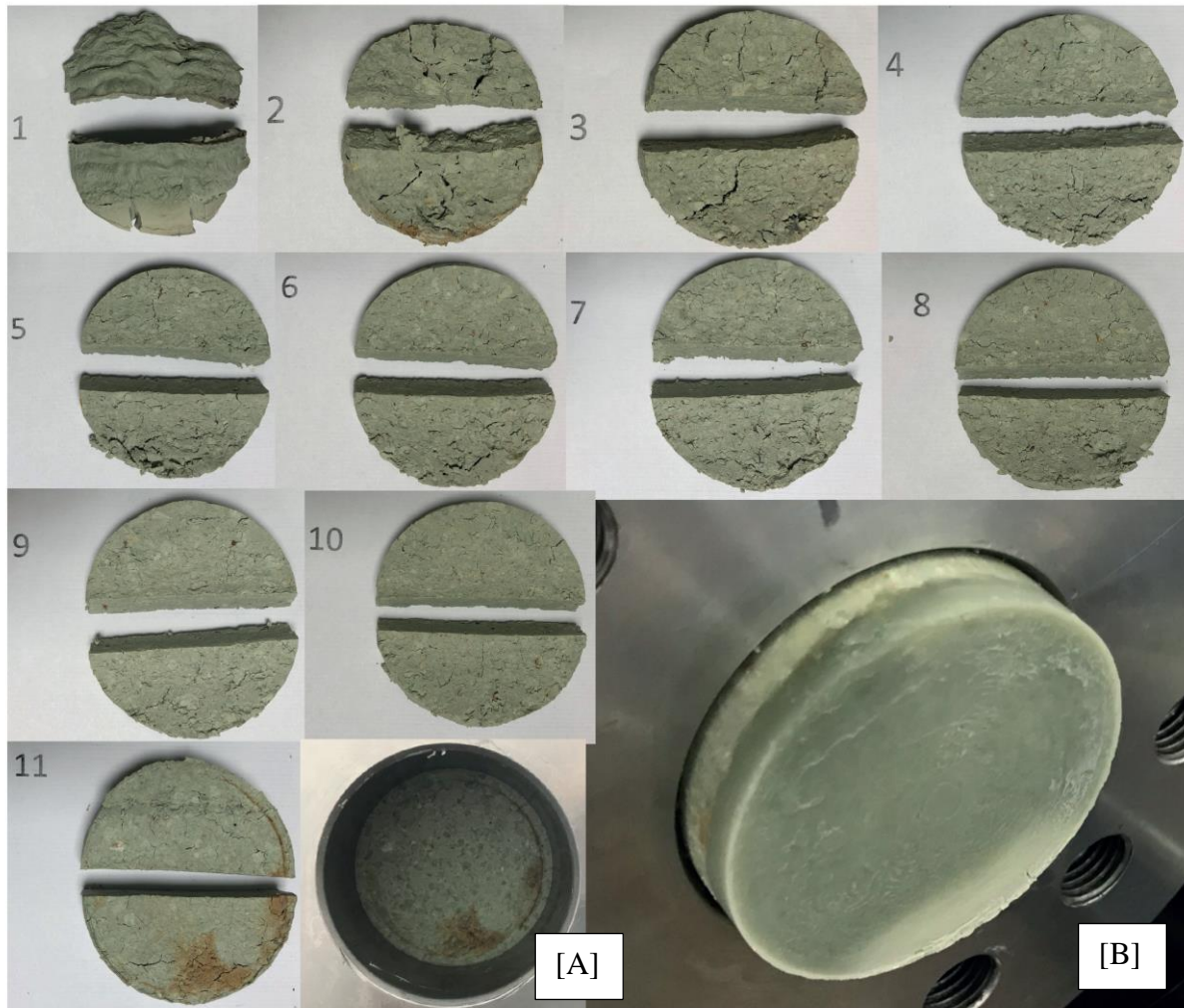
Figure 4-22: Slices 1-11 of the post-test FPR-BE-6 sample. In the same was as for the FPR-BE-3 sample, each slice has been cut in half and weighed before drying to determine the moisture content both along the sample length and vertically at each axial position. The inset photographs show [A] the surface of the clay at the Pump A end of the sample as the end closure was removed after the test was terminated, and [B] the sample being extruded from the vessel before the first slice is removed. The Ca-rich clay sample is a greener colour than the Mx-80. A thin layer (~1cm) of calcium-gel can be seen at the top/unconfined edge of the sample (the opposite end from the end shown in photograph [A])

4.1.4 Summary

Six homogenisation tests have been successfully performed on pre-compacted samples of bentonite, which have been allowed to swell into a fixed volume void. Two tests are still on-going. Four completed tests were performed vertically with the sample placed at the base of the vessel, two under ambient temperature conditions (FPR-BE-1 and -5) and the other two at 90 °C (FPR-BE-2 and -4). The last two completed tests were performed horizontally under ambient temperature conditions. The data show that the development of swelling pressure is spatially complex and time-consuming and that after 100 days of testing, significant variance still exists. However, bentonite under zero hydraulic gradient is able to swell and ultimately fill the start void, creating a small but measurable swelling pressure throughout the internal volume of the test apparatus. Close inspection of stress data during hydration shows little evidence of classic stick-slip behaviour. However, sidewall friction coupled to the volumetric constraint imposed by the apparatus, clearly played an important role in the redistribution of water within the original sample. This was evidenced by the near uniform increase in moisture

71

content throughout the original sample volume. Further analysis of flows below and above the clay also indicated differential swelling, probably linked to friction between the sample and vessel walls. Minor differences in moisture contents and density profiles were also observed between the ambient tests. Evidence of gravity segregation was present in the tests performed horizontally.

Tests performed under ambient temperature conditions showed similar trends in the development of axial swelling pressure, though differences in radial stress values were observed. However, the development of swelling pressure under elevated temperature conditions was markedly different. Testing at elevated temperatures showed stresses equilibrated faster than those under ambient conditions. This was accompanied by slightly increased homogenisation as evidenced through post-test moisture content measurements. This response was accompanied by higher inflow rates during testing caused by the reduction in fluid viscosity. Peak values of axial and radial pressure were suppressed during thermal loading though asymptotic values were considerably higher than those observed under ambient conditions. Larger differential stresses were also noted when the clay was under thermal load, though significant uncertainty remains in the longevity of these features.

4.2 Swelling into a void under suction control or flow control (CIEMAT)

4.2.1 Objectives and methods

The objective of this kind of tests is to follow the density and water content changes in a block sample saturated under limited axial swelling conditions and at the same time observe the closing of the initial gap. Febex bentonite samples were compacted inside stainless steel rings and a gap was left on top. In all cases the granulated bentonite was initially compacted with its hygroscopic water content (~14%) at a dry density of 1.7 g/cm^3. These samples were hydrated with water either in vapour (GAP-vapour) or liquid phase (GAP-liquid) and were dismantled after different periods of time. The final water content and dry density of the bentonite at different levels of the sample were measured, as well as the pore size distribution.

In the GAP-vapour tests the samples were compacted in a cell with perforated lids, and saturated from the top surface using the vapour transfer technique (Figure 4-23), which consists in subjecting the sample to a certain relative humidity in a close container (vacuum desiccator). The diameter of the samples was 3.8 cm and the initial height was 2.5 cm. The bottom part of the cell was sealed, and on the top surface of the sample a porous stone was placed. The evolution over time of the gap closing and the changes in bentonite overall water content and dry density were followed. A total of 22 cells have been tested so far and dismantled at different periods of time between 15 days and 10 months. In all of them the initial gap thickness was of 0.5 cm. The samples were subjected to relative humidities corresponding to total suctions of 6 and 0.5 MPa keeping a constant temperature of 20°C.

3.8 cm

Clay | Porous stone | Steel | Copper
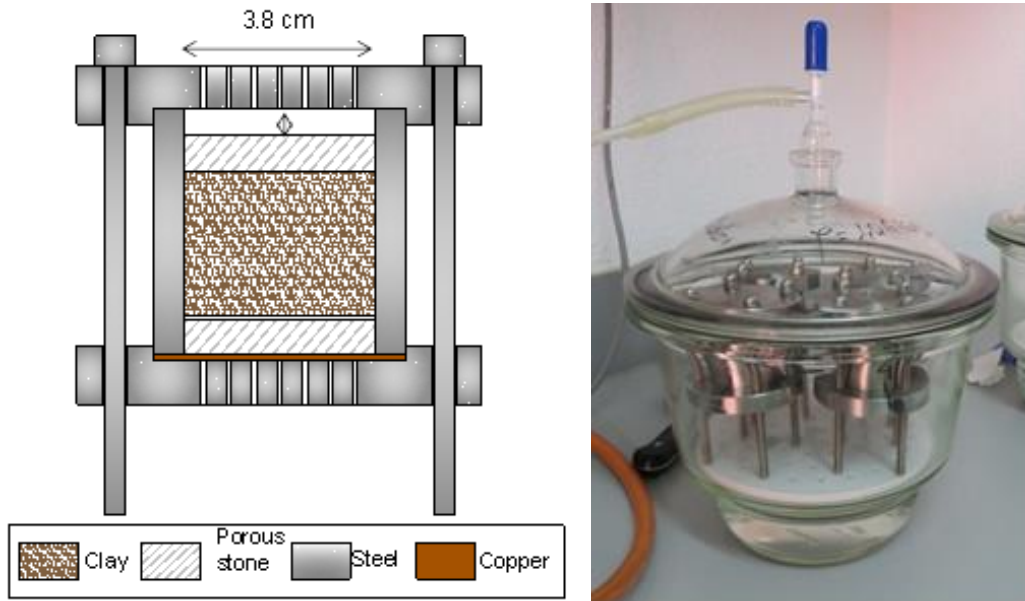
Figure 4-23. Schematic representation of the GAP-vapour test cells and desiccator with cells inside

The GAP-liquid tests were similar to those mentioned in the previous paragraph, but the bentonite was saturated with water in the liquid phase under a very low pressure from the bottom surface, opposite to the gap (Figure 4-24). The diameter of the sample was 5.0 cm and its height was 2.6 cm. The height of the initial gap was 0.8 cm. The sample was sandwiched between porous stones and the upper part of the stainless steel cell, above the gap, was open to the atmosphere. Deionised water was injected through the bottom from a pressure/volume controller at a rate of 0.07 cm^3/h. The tests were performed at laboratory temperature (22.5±1.3°C).

Data acquisition

Gap

Bentonite

Presure/volume controller

Stainless steel cell
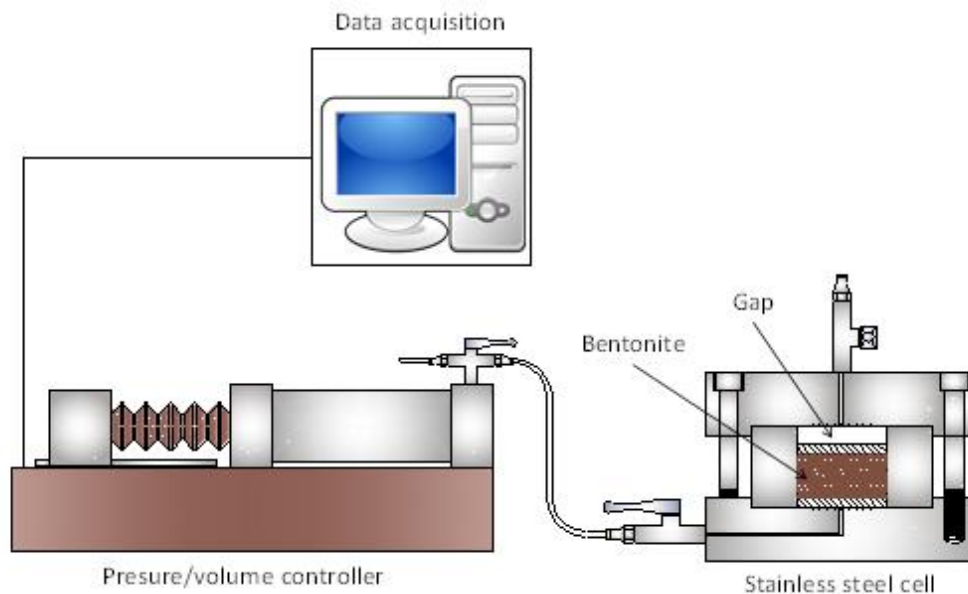
Figure4-24. Schematic representation of the assembly for GAP-liquid tests

At the end of the two kinds of tests the samples were cut in vertical subsections and in each of them water content, dry density and pore size distribution were determined.

The gravimetric water content (w) is defined as the ratio between the mass of water and the mass of dry solid expressed as a percentage. The mass of water was determined as the difference between the mass of the sample and its mass after oven drying at 110°C for 48 hours. Dry density (ρ_d) is defined as the ratio between the mass of the dry sample and the volume occupied by it prior to drying. The volume of the specimens was determined by immersing them in a recipient containing mercury and by weighing the mercury displaced, considering a density of mercury of 13.6 g/cm^3.

The pore size distribution of each subsample was determined by mercury intrusion porosimetry (MIP). The samples were put in the ice condenser of a Telstar LioQuest equipment at -30°C for 3 hours. Subsequently, they were lyophilised for 22 hours at a temperature of -50°C under a vacuum of 0.2 mbar, so that to eliminate the water in the pores by sublimation. Thereafter, they were heated at 25-30°C for 3 hours. The samples were later kept in a desiccator until the MIP analysis. The porosimeter used was a Micromeritics AutoPore Series IV 9500, which allowed the exploration of pore diameters between 0.006 and 600 µm. Prior to mercury injection the sample was outgassed by applying a vacuum of 50 µm-Hg. Afterwards the mercury injection pressure was increased from 2.7 kPa to 220 MPa in 109 steps. To determine the extrusion branch of the curve, the pressure was released in 56 steps down to a pressure of 68.6 kPa. A contact angle of mercury of 139° both on advancing and of receding on the clay surface was considered.

4.2.2 Results

The GAP-vapour cells were checked every week. For that, the lids were unscrewed and the cell with the sample inside was weighed and the height of the gap measured (Figure 4-25). This way, the evolution over time of the overall bentonite water content and dry density was followed. Since the bentonite was compacted with hygroscopic water content, the initial suction of the samples was very high, about 100 MPa. For this reason all the samples took water under the two suctions applied, swelled and tended to close the gap. Figure 4-26 and Figure 4-27 show the evolution of water content and dry density in the tests performed under suctions 6 and 0.5 MPa. All the tests were performed in duplicate, and in most cases the results of the two samples were coherent.

Figure 4-25. Periodic check of weight and dimensions of samples of GAP-vapour tests
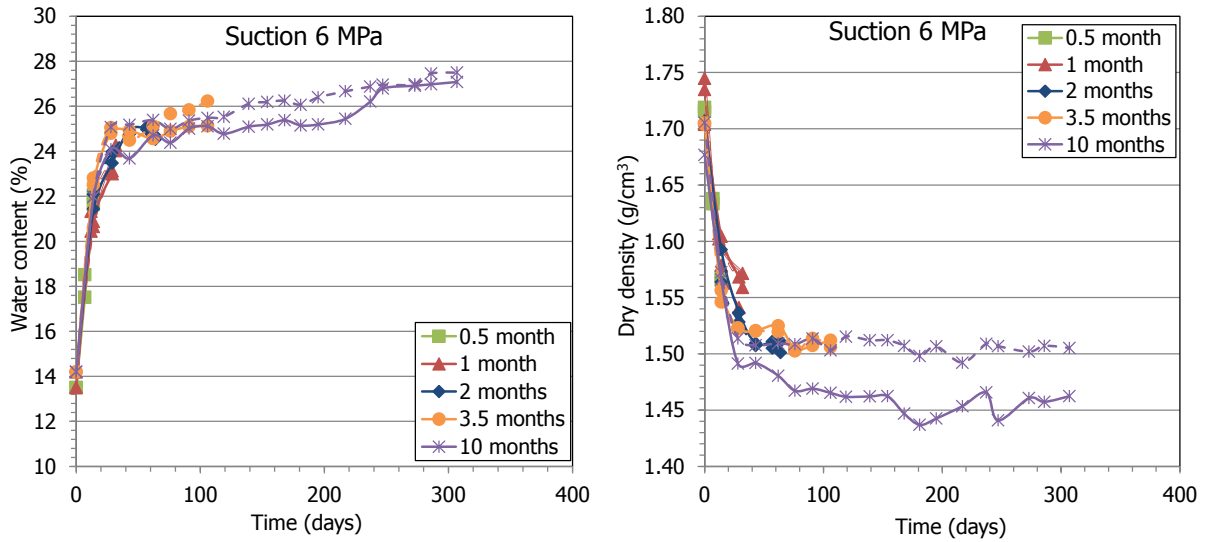
Figure 4-26. Evolution of water content and dry density in GAP-vapour tests under suction 6 MPa
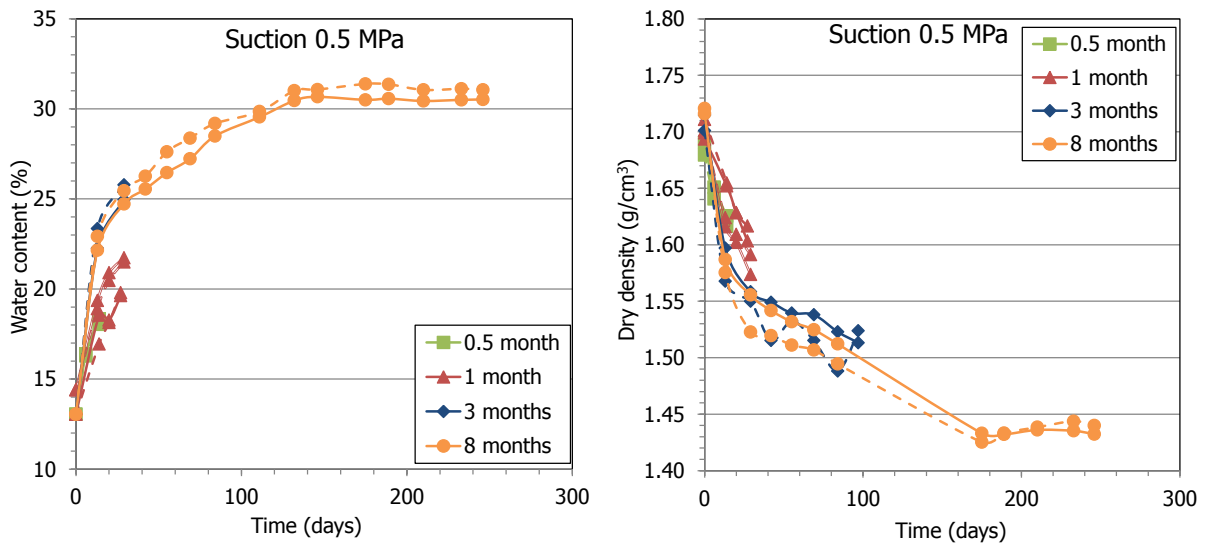
Figure 4-27. Evolution of water content and dry density in GAP-vapour tests under suction 0.5 MPa

The final values of dry density and water content for each test performed under the two different suctions are shown in Figure 4-28. In the first stages, for times shorter than 40 days, the samples under 6 MPa took more water and swelled more. For longer equilibration times the trend inverted and consequently the final water contents of samples under 0.5 MPa were higher and their dry densities lower. After approximately 300 days the equilibrium water content for a suction of 6 MPa was reached (~27%), whereas for suction 0.5 MPa about 250 days were needed to reach the equilibrium water content (~31%). These equilibrium values agree well with the water retention curves of the FEBEX bentonite at different dry densities shown in Figure 4-29.
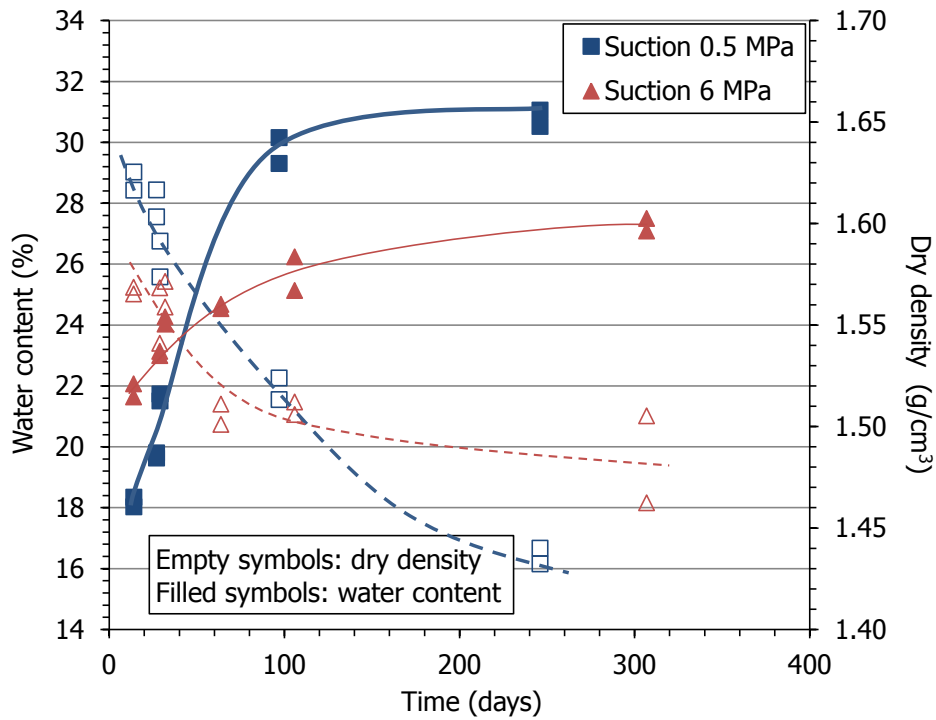
Figure 4-28. Final results of dry density and water content in GAP-vapour test
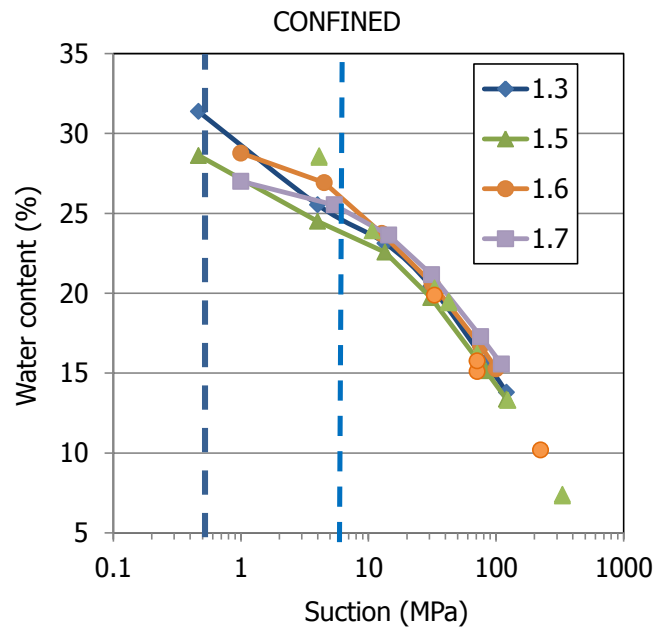
Figure 4-29. Water retention curves of FEBEX bentonite compacted to different dry densities (indicated in g/cm3). Results from Villar 2007, Villar et al. 2012 and unpublished. The dotted vertical lines indicate the suction values used in the GAP-vapour tests

After different equilibration times the cells were dismantled, the bentonite weighed and measured and cut into subsamples for the post mortem determinations (Figure 4-30). The results obtained for the different samples in terms of water content and dry density are shown in Figure 4-31 and Figure 4-32. In the case of the samples tested under suction 6 MPa, the shorter tests showed a water content gradient from top to bottom. This gradient attenuated over time and was coupled to an inverse dry density gradient: towards the top of the sample,

76

where the gap was, the water content was higher and the dry density lower. In fact, the upper surface of the sample crumbled easily, since it swelled into a void (see Figure 4-30). For this reason it was difficult in some cases to cut subsamples and the determination of their dry density. The water content gradients in the samples tested under suction 0.5 MPa were in all cases less steep and kept more or less constant as the overall water content increased. As well, the dry density gradients were softer for the samples tested under the lower suction. This could be explained by the slowness of the saturation process in the last case (Figure 4-28).

Figure 4-30. Appearance of samples after extraction of the cells and subsampling for post mortem analyses
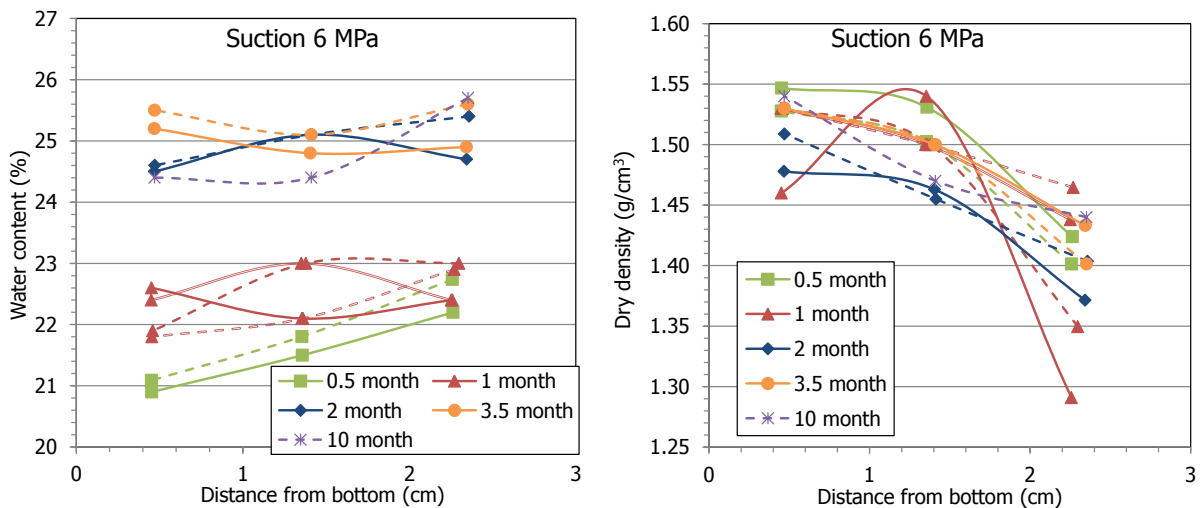
Figure 4-31. Final water content and dry density of subsamples of the tests performed under suction 6 MPa
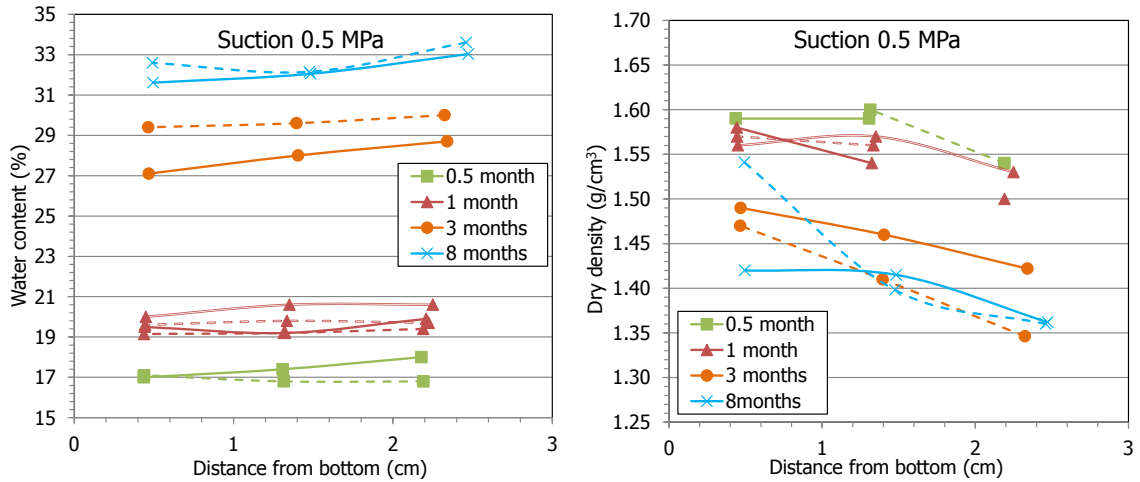
Figure 4-32. Final water content and dry density of subsamples of the tests performed under suction 0.5 MPa

From each cell three other subsamples taken at different distances from the gap were used to determine the pore size distribution by MIP. Figure 4-33 and Figure 4-34 show the incremental curves of mercury intrusion as a function of the mean pore diameter of the diameter size intervals corresponding to each pressure increase step (the determination was performed in all the subsamples, but only those corresponding to the shorter and longer tests performed under each suction are shown). The curve corresponding to a FEBEX sample compacted with approximately the same dry density and water content as the initial conditions used in the cells (1.69 g/cm^3, 13.5%) is also included (labelled "Initial"). For all the samples there were two pore families corresponding approximately to pores larger and smaller than 200 nm. In several THM models, this pore size represents the limit separating inter-aggregate from intra-aggregate pores, the latter not affected by density changes (e.g. Sánchez et al. 2005). The Figures show that the volume of pores larger than 200 nm increased during testing, particularly as the test was longer. The average size of the macropores also tended to increase.
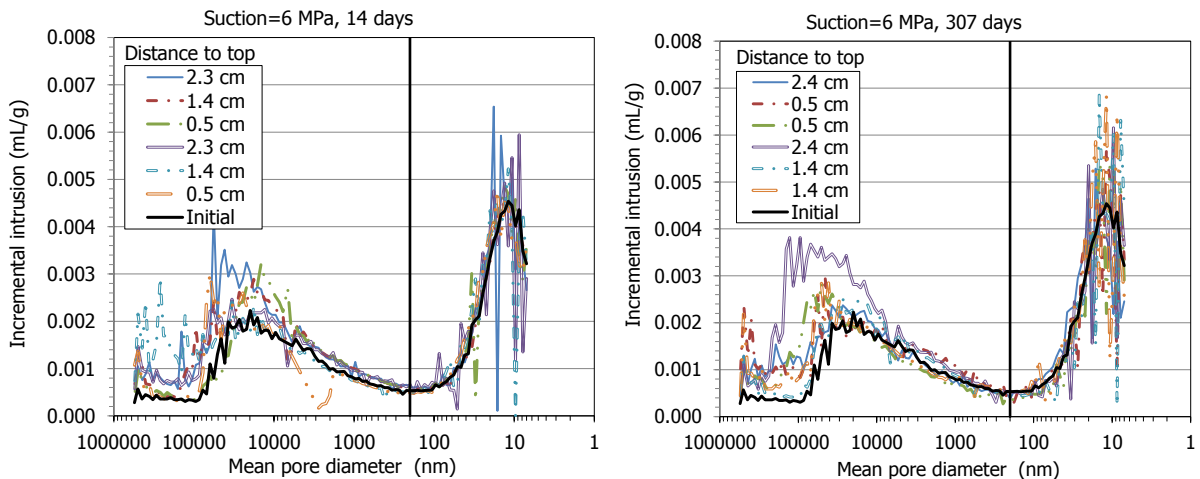
Figure 4-33. Pore size distribution of subsamples tested in GAP-vapour cells under suction 6 MPa for two different times and for the initial block expressed as incremental mercury intrusion
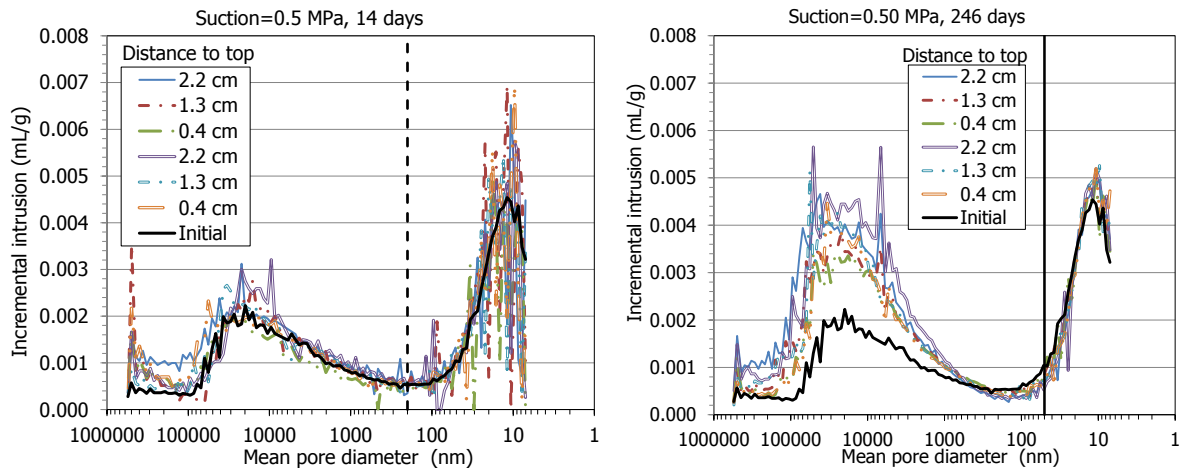
Figure 4-34. Pore size distribution of subsamples tested in GAP-vapour cells under suction 0.5 MPa for two different times and for the initial block expressed as incremental mercury intrusion

Because of the technical characteristics of the porosimeter used, mercury did not intrude pores of a size of less than 6 nm, and in clay materials the percentage of pores smaller than this size can be relevant. Considering that most of the non-intruded porosity corresponds to the pores of a size smaller than this limit, an estimation of the percentage of pores actually intruded can be made by comparing the actual void ratio of the samples (computed from their dry density and density of solid particles, 2.7 g/cm³) and the apparent void ratio calculated from mercury intrusion. The percentage of pores intruded by mercury in these subsamples was between 42% and 74%. Taking this into account, the void ratio corresponding to pores larger and smaller than 200 nm was recalculated and is plotted in Figure 4-35 and Figure 4-36 for subsamples of the specimens tested under suctions 6 and 0.5 MPa, respectively. In all cases the largest proportion of void ratio corresponded to the pores of diameter smaller than 200 nm, the percentage of which increased during testing with respect to the reference sample. Also, the percentage of void ratio corresponding to pores larger than 200 nm increased with respect to the reference block, since the total void ratio increased because of the bentonite swelling into the gap. In fact, the highest increase in void ratio was experienced by the samples closest to the gap, which agrees with their lower dry density (Figure 4-31and Figure 4-32). The overall void ratio increase took place very quickly in the samples tested under 6 MPa (it was already clear after 15 days) but took longer in the samples tested under suction 0.5 MPa. This agrees with the different hydration kinetics of the two set of tests commented above and would indicate that hydration under free swelling conditions brought about an increase in the volume of all pore sizes. However, there were no clear trends in the ratio between the void ratio corresponding to pores smaller (e_m) and larger (e_M) than 200 nm, which is plotted on the right-hand side of the Figures.
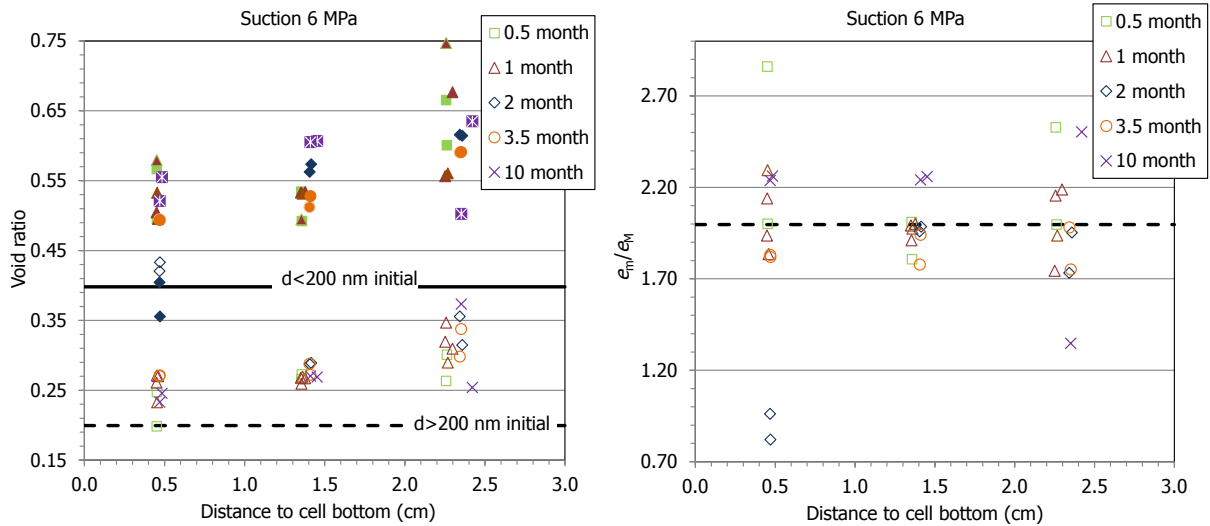
Figure 4-35. Void ratio corresponding to pores smaller (em, filled symbols) and larger than 200 nm (eM, empty symbols) obtained by MIP in samples tested under suction 6 MPa (right) and ratio between both (left). The thick horizontal lines indicate the values for the reference block
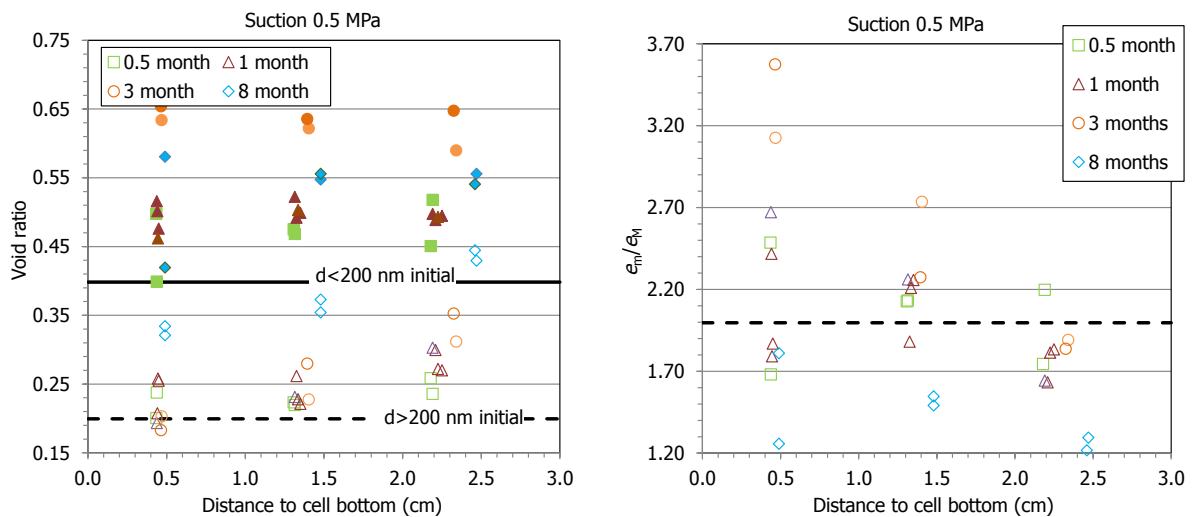
Figure 4-36. Void ratio corresponding to pores smaller (em, filled symbols) and larger than 200 nm (eM, empty symbols) obtained by MIP in samples tested under suction 6 MPa (left) and ratio between both (right). The thick horizontal lines indicate the values for the reference block

For the GAP-liquid tests only the state of the sample at the end of each test is available, because their state was not periodically checked. Five tests of the same initial characteristics were performed and dismantled after different hydration times. The evolution of the gap height (which was initially 0.8 cm) and of the bentonite degree of saturation are shown in Figure 4-37. After about 30 days the gap was completely closed and the samples were fully saturated.

In contrast with the GAP-vapour tests, the gap in the GAS-liquid tests was in the opposite side to the hydration surface. The water content and dry density at different levels of the samples measured at the end of the tests are plotted in Figure 4-38. The water content increased overall with time but was always higher towards the hydration surface. In the same way the dry density decreased as the gap was filled and was always lower towards the hydration surface. Although the gradients attenuated over time, they did not disappear, even when

the sample was completely saturated: the water content near the hydration surface remained higher and the dry density lower.
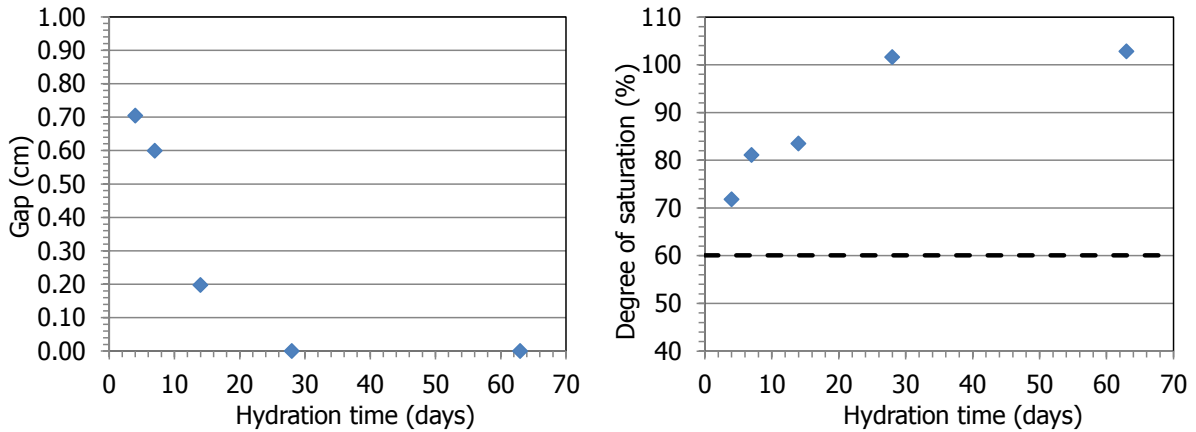
Figure 4-37. Evolution of gap height and of bentonite degree of saturation in GAP-liquid tests
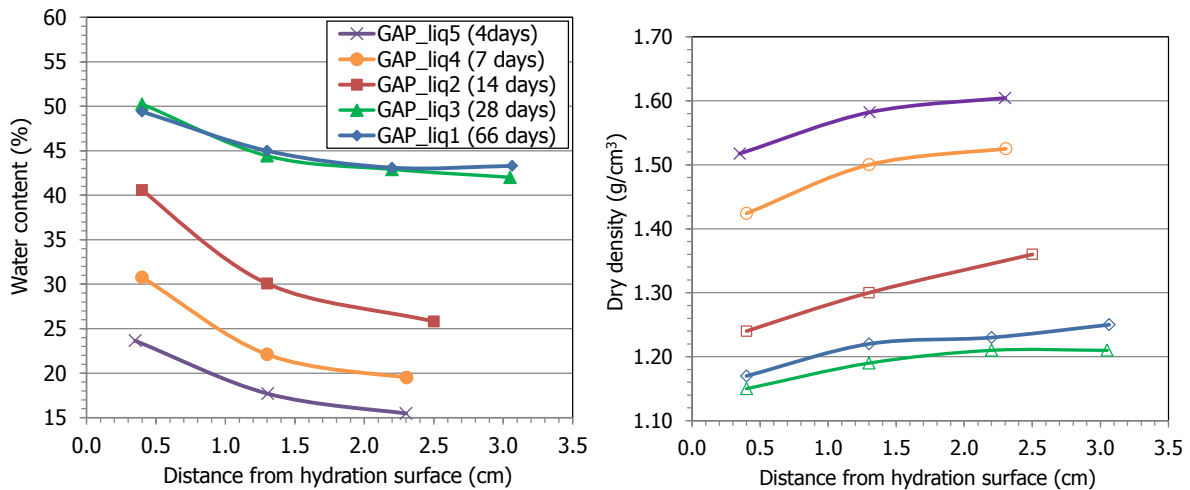
Figure 4-38. Final water content and dry density of GAP-liquid tests at different levels of samples

The same analysis of the final pore size distribution of the subsamples described for the GAP-vapour tests was performed with the subsamples of the GAP-liquid tests. As an example, Figure 4-39 shows the incremental curves of mercury intrusion for the subsamples of the tests lasting 14 and 66 days and for a FEBEX sample compacted with approximately the same dry density and water content as the initial conditions used in the cells (1.69 g/cm^3, 13.5%). In some tests it was not possible to get material from the upper part of the specimens (the one swelling into the void) for the MIP tests because of its inconsistency. Again, two pore families corresponding approximately to pores larger and smaller than 200 nm could be told apart. The volume of pores larger than 200 nm increased during testing, particularly as the test was longer.

The percentage of pores intruded by mercury in these subsamples was between 53 and 85%. Taking this into account, the void ratio corresponding to pores larger and smaller than 200 nm was calculated (Figure 4-40). Although the volume of pores smaller than 200 nm was initially higher, over time the volume of macropores increased more. In fact, the ratio between the void ratio corresponding to pores smaller (e_m) and larger (e_M) than 200 nm significantly decreased during testing for the longer tests.
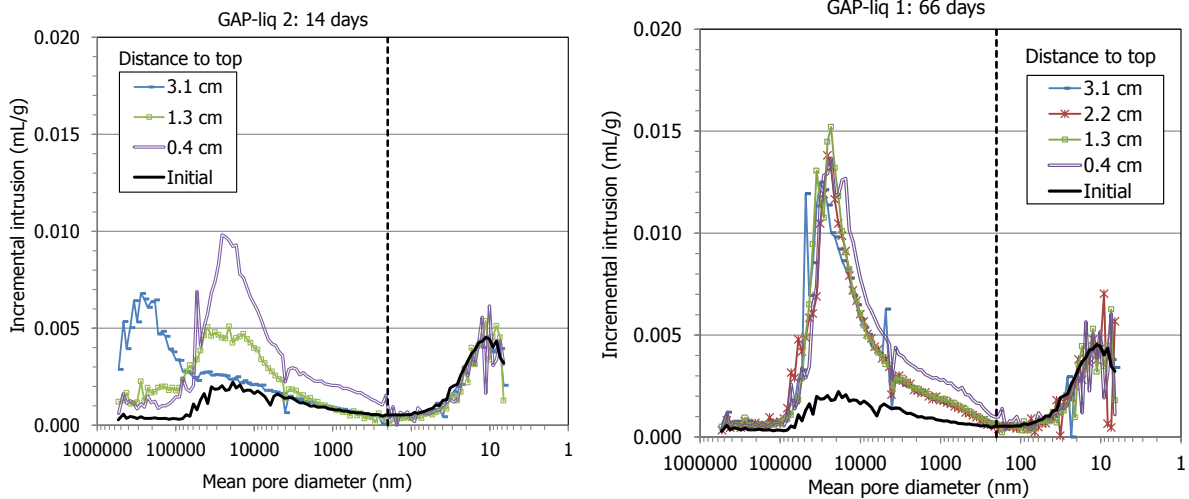
Figure 4-39. Pore size distribution of samples tested in GAP-liquid cells for 14 days (GAP-liq 2) and 66 days (GAP-liq 1) and for the initial block expressed as incremental mercury intrusion
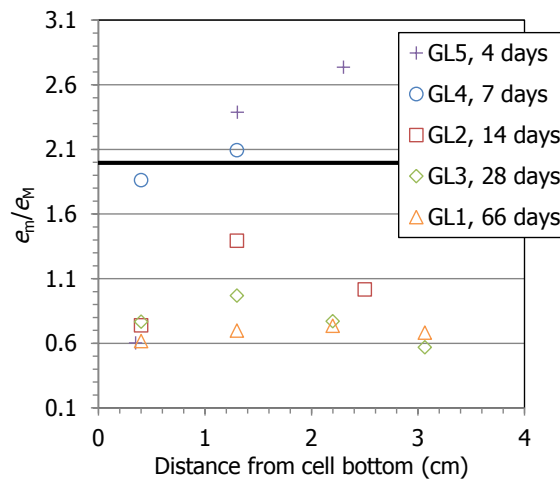
Figure 4-40. Ratio between void ratio corresponding to pores smaller (e_m) and larger (e_M) than 200 nm obtained by MIP in samples tested in GAP-liquid cells for different times. The thick horizontal line indicates the value for the initial block

The evaluation of these results along with those obtained in the GAP-vapour tests indicates that the persistence of water content and dry density gradients was linked to the velocity of saturation: the quicker the hydration took place, the steeper and more persistent the gradients were. Hence the gradients were more remarkable and persistent when hydration took place in the water phase, then under "high" suction and finally under low suction. As it was shown above, the samples under 6 MPa hydrated faster and the strains that occurred under quick hydration were larger and irreversible. Hydration brought about an overall increase in void ratio (because of the swelling into the gap). When hydration was quicker, i.e. when it was accomplished with liquid water, the increase took place particularly in the volume of pores larger than 200 nm.

4.3 X-ray imaging and wetting of semi-free swelling bentonite in a sample chamber (JYU)

An extensive experimental measurement series of semi-free swelling of bentonite using X-ray imaging and numerical image analysis is ongoing. The compressed bentonite samples that initially partially fill the custom build sample chamber are wetted and sample saturation process and semi-free swelling into the chamber void is monitored by using X-ray imaging and axial pressure measurement at both ends of the sample. The specific research plan consists of 30 experiments, which further include samples of varying material and initial dry density and wetting water of differing composition and salinity. The individual experiment spans approximately 16 days and covers 10 X-ray imaging sessions throughout the wetting cycle. Detailed sample information is shown in Table 4-3 and their position in the three times repeated measurement block is in the Table 4-4.

Currently altogether 18 (three statistically separate sets of six) tracer particle doped samples have been X-ray imaged and are being analyzed with different numerical methods to obtain the best suitable results in terms of minimizing X-ray image noise. All said samples are Bara-Kade bentonite but experiments will be broadened to two purified bentonite samples after Bara-Kade tests. At present, research plan is adjusted by adding additional six Bara-Kade experiments. This alteration is due to the modifications on imaging cycle between the first and second sample sets and pressure measurement problems in the first set. Furthermore, additional Bara-Kade test runs ensure that method is fully functioning before experiments continue into less abundant and more expensive purified bentonite samples.

Table 4-3. Detailed sample information for the experiments

Bentonite	Dry density (g/cm³)	Solution composition	Ionic strength (mmol/l)	Test ID
BaraKade	1.4	NaCl + CaCl$_2$	3.5	T1
BaraKade	1.4	NaCl + CaCl$_2$	489	T2
BaraKade	1.4	NaCl + CaCl$_2$	975	T3
BaraKade	1.8	NaCl + CaCl$_2$	3.5	T4
BaraKade	1.8	NaCl + CaCl$_2$	489	T5
BaraKade	1.8	NaCl + CaCl$_2$	975	T6
NaMMT	1.4	NaCl	975	T3.Na
NaMMT	1.8	NaCl	3.5	T4.Na
CaMMT	1.4	CaCl$_2$	975	T3.Ca
CaMMT	1.8	CaCl$_2$	3.5	T4.Ca

Table 4-4. Individual measurement block, which is repeated three times

Test ID	BaraKade	NaMMT	CaMMT
T1	X		
T2	X		
T3	X	X	X
T4	X	X	X
T5	X		
T6	X		

The results thus far show that method gives sufficient data on time development of inhomogeneities throughout the sample although none of the samples will reach fully homogenized state, which is somewhat expected with just 16 days wetting cycle. Numerical image analysis is based on reading pixel specific gray scale values. These values change very little due to the wetting and thus are

prone to noise. This fact introduces noticeable errors to the tracer particle tracking based deformation determination and hence partial densities of both water and bentonite have steep variations between different layers of the sample. Said problem might be unsolvable with current imaging equipment and measurement methods but we can give approximation of the partial densities at the end state with help of estimated independent water and granular bentonite densities and by assuming degree of saturation to be at 100%. This theoretical calculation is demonstrated in Figure 4-41 that also shows partial density and deformation progress between 1st hour and 16th day of the irrigation series. Partial density curves for assumed saturated end state gives us better estimate for the status of homogenization than the perturbed density field that depends on deformation field.

Temporary repository web page for the data bank is now under construction and will open in near future. Collected data will be made available online in original .mat and in more condensed .csv file formats.
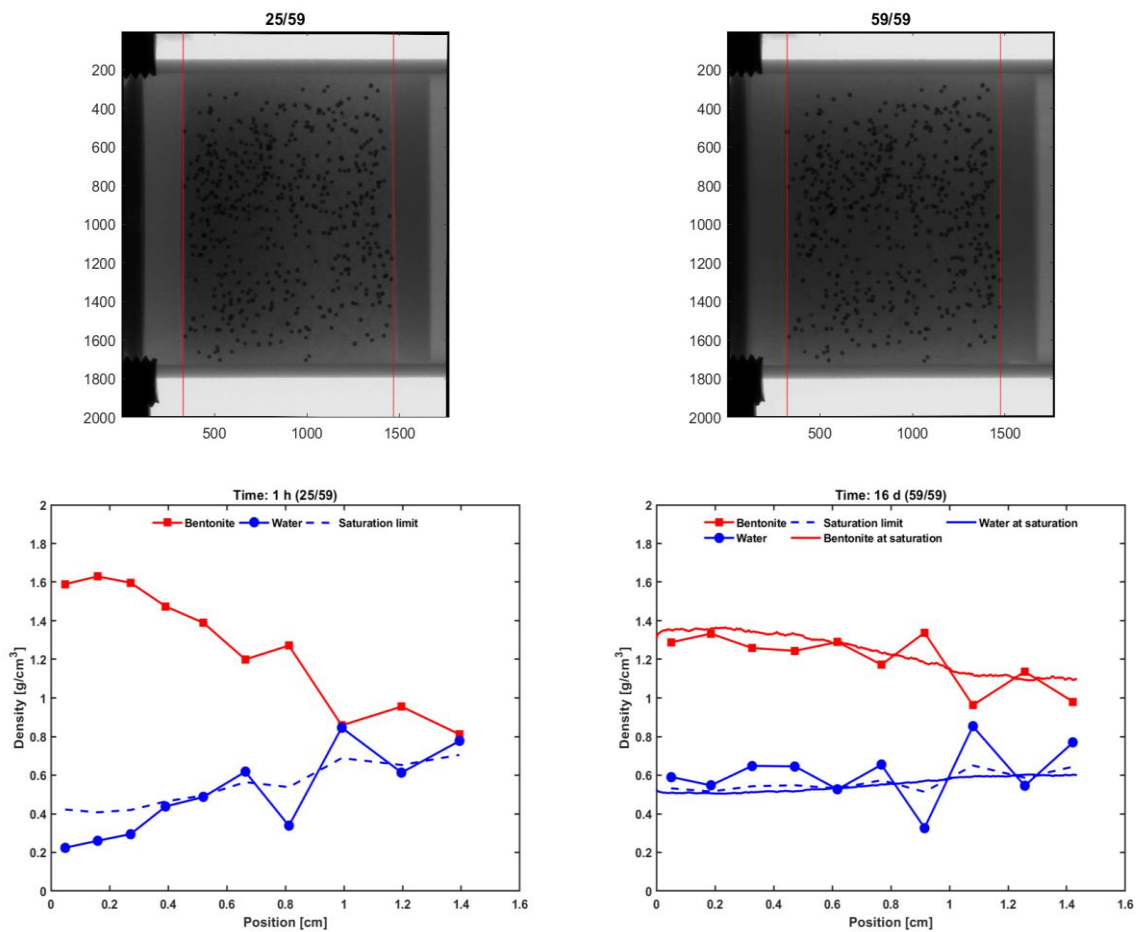
Figure 4-41. Time evolution of sample deformation and bentonite and water partial densities in different layers of the sample (dotted lines) with water saturation limit (dashed line) and additional approximation curves for saturated end state (uniform lines)

4.4   Single pellet investigations (KIT)

84

4.4.1 Introduction

The work performed at KIT/INE focused on the bentonite homogenization and spatially resolved swelling pressure evolution on the single-pellet scale. The experiments devised employ an innovative instrumentation type for small-scale resolved pressure measurement. First tests have been performed. The experiments of the next stage will be used to develop a conceptual model linking the density distribution of a saturated granular buffer to the overall hydraulic properties after re-saturation.

SKB has provided MX-80 pellets for the experiments. An acrylic glass based experimental pressure cell was constructed with four separate cylindrical chambers equipped each with film pressure sensors on the top plane to investigate the temporally and spatially resolved pressure evolution. In each chamber, a single pellet is emplaced with or without additional pellet fragments, taking at least 50% of the cell volume. The remaining volume is filled with two different contacting waters: (i) natural groundwater from the Grimsel test site with low ionic strength of 1.2 mM/L and (ii) synthetic Pearson type A1 water with higher ionic strength of 380 mM/L. The spatial pressure evolution is recorded.

4.4.2 Materials and Methods

Bentonite pellets

The pellets (Figure 4-42) are pillow-shaped, have a dry density of 1620 kg/m3 and a water content of 12%.

Figure 4-42. Pillow-shaped MX-80 bentonite pellets from Äspö hard rock laboratory

Contact water

Two contact waters have been used for single pellet investigations. On the one hand a synthetic clay rock pore water (Pearson type A1) and on the other hand natural groundwater (GGW) from the Grimsel Test Site (GTS) that can be described as glacial melt water. Components and geochemical analysis of the contact waters can be found in Table 4-5.

Table 4-5. Pearson A1 and GGW composition

	Pearson A1	GGW [98]
pH	7.6	9.67
Ionic strength	380 mM/L	1.2 mM/L
$[Mg^{2+}]$	413.19 mg/L	12.6 µg/L
$[Ca^{2+}]$	1034.06 mg/L	5.3 mg/L
$[Na^+]$	5550.01 mg/L	14.7 mg/L
$[K^+]$	62.95 mg/L	-
$[Al^{3+}]$	-	42.9 µg/L
$[Fe^{2+/3+}]$	-	< d. l.
$[Sr^{2+}]$	44.69 mg/L	182 µg/L
$[Cl^-]$	10635.9 mg/L	6.7 mg/L
$[SO_4^{2-}]$	1354.41 mg/L	5.8 mg/L
$[F^-]$	-	6.3 mg/L
$[Si]$	-	5.6 mg/L
$[HCO_3^-]$	25.75 mg/L	3.0 mg/L

GGW is a Na^+/Ca^{2+}-HCO_3^--SO_4^{2-} groundwater type with a pH of 9.6 and an Eh_{SHE} below -200mV. Low salinity of 1.2 mM makes this groundwater comparable to expected glacial melting water. The water was filled in 50 L Teflon coated Al- barrels which were cleaned and filled with Argon gas thoroughly before they were transported to the GTS for sampling. Sampling was performed under low flow rates (< 10mL/min). Once filled, the barrels remained for several days on the opened sampling line and the water was flushed through the barrels in order to exclude any interaction with oxygen or CO_2 that may still have been inside the barrels.

The Pearson A1 water was prepared in the GRS laboratory by successively dissolving the chemicals $NaCl$, KCl, $MgCl_2$, $CaCl_2$, $SrCl_2$, Na_2SO_4, and $NaHCO_3$ in high-purity water.

Test cell parameters

Single pellet investigations have been performed under isochoric conditions in a cylindrical cell geometry. The test cell is 23 mm in diameter and 9 mm in height. Water is added over a 1.5 mm drill hole. The set-up is sealed by a 0.5 mm compressible sealing film. Thereby a slight uncertainty is added to the cell height. The cell was constructed to hold a single pellet with a distinct ratio of free volume comparable to a pellet filling. Four single pellet test cells have been arranged on the acrylic glass measurement set-up to investigate reproducibility or to perform slightly different experiments in parallel (Figure 4-43).

Figure 4-43. Single pellet test cell array for four experiments in parallel

Film pressure sensors

Film pressure sensors (Tekscan Inc., Sensor Model 6900) are applied to investigate temporally and spatially resolved swelling pressure evolution. These sensors consist of four independent sensor areas that each map 121 pressure values on an area of 14 x 14 mm leading to a spatial resolution of 1.6 mm^2 (Figure 4-44). Calibration was performed directly in the test cell by applying water pressure at values between 33 kPa and 7580 kPa. During the experiment, each sensor is placed on top of one bentonite pellet between the sealing film and the lid of the set-up.

Figure 4-44. Test cell array with bentonite pellet samples. The cells are still open and the pressure sensors can be found above the sample cells

4.4.3   Experimental plan

Each experiment included one intact bentonite pellet. Higher bentonite dry density was achieved by addition of loose material. Contact water was added only at the beginning of the experiment and the cell was closed after addition. Thereby the space around the bentonite sample was completely filled with contact water. An overview of the experiments can be found in Table 4-6.

Table 4-6. Experimental overview

Effective bentonite dry density [kg/m^3]	Contact water	Number of experiments
700	GGW	4

700	Pearson type A1	4
900	GGW	4
900	Pearson type A1	4
1000	GGW	4
1000	Pearson type A1	4
1100	GGW	4
1100	Pearson type A1	4
1200	GGW	4
1200	Pearson type A1	4

4.4.4   Results & discussion

First experiments were carried out by using one single pellet that occupied ~50% of the cell volume. The effective bentonite dry density calculated on the cell volume is 700 kg/m³. A basic requirement was that the pellet is in contact with the film sensor already at the beginning of the experiment. A visualization of the initial condition is found in Figure 4-45.
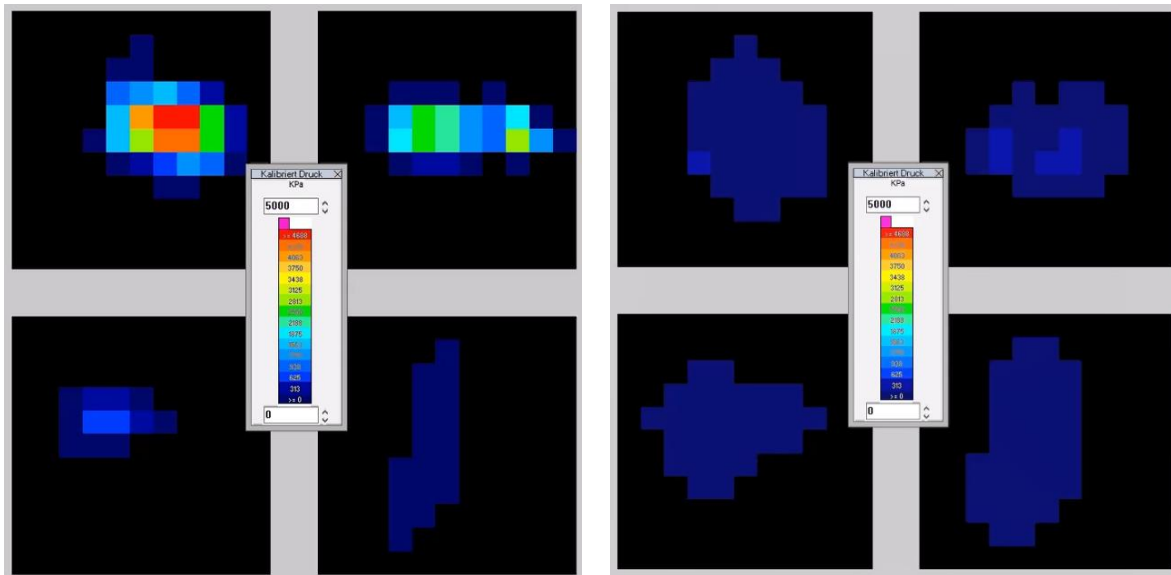
Figure 4-45. Left: Initial condition of the single pellet test at 700 kg/m3 bentonite dry density. Each square represents one test cell. The sample is already in contact with the pressure film before contact water is added. Right: Equilibrium condition at the end of the experiment. Equilibrium pressure is low. Areas in black are below the detection limit of 33 kPa

Maximum pressure evolution is described in Figure 4-46. Four experiments under equal conditions are shown in each figure. The difference at the beginning of the experiment is explained by the basic requirement of contact between pellet and sensor. As the pellet geometry changes slightly from one pellet to another, the initial pressure in the closed cell is also different. As soon as the contact water is added to the sample, maximum pressure rises at first before pressure values decrease due to radial swelling into the free cell volume. It is remarkable that maximum pressure values reach steady state already after ~8 h in case of experiments with Pearson type A1 which is significantly faster in comparison with experiments with GGW as contact water. In the latter case steady state is not reached in the experimental time of ~22 h. In addition, an effect of the more saline Pearson type A1 water can be investigated as maximum pressure values during the experiment are lower in comparison to the experiments using GGW. Pressure values are overall low and there are

areas with pressure values below the detection limit. These areas are located especially at the outer region of the pressure film, far from the area where the pellet was in contact with the film at the beginning of the experiment (Figure 4-45).
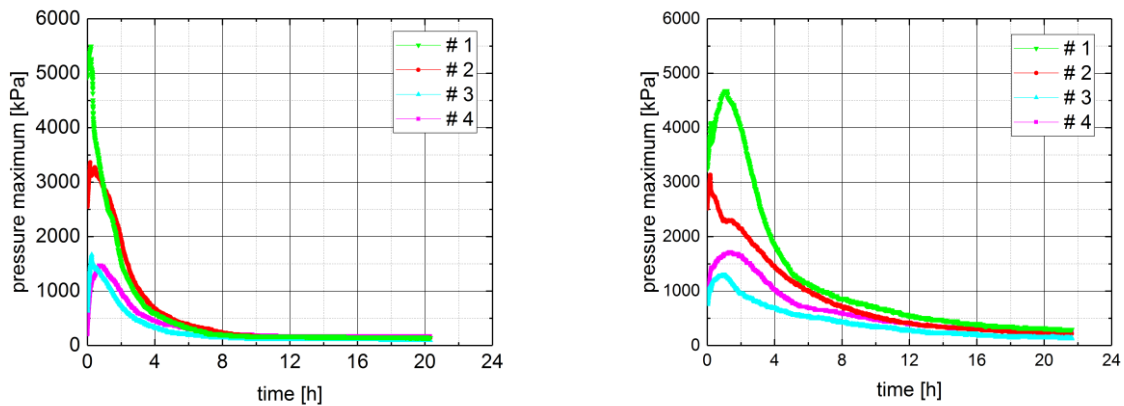
Figure4-46. Maximum pressure evolution for experiments with Pearson type A1 (left) and GGW (right). The values represent an area of 2X2 sensor points that show highest pressure values. The area may change during the experiment

Reaching higher, more realistic equilibrium pressure values required an increase of the effective bentonite dry density. Therefore, additional experiments with effective bentonite dry density between 900 and 1,200 kg/m^3 have been performed. Contact water volume decreased with increasing bentonite load as the total cell volume did not change. Comparison of experiments with different effective bentonite dry density can be found in Figure 4-47. Four experiments for each effective bentonite dry density have been merged together to one line, respectively. Maximum pressure values show little difference in case of experiments with 900 kg/m^3 and 1,000 kg/m^3 but increase with higher effective bentonite dry density. Bentonite samples contacted with GGW show higher pressure values at the same effective bentonite dry density.

By increasing the bentonite load in each cell, the pressure exposed sensor area increases (Figure 4-48). However, the sensor surface is never loaded completely and areas without significant pressure values are located especially at the rim of the film sensor. Pressure distribution is stable after ~30 hours, indicating that further homogenization does not take place. As the contact water is added only at the beginning of the experiment, a limited volume is in contact with the bentonite sample leading to a partly saturated inhomogeneous system.

89
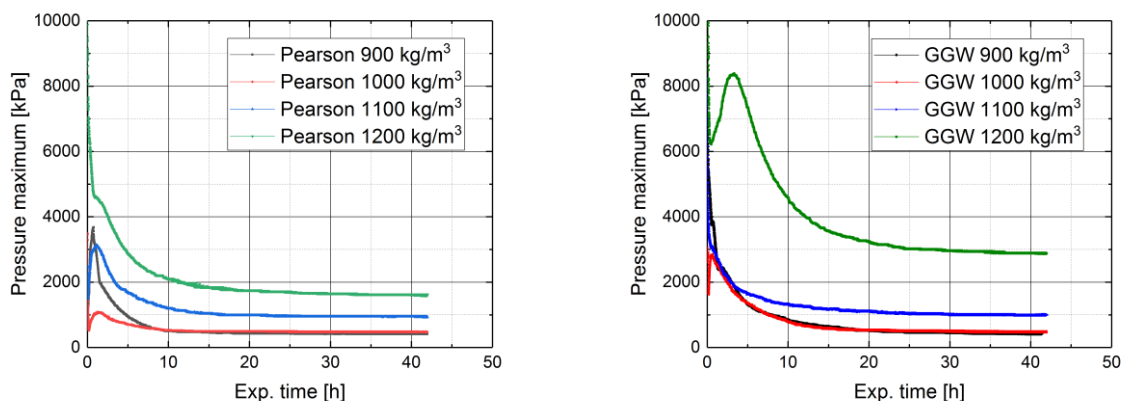
Figure 4-47. Maximum pressure evolution for experiments with Pearson type A1 (left) and GGW (right) with varying effective bentonite dry density. The values represent an area of 2X2 sensor points that show highest pressure values. Each line represents four experiments under equal conditions. The area may change during the experiment
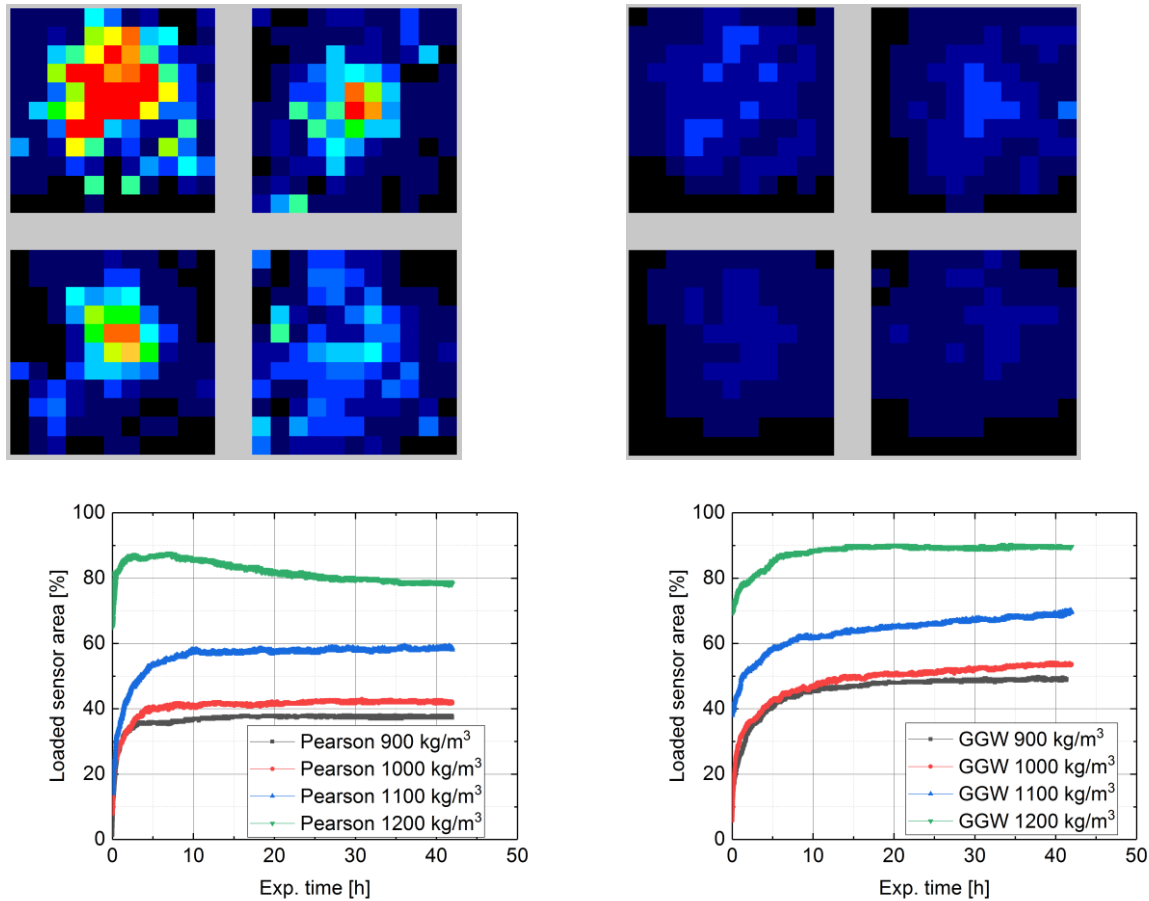
Figure 4-48. Initial state (top left) and steady state (top right) of experiments with Pearson type A1 and 1,200 kg/m3 effective bentonite dry density. Areas in black are below the detection limit. Loaded sensor area evolution for Pearson type A1 (bottom left) and GGW (bottom right) experiments with increasing effective bentonite dry density. Each line represents four experiments under equal conditions

4.4.5   Future work

Experiments performed so far only show partly saturated systems in equilibrium with heterogeneous pressure distribution. Next step will include an adjustment of the test cell. The aim is to facilitate continuous contact water supply to the bentonite sample in order to achieve full sample saturation and homogeneous pressure distribution. Therefore, a water reservoir will be added to the test cell. Sample cell and water reservoir will be separated by a frit to ensure isochoric conditions.

5   Binary mixtures or artificial inhomogeneities

5.1   Saturation of pellet/block systems under isochoric conditions (CIEMAT)

5.1.1   Objectives and methods

CIEMAT carried out a series of hydration tests in isochoric cells to qualitative and quantitative evaluate one of the possible sources of bentonite heterogeneity: the combination in the same barrier of pellets and blocks of compacted bentonite, whose initial dry densities and structures noticeably differ.

Two types of cells were used: a large-scale oedometer (MGR) and a transparent cell (CW). In both kinds of cells the lower half was filled with bentonite pellets with an average dry density close to 1.30 g/cm^3 and the upper part by a 1.60-g/cm^3 bentonite block. In both cases hydration with deionised water took place through the bottom (the pellets half). These kinds of tests were complementary: whereas MGR tests provided quantitative data, the information provided by the CW test was mostly visual and qualitative.

The material used in all the tests was the FEBEX bentonite. The block part of the sample was compacted from the granulate material with its hygroscopic water content, which is ~14%. The pellets were prepared in a factory for the EB project (ENRESA 2005). The bentonite was dried and milled in a three-step process to produce a fine grade powder with a water content of 3.3%. Later, a commercial plant with an in-line highly automated briquetting process produced coarse (>7 mm) and fine (0.4-2 mm) grained materials with dry densities of 2.11 and 2.13 g/cm^3, respectively. These two grain size fractions were subsequently combined to fit a Fuller shape curve with a maximum diameter of 12.7 mm and a minimum diameter of 0.425 mm, in order to reduce segregation. The different grain sizes were kept separated and mixed in the right proportion just before every test. The lab run out of pellets larger than 9.5 mm, and the granulometric distribution of tests MGR23 and MGR24 was modified to keep the Fuller's curve (Table 5-1). Also, in these tests the pellets were softly dried to a water content closer to the fabrication one, because the water content of the pellets increased during storage.

Table 5-1. Granulometric curve of the pellets of Febex bentonite used in the tests

Sieve sizes (mm)	Percentage retained (%)	
Test	MGR21, MGR22	MGR23, MGR24, CW1
9.5	17	0
4.75	31	37
2.0	26	31
1.18	11	13
0.59	10	12
0.425	5	6

The large-scale oedometer consists of a cylindrical body with base and an upper piston that may move in the cylinder (Figure 5-1). The body has an inner diameter of 10.0 cm and the

length of the sample inside was 10 cm. The top and bottom of the sample were in contact with filter papers and ceramic porous discs connected to outlets. The cell was placed in a rigid frame that guaranteed the constant volume of the sample by hindering the displacement of the piston. An external LVDT measured the potential axial displacements, whereas a 10-t load cell in the upper part of the frame measured the force developed by the specimen.

The bentonite block was directly compacted inside the cell and the pellets were poured on it and carefully shaken as necessary to get the target density. Then the cell was overturned. The water intake took place thorough the bottom surface, either under a low injection pressure (a 1.4-m water column, 14 kPa, simulating reduced water intake conditions, e.g. Opalinus clay in Mont Terri) or under a constant low flow (0.05 cm^3/h), simulating a continuous contribution of water, e.g. Grimsel granite). In the first case the water intake was measured with an automatic volume change apparatus and in the second case with a pressure/volume controller. During hydration the top outlet remained open to atmosphere and the pressure exerted by the material, the sample deformation and the water intake were measured and automatically recorded. The tests were performed at laboratory temperature. A summary of the tests performed and of their characteristics is given in Table 5-2.
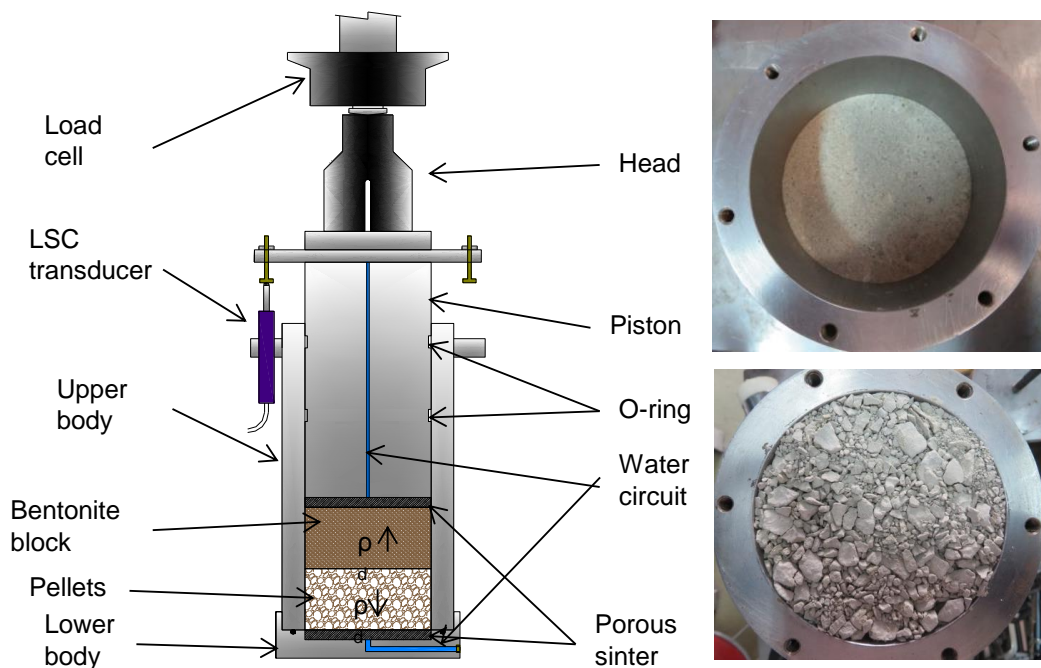
Figure 5-1. Schematic representation of the MGR cell (left) and images of the block (upper right) and pellets (lower right)

Table 5-2. Characteristics of the MGR tests

Test	Hydration	Duration (days)	Dates	T (°C)
MGR21	Constant pressure: 14 kPa	34	Aug – Sept 2017	23.1±0.6
MGR22	Constant flow: 0.05 cm³/h	266	Sept 2017 – Aug 2018	22.4±1.3
MGR23	Constant pressure: 14 kPa	210	Aug 2018 – Mar 2019	22.6±1.5
MGR24	Constant pressure: 14 kPa	14	Mar – Apr 2019	22.5±0.6

The transparent cell is a custom-built square cell consisting of two transparent methacrylate faces reinforced with steels frames (Figure 5-2). The inner dimensions of the central steel frame are 121x118x20 mm. A square block of the same dimensions was compacted in a bespoke mould and half sectioned. One of the halves was placed in the cell and the rest of the cell was homogeneously filled with the pellets while the cell was horizontally laid.

During assembly the fine fractions moved towards one of the sides of the cell (the one at the bottom during installation). As a result, the two faces, A and B, of the cell presented different appearance (Figure 5-3).

Two geotextile layers were placed at the upper and bottom sides of the cell. Hydration took place through the bottom with a 30-cm (3 kPa) water column, and the water intake was measured with an automatic volume change apparatus. Photographs of side A were periodically taken with the aim of performing digital analysis of the hydration evolution. Test CW1 lasted 379 days and run between February 2018 and March 2019.
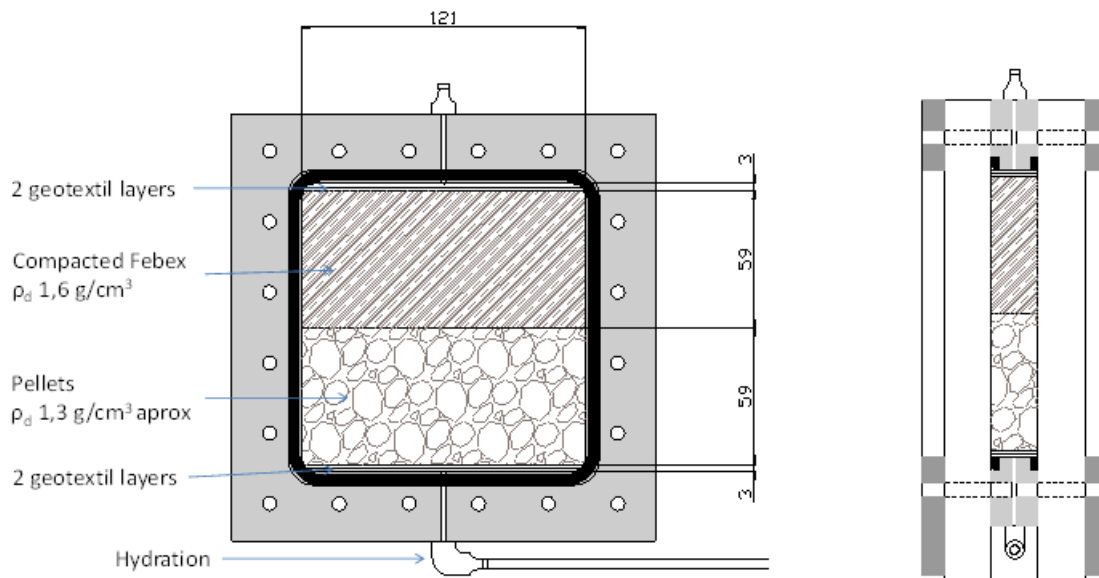
Figure 5-2. Schematic design of the transparent cell (front and lateral views)

93

Figure 5-3. Appearance of faces A (left) and B (right) of test CW1

At the end of the tests the bentonite was subsampled to determine water content, dry density and pore size distribution, as described in Section 4.2.1. The blocks from MGR tests were sliced in 6 horizontal levels (3 for pellets and 3 for block). The CW1 sample was cut into 16 parts (5 rows and 3 columns, with 2 samples instead of 1 in the central part).

5.1.2   Results

Figure 5-4 and Figure 5-5 show the evolution of water intake and axial pressure for the four MGR tests. There was a significantly different behaviour between the three tests performed under constant injection pressure (MGR21, MGR23 and MGR24) and test MGR22 performed under constant water inflow rate. In the three first tests the water intake was very quick and more than half of the water volume necessary for full saturation was taken in about 10 days. The reason is probably the high permeability of the pellets part. The axial pressure development was also steep at the beginning, but started after the water intake was between 80 and 100 cm^3 (Figure 5-6), corresponding to degrees of saturation of ~60%. After the sharp initial increase (the peak was reached after 30-40 days), in the longest test (MGR23) there was an intermediate stage of slight pressure decrease, and when the average degree of saturation was ~95% the axial pressure steadily increased again until full saturation was reached, with a stable pressure value of 3 MPa. Test MGR22 went also on until full saturation was reached. Since in this test the inflow was very low and controlled, the pressure development kinetics was very different to the other tests. Axial pressure started to develop slightly later than in the other tests (after 10 days), and when the degree of saturation was much lower than in the other tests (37%). The first peak was reached after 80 days and the intermediate stage lasted until 200 days had elapsed. During this time the degree of saturation increased from 58 to 96%. Afterwards, there was a new steep increase in axial pressure until the final value of 3 MPa. When full saturation was reached, the injection pressure inadvertently started to increase (the equipment was not able to keep a constant low injection flow into a saturated sample without increasing the injection pressure), and this explains the odd final shape of the curves for test MGR22.
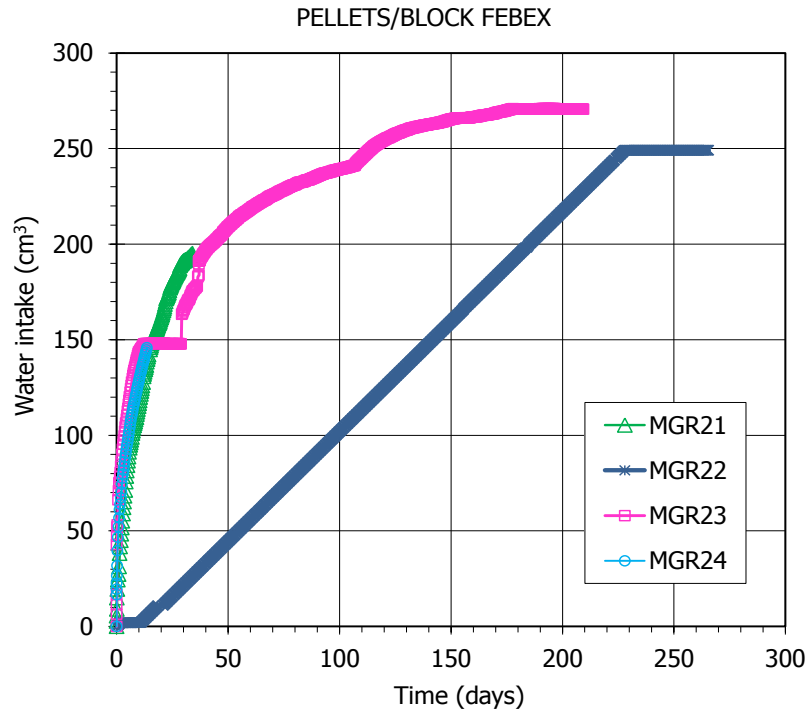
Figure 5-4. Water intake evolution in MGR tests (constant flow was prescribed in test MGR22)
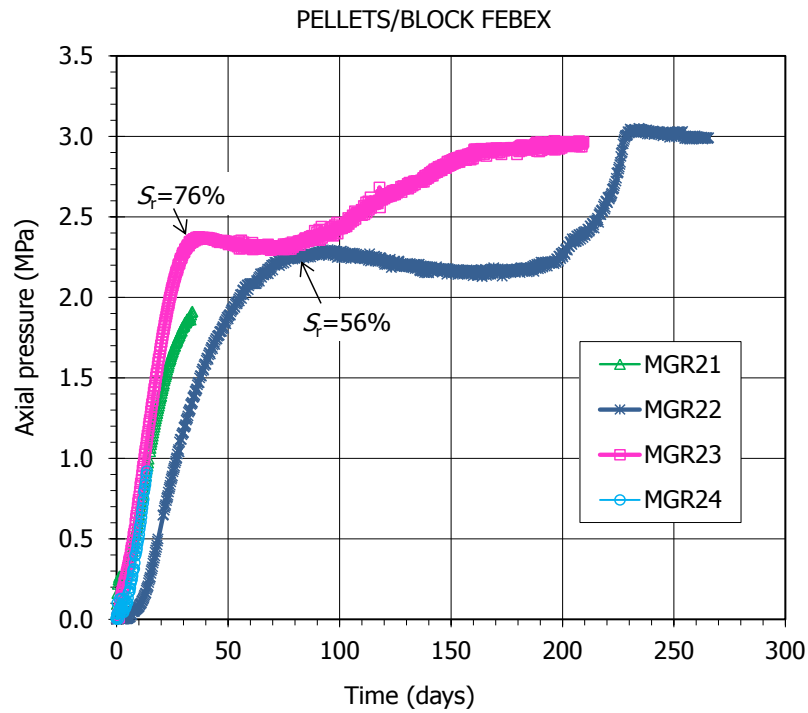
Figure 5-5. Axial pressure evolution in MGR tests

PELLETS/BLOCK FEBEX
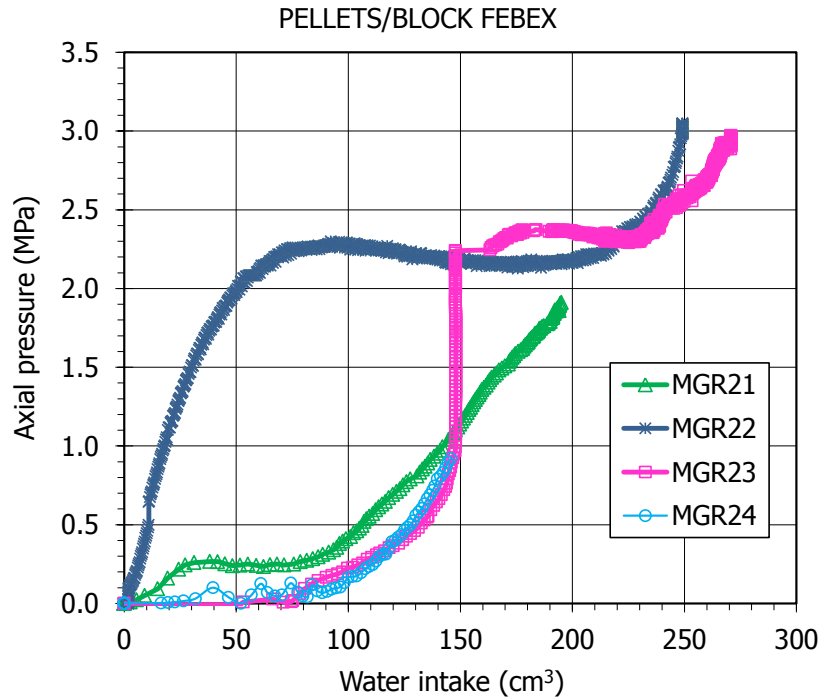
Figure 5-6. Axial pressure as a function of water intake in MGR tests

The final axial pressure measured was linked to the degree of saturation reached (Figure 5-7), and for the two tests that had reached full saturation was higher (3 MPa) than the swelling pressure expected for a FEBEX bentonite sample compacted to the average dry density value of the MGR tests (1.45 g/cm3). This theoretical value would be 2.0±0.5 MPa, according to the empirical correlation between dry density and swelling pressure obtained in small standard oedometers (Villar 2002). Previous researches showed that there is a scale effect on the swelling pressure measured in the laboratory, which tends to be higher as the testing cell is larger (Imbert & Villar 2006). This could maybe explain the higher pressure obtained in the large-scale oedometer with respect to the theoretical value obtained from empirical correlations.
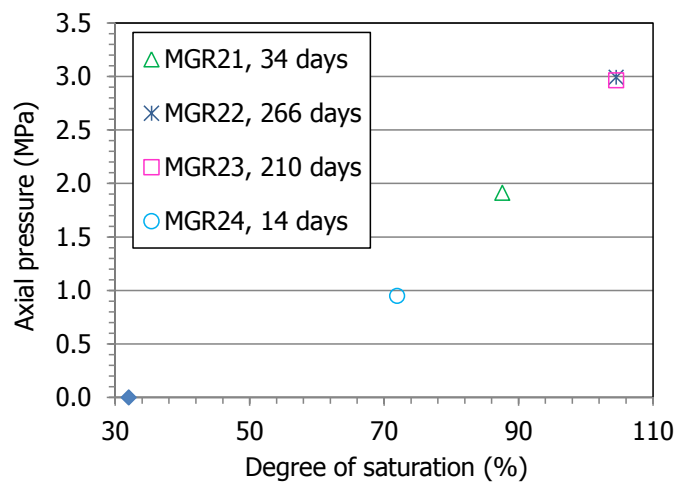
Figure 5-7. Final axial pressures measured as a function of the final degree of saturation of MGR tests

The tests were dismantled after different running times. The final appearance of the samples once extracted from the cell is shown in Figure 5-8. The sample from the shorter test (MGR24)

shows a quite saturated bottom in which the pellets cannot be told apart, but the upper part of the pellets half still showed open voids. The two halves of this sample (pellets and block) could easily be detached. In the other three cases the two halves were sealed and had to be separated with a knife.

MGR24: 14 days   MGR21: 34 days   MGR23: 210 days   MGR22: 266 days

Figure 5-8. Appearance of the MGR samples at the end of the tests

Table 5-3 shows a summary of the initial and final characteristics of the samples of the four MGR tests performed. The water content, dry density and degree of saturation values measured in subsamples are plotted in Figure 5-9 to Figure 5-11 as a function of the distance to the hydration surface. The initial values are indicated with thick horizontal lines. In two of the tests (MGR23, MGR24) the pellets were dried to the values they had after manufacturing. During the tests the water content and degree of saturation decreased from the hydration surface (sample bottom) upwards whereas the dry density increased. These gradients were steeper as the test duration was shorter and attenuated over time. The pellets/block interface did not seem to have any effect on the continuous gradients. The final dry density and water content values were similar in the two longest tests, despite the different hydration conditions (constant flow or pressure). Although the bentonite was finally fully saturated, the dry density and water content along the samples did not equalise.

Table 5-3. Initial and final characteristics of MGR tests

	Initial				Final			
	w (%)	h (cm)	ρ_d (g/cm³)	S_r (%)	w (%)	ρ_d (g/cm³)	h (cm)	S_r (%)
Test	**MGR21**							
Pellets	9.5	4.97	1.26	23	35.9	1.31	4.80	91
Block	13.3	5.01	1.60	52	22.9	1.50	5.33	78
Total[a]					29.0	1.43	10.00	88
Total[b]	11.6	9.98	1.43	35	28.6	1.41	10.13	85
Test	**MGR22**							
Pellets	9.9	5.04	1.28	25	35.3	1.35	4.79	95
Block	13.6	4.94	1.61	55	30.7	1.51	5.27	106
Total[a]					33.9	1.44	10.01	105
Total[b]	11.9	9.98	1.45	37	32.7	1.43	10.06	100
Test	**MGR23**							
Pellets	3.5	5.00	1.30	9	35.7	1.34	4.84	95
Block	14.2	4.98	1.60	56	31.1	1.51	5.29	107
Total[a]					33.9	1.44	10.01	105
Total[b]	9.4	9.98	1.45	29	32.7	1.43	10.12	100
Test	**MGR24**							
Pellets	5.7	5.02	1.28	14	31.0	1.30	4.93	78
Block	13.7	4.97	1.62	55	16.2	1.57	5.13	61
Total[a]					23.0	1.45	10.00	72
Total[b]	10.1	9.99	1.45	32	22.8	1.43	10.06	70

[a] from online measurements, in test MGR22 the water intake includes the intake of the porous stone, [b] from measurement of dimensions and water content, the final values affected by decompression
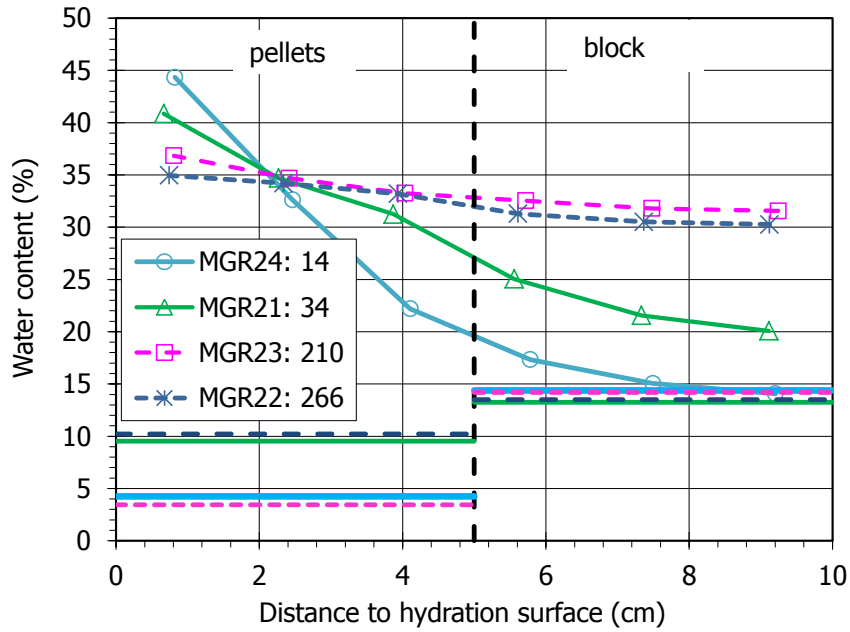
Figure 5-9. Final water content along the samples of MGR tests. The duration of the tests is indicated in days. The thick horizontal lines indicate the initial values
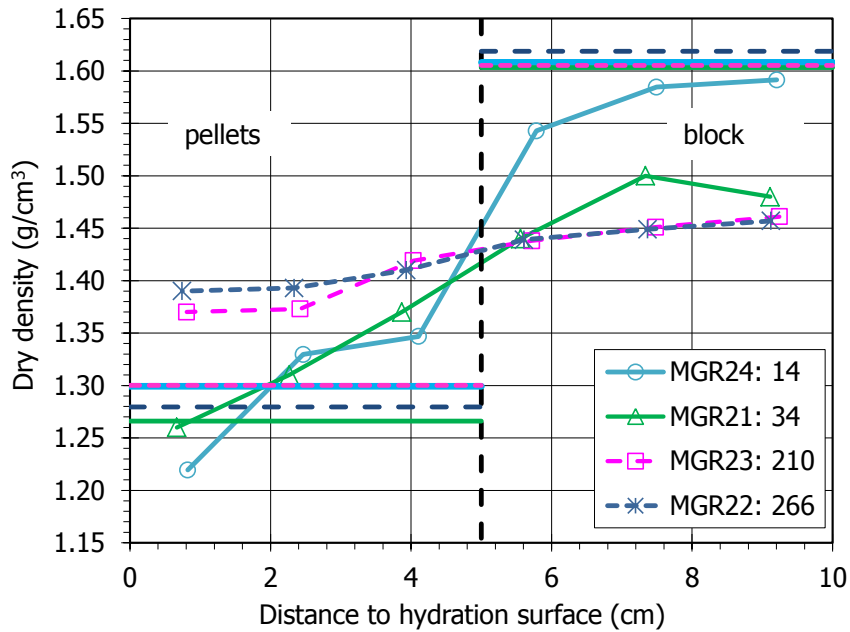
Figure 5-10. Final dry density along the samples of MGR tests. The duration of the tests is indicated in days. The thick horizontal lines indicate the initial values
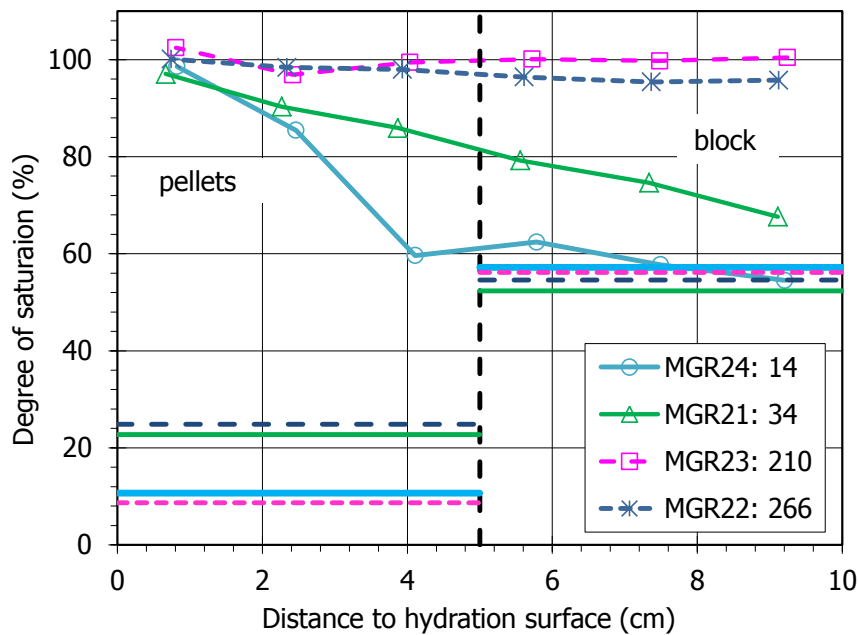
Figure 5-11. Final degree of saturation along the samples of MGR tests. The duration of the tests is indicated in days. The thick horizontal lines indicate the initial values

The same analysis of the final pore size distribution of the subsamples described for the GAP-vapour tests was performed with the subsamples of the MGR tests. As an example, Figure 5-12 and Figure 5-13 show the incremental curves of mercury intrusion for the subsamples of the tests lasting 14 (MGR24) and 210 days (MGR23) and for FEBEX samples of the same characteristics as the initial conditions used in the cells. In some subsamples duplicates were tested. For the block part of the samples, the curve corresponding to a sample compacted at dry density 1.59 g/cm³ with a water content of 14% was used. For the pellets part, a mixture of pellets having approximately a Fuller's curve grain size distribution, with a resulting dry density of 1.29 g/cm³ and a water content of 10%, was used. The usual two pore families corresponding approximately to pores larger and smaller than 200 nm could be told apart in all samples, except for the initial pellets curve, which showed that most of the pores had a size around 300 µm. In the shorter test (Figure 5-12), the pore size distribution of the subsamples taken from the block half, was similar to that of the initial block. Indeed, no relevant changes in the dry density and water content of these samples took place during the oedometer test, because it was too short. In contrast, the pore size distribution of the pellet half significantly changed. Although most of the porosity still corresponded to pores larger than 200 nm, the size of these pores decreased with respect to the initial pellets mixture, particularly for the subsamples taken farther away from the hydration surface. In the subsamples from the block half of the longer test (Figure 5-13), the size of the macropores increased with respect to the original block, whereas in the pellets half, the percentage of pores smaller than 200 nm increased and the size of the macropores decreased with respect to the original pellets.
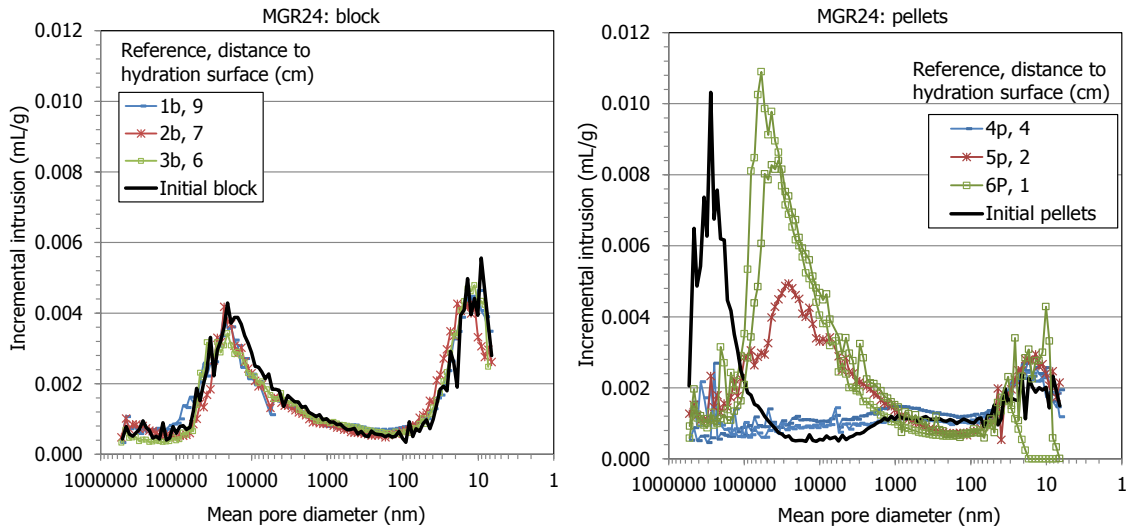
Figure 5-12. Pore size distribution expressed as incremental mercury intrusion of samples from the MGR24 test (lasting 14 days), corresponding to the block (left) and pellets (right) halves. In both cases the curves for the initial materials (blocks and pellets) are included
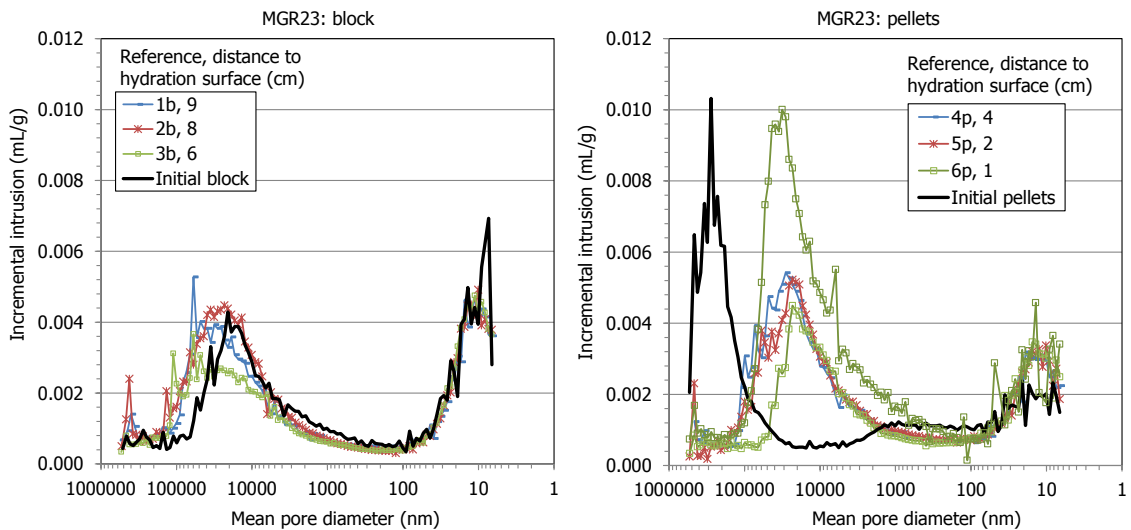
Figure 5-13. Pore size distribution expressed as incremental mercury intrusion of samples from the MGR23 test (lasting 210 days), corresponding to the block (left) and pellets (right) halves. In both cases the curves for the initial materials (blocks and pellets) are included

The percentage of pores intruded by mercury in these subsamples was between 35 and 70%. Taking this into account, the void ratio corresponding to pores larger and smaller than 200 nm was recalculated. In all cases the largest proportion of void ratio corresponded to the pores of diameter smaller than 200 nm, but the relationship between the void ratio corresponding to pores smaller (e_m) and larger (e_M) than 200 nm increased in all tests, which would indicate an increase in the volume of macropores during testing (Figure 5-14).
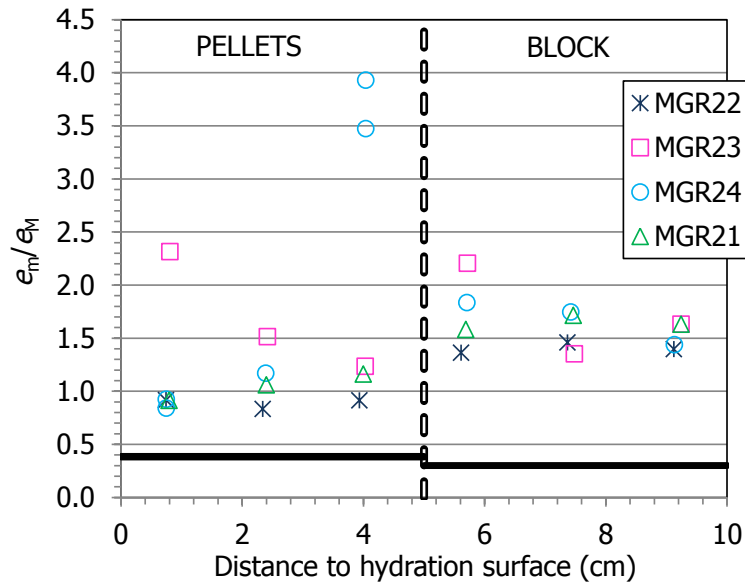
Figure 5-14. Ratio between void ratio corresponding to pores smaller and larger than 200 nm (em and eM) obtained by MIP in subsamples from the MGR tests (the thick horizontal lines indicate the initial conditions)

The CW1 test was going on for 379 days. During the test, variations in the coloration of the grains, changes in texture and shape, and displacement of the particles, especially in the pellets zone could be observed (Figure 5-15). The appearance of the saturated pellets was gel-like and the sharpness of particles was lost. The evolution of hydration was slower in face B, where fine particles predominate. The reason could be the absence of large voids where water could quickly and easily penetrate. The face-A images for the three first months of hydration were analysed and some observations could be highlighted. The area of the pellets increased with no preferential direction, which indicates their swelling. Over time, the pellets/bentonite interface displaced downwards (as a result of the higher swelling capacity of the block) and became less distinct. The images were also treated with the GIMP Image Manipulation Program by applying an edge detector filter (Figure 5-16), although no results are available yet.

Unfortunately, the water intake measurement during the test was not satisfactory. Consequently, the final average water content was computed from the final sample weight, and the final dry density from the measured dimensions (Table 5-4). Also, a very detailed characterisation of the final state of the bentonite was carried out in subsamples taken according to the schema shown in Figure 5-17. In all of the subsamples water content and dry density were determined and the values are plotted in Figure 5-18 and their averages given in Table 5-4. Despite the fact that the sample was fully saturated at the end of the test (Figure 5-19), there were clear water content and dry density continuous gradients in which the interface between pellets and block did not seem to play any role. However, a small border effect was observed at the bottom of the cell: the water content of the subsamples close to the border (5.1 and 5.3 in 5-17) was slightly higher than that of the middle subsample (5.2), whereas the dry density was lower. The cell border effect was no longer observed at 4 cm from the hydration surface (subsamples 4-1 to 4.3).
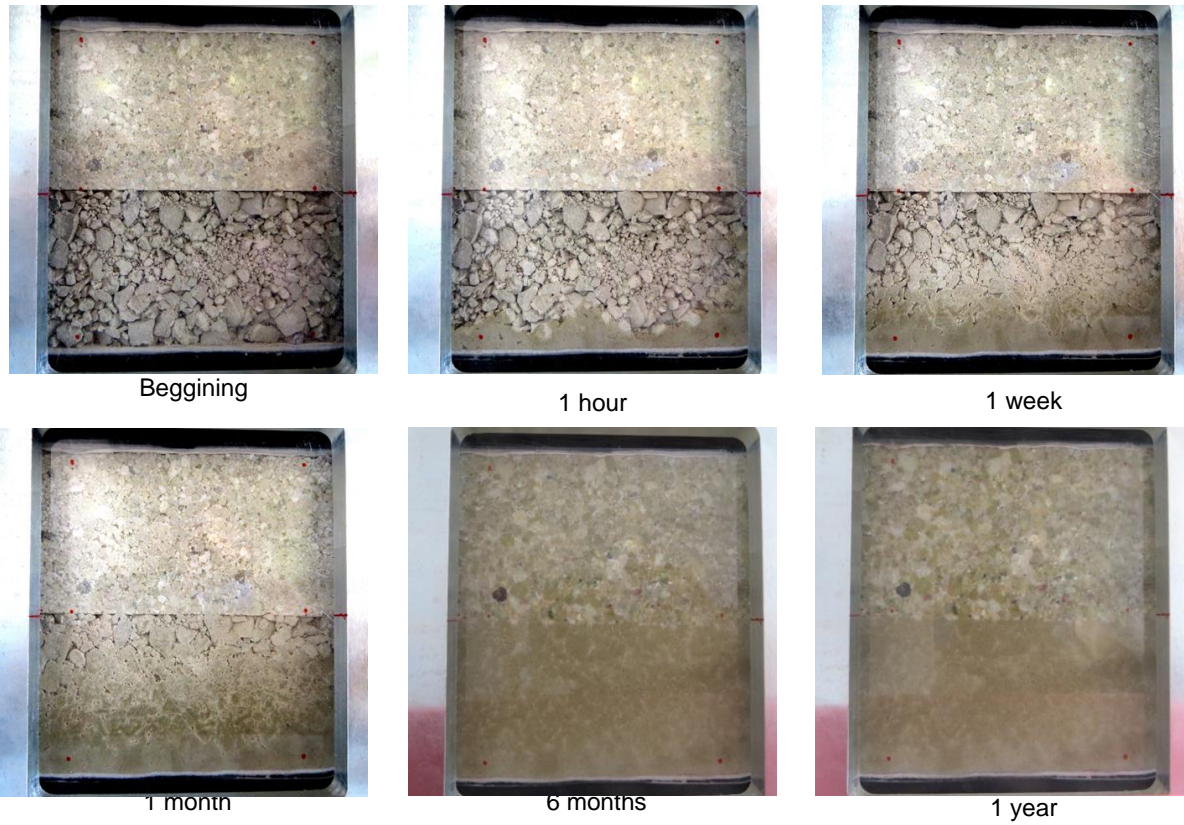
Figure 5-15. Evolution of the appearance of test CW1 upon saturation (face A)

Table 5-4. Initial and final characteristics of test CW1

	Initial				Final			
	h (cm)	w (%)	ρd (g/cm3)	Sr (%)	h (cm)	w (%)	ρd (g/cm3)	Sr (%)
Pellets	5.75	10.1	1.30	25	5.69	39.7	1.28[a]	97[a]
Block	6.03	14.0	1.58	53	6.37	32.8	1.41[a]	97[a]
Average	11.80	11.9	1.45	37	12.06	35.9	1.38[b]	102[b]

[a] affected by subsampling and trimming, [b] affected by compression of geotextile
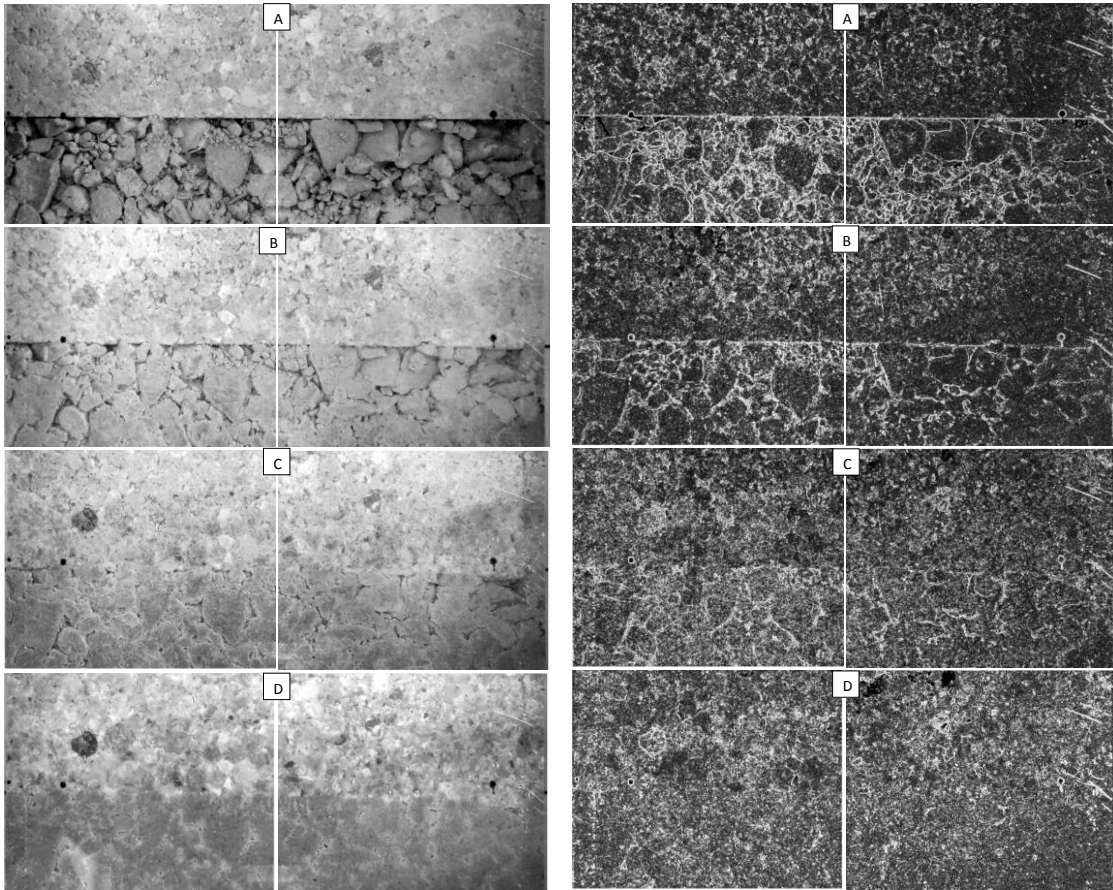
Figure 5-16. Appearance of the block/pellets interface in CW1 test at different stages of hydration in raw images (left) and images treated applying an edge detecter filter (right). (A: beginning, B: 1 month, C: 2 months, D: 3 months)
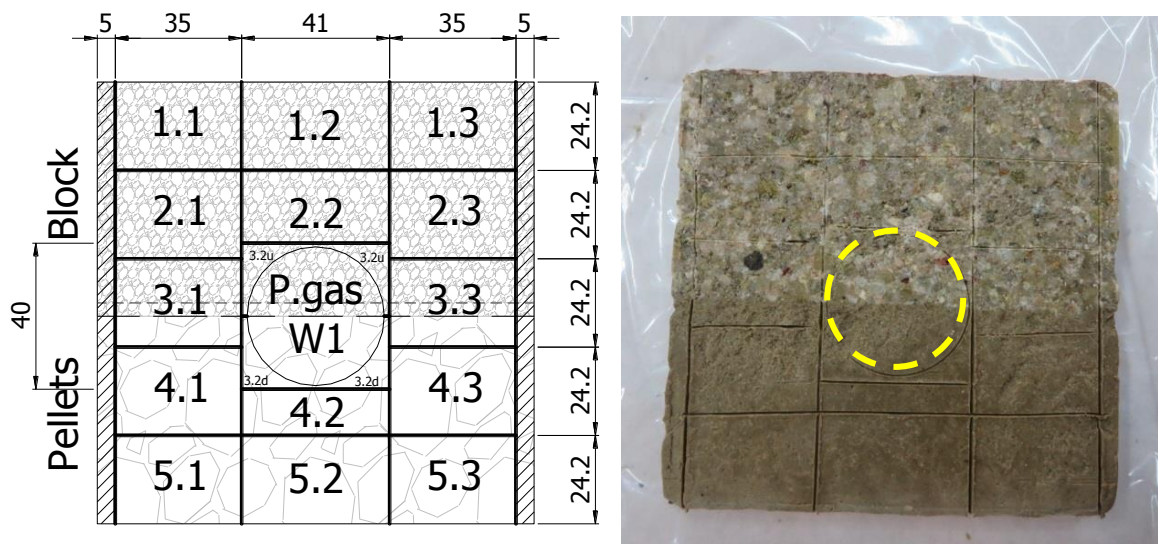
Figure 5-17. Final subsampling of test CW1 (left) and location of sample for gas permeability (right)

104
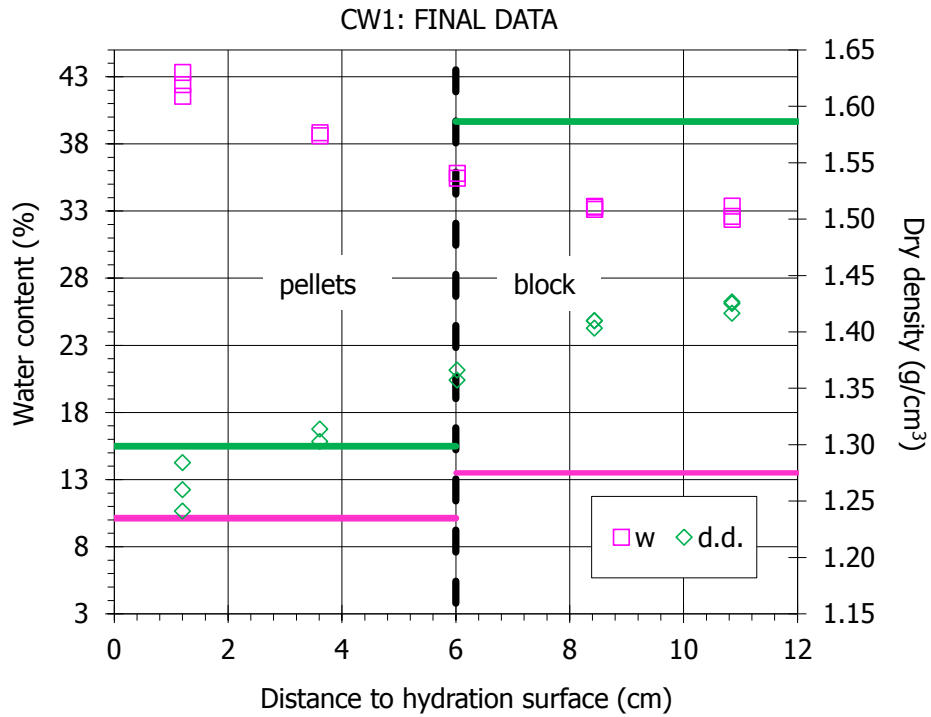
Figure 5-18. Final water content and dry density along the sample of test CW1. The thick horizontal lines indicate the initial values
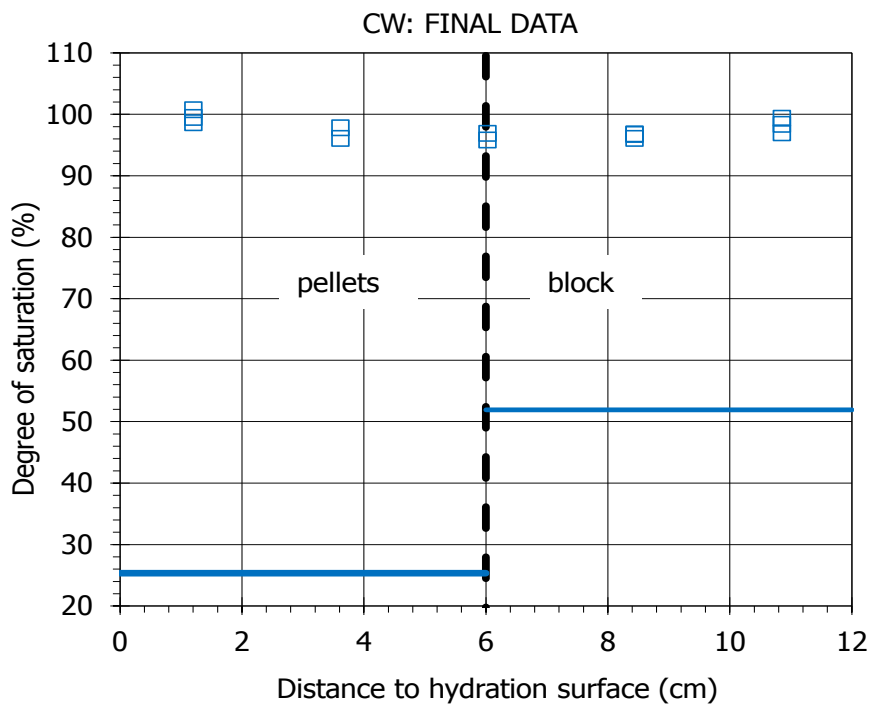
Figure 5-19. Degree of saturation along the sample of test CW1. The thick horizontal lines indicate the initial values

Additionally, a cylindrical subsample was obtained by drilling in the middle part of the block to measure the gas breakthrough pressure as an indicator of the sealing quality of the

interface between the pellets and the block. This subsample was vertically crossed by the interface (Figure 5-17). The core diameter was fit to 3.8 cm by using a cutting ring and knife. The resulting specimen was 2.2 cm in height and its initial dry density and water content were 1.35 g/cm^3 and 33.8%. Filter paper and porous stones were placed on top and bottom of the sample and it was laterally wrapped in double latex membranes. Vacuum grease was applied between membranes in order to prevent the loss of gas. The wrapped sample was placed in a triaxial cell filled with de-aired water and pressurized to ensure perfect adherence of the membranes to the surface of the sample and to avoid gas transport along it. A confining pressure corresponding to the swelling pressure of the bentonite (3 MPa) was applied. The cell inlet at the lower part of the sample was connected to a nitrogen gas cylinder applying the gas injection. The outlet of the cell connected to the top of the sample was open to atmosphere, with a series of different range gas mass flowmeters measuring the gas outflow. More experimental details about the equipment and the equations used to compute permeability are given in Villar et al. (2018).

The injection pressure was increased 0.1 MPa every two hours, from 0.2 to 2.95 MPa. There was no flow until the injection pressure reached 2.00 MPa. For injection pressures from 2.00 to 2.20 MPa there were barely measurable flow pulses, more significant for a gas injection of 2.24 MPa. There was again no flow from 2.20 to 2.85 MPa of injection pressure. For gas injection pressure of 2.90 MPa unsteady flow pulses close to the turndown value of the flowmeters were detected. At the end of the test the specimen had a dry density of 1.45 g/cm^3 and a water content of 31.2%. This means that the sample had consolidated as a result of the confining and gas pressure applied and its water content had slightly decreased, which would indicate that some water movement took place during the test.

It can be considered that the gas breakthrough pressure was ~2.2 MPa, although no steady, correctly measurable flow was measured at any moment. This breakthrough pressure would be in the order of the values expected for FEBEX samples compacted to dry densities between 1.35 and 1.45 g/cm^3, which would be between 1.5 and 3.5 MPa (Gutiérrez-Rodrigo 2018). The tentative permeability value computed from these flow pulses is in the order, or even below, that expected for FEBEX samples of the same accessible void ratio with no interface in them, which indicates that the pellets/block interface was perfectly healed and sealed.

The results obtained in the tests performed in the large-scale cells MGR and CW with combinations of pellets and bentonite blocks allow to draw the following conclusions:

– The way of hydration conditioned the water intake and the pressure development kinetics: slow hydration (e.g. under a controlled low flow) delayed the start of pressure development, but allowed higher pressures to be reached for lower degrees of saturation. The reason could be the longer time available for water redistribution from the macropores to the microstructure (particularly the montmorillonite interlayer), which would be the responsible for swelling.

– In the tests performed under constant pressure hydration, even though it was very low, the initial water intake was very high, probably because of the large voids in the pellets half, from which hydration took place. This explanation would be confirmed by the fact that in CW1 test, hydration was slower in the side of the cell where powder predominated (face B).

– Irrespective of the way of saturation (constant flow or pressure), the pressure development was not continuous. After a first sharp increase (which was quicker under constant pressure), there was an intermediate period of pressure stabilisation. Only when the degree of saturation reached ~95%, the pressure increased again until its final equilibrium value. This pressure development pattern was observed also in samples of compacted bentonite and of pellets. The scale effect was probably responsible for the fact that the

final pressure value was higher than the value expected for smaller samples of compacted bentonite.

– The water content and dry density gradients were not affected by the pellets/block interface. The gradients were dependent on the hydration time and although they attenuated over time, they persisted even after full saturation was reached. After full saturation the pellets/block interface was impervious to gas.

5.2 Stress field evolution and final state of heterogeneous samples saturated under isochoric conditions (CEA)

5.2.1 Objectives and methods

The objectives of this series of tests is to investigate the resaturation in isochoric conditions of initially heterogeneous samples of MX-80 bentonite in controlled conditions. Although the heterogeneities in terms of dry density and water content are characterized only in a post-mortem way (in the final state of the experiment), the swelling pressure field development upon saturation (and heterogeneities) is assessed using an array of sensors at various spatial locations. The test cases are chosen so that a simple geometry and boundary conditions are ensured as well as, for example, comparable average dry density, so that effects of the type of heterogeneity can be more readily assessed.

A multi-sensor cell is designed for this purpose (Figure 5-20) : it is essentially an oedometric cell of diameter 57 mm equipped with 9 pressure sensors (total pressure or interstitial pressure) at 3 vertical positions (6.6 mm, 23.3 mm and 40 mm) and angular positions (0°, 90° and 180°). These sensitive elements are 9 mm in diameter. 3 thermohygrometers are positioned at 270° and the same vertical positions. The cell is also equipped with continuous measurement of the axial pressure and displacement (top lid only) and injected water mass. Water is injected with a very small hydraulic head of 60-70 cm through porous plates on the bottom side (and/or the upper side) of the chamber, blocked at approximately zero displacement. In the case of unilateral hydration the other side is placed at laboratory conditions to ensure evacuation of entrapped air.
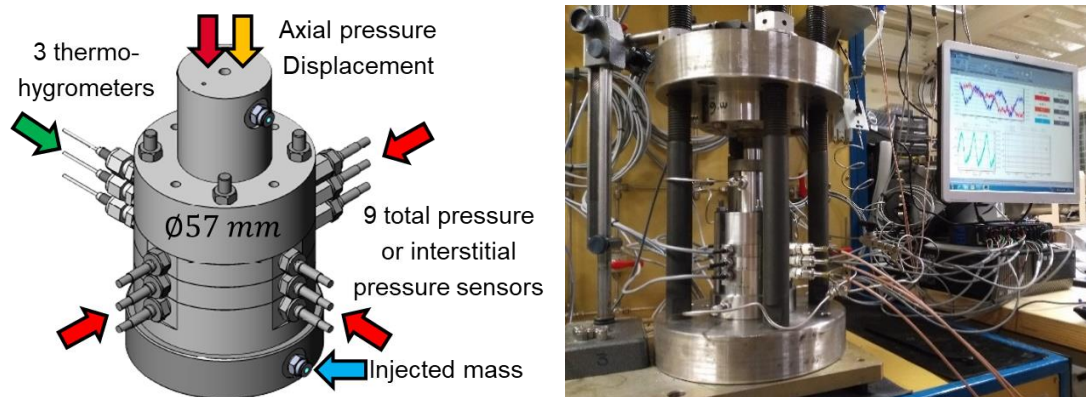
Figure 5-20. Schematic of the multi-sensor cell and photograph of the experimental apparatus

5.2.2 Investigated test cases and global measurements

The investigated test cases are summarized in the schematics below (Figure 5-21). Tests 1 and 2 are carried out on pellet/powder mixes arranged to minimize macroscopic gradients by building layer by layer dense arrangements of pellets with a fraction of powder (obtained from crushed pellets) filling the inter-pellet gaps. Tests 3 to 5 (5 is still ongoing at the time of this report) are obtained by stacking blocks (for high density) or powder (for low densities).

BEACON_C_1

Top BC : lab. conditions

66.9% /33.1% mix (dry mass)

| 122.90g pellets w=5.1%, ρ_d~2.12 g/cm3 |
| 60.81g powder w=10.3%, ρ_d=0.93g/cm3 |

h=45.0 mm (final)

Bottom BC: site water (~70 cmH$_2$O)

Final estimated ρ_d: 1.498 g/cm^3

BEACON_C_2

Bot. BC: site water (~60 cmH$_2$O)

66.9% /33.1% mix (dry mass)

| 120.63g pellets w=5.1%, ρ_d~2.12 g/cm3 |
| 62.80g powder w=10.3%, ρ_d=0.93g/cm3 |

h=45.2 mm (final)

Bottom BC: site water (~70 cmH$_2$O)
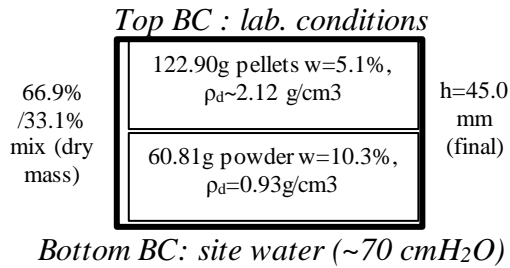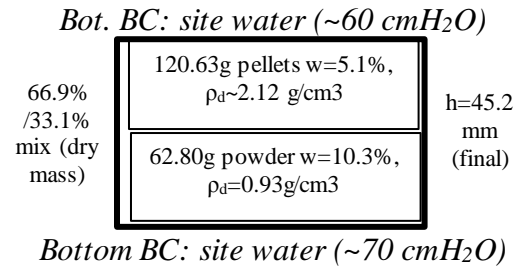
Final estimated dry density: 1.488 g/cm^3

BEACON_C_3

Top BC : lab. conditions

Stacked

| 65.70g powder w=10.3%, ρ_d=0.975g/cm3 |
| 122.13g block w=10.3%, ρ_d=1.99g/cm3 |

h=44.2 mm (final)

Bottom BC: site water (~70 cmH$_2$O) (discontinuous)
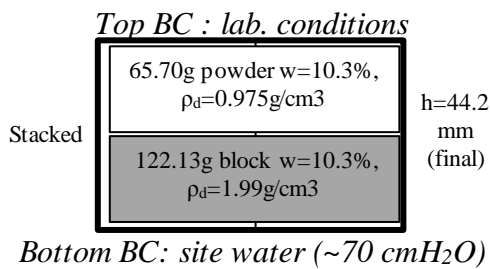
Final estimated dry density: 1.511 g/cm^3

BEACON_C_4

Top BC : lab. conditions

Stacked blocks

| 112.67g block w=10.3%, ρ_d=1.561g/cm3 |
| 98.46g block w=10.3%, ρ_d=1.397g/cm3 |

h=50.2 mm (final)

Bottom BC: site water (~70 cmH$_2$O)
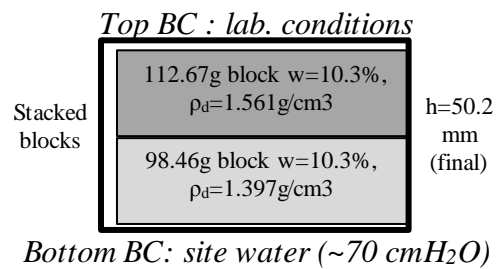
Final estimated dry density: 1.477 g/cm^3

BEACON_C_5 (ongoing)

Top BC : lab. conditions

Stacked blocks

| 98.79g block w=10.3%, ρ_d=1.406g/cm3 |
| 112.70g block w=10.3%, ρ_d=1.570g/cm3 |

h=53.5 mm (current)

Bottom BC: site water (~70 cmH_2O)
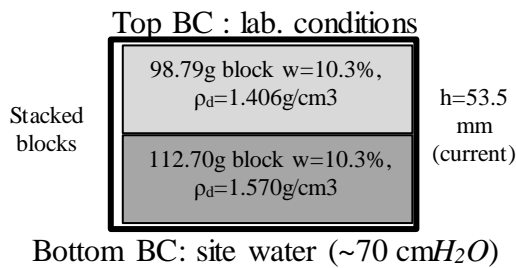
Current estimated dry density: 1,405 g/cm^3

Figure 5-21. Samples resaturated in the multi-sensor cell

The goal of the experimental plan is to examine the separate effects of the initial heterogeneity types (pellet/powder or pellet only assemblage, compacted blocks, compacted blocks combined with granular material). The effects of the average dry density and density gradient are investigated. Test 3 with a very large density gradient was saturated in a discontinuous manner by injecting small amounts of water until a local pressure sensor reaches the value near 10 MPa (in order not to damage the sensors). Its interpretation is then mostly qualitative since the hydration history is not well known.

Global measurements (total injected water mass and axial (top lid) swelling pressure are presented below (Figure 5-22). Relative humidity at three different heights and temperature are measured and can be provided upon request. The final swelling pressure values do not

show a simple correlation with the sample properties; indicating that this parameter largely depends on the hydromechanical history for these different assemblages.

BEACON_C_1
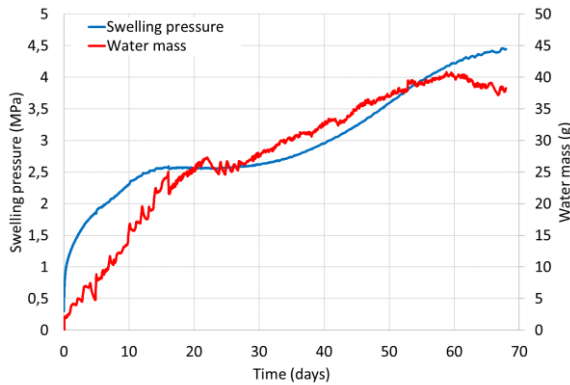
BEACON_C_2
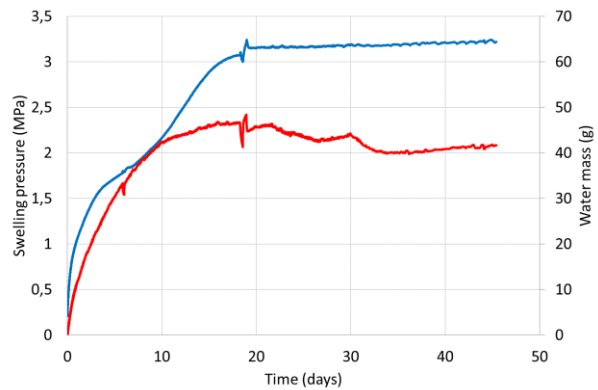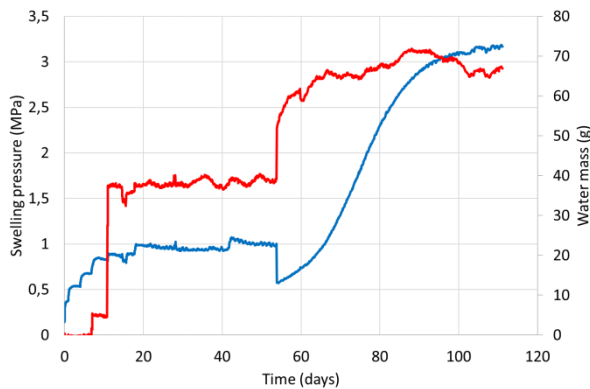
BEACON_C_3

BEACON_C_4
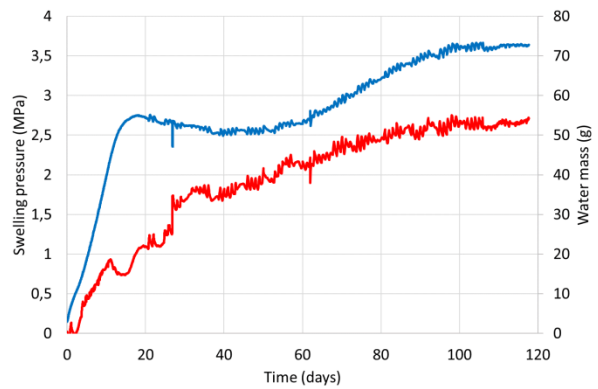
Figure 5-22. Total injected water mass and axial swelling pressure measurements

5.2.3 Stress field evolution

Radial total pressures averaged between the three sensors at the same vertical position (noted bottom, middle, top) are presented below (Figure 5-23) and compared to the axial (top lid) swelling pressure. Single sensor responses are omitted for brevity and are available upon request. A first observation is the similarity of pressure measurements between the average of top radial sensors and the upper axial sensor, especially close to saturation: this seems to indicate an isotropic stress state; small discrepancies are easily explained by the dispersion in local measurements and the different measurement locations. Very high stress heterogeneities can be observed at early stages of hydration for compacted blocks, where the effect of friction appears more important; swelling pressures at the sample bottom are very partially transmitted to the upper regions. The pellet/powder arrangements do not show such high stress gradients and the effect of friction is much less predominant.

Tests 1, 2 and 4 can be reliably compared since the average parameters of these samples are approximately equal. They differ by the type of hydration (one or two sided) and the type of heterogeneity (pellet powder and stacked blocks). The usual collapse is observed at some point of the hydration process although much more pronounced for the compacted blocks, and only in the regions far from the hydration front; these regions always have higher final swelling pressures. For pellet-powder samples the hypothesized scenario is that:

- The first stages of the hydration process form a saturated low density region that controls water transport,
- The swelling pressure of this area induces a compaction of far regions (relatively low friction of the granular material allows for rearrangements, filling to macrovoids, etc.),
- At some point the hydration of these far, overly dense areas exerts a sufficient swelling pressure to cause a recompaction of the regions close to the hydration front.

For the blocks the process could be different because of higher initial stiffness, friction and the existing heterogeneity (large top density).

BEACON_C_1   BEACON_C_2
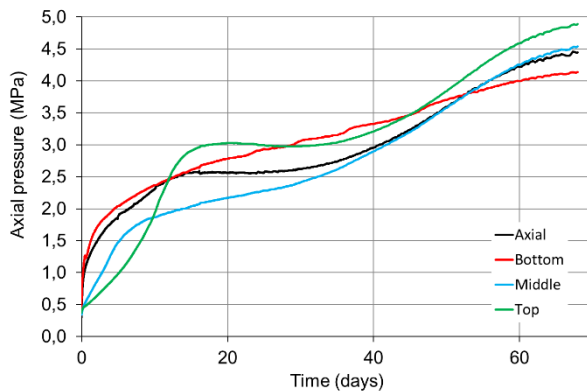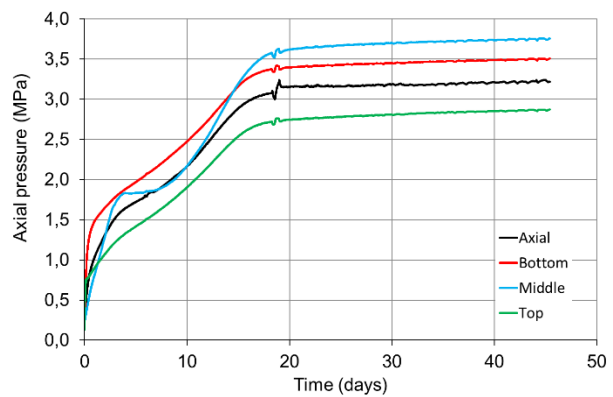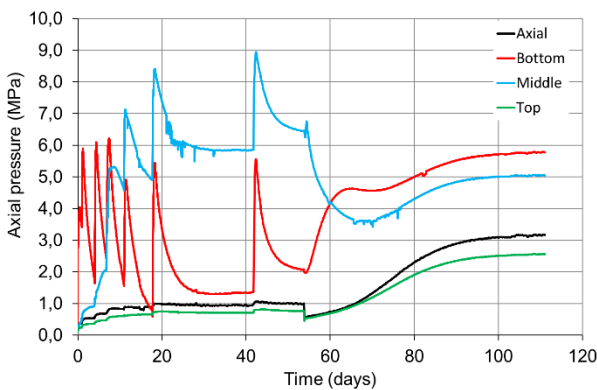
BEACON_C_3   BEACON_C_4
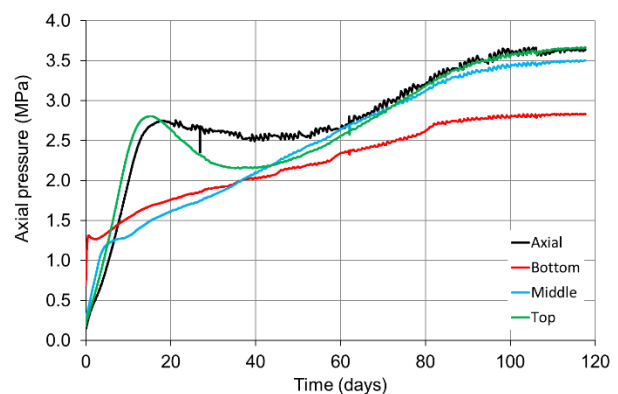
Figure 5-23. Local stress measurements averaged per height (3 sensors) compared with the axial pressure measurement

Test 3 shows the effect of discontinuous hydration on a very heterogeneous sample (each pressure peak corresponds to a small injected amount of water). The method allowed to progressively relax the large stresses in the very dense bottom region by wetting/drying cycles. These cycles seem to accelerate hydration of the upper regions maybe via drying damage acting as channels through the lower areas.

5.2.4   Characterization of the final states

Final states have been characterized by cutting samples into 12 equal subvolumes corresponding to positions in front of sensor ports, except with test 4 where the sample also was split along the former block interface (mid section). Water content measurements are carried out using treatment at 105°C for 24h; apparent density measurements are carried out

using hydrostatic weighting in mineral oil. Dry density and water content measurements at dismantling are presented for each sample below (Figure 5-24).

BEACON_C_1
Av. ρ_d=1.511 g/cm^3, W=29.5% (S=95.8%)
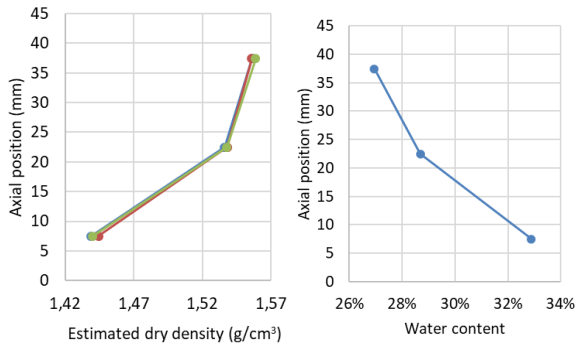
BEACON_C_2
Av. ρ_d=1.446 g/cm^3, W=32.1% (S=102.6%)
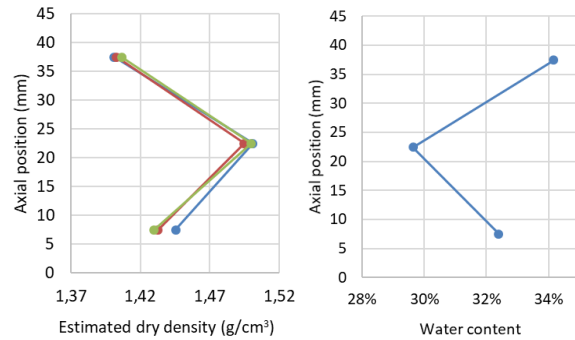
BEACON_C_3
Av. ρ_d=1.444 g/cm^3, W=32.0% (S=106.1%)
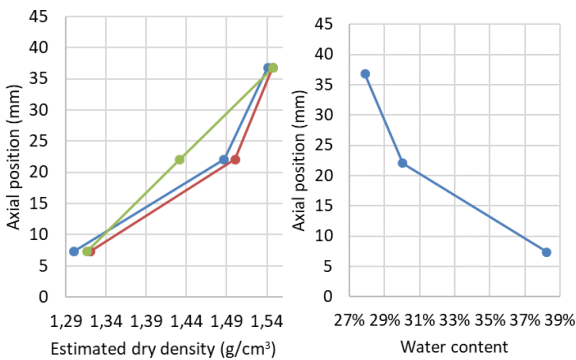
BEACON_C_4
Av. ρ_d=1.453 g/cm^3, W=31.8% (S=100.1%)
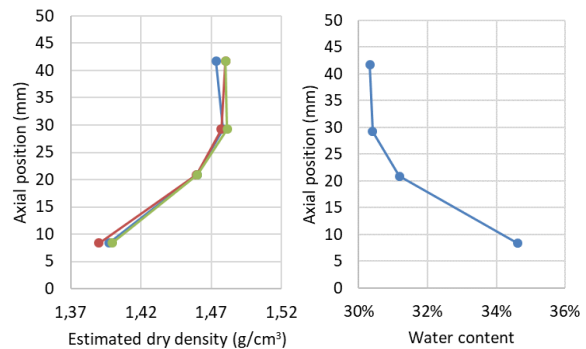
Figure 5-24. Local dry density and water content measurements

All final states show similar qualitative features compatible with the observations made previously : a vertical density gradient is observed in the direction of hydration, inversely correlated with water content. In test 3, the final density gradient is actually inverted compared to the initial state and is therefore the result of the hydration process and not residual heterogeneity.

Mercury Intrusion Porosimetry (MIP) measurements were performed on freeze-dried samples taken from tests 1 and 2 and presented below (Figure 5-25), compared with MIP results obtained on pure pellets and pure powder. It mainly shows :

- A main 17 nm peak mesoporosity characteristic of the intra-aggregate spacing, which appears lower in the injection area,
- A 200 – 400 nm mesoporosity, largely more represented in the injection area,
- A large porosity characteristic of thin microcracking in pellets at 5-10 µm, absent in powder. Larger cracking is observed on freeze-dried samples after hydration up to 50 µm,
- Intergrain and interpellet spacing starting at approximately 70 µm up to the upper limit of the MIP technique.

BEACON_C_1   BEACON_C_2
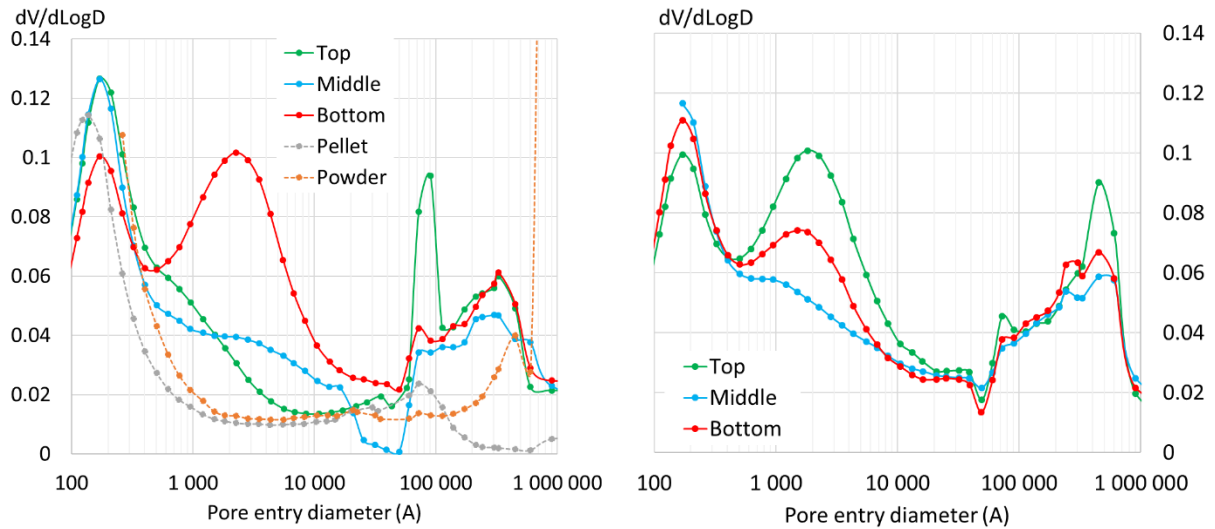
Figure 5-25. MIP characterization of several samples in tests 1 and 2

5.2.5   Conclusions and perspectives

A first analysis of dual density systems resaturated in 1D at constant volume in an instrumented cell has been carried out. Heterogeneities in the final state have been observed which are due mostly to the hydromechanical scenario, due to the coupling between differential stiffness, swelling pressure, friction coefficient and transport properties in several parts of the sample at different suction levels. The dry density gradient observed is qualitatively similar to the REM_MM experiment (provided as WP3-5 test case 1b) on larger dimensions and time scales.

In the next steps, other types of heterogeneities will be investigated by varying the hydration conditions, average dry density, density gradient and geometry of these dual density systems. Interrupted tests may enable to have access to an intermediary unsaturated state.

5.3 X-ray tomographic imaging of pellet/powder mixes saturated under isochoric conditions (CEA)

5.3.1 Objectives and methods

The goal of in-situ X-ray tomographic imaging (X-CT) of the resaturation of these heterogeneous bentonite assemblies is to provide qualitative and, if possible, some quantitative information on the hydromechanical processes happening inside cells. Indeed, it could provide access to:

- Displacement fields (of solid), through the use of image correlation techniques, providing insights into mass transport of clay and therefore into the homogenization/creation of heterogeneities,
- Water content field, through the use of properly calibrated CT gray levels and displacement fields,

Through these measurements, access to the global 3D phenomenology of a test as a function of time, such as:

- Evidence of friction phenomena,
- Information on the macroporosity at a scale above several microns and its evolution (interpellet porosity, cracks),
- Etc.

For this purpose, a dedicated experimental apparatus ("Tomobento_1") has been designed (Figure 5-26), which allows unilateral hydration of bentonite at approximately constant volume, axial swelling pressure measurement and X-ray imaging. It is composed mainly of a PEEK (PolyEtherEtherKetone) cell of internal diameter 57 mm with PE porous injection/exhaust ports, and a standard 25 kN load cell with a spherical contact and displacement locking.
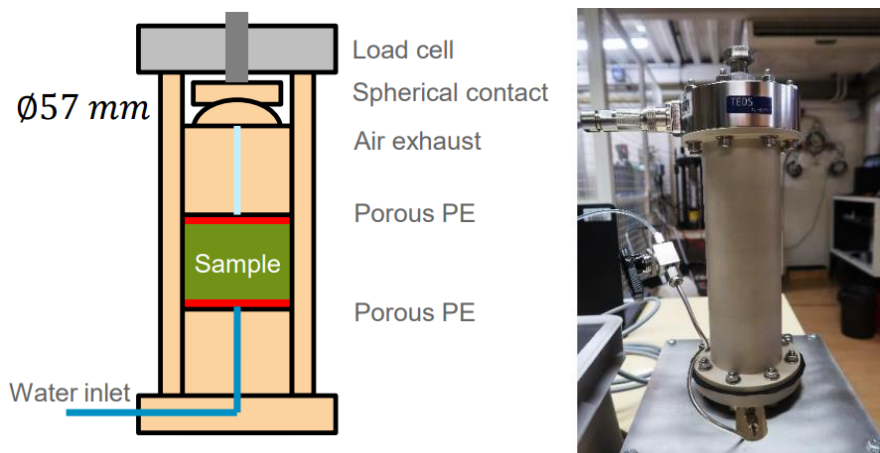
Figure 5-26. Schematic of the "Tomobento_1" cell and photograph of the experimental apparatus

5.3.2 Testing and improvements

A first validation test was carried out on a single 32 mm pellet sample surrounded by MX-80 crushed pellet powder already used in tests 1 and 2 presented previously (Figure 5-27). The sample was resaturated using pure water during 44 days and disconnected from their water source for approximately 1h for CT scans carried out at 0h, 1h, 22h, 45h, 6 days, 13 days, 21 days, and 43 days. These correspond to specific time scales on the swelling pressure kinetics.

The CT scan was acquired with a GE Phoenix v|tome|x m instrument at 200 kV/185 µA and 37 µm per pixel using standard cone beam acquisition and reconstruction. As a first approach, gray values were calibrated relatively to each other using a low absorption reference (PEEK) and an internal dense particle (accessory mineral).

Tomobento_1

Top BC : lab. conditions

89.7g powder
w=5.35%,
ρ_d~0.93 g/cm3

122.90g
pellets
w=5.1%,

h=33.2
mm
(initial)

Bottom BC: demineralized water (~70 cmH_2O)

Initial estimated dry density : 1.50 g/cm^3
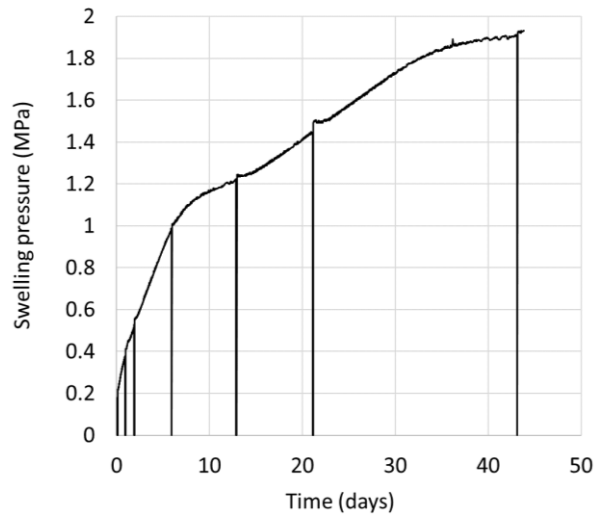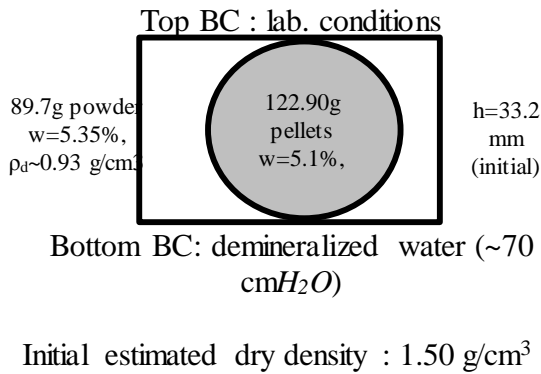
Figure 5-27. Sample properties and swelling pressure curve (straight lines indicate X-CT scans)

First qualitative observations on this test are (Figure 5-28):

- A confirmation of the rearrangement and compaction of the powder in the upper regions, and closing of the technological voids due to the initial swelling phase,
- Cracking in the pellet in the area of large humidity gradients, beyond the water front,
- The quick formation of a dense saturated layer controlling transport,
- The reaching of a homogeneous state relatively to X-CT as seen on the final scan.

However, some limits of this method are evidenced, and modifications implemented:

- Large transformations of the material exclude easy displacement measurements by Digital Volume Correlation (DVC) techniques. The mixing with powder of dense marker particles (ZrO2) at the scale of 200 µm in diameter allowing the use of particle tracking algorithms.
- Cone beam artefacts induce gray values not representative of the material true absorption in the top and bottom ends of the sample. The use of helical tomography can be used since it is devoid of cone beam artefacts.
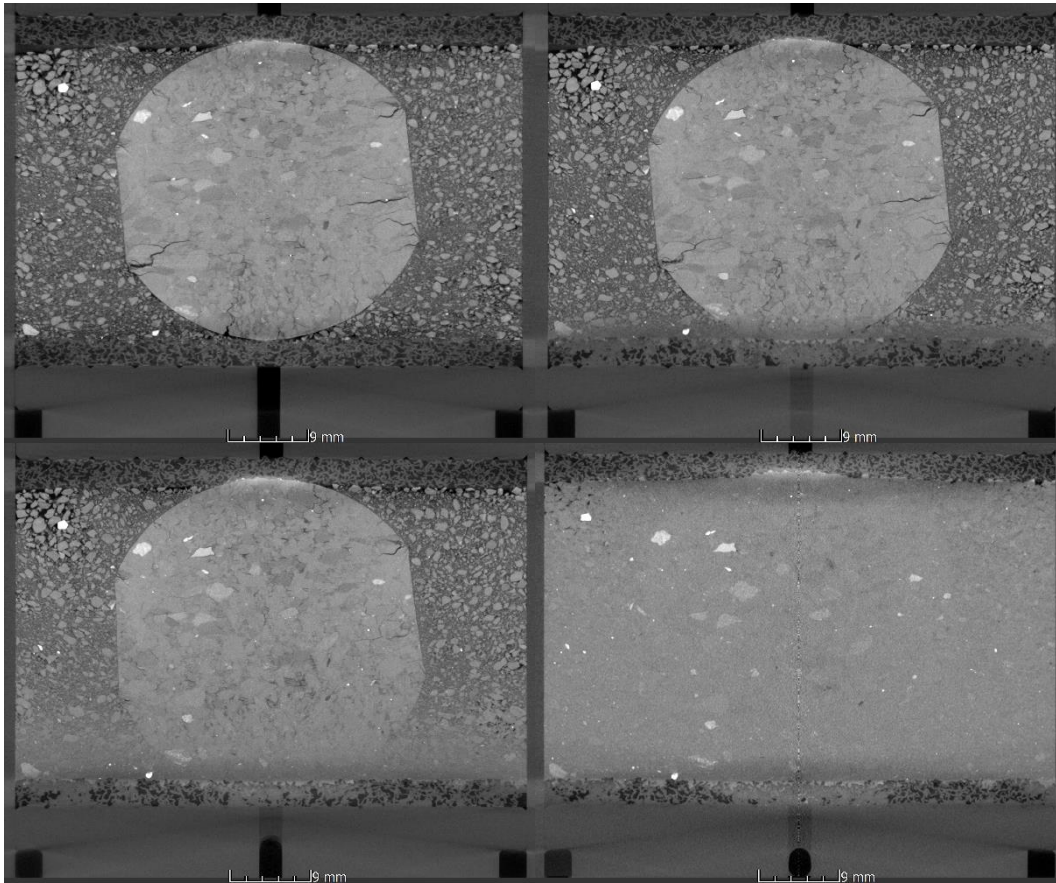
Figure 5-28. Vertical slices of the Tomobento_1 sample at 0h, 1h, 45h and 43 days

The modifications shown in Figure 5-29 are used in Tomobento_2 sample.

This test validates the choice of marker particles and the moderate level of artefacts. Some issues with higher beam hardening levels can be solved by using higher tube voltage and additional beam filtering.

Tomobento_2

Top BC : lab. conditions

80.28g pellets w=5.1%, ρ_d~2.12 g/cm3	
36.1g powder w=10.3%, ρ_d=0.93g/cm3	

Pellet/powder mix

h=28.2 mm (initial)

Bottom BC: demineralized water (~70 cmH_2O)
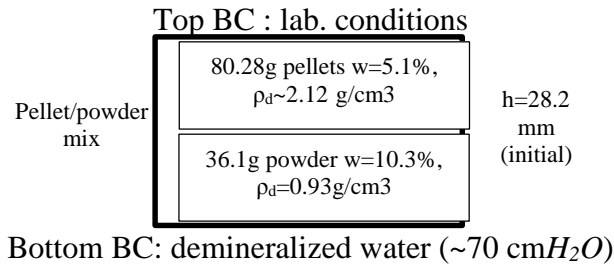
Initial estimated dry density : 1.519 g/cm³
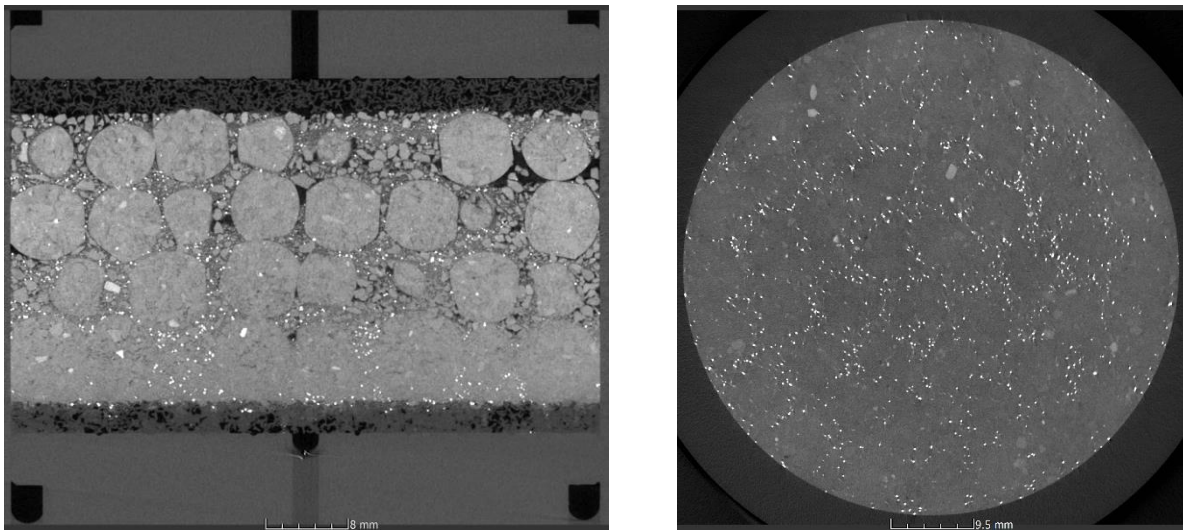
Figure 5-29. Sample description, vertical slice, and horizontal slice at the midplane of the first pellet layer, for the Tomobento_2 sample at 1-day hydration

5.3.3 Conclusions and perspectives

The use of X-CT to perform in-situ observations of the macroscopic phenomena in swelling tests of pellet/powder mixes is validated. Further work is needed for 3D measurements of the displacement field using particle tracking and/or Digital Volume Correlation and a quantitative analysis of the gray levels.

116

6 Influence of the degree of saturation on the shearing behaviour at the bentonite – steel interface (EPFL)

6.1 Background

The objective of this experimental study was to determine the shear strength of bentonite in its hygroscopic state and to get insight into the shearing behaviour of bentonite-steel interface at various saturation stages. In order to investigate these processes, a series of direct shear tests were carried out.

6.2 Materials and methods

6.2.1 Tested material

The tested material is MX80 bentonite in granular form, and it is described in section 1. Two granulometries (Fuller-type and unifractional) have been tested for shearing behaviour, these are shown in Figure 6-1.
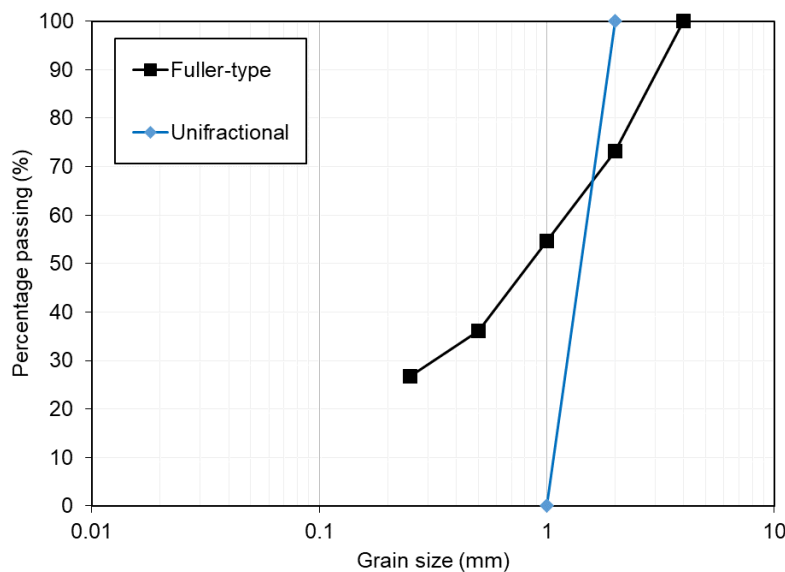
Figure 6-1. Grain size distribution of the tested samples

6.2.2 Experimental setup

Experimental set-up for the internal shearing

The tests of internal shearing were conducted using a commercially available direct shear device produced by GDS Instruments™.

Normal and shear forces can be controlled by two electromechanical force actuators, which can be used to pilot the tests in both displacement and force. Two load cells are installed to measure the vertical and horizontal loads that are applied to the sample. To measure the horizontal and vertical displacements, two LVDTs (Linear Variable Differential Transformers)

117

are used. The maximum vertical and horizontal force attainable is 5 kN, the maximum vertical displacement is ±12.5 mm and the maximum horizontal displacement is ±25.0 mm. The maximum vertical stress applicable is 2.47 MPa.

Testing set-up for the interface shearing

To investigate the influence of water content on the interface shearing, a shear box was equipped with a system allowing circulation of water in vapour phase through the sample under testing. The testing set-up is depicted in Figure 6-2. The lower part of the shearing box was replaced by a steel plate of dimensions 105 mm x 60 mm and a height of 16 mm. The roughness of steel plate surface is 1.6 μm. This set-up assures that during all the shearing process the contact area between the specimen and steel surface remain constant. This shear box, which can be seen in Figure 6-3, allows to introduce and circulate the vapour inside the sample. The size of the samples (square base of 30x30 mm and a maximum of 20 mm height), was chosen in order to minimize the time for the samples to reach equilibrium with the imposed relative humidity as well as to achieve a high vertical pressure. With this set up the maximum vertical stress applicable is 5.55 MPa.
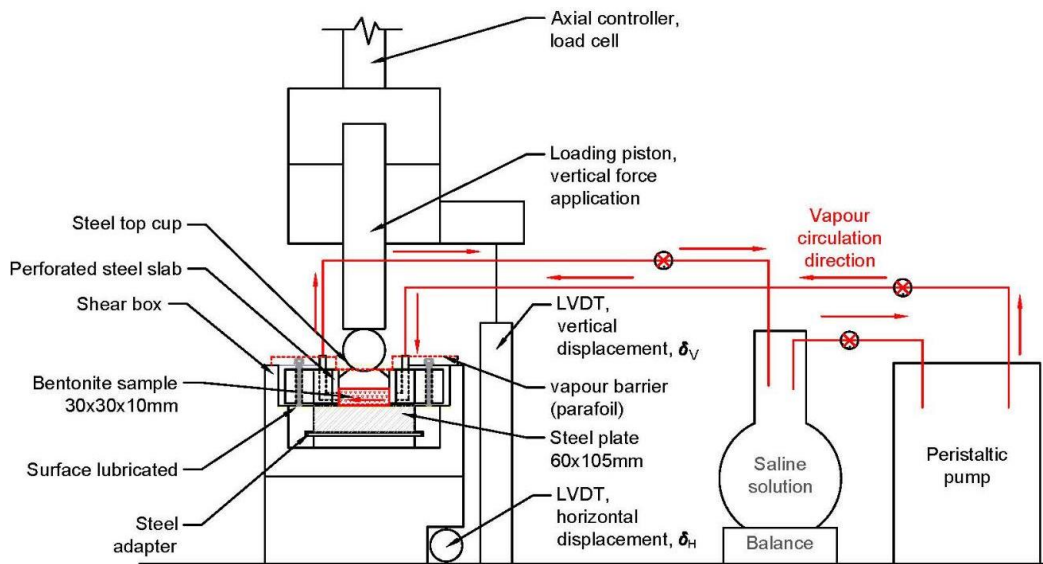
Figure 6-2. Experimental set-up for the interface shearing

118
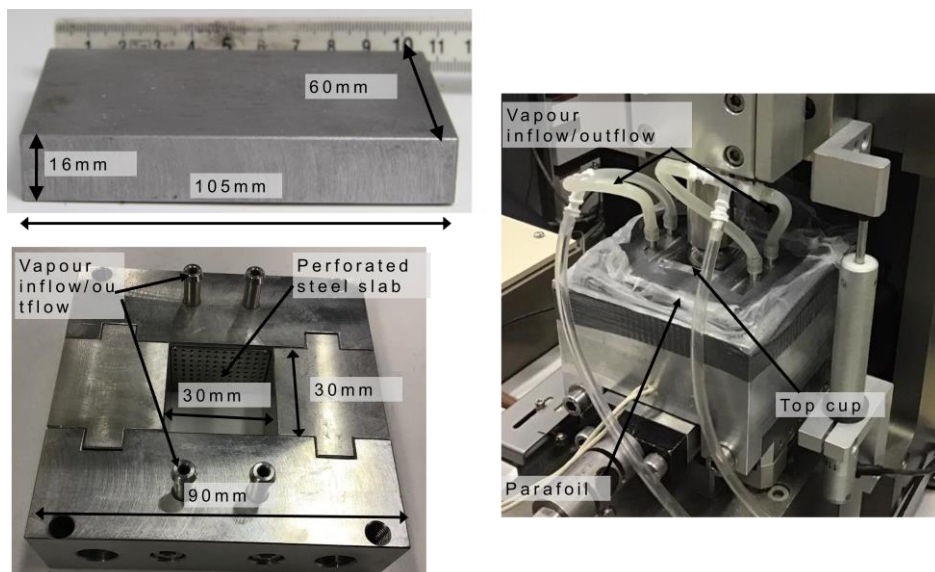
Figure 6-3. Parts of interface shear apparatus a) steel plate, b) modified upper box of shearing apparatus, c) sealed apparatus

6.2.3   Sample preparation

The granular bentonite was hydrated under free volume conditions in sealed glass containers applying vapour equilibrium technique (Figure 6-4). Total suctions of 11 MPa and 4 MPa were imposed by using respectively KNO3 and K2SO4 salts. Bentonite was subsequently poured into the direct shear box and compressed up to the desired vertical stress.
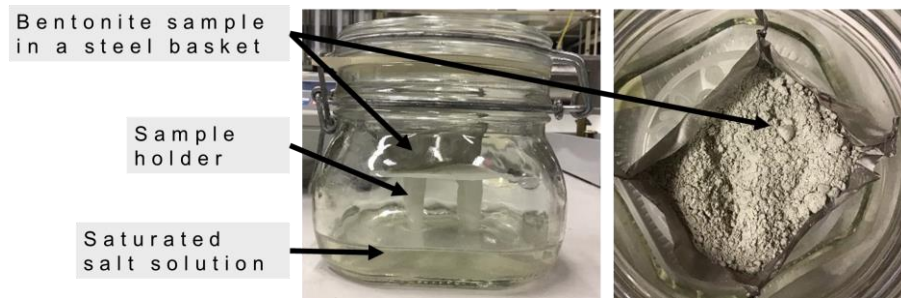
Figure 6-4. Volumetric free swelling hydration of bentonite applying VET

All tests were performed in temperature-controlled room where temperature changes were within 1°C, having a negligible impact on the imposed relative humidity.

6.2.4   Testing procedure

The first series of test included the internal (bentonite-bentonite) and interface (bentonite-steel) shearing of bentonite characterized by two granulations before hydration (total suction around 150 MPa). The thickness of the samples was of 20±1mm for soil-soil tests and 10mm ±1mm for the interface shearing tests. Table 6-1 summarises the roughness parameters related to these tests. Since two tested granulations present different average grain diameter, the interfaces vary with the relative roughness.

Table 6-1. Relative roughness of the steel-bentonite interfaces

Interface	D_{50} (mm)	Surface roughness R_{max} (µm)	Relative roughness $R_n(-)$
Steel / Fuller – type GSD	0.8	16	0.0020
Steel / unifractional GSD	1.5		0.0011

After pouring the material inside the shearing box, static compression up to 250 kPa, 500 kPa, 1000 kPa and 2000 kPa was performed for both internal shearing and interface shearing tests. Subsequently the shearing stage was performed.

The second series of tests aimed to study the influence of water content on the behaviour of steel-bentonite interface during shearing. After pouring the wetted granular bentonite into the shear box, the apparatus was connected to the vapour supply system and sealed with parafoil to maintain constant relative humidity during the test. Afterwards, compression was performed up to 250 kPa, 500 kPa, 1000 kPa and 2000 kPa of vertical stress, before proceeding to the shearing stage. The response upon compression is shown in Figure 6-5;

reproducibility of sample preparation can be verified by comparison with oedometric compression tests performed by Seiphoori (2014) on the same material.
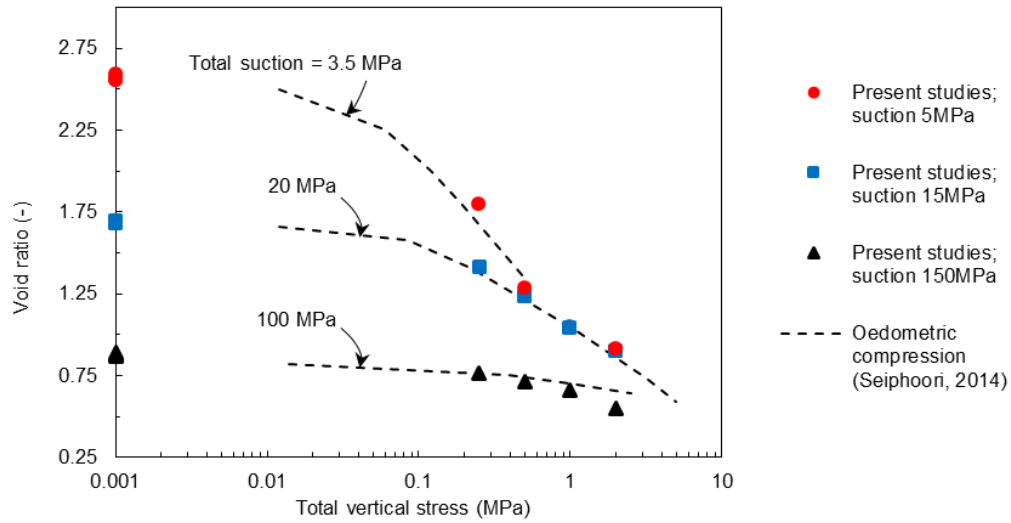
Figure 6-5. Response of the samples with Fuller-type granulation upon static compaction inside direct shear apparatus, in comparison with the oedometric compression tests performed by (Seiphoori, 2014)

6.3   Results

6.3.1   Influence of the granulation on the internal shearing and interface shearing

In Figure 6-6 the results of direct shear test of internal shearing of bentonite characterized by a Fuller–type granulation are shown. Horizontal stress (equivalently shear stress)-displacement curves are shown for each applied vertical stress together with the failure envelope of peak shear strength. The computed peak angle of internal friction is φ_{peak} =38° and the cohesion c =80kPa.
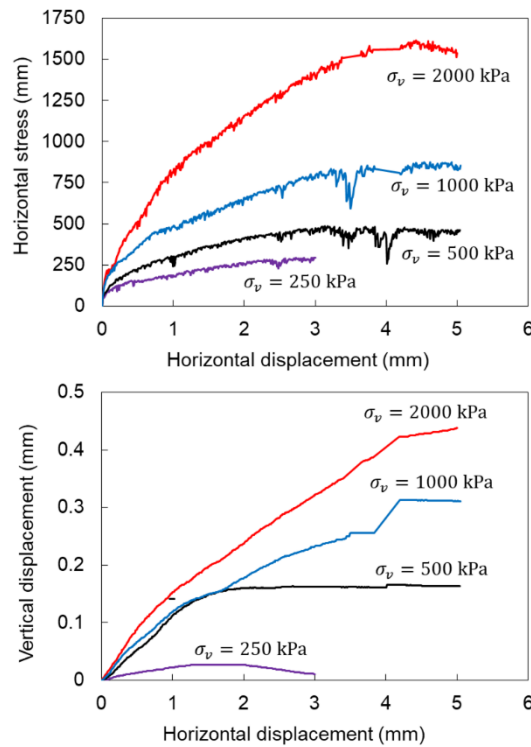
Figure 6-6. Internal shearing response of MX80 bentonite with Fuller-type granulation at hygroscopic water content

The contraction behaviour is also presented in terms of vertical displacement versus horizontal displacement curves. Upon shearing, regardless the applied vertical stress all samples contracted. For the samples sheared with vertical stresses up to 1000 kPa, the maximum shear stress remained constant until the test finished. A slight reduction of shear stress (after about 4.5 mm of horizontal displacement) was visible when shearing was performed under a vertical stress of 2000 kPa.

The results of internal shearing of bentonite characterized by a unifractional granulation are presented in Figure 6-7. As in the case of Fuller-type granulation, all samples contracted upon shearing. The maximum value of shear stress was achieved for a displacement of approximately 4 mm and remained constant until the end of the test. The peak angle of internal friction is 27° and the cohesion 83kPa.

In Figure 6-8 and 6-9 the results of the interface shearing of steel-bentonite with Fuller-type granulation and steel-bentonite with unifractional granulation respectively, are presented. Results in both figures were obtained upon shearing the material at hygroscopic conditions. For the two granulations, as in the case of internal shearing, the material contracted upon shearing. The maximum values of shear stress and of axial displacement at corresponding axial stress levels are lower than in the case of interface shearing. The values of the peak angle of interface shearing are δ =22° for the Fuller-type granulation and 19° for the unifractional granulation. A value of interface adhesion of c_{ad} =4 kPa is obtained by extrapolating the results of the Fuller-type granulation.
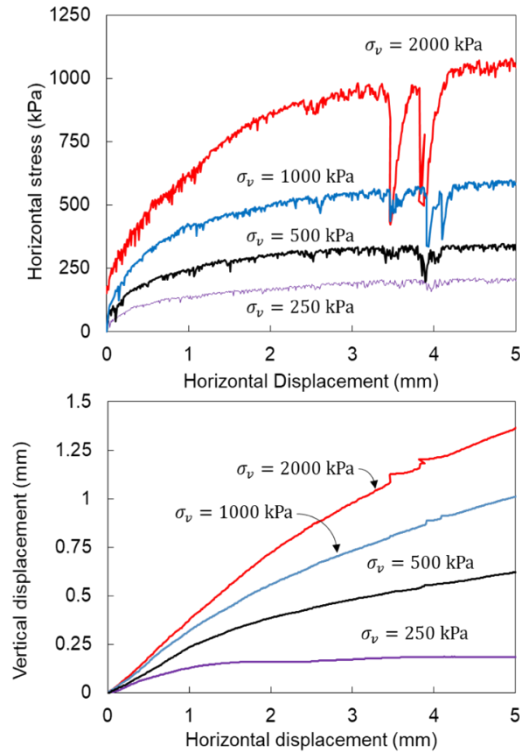
Figure 6-7. Internal shearing response of MX80 bentonite with unifractional granulation at hygroscopic water content
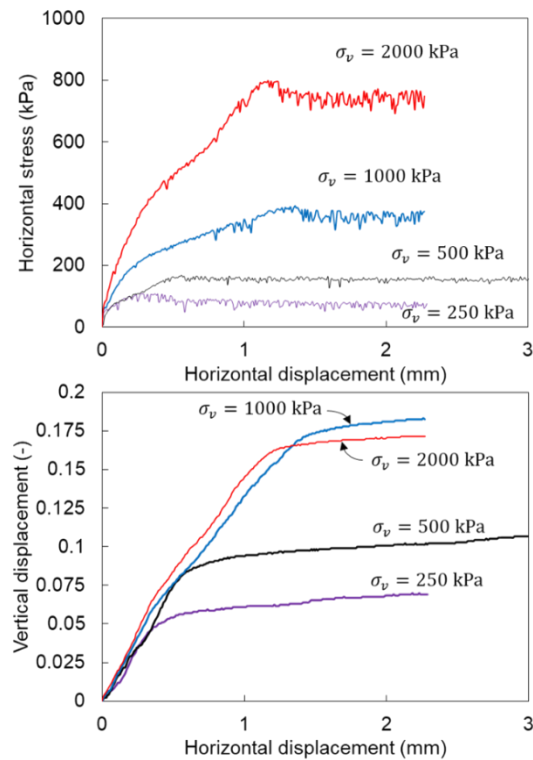
Figure 6-8. Results of bentonite-steel interface shearing, for granular bentonite with a Fuller-type granulation at hygroscopic conditions
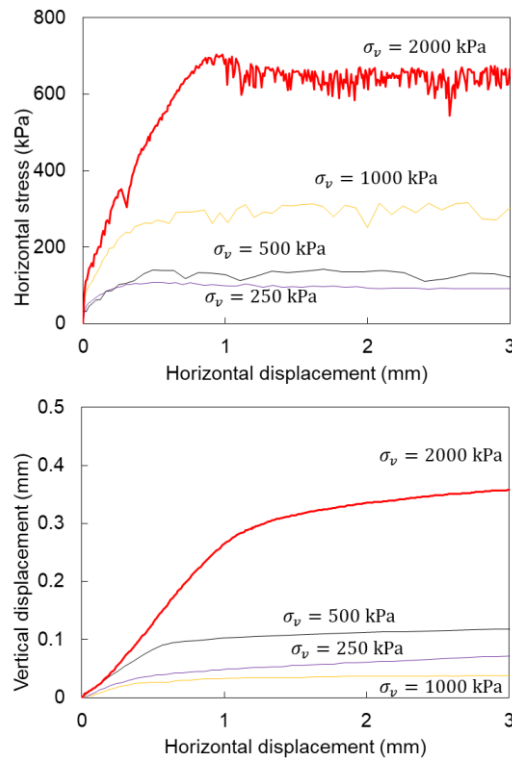
Figure 6-9. Results of bentonite-steel interface shearing, for bentonite with a unifractional granulations at hygroscopic water content

6.3.2 Influence of water content and suction on the response upon shearing

In Figure 6-10 the results of interface shearing for the samples characterized by initial total suction of 15 MPa and water content of 0.20 are presented. When shearing was performed under 250 kPa and 500 kPa of vertical stress, the maximum value of shear stress was achieved after 1 mm of horizontal displacement and remained constant until the end of the test. For higher values of applied vertical stress, namely 1000 kPa and 2000 kPa, a peak shear stress was reached followed by a reduction to a post-peak stress. The maximum value of the shear stress was obtained at 0.5mm of horizontal displacement for 1000 kPa and 2 mm for 2000 kPa. The sample behaved contractive during all the shearing stage (for pre-peak and post-peak shearing stages). The obtained peak angle of interface shearing is 22° and the interface adhesion is 58 kPa.

In Figure 6-11 the results of interface shearing of samples with initial total suction of 5 MPa and water content of 0.29 are presented. For samples sheared under vertical stresses of 500 kPa, 1000 kPa and 2000 kPa, a peak shear stress was obtained followed by a reduction to a post peak stress. For the sample sheared under a vertical stress of 250 kPa no considerable decrease of shearing stress is noticed. The samples showed contraction during all the shearing stages. The envelope reveals a peak angle of interface shearing of 17° and an interface adhesion of 168 kPa.
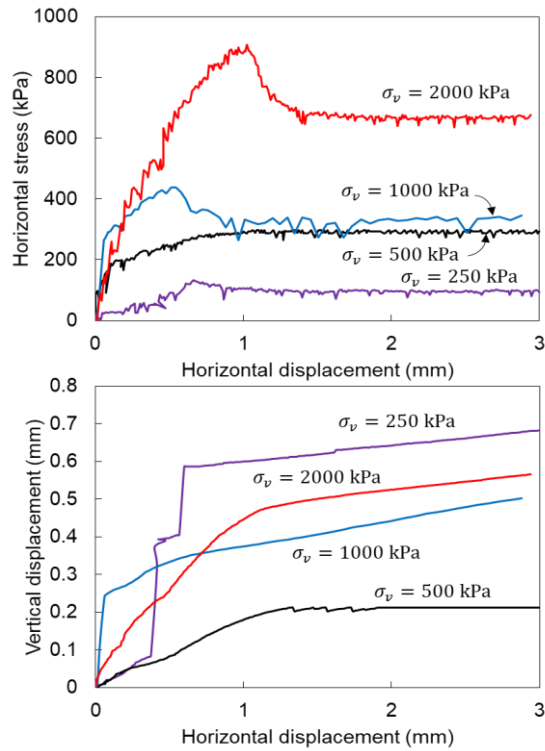
Figure 6-10. Results of bentonite-steel interface shearing, for bentonite with a Fuller-type granulation with a water content of 0.20 and total suction of 15 MPa
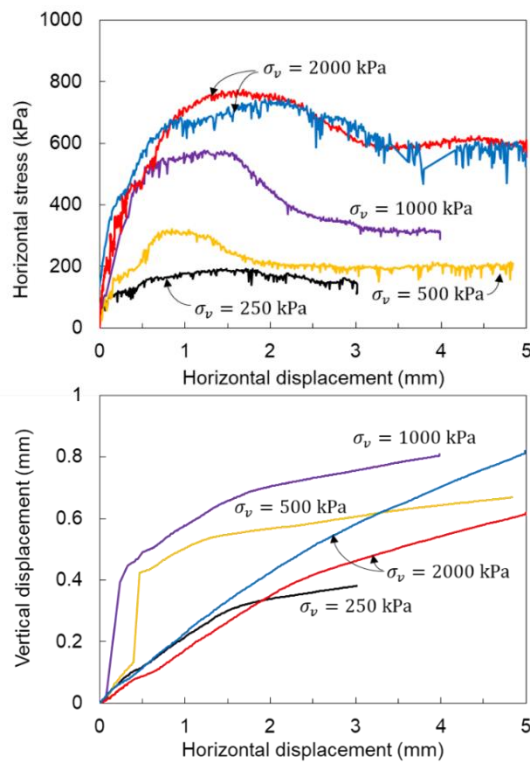
Figure 6-11. Results of bentonite-steel interface shearing, for bentonite with a Fuller – type granulation with a water content of 0.29 and total suction of 5 MPa

6.3.3 Discussion

Influence of the granulation on the response of the material on internal and interface shearing.

Table 6-2 provides a summary of the fitting parameters that are obtained from the envelopes of peak shear strength (maximum horizontal stress) from bentonite at hygroscopic state.

Table 6-2. Summary of results for shearing at the interface between different materials

Interface	Ψ (MPa)	φ_{peak} or δ_{peak} (deg)	c or c_{ad} (kPa)	$F_r = \frac{\delta_{peak}}{\varphi_{peak}}$ (-)
Fuller–type GSD / Fuller–type GSD		38	80	
Steel/Fuller–type GSD	150	22	10	0.6
Unifractional GSD / unifractional GSD		27	83	
Steel / Fuller–type GSD		19	-	0.7

Failure envelopes for the soil-soil and steel-soil interface shearing for Fuller-type granulation and unifractional granulation are depicted in Figure 6-12. For both granulations, the peak angle of interface friction is lower than the peak angle of internal friction. The friction ratio for the Fuller-type granulation is 0.60 and for the unifractional granulation is 0.70.
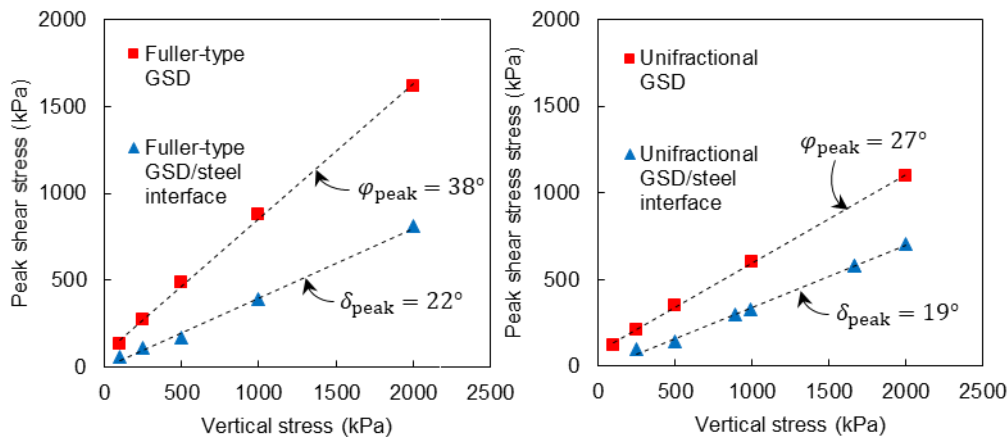
Figure 6-12. Failure envelopes of soil-soil and steel-soil interfaces for the bentonite of Fuller – type GSD (left) and unifractional GSD (right) at hygroscopic conditions

Influence of water content on the response on the interface shearing

The results of direct shear tests are presented in Figure 6-13 in the total normal stress–shear stress plane. In the range of 250-1000 kPa the shearing strength increased with increasing water content, mostly due to the increase of interface adhesion.
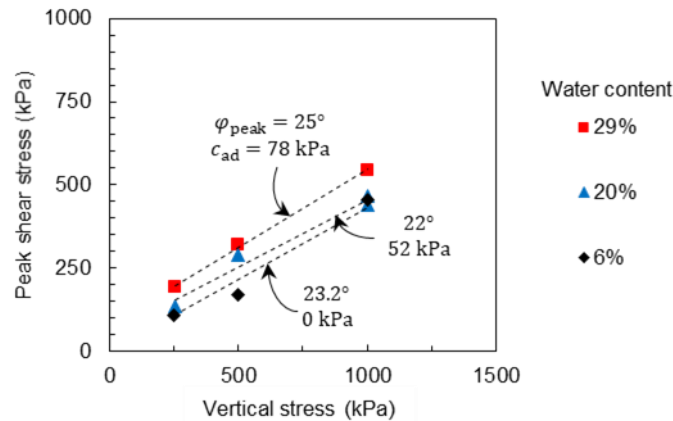
Figure 6-13. Peak failure at different water content in the net normal stress–shear stress plane from interface direct shear tests, considering interface shearing over the normal stress in the range 250-1000 kPa

6.3.4   Conclusions

The objective of this experimental study was to investigate the internal shearing of granular MX80 bentonite as well as the shearing at steel-bentonite interface. A series of direct shear tests were carried out to determine the internal shearing behaviour of the bentonite at hygroscopic conditions and the impact of the granulation of the soil. Moreover, the influence of water content and suction was investigated.

The following conclusions are drawn from this study:

1. At hygroscopic conditions, samples prepared following an unifractional GSD showed lower values of shear strength parameters in comparison to those prepared with a Fuller – type granulation.
2. For both tested granulations, the interface shearing strength of the material at hygroscopic state was lower than the internal shearing. For samples satisfying Fuller-type granulation, the value of friction ratio presented as a function of relative roughness follows the same trend as effective parameters of sand/steel interfaces shearing found in the literature.
3. All samples tested showed contraction upon shearing.
4. Samples characterized by a higher water content showed a higher peak of shearing strength when compared with samples of lower water content. The increase of strength appears to be governed by the increase of adhesion between steel-bentonite upon hydration.
5. The response upon shearing depends on water content and applied total stress. For samples at hygroscopic conditions, after achieving the maximum value of shear stress, no specific decrease was noted. For samples with water content between 0.2 to 0.29, a peak value of shear strength was followed by a decrease up to post peak value; this was particularly noticeable at high values of vertical stress upon shearing.
6. Peak shear strength increased with increasing water content.

7 Conclusions and future work

7.1 Conclusions

The experiments performed in the frame of Beacon are aimed at obtaining a more complete cognition of bentonite behaviour – by investigating different wetting dynamics or load scenarios, looking at different granulations and inhomogeneous systems or at different bentonite types, and by developing new methods of measurement. The ongoing work has led to the following specific conclusions.

7.1.1 Hydro-mechanical behaviour of macroscopically homogeneous bentonite material

EPFL investigated the influence of initial granulometry on the final state of resaturated bentonite samples. While swelling pressure of confined samples was only influenced by the differences in initial dry density of the differently grained samples, free swelling experiments showed a higher volume increase of lower density unifractional samples compared to bifractional samples with a higher initial density. This result indicates that not only dry density, but also initial granulation should be considered when analysing swelling phenomena.

A second set of experiments addressed the Influence of different hydro-mechanical paths on final macroscopic properties and microstructure of the bentonite. Granular bentonite with a fuller-type granulation was either (a) hydrated under constant low stress (nearly free swelling), and stress was afterwards increased, or (b) hydration was performed at constant volume conditions, and stress was afterwards increased to the same value as in (a). A clear effect of the stress path followed was observed comparing the final state of samples. Despite having the same degree of saturation and being subjected to the same final value of vertical stress, a difference in void ratio of 0.13 (15% of initial void ratio) between the two samples was obtained.

The porosity distribution of all samples used as determined after experiment completion. For all tested granulations, the dominant size of micro porosity is in similar range regardless of applied wetting scenario or stress level. The applied hydro-mechanical paths as well as the initial granulation influenced mostly the inter-aggregate (macro) porosity.

The microstructure of the material saturated in free swelling conditions seems to be noticeably modified in comparison with the material in initial hygroscopic state. After free swelling saturation, no outlines of initial grains were visible. For the case of isochoric saturation, full development of clay aggregates was not possible. The grains swelled in limited range. The initial structure characterised by the compacted grains was rather preserved after full saturation and outlines of the as – poured state can be distinguished.

CU and CTU performed experiments on the Czech Cerny vrch bentonite in order to provide calibration data for the development of constitutive models. CU performed constant load tests of samples with different dry densities, from nearly free swelling to maximum loads of 4 MPa. In addition to void ratio change, water retention properties, porosimetry and ESEM were performed. CTU performed additional constant volume tests on homogeneous, dual-density and granular bentonite samples, measuring total pressure evolution, hydraulic conductivity, saturation evolution and final density and water content distribution. Thus, the dataset on the Cerny vrch bentonite was considerably broadened.

7.1.2   Swelling into limited void

Four experiment teams have been working on bentonite swelling into a limited void. JYU and KIT are currently concentrating on the development of new measurement techniques: Particle movement tracking (JYU) and small-scale spatially-resolved swelling pressure measurement. Both approaches are very promising and are expected to provide valuable results to the Beacon project.

BGS and CIEMAT performed test series of bentonite swelling, using bentonite blocks in isochoric cells leaving a void at one end of the sample. BGS investigated the influence of the ratio between block and void volume at ambient and elevated temperature, concentrating on swelling pressure and pore pressure evolution. They found that swelling pressure evolution is spatially complex, and at ambient temperature a variance remains even after 100 days. Sidewall friction seemed important in these tests. At elevated temperature, however, a faster stress equilibration and a slightly more homogeneous moisture content distribution was achieved.

CIEMAT concentrated on the effect of hydration dynamics, performing experiments with liquid water resaturation and resaturation by a vapour phase at two differen suction states at ambient temperature. The experiments were performed as test series of different duration, i.e., they were stopped at different intermediate saturation states. Then, water content distribution, dry density distribution, and pore size distribution could be determined. An important finding was that the quicker the hydration took place, the steeper and more persistent the gradients in water content and dry density were. Hydration led to an overall increase in void ratio, and both the micropores (< 200 nm) and macropores ratio increased. At quick hydration (i.e., using liquid water), however, the volume of larger pores increased much more significantly.

Since BGS and CIEMAT concentrated on different measurements and phenomena, a direct comparison of results is not possible, instead, the experiments complement each other. They do, however, agree in two observations:

- In all experiments, the bentonite was able to fill the complete void, no open space remained.
- In all experiments, an inhomogeneous water content (and thus dry density) distribution remained.

In CIEMAT's vapour tests, resaturation was from the "gap side", while in the liquid tests, the void was opposite to the resaturation face. The highest moisture contents, however, were always measured on the side of the resaturation face.

7.1.3   Binary mixtures or artificial inhomogeneities

CIEMAT and CEA performed hydration tests under constant volume conditions using initially heterogeneous samples. CEA performed small-scale dual density tests in diameter 57 mm with superimposed blocks of MX-80 bentonite compacted at different dry density or pellets/powder mixes. CIEMAT performed tests in 10x10 cm cylindrical samples half of which were composed of pellets and the other half of a compacted block of FEBEX bentonite. The tests run for different periods of time and the analysis of both sets of results allows to draw the following conclusions at this stage of the WP4 work programme:

- The bentonite sample initial fabric (mix of different dry density blocks, pellets and blocks, etc.) does not seem to affect the axial pressure development pattern, which systematically starts with a sharp initial increase, followed by a stabilization/attenu- ation phase leading to the final increase (e.g. Fig. 3-3 and Fig. 4-5). This kind of pattern has been repeatedly observed in pellets or compacted samples.

- Hydration leads to water content and dry density gradients that tend to soften over time, although complete homogenization was not reached in any test, not even in those in which full saturation was reached (at time scales accessible in the lab). The local stresses in bentonite samples also exhibit large heterogeneities and do not converge at the same accessible time scales.
- Hydration speed seems to control these persistent heterogeneities: the higher the rate, the steeper the dry density gradient in the direction of flow.
- Residual heterogeneities are not dependent on (or have a simple relation with) the initial sample heterogeneity.
- The volume of pores larger than 200 nm increases with hydration when the bentonite is allowed to swell, i.e. when its dry density decreases.

Final dry density gradients seem mostly driven by the speed of the hydration process and not directly by the initial heterogeneities. In turn, this hydration process (and the time available for water redistribution inside the bentonite) can be controlled either by the boundary conditions or by the initial heterogeneities. The reason behind may be that if the deformation that takes place initially is very large, it affects the macrostructure and becomes irreversible, conditioning the subsequent evolution of the system, as shown by porosimetry measurements. This would be supported by the fact that it is the macropore volume that gets mostly modified as a result of the initial hydration and swelling. Double-structure models considering the interaction between the micro and macrostructure would be able to explain this kind of behaviour.

7.1.4 Influence of the degree of saturation on the shearing behaviour at the bentonite – steel interface

EPFL investigated the internal shearing of granular MX80 bentonite as well as the shearing at a steel-bentonite interface, for a fuller-type and a unifractional grain size distribution. For both tested granulations, the interface shearing strength of the material at hygroscopic state was lower than the internal shearing. Unifractional samples showed lower values of shear strength parameters in comparison to those prepared with a Fuller-type granulation. Samples characterized by a higher water content showed a higher peak of shearing strength when compared with samples of lower water content. The increase of strength appears to be governed by the increase of adhesion between steel-bentonite upon hydration.

7.2 Future work

A large amount of information has already been obtained from the Beacon experimental work and can be used by for model development and validation purposes. However, not all of the investigations are completed yet – as can be expected at project mid-term. Experimentation is going on, and especially the development of new or improved test methods, like particle tracking, small-scale pressure measurement or X-CT in-situ observation needs further attention.

More detailed information of the work planned in the future is given in the previous chapters of this report. The next half of the Beacon project can be expected to yield further important insight into bentonite behaviour.

References

ASTM D2435/D2435M-11. 2011. "Standard Test Methods for One-Dimensional Consolidation Properties of Soils using Incremental Loading." ASTM International: West Conshohocken, PA.

ASTM 2004. C914-95: Standard test method for bulk density and volume of solid refractories by wax immersion. West Conshohocken, PA, USA: ASTM International.

Bucher, F., Müller-Vonmoos, M., 1989. Bentonite as a containment barrier for the disposal of highly radioactive wastes. Applied Clay Science 4, 157–177.

Delage, P., Howat, M. D. & Cui, Y. J. 1998. The relationship between suction and swelling properties in a heavily compacted unsaturated clay. Engng Geol. 50, No. 1–2, 31–48.

Delage, P., Lefebvre, G., 1984. Study of the structure of a sensitive Champlain clay and of its evolution during consolidation. Can. Geotech. J. 21, 21–35. https://doi.org/10.1139/t84-003

Feligha, M., Hammoud, F., Belachia, M., Nouaouria, M.S., 2016. Experimental Investigation of Frictional Behavior Between Cohesive Soils and Solid Materials Using Direct Shear Apparatus. Geotechnical and Geological Engineering 34, 567–578. https://doi.org/10.1007/s10706-015-9966-5

Ferrari, A., Favero, V., Laloui, L., 2016. One-dimensional compression and consolidation of shales. International Journal of Rock Mechanics and Mining Sciences 88, 286–300.

Ferrari, A., Laloui, L., 2013. Advances in the testing of the hydro-mechanical behaviour of shales, in: Multiphysical Testing of Soils and Shales. Springer, pp. 57–68.

Gens, A., Alonso., E., 1992. A framework for the behaviour of unsaturated expansive clays. Canadian Geotechnical Journal 1013–1032.

Goldstein, J., 2017. Scanning electron microscopy and x-ray microanalysis, 4th edition. ed. Springer Science+Business Media, LLC, New York, NY.

Gutiérrez-Rodrigo V, 2018. Transporte de gas en materiales de barrera. Tesis Doctoral. Universidad Complutense de Madrid. Colección Documentos CIEMAT. ISBN: 978-84-7834-802-2. Madrid, 303 pp.

Hamid, T.B., Miller, G.A., 2009. Shear strength of unsaturated soil interfaces. Can. Geotech. J. 46, 595–606. https://doi.org/10.1139/T09-002

Hausmannová, L., Hanusová, I., Dohnálková, M. (2018). Summary of the research of Czech bentonites for use in the deep geological repository – up to 2018, TZ 309/2018/ENG, SÚRAO

Imbert C, Villar MV, 2006. Hydro-mechanical response of a bentonite pellets/powder mixture upon infiltration. Applied Clay Science 32: 197-209.

Juang, C. H. & Holtz, R. D. 1986. A probabilistic permeability model and the pore size density function. Int. J. Numer. Analyt. Methods Geomech. 10, No. 5, 543–553.

Karnland, O., Nilsson, U., Weber, H., Wersin, P., 2008. Sealing ability of Wyoming bentonite pellets foreseen as buffer material – Laboratory results. Physics and

Chemistry of the Earth, Parts A/B/C, Clays in Natural & Engineered Barriers for Radioactive Waste Confinement 33, S472–S475.

Lin, B. & Cerato, A. B. 2014. Applications of SEM and ESEM in microstructural investigation of shale-weathered expansive soils along swelling-shrinkage cycles. Engng Geol. 177, 66–74.

Lloret, A., Villar, M.V., Sánchez, M., Gens, A., Pintado, X., Alonso, E.E., 2003. Mechanical behaviour of heavily compacted bentonite under high suction changes. Géotechnique 53, 27–40. https://doi.org/10.1680/geot.2003.53.1.27

Montes-H, G. 2005. Swelling–shrinkage measurements of bentonite using coupled environmental scanning electron microscopy and digital image analysis. J. Colloid Interface Sci. 284, No. 1, 271–277.

Plötze, M., Weber, H.P., 2007. ESDRED: Emplacement tests with granular bentonite MX-80 (No. NAB 07-24), Laboratory results from ETH Zürich. Wettingen, Nagra.

Potyondy, J.G., 1961. Skin Friction between Various Soils and Construction Materials. Géotechnique 11, 339–353. https://doi.org/10.1680/geot.1961.11.4.339

Romero, E., Della Vecchia, G. & Jommi, C. 2011. An insight into the water retention properties of compacted clayey soils. Géotechnique 61, No. 4, 313–328.

Romero, E., Gens, A., Lloret, A., 1999. Water permeability, water retention and microstructure of unsaturated compacted Boom clay. Engineering Geology 54, 117–127. https://doi.org/10.1016/S0013-7952(99)00067-8

Sánchez M, Gens A, Guimarães L, Olivella, S, 2005. A double structure generalized plasticity model for expansive materials. International Journal for Numerical and Analytical Methods in Geomechanics 29: 751–787. DOI:10.1002/nag.434.

Seiphoori, A., 2014. Thermo-hydro-mechanical characterisation and modelling of MX-80 granular bentonite. PhD Thesis. École Polytechnique Fédérale de Lausanne, Switzerland.

Seiphoori, A., Ferrari, A., Laloui, L., 2014. Water retention behaviour and microstructural evolution of MX-80 bentonite during wetting and drying cycles. Géotechnique 64, 721–734. https://doi.org/10.1680/geot.14.P.017

Shakir, R.R., Zhu, J., 2009. Behavior of compacted clay-concrete interface. Front. Archit. Civ. Eng. China 3, 85–92. https://doi.org/10.1007/s11709-009-0013-6

Sinnathamby, G., Korkiala-Tanttu, L., Gallardo Forés, J., 2014. Interface shear behaviour of tunnel backfill materials in a deep-rock nuclear waste repository in Finland. Soils and Foundations 54, 777–788. https://doi.org/10.1016/j.sandf.2014.06.027

Sinnathamby, G., Korkiala-Tanttu, L., Salvador, L.T., 2015. Shear resistance of bentonite backfill materials and their interfaces under varying hydraulic conditions in a deep rock nuclear waste repository. Applied Clay Science 104, 211–220.

Subba Rao, K.S., Allam, M.M., Robinson, R.G., 2000. Drained shear strength of fine-grained soil–solid surface interfaces. Proceedings of the Institution of Civil Engineers - Geotechnical Engineering 143, 75–81. https://doi.org/10.1680/geng.2000.143.2.75

Subba Rao, K.S., Rao, K.S.S., Allam, M.M., Robinson, R.G., 1998. Interfacial friction between sands and solid surfaces. Proceedings of the Institution of Civil Engineers - Geotechnical Engineering 131, 75–82. https://doi.org/10.1680/igeng.1998.30112

Sun, H., Mašín, D., Najser, J., Neděla, V. and Navrátilová, E., 2018. Bentonite microstructure and saturation evolution in wetting–drying cycles evaluated using ESEM, MIP and WRC measurements. Géotechnique, pp.1-14.

Tang, A.-M., Cui, Y.-J., Eslami, J., Défossez, P., 2009. Analysing the form of the confined uniaxial compression curve of various soils. Geoderma 148, 282–290. https://doi.org/10.1016/j.geoderma.2008.10.012

Thewes, M., 1999. Adhäsion von Tonböden beim Tunnelvortrieb mit Flüssigkeitsschilden [adhesion of clay soil during tunneling with liquid shields] (PhD Thesis). Ph. D. thesis, Universitaet Wuppertal, Wuppertal, Germany.

Tsubakihara, Y., Kishida, H., 1993. Frictional behaviour between normally consolidated clay and steel by two direct shear type apparatuses. SOILS AND FOUNDATIONS 33, 1–13. https://doi.org/10.3208/sandf1972.33.2_1

Tsubakihara, Y., Kishida, H., Nishiyama, T., 1993. Friction between cohesive soils and steel. Soils and Foundations 33, 38–49.

Vanapalli, S.K., Fredlund, D.G., Pufahl, D.E., Clifton, A.W., 1996. Model for the prediction of shear strength with respect to soil suction. Canadian Geotechnical Journal 33, 379–392.

Villar MV, 2007. Water retention of two natural compacted bentonites. Clays and Clay Minerals 55(3): 311-322.

Villar MV, Gómez-Espina R, Gutiérrez-Nebot L, 2012. Basal spacings of compacted bentonite. Applied Clay Science 65-66: 95-105.

Villar MV, Carbonell B, Martín PL, Gutiérrez-Álvarez C, Barcala JM, 2018. Gas permeability of bentonite samples of the FEBEX Dismantling Project (FEBEX-DP). Informe Técnico CIEMAT 1431. Madrid, 89 pp.

Zimnik, A.R., van Baalen, L.R., Verhoef, P.N.W., Ngan-Tillard, J.M., 2000. The adherence of clay to steel surfaces 7.

Zumsteg, R., Puzrin, A.M., 2012. Stickiness and adhesion of conditioned clay pastes. Tunnelling and Underground Space Technology 31, 86–96. https://doi.org/10.1016/j.tust.2012.04.010